Structural Integrity Assessment of Wire Arc Additively Manufactured Low Carbon Steel Components for Marine Applications

A Thesis submitted for the Engineering Doctoral Degree in

Renewable Energy Marine Structures (REMS EngD)

by

Anna Ermakova

Glasgow, April 2023

Department of Naval Architecture, Ocean & Marine Engineering

University of Strathclyde, United Kingdom

G1 1XQ

Abstract

In order to increase manufacturing efficiency of large engineering structures, wire arc additive manufacturing (WAAM), that belongs to direct energy deposition (DED) family of additive manufacturing (AM) processes, has been developed. This manufacturing method has significant potential to improve material design and efficiency of structural components, subsequently reducing production cost and lead times. Some industries, such as aerospace and automotive, have already employed WAAM technology into their manufacturing processes. However, insufficient testing data on WAAM components performance for various materials and operational conditions is one of the main barriers to rapid adoption of WAAM technology in the wider range of industrial applications. Particularly, the sensitivity of mechanical and fatigue properties of WAAM materials to corrosive environment needs to be understood to adopt WAAM technique in marine applications, for instance, in offshore wind structures. Moreover, the WAAM method involves repetitive welding, resulting in high stress concentration between adjacent welded layers and residual stress fields in WAAM components. Since welded joints in offshore constructions are known to be weak points for fatigue failures and crack initiation, it is necessary to conduct the structural integrity assessment of WAAM built steel components and compare their performance with the currently used wrought materials, to investigate the suitability of the WAAM technique for offshore applications.

This thesis investigates the structural integrity of WAAM built ER70S-6 and ER100S-1 steel specimens, defining the hardness, tensile, fracture toughness, fatigue crack growth, uniaxial, torsion and multiaxial fatigue properties. Aiming to make a contribution for marine applications, corrosion-fatigue crack growth assessment has been also conducted, along with investigation of fracture characteristics of components previously exposed to corrosive environment. Due to heterogeneity of WAAM built components, the results from this study were analysed with respect to the extraction location and orientation from the WAAM walls. Different load levels were examined for fatigue crack growth tests, confirming the sensitivity of specimen behaviour. The obtained trends were compared with the corresponding recommended lines from the standards and with variety of data sets available in the literature on performance of wrought carbon steels which are widely used in offshore structures, to draw conclusions on suitability of WAAM steel components for the offshore industry. Furthermore, recognising the limitations of the welding based WAAM technique, life enhancement methods were considered, introducing rolling and laser shock peening as post-manufacturing surface treatments techniques. The efficiency of these methods was analysed by examining the fatigue crack growth and corrosion-fatigue crack growth performance of the treated specimens. The residual stress trends were measured by means of neutron diffraction and X-ray scattering to quantify the introduced changes after surface treatment application. Throughout the research, comprehensive microstructural investigations were conducted, including fractography analysis, evaluating the fracture and fatigue mechanisms, using optical and scanning electron microscope. The conclusions from this research have resulted in several journal publications, also presented in the thesis, that contribute to the overall understanding of WAAM steel components behaviour and extending the application of WAAM technology to the marine environments in the future.

Acknowledgements

First and foremost, I would like to express my sincere gratitude to my supervisor, Prof Ali Mehmanparast, for his continuous academic support, guidance, and tutelage during my EngD journey. His unconditional support has been a constant source of encouragement in pushing my boundaries and succeeding at the highest level and for that, I am thankful.

My gratitude extends to Assoc Prof Javad Razavi and Prof Filippo Berto from NTNU for conducting the fatigue tests in their laboratory, for valuable feedback on my work, and for providing an inspiring placement at their university. I would also like to thank Dr Supriyo Ganguly from Cranfield University for his expertise in welding and material science that greatly influenced and benefited my project. Over the past four years all of us have become a great team together, which is reflected in many of our joint publications.

I am also grateful to EPSRC UKRI for funding my EngD project through the REMS CDT and for making it possible for me as an international student to conduct research in the UK.

Special thanks go to Jarryd Braithwaite, the technical expert at Cranfield University, for his continuous assistance in my experiments and for being a reliable contact throughout my research. I wish to also thank Senior Technical Officer Steve Pope from Cranfield University for his microscopy services and kind attitude to students.

I am very grateful to be a part of the REMS family and would like to specially thank them for sharing this journey with me, providing friendship, and supporting each other.

Above all, I am grateful to my family, for their unconditional love and belief in me. Special thanks to my husband Sourya Ghosh, who taught me that impossible is possible with hard work and a little patience.

Declaration

I hereby declare that this thesis is the result of my original research and has not been previously submitted for examination which has led to the award of a degree. However, the core chapters of this thesis ‘by publication’ consist of papers that have been submitted for publication, have been accepted for publication, or have already been published, as have been acknowledged in the text accordingly. Information derived from the published and unpublished work of others has been acknowledged in the text and references are given in the list of sources.

Contents

List of Figures

List of Tables

Nomenclature

a_0	initial crack length in CT specimens
a_i	instantaneous crack length
$a_{i,p}$	crack length after pre-fatigue cracking
$a_{f,c}$	final crack length (compliance data)
$a_{f,op}$	final crack length (fracture surface)
A_p	plastic area
Δa	crack extension
B	total thickness of CT specimens
B_e	effective thickness
B_n	net thickness
C	material constant in the Paris law equation
C_i	instantaneous unloading compliance
d	lattice spacing
d_0	Stress-free reference point for lattice spacing
da/dN	fatigue crack growth rate
D	gripping diameter
E	Young's modulus
F_{max}	maximum load for pre-fatigue cracking
H	height of CT specimens
hkl	Miller indices
J	elastic-plastic fracture mechanics parameter
J_{IC}	fracture toughness
K	stress intensity factor
k	inverse slope in S-N curve
K_{eff}	effective stress intensity factor
K_{max}	stress intensity factor corresponding to P_{max}
ΔK	stress intensity factor range
K_{RS}	residual stress intensity factor
L	length of uniaxial cylindrical specimens
m	material constant in the Paris law equation
N	number of cycles
N_f	number of cycles to failure
n	Paris-law constant
P_{max}	maximum load
P_{min}	minimum load
R	load ratio
R^2	Coefficient of determination
T_σ	Scatter index
W	width of CT specimens

ε	residual strain
$\varepsilon_{f,axial}$	axial strain
ε_{ROA}	reduction of area
η	geometry dependent function
θ	scattering angle
λ	biaxiality ratio
λ_n	neutron wavelength
ν	Poisson's ratio
$\Delta\sigma$	stress range
$\Delta\sigma_{50\%}$	fatigue strength at 2×10^6 cycles
σ_{eff}	effective stress
σ_i	stress component
σ_{max}	maximum stress
σ_{UTS}	ultimate tensile strength
σ_Y	yield stress
Φ	phase angle
AM	Additive Manufacturing
AV	Average data
B	Bottom
BFS	Back Face Strain measurement technique
BM	Beach Marking
CFCG	Corrosion-fatigue crack growth
C(T)	Compact Tension specimen
CMT	Cold Metal Transfer
DED	Directed Energy Deposition
DIC	Digital Image Correlation
EBSD	Electron Backscatter Diffraction
EDM	Electrical Discharge Machining
FEA	Finite Element Analysis
FCG	Fatigue Crack Growth
H	Horizontal
HAZ	Heat Affected Zone
IPF	Inverse pole figures
LLD	Load Line Displacement
LP	Laser peening surface treatment
MN	Mean line
MUD	Multiple of uniform density
ND	Neutron diffraction
R	Rolling surface treatment
SB	Smooth round bars
SD	Standard Deviation
SEM	Scanning Electron Microscope
SEN(B)	Single Edge Notched Bend specimen
SIF	Stress Intensity Factor
T	Top

UTS	Ultimate Tensile Strength
V	Vertical
WAAM	Wire + Arc Additive Manufacturing
XR	X-ray

Chapter 1 : Introduction

Additive manufacturing (AM) is a relatively new layer-by-layer production technique that enables functionally superior designs at a lower cost with increased productivity and sustainability, and it is poised to revolutionise many industries around the world. By addressing current manufacturing challenges and geometrical constraints, AM can be viewed as an alternative fabrication method for complex engineering components and structures. The new AM technology allows the creation of hybrid components made of various alloys that are deposited in a form of powder or wire. The AM technique is rapidly developing from a simple prototyping method to production and repair of the key structural components. Furthermore, this method is more sustainable and significantly reduces material waste since it adds material layer-by-layer instead of removing it from a manufactured workpiece. Depending on the type of the selected AM technique, deposition process, layer thickness and material, mechanical and microstructural characteristics of the final part may vary.

Wire and arc additive manufacturing (WAAM) is one of the existing AM techniques, that uses an electric or plasma arc to melt a metallic wire at a regulated rate to create a multi-layer component. It is well-known as a low-cost method that achieves the highest deposition rates of several kilograms of metal wire per hour and, hence, is suitable for large-scale production. The WAAM technique does not require an expensive conventional manufacturing set-up and equipment, and the production process is conducted by a robotic arm in open air, which makes it suitable for manufacturing and repair in remote areas, such as offshore platforms. Moreover, compared with powder-based AM techniques, using wire in WAAM poses less safety concerns.

On the other hand, in addition to the benefits listed above, this approach may have a number of drawbacks. One of them is surface roughness and subsequent dimensional inaccuracies that require post-processing. Also, this method is solely based on a welding process that deposits one layer of metal on top of another while continuously re-heating and cooling down the manufactured part. As a result, microstructural homogeneity and mechanical isotropy are uncertain. Furthermore, the associated weld flaws could be weak points where fracture and fatigue failure could occur. Evaluating the impact of welding procedures integrated into the WAAM process on mechanical and fracture parameters of the built component in comparison to those obtained from wrought material is a significant challenge in the structural integrity of WAAM components. Moreover, to minimise the safety risks, the metallurgical differences, microstructural variations, and locked-in residual stresses must be carefully examined and categorised in addition to the mechanical response, before using such components in critical applications.

The WAAM technology has been under development and study since 1990, gaining popularity in various industries, including aerospace and automotive. Consequently, the available testing data in the literature predominantly focuses on titanium, aluminium, or stainless steel. To determine the applicability of the WAAM technique in other high-production-rate industries, such as offshore renewable energy, which demand low-cost fabrication of large-scale structures, it is crucial to fully characterise WAAM built components made of mild steels. This characterisation should be conducted under various loading conditions and in different

environments, and their behaviour should be compared with that of conventional wrought steels. The above considerations form the primary motivation for the current study.

1.1. Aims and Objectives

The overall aim of this research is to fully characterise WAAM built specimens made with two different grades of mild steel ER70S-6 and ER100S-1, to assess the possibility of using such manufacturing technique and materials in marine applications, such as offshore wind structures. The main objectives of this work are as follows:

- Characterise the mechanical and fracture properties of WAAM steels.
- Investigate fatigue crack growth behaviour of the WAAM built specimens in air and seawater environments.
- Evaluate the fatigue performance of WAAM built specimens under uniaxial, torsion, and multiaxial loading conditions.
- Examine the potential for life enhancement by applying surface treatment techniques to WAAM steel specimens and quantify efficiency through nondisruptive residual stress measurements.
- Understand the impact of specimen extraction location and orientation on the performance of WAAM built samples.
- Analyse the microstructural characteristics and failure mechanisms of WAAM built steel specimens.

1.2. Structure of Thesis

The presented thesis by publication consists of the papers that have been submitted, accepted for publication, or already published in scientific journals. Corresponding references are provided at the beginning of each paper. The structure of the thesis is presented in Figure 1.1, where all chapters are listed along with the papers linked to them.

The introduction Chapter 1 is followed by a literature review summarised in Chapter 2, which includes the details on the current state and existing challenges associated with additive manufacturing techniques for application in the marine environment. Chapter 2 describes different additive manufacturing methods and WAAM in particular, listing available data for mechanical and fatigue testing of components produced with WAAM technique and highlights the gap in the knowledge.

The mechanical characteristics, such as tensile, hardness and fracture toughness, of ER70S-6 and ER100S-1 WAAM built specimens are examined in Chapter 3. Also, this chapter includes the discussion on a different response of the specimens based on the extraction location and orientation of the specimen with respect to the WAAM walls. Furthermore, the fracture properties have been analysed for WAAM steel specimens previously exposed to corrosive environment, which were then compared with the results for control specimens tested in air.

Chapter 4 and Chapter 5 summarise the fatigue crack growth and corrosion-fatigue crack growth assessment for ER70S-6 and ER100S-1 WAAM specimens, respectively. They include the manufacturing process, specimen extraction, testing procedures, crack growth measurement techniques and data analysis methods employed in this work. Moreover, a sensitivity analysis has been performed for the tests, to understand the dependency of the results

on extraction location and orientation of the specimens. Fractography and microstructural assessments were performed on each test specimen. Moreover, comparisons have been made with wrought S355 steel behaviour and BS7910 standard lines.

Chapter 6 is dedicated to uniaxial, torsion and multiaxial testing of ER70S-6 and ER100S-1 WAAM built specimens. The results have been presented and discussed based on orientation of the extracted specimens. Comparisons with the data on carbon steels from the literature and DNV recommended lines have been conducted. Also, fracture mechanisms were analysed and discussed for each of the test specimens.

In Chapter 7 the possibility for life enhancement of WAAM built components is investigated and discussed, using two types of surface treatment techniques: rolling and laser shock peening. The efficiency of two methods was assessed by examining the fatigue crack growth and corrosion-fatigue crack growth performance of the specimens after the application of surface treatment. Moreover, the residual stresses were measured in the specimens, using neutron diffraction and X-ray methods, to understand and quantify the effect of the surface treatments methods.

The summary of findings, observations and conclusions from this research is presented in Chapter 8. It also includes suggestions for future work, arising from the scope of the current work.

Lastly, a few additional co-authored papers are presented in Appendix section of the thesis.

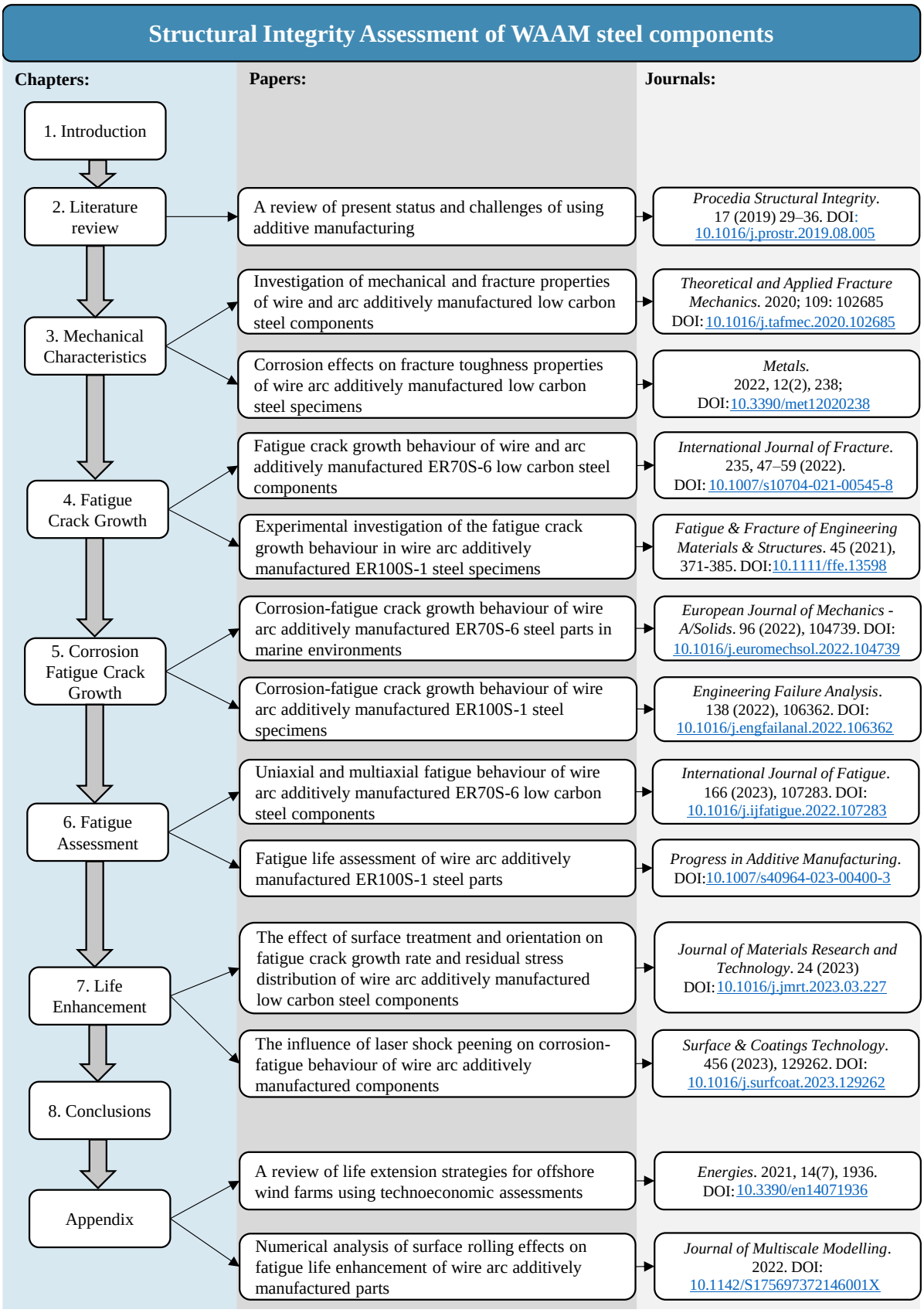

Figure 1.1: Structure of thesis

Chapter 2 : Literature review on additive manufacturing processes and challenges

In this chapter, a literature review was conducted to analyse the current state and present challenges for employment of additive manufacturing techniques in marine applications. The chapter consists of the following paper:

Paper I: A review of present status and challenges of using additive manufacturing

2.1. Paper I: A review of present status and challenges of using additive manufacturing

Anna Ermakova[a], Ali Mehmanparast[a*], Supriyo Ganguly[b]

[a] Offshore Renewable Energy Engineering Centre, Cranfield University, MK43 0AL, UK

[b] Welding Engineering & Laser Processing Centre, Cranfield University, MK43 0AL, UK

Abstract[1]

Offshore wind is an efficient sustainable source of energy, which is a preferable alternative to burning fossil fuels in Europe and worldwide. About 85% of existing offshore wind turbines are supported using monopile foundations, which are made of large welded plates. The locked in residual stresses in a monopile structure have a great impact on its fatigue life. The new emerged technology of additive manufacturing (AM), which is widely used in other industries such as aerospace and automotive, has the potential to significantly improve a lifespan of the structure by managing the residual stress fields and microstructure in the future monopiles, and moreover reduce the manufacturing cost. In order to achieve this goal, new materials that are used for additive manufacturing parts fabrication and their behaviour in the harsh marine environment and under operational loading conditions need to be understood. Also, purely welding fabrication technique employed during AM process is likely to significantly affect crack growth behaviour in air as well as in seawater. This paper presents a review of additive manufacturing technology and suitable techniques for offshore structures. Existing literature that reports current data on fracture toughness and fatigue crack growth tests conducted on AM parts is summarised and analysed, highlighting different steel grades and applications, with the view to illustrating the requirements for the new optimised functionally graded structures in offshore wind structures by means of AM technique.

Keywords: Offshore wind; Additive manufacturing; Fatigue crack growth.

---

* corresponding author

[1] *Procedia Structural Integrity*. 17 (2019) 29–36. (DOI: 10.1016/j.prostr.2019.08.005)

2.1.1. Introduction

The urge for the renewable energy source is dramatically increasing the number of wind farm installations worldwide. Offshore wind energy is attracting more interest in recent years due to constrains of suitable onshore space and reducing trend in the levelised cost of offshore wind energy. Offshore sites ensure larger space and better wind potential, hence more efficient energy outcome, but at relatively higher cost.

The majority of the existing offshore wind farms are located in shallow waters with maximum depth of 30 m and about 85% of them are supported by monopile structures, due to design simplicity and cost effectiveness. Monopiles are fabricated out of thick plates of new grades of steel such as S355 and comprise of several cylindrical sections circumferentially welded together. Typical monopile dimensions range from 50 to 70 m in length, 3 to 10 m in diameter and 40 to 150 mm in wall thickness[1]. However, due to rapid development of the wind industry and increasing demand for more efficient wind turbines, the monopile structures may have to be increased, and this will significantly increase the associated production and installation costs. The installation phase is the most critical stage of commissioning an offshore wind turbine which is time consuming and involves the high capital cost[2,3].

Monopiles are installed by placing them into the seabed. Thus, the structure should withstand the hammering loads, which depend on the soil condition and vary from site to site. During operation, monopiles are subjected to wind, sea wave and current cyclic loads as well as static gravitational, hydrostatic, and aerodynamic loads. Therefore, they have to be designed against failure for a certain period of fatigue life and for corresponding magnitudes of static loads. Apart from the operational loads, monopile foundations are subjected to relatively harsh marine environment. Corrosion-fatigue is reported as the dominant mode of failure in monopiles across relatively narrow band of frequencies[4]. Moreover it has been presented in many researches that welding residual stresses alter the mean stresses under cyclic loading and consequently influence fatigue crack growth behaviour of materials[5,6].

Emerging new materials and manufacturing techniques can be considered to address the current challenges of the renewable wind industry and future sustainable goals.

2.1.2. Additive Manufacturing Techniques

Nowadays additive manufacturing (AM) has gained considerable attention for industries that are targeting low volume production of highly customised parts for specific applications. The technology offers building the 3D model layer upon layer using additive process instead of conventional subtractive method, which can lead to waste reduction. This new manufacturing technology has opened new avenues for fabricating net-shaped structures and assemblies of complex geometries that traditional manufacturing is unable to provide[7,8]. With less geometrical constrains AM provides benefits to industries for building lighter and cleaner products by establishing new design paradigms within shorter lead times and with lower cost[9,10]. Moreover, AM allows the ability to remote manufacturing and repair upon request as

well as manufacturing of functionally-graded components, which makes it beneficial and suitable for the offshore wind energy applications[11].

However, there are some metallurgical differences between conventional and AM built components, such as mechanical anisotropy, residual stress, and defects inherent in AM processes that must be addressed for critical applications, related to fatigue exposure in particular[12]. The behaviour of new materials used in AM needs to be understood with respect to the area of application. Also, the new fabrication technique mostly consisting of welding process is likely to influence crack growth behaviour of the materials in air, as well as in sea water environments. This is caused due to changes in microstructure of the welded material and level of residual stresses accumulated during welding process[13]. Thus, the new database on fracture toughness and air/corrosion-fatigue crack growth tests needs to be generated for each new material and technique.

During AM process the feedstock material, such as powder or wire, is consolidated into a dense metallic part by melting and solidification by means of energy source such as laser, electron beam or electric arc[13]. The typical metal AM techniques can be divided into two main groups based on type of deposited material: powder bed fusion (PBF) and direct energy deposition (DED). Comparison of the main techniques' features is presented in Table 2.1.

Based on the comparative study and the scale of offshore wind turbine support structures, DED AM seems to be the most suitable technique to be considered for further analysis. DED represents such technologies as Laser Engineering Net Shape (LENS), Electron Beam Additive Manufacturing (EBAM) and Wire + Arc Additive Manufacturing (WAAM), which use of laser, electron beam and electric arc for fusion respectively.

Table 2.1: Comparison of PBF and DED AM techniques

AM technique	Advantages	Disadvantages
PBF	- High density parts - can achieve a density over 99%, hence properties similar to the bulk material - High geometrical accuracy of fabricated parts ±0.05 mm	- Time consuming, as the height of a powder layer is typically between a few tens of microns to just below 100 microns, depositing around 10 g/min - Fine powders as the starting material can pose health and safety concerns - Low availability and high cost of raw material, costly recycling - High porosity level, that reduces the fatigue life
DED	- Cheaper raw material (wire) and less waste, as up to 100% of the wire is deposited into component - Fast builds with rapid material deposition (330 g/min for steel) - Process allows parts repair	- Poor surface finish and less accuracy of wire process - Limited options of materials

2.1.3. Wire + Arc Additive Manufacturing

Wire + Arc Additive Manufacture (WAAM) is a promising DED technology for fabricating large components with moderate complexity from a variety of metallic alloys. WAAM is a direct feed process with an arc heat source and metallic wire as the feedstock. The component fabricated by WAAM consists of weld beads, deposited on top of each other. Due to high deposition rates, relatively low equipment and material cost and good structural integrity of built parts, WAAM is becoming a beneficial replacement for machining parts out of solid wrought material[14].

Essentially, WAAM technology divides the three-dimensional model into several two-dimensional layers with nominal height, where layer height is limited and depends on process setup[15]. Each layer is built by moving the torch along the required tool path. The quality of each layer affects the locked-in residual stresses, dimensional inaccuracies, defects, distortion, etc. Therefore, it is essential to select a building strategy which will result building a flat surface to be a good base for the following layers. The simplest strategy is a wall, when the thickness of the required product matches the thickness of the deposited material. In order to build wider walls, parallel or oscillation building strategies can be implemented. For the first method wall layer is divided into several parallel weld beads, whereas for the second, oscillation manner is used (Figure 2.1).

Oscillation patterns offer several advantages compared to the parallel, such as flexibility of building various wall widths without continuous change of weld parameters. Therefore, it provides more accurate control of wall thickness. Also, oscillation strategy reduces the probability of fusion defects since this process is warmer compared to the parallel deposition. Moreover, due to continuous deposition of one layer, this strategy is less time consuming[16].

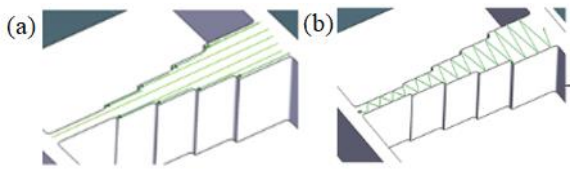

Figure 2.1: Geometric patterns for layer depositing: (a) parallel and (b) oscillation[16]

One of the major concerns in WAAM process is the control of residual stresses and distortions, especially for the large-scale parts fabrication, as it affects the tolerance and causes premature failure. The reason for thermally induced stresses in welding is thermally induced strains given by non-uniform expansion and contraction of material. Moreover, once the completed part is unclamped from the fabrication table, residual stresses are redistributed which may result in the distortion of the AM built component. Even though the residual stresses can be minimised by post processing techniques, the distortion due to the stresses can only be limited by controlling the residual stresses during the deposition[17].

2.1.4. Mechanical and Fatigue Properties of WAAM components

- **WAAM strategies**

Different WAAM strategies have been investigated on thermal stresses, altering deposition patterns and sequences, reliable printing parameters, and adjusting the cooling time between layers. It was reported by Ding D. et al.[17] that stresses across the deposited wall are typically uniform with little influence from the adjacent layers. Xiong et al.[18] worked on effective adjustment of the weld bead width. Later Xiang and Zhang[19] presented a control system for consistent nozzle height position. Meanwhile Ding J. et al.[20] developed a gas shielding device for WAAM system. Xiong et al.[21] have investigated a closed loop control process for metal deposition. Effects of deposition pattern, sequences on residual stress available in the literature mainly present two dimensional layers or thin wall structures. Thus, for real engineering applications, the optimum deposition strategy for reducing the residual stresses caused by WAAM are not yet defined.

- **Layer by layer material properties**

The material properties of steel subjected to WAAM process are poorly characterised to date. Suryakumar et al.[22] reported that number of layers affects the hardness of the product; the layers on the top of the part experience fewer thermal cycles and this leads to improved hardness of the material (Figure 2.2). Also, they revealed that residual effects do not propagate deeper than five layers.

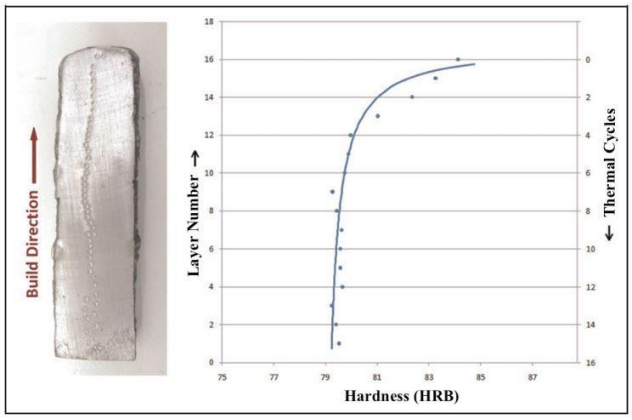

Figure 2.2: Hardness of WAAM wall against number of layers[22]

Ding et al.[23] developed a thermo-mechanical properties model to predict residual stresses in the fabricated part and associated distortions. It was stated by Colegrove et al.[24], that post processing treatment, such as rolling, can release the residual stresses and hence distortions, particularly in the layers close to the base plate. Moreover, high-pressure rolling causes grain refinement and leads to improvement in microstructure of WAAM mild steels.

- **Yield and ultimate tensile strength variation**

Mechanical properties of WAAM specimens have been extensively investigated by such research groups as[22,25–27]. Haden et al.[25] have suggested that WAAM material properties can be controlled and designed by careful toolpath planning. Samples extracted from WAAM wall built out of ER70S-6 were investigated in their study and the effect of horizontal and vertical orientation on the test results was examined. A single line microhardness test was conducted to compare material strength of WAAM printed wall to wrought part. The results shown that the printed material has an average value between minimum and maximum values for bulk ASTM A36, composition of which is nearly identical to ER70S. Uniaxial tensile test of WAAM specimen (Figure 2.3 (a)) revealed typical behaviour of wrought material for low carbon steels. The AM printed mild steel yield strength is also similar to characteristics of wrought A36 steel (Figure 2.3 (b)). As it can be seen in Figure 2.3 (b) that the orientation of specimen does not show significant difference in yield stress and the results from both orientations have shown similar ranges. Similar observation has been made in the ultimate tensile strength results obtained from samples with different orientations with about 5% difference between the two (Figure 2.3 (c)). Similar results have been observed and reported by Lu et al.[26].

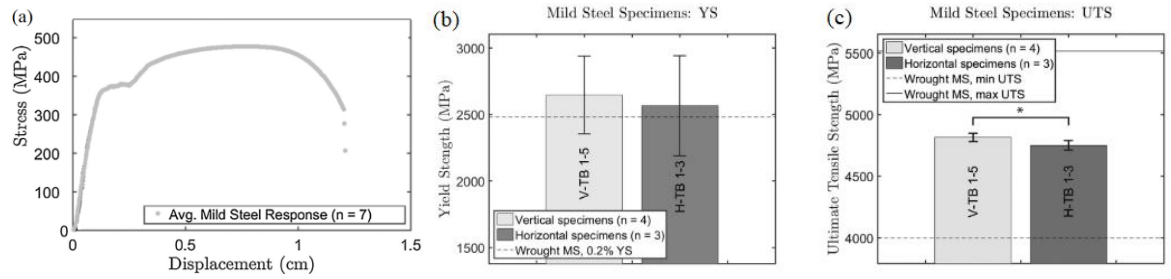

Figure 2.3: ER70S-6 material characteristics (a) stress-displacement curve (b) yield strength (c) ultimate tensile strength[25]

Suryakumar et al.[22] investigated all three orientations of ER70S samples, adding a stepover direction – perpendicular to the torch direction in XY plane. It was found in their study that ultimate strength in the stepover direction shown the best result. However, variations of yield and ultimate strength between torch and stepover directions is within 7.6% and 4.8% respectively, whereas the difference between XY plane and vertical direction is more significant: 10.6% and 10.8%. Moreover, it was observed in their study that the tensile strength can be further improved by increasing the current of welding arc.

- **Charpy impact tests**

Charpy impact tests were conducted by Waqas et al.[28] on sub-size specimens made of ER70S-6 steel. It was concluded that the impact toughness of printed steel is higher than the wrought low carbon steel with comparable hardness. Parallel and perpendicular orientations of the samples did not show significant difference of results (within 10%) indicating relatively homogenous properties with ductile behaviour across the volume of the AM build component.

- **Fracture toughness analysis**

Fracture toughness tests were performed on the standard compact tension, C(T), specimens printed by WAAM technique from Ti-6Al-4V wire by Zhang et al.[29]. It was observed that fracture toughness of such specimens is comparable or greater than properties of wrought titanium material. Also, it was found that fracture toughness results depend on orientation of the sample and is higher when crack propagates perpendicular to the additive layers.

- **S-N characterisation**

Flat dog-bone specimens for this research by Gordon et al.[27] were extracted from single bead WAAM walls fabricated from 304L stainless steel. The experimental S-N curves can be seen in Figure 2.4, summarising the mean values for horizontal and vertical WAAM specimens fatigue data. The graph shows that build orientation also affects fatigue life of WAAM samples, and for vertical specimens the fatigue life is longer. Additionally, AM samples have greater median number of cycles to failure than conventionally built samples.

- **Fatigue analysis**

There are limited studies on the fatigue crack initiation and propagation in WAAM steels available in the literature. Fatigue crack growth of WAAM fabricated components using 304L stainless steel was investigated by Gordon et al.[30] and their observations were explained in terms of the microstructure, texture and locked-in residual stresses in the specimens. The fatigue crack growth behaviour of the Paris region of the WAAM samples have shown better results compared to conventional wrought stainless steel (Figure 2.5), as WAAM printed material provides improved fatigue crack growth resistance and monotonic properties. Different fatigue crack growth rates for vertical and horizontal specimens can be justified by presence of long columnar grains and stronger texture in build direction. Moreover, it was observed that retained residual stresses positively affect fatigue crack growth for specimens in both orientations when the test results from as-printed samples were compared with stress relieved specimens.

The examination of fatigue crack growth of WAAM titanium samples has been extensively investigated by other researchers such as[29,31]. For example, analysis of WAAM Ti-6Al-4V specimens by Zhang et al.[29] shown that fatigue crack growth rate is considerably lower than in the wrought alloy. Moreover, it was observed that the rate is slightly faster (within the range of data scatter) when the crack propagates through AM layers, this indicates that WAAM material can be considered to have isotropic fatigue crack growth rate. The effect of microstructure and residual stress on fatigue crack growth behaviour was studied by Zhang et al.[31]. Where the Ti-6Al-4V specimens contain a combination of WAAM and wrought material in different orientations. Conclusion was made that crack propagation rate in WAAM material is lower, due to tortuous path in lamellar structure of WAAM alloy.

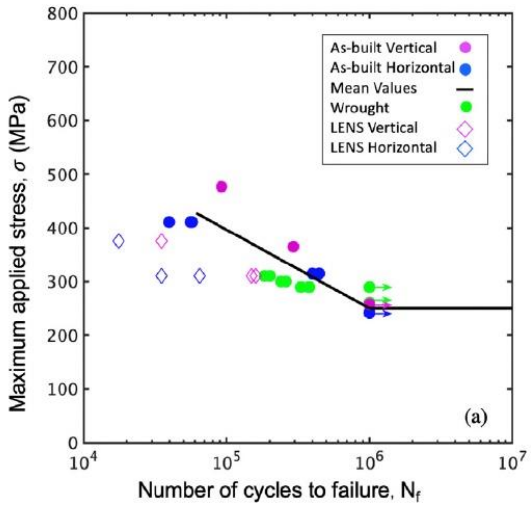

Figure 2.4: S-N curve for printed WAAM and wrought 304L steel[27]

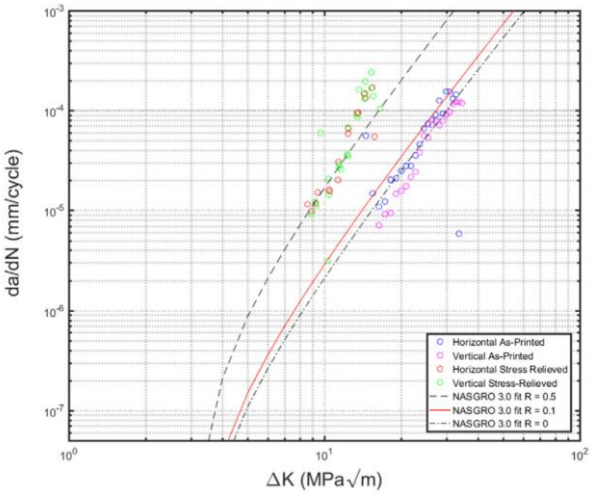

Figure 2.5: Comparison of fatigue crack growth rate of WAAM as-build and heat-treated specimens to wrought material (NASGRO model)[30]

The limited results available in the literature suggest that AM process significantly affects the corrosion performance of materials, however more studies need to be performed to achieve solid conclusions, especially to examine corrosion damage in WAAM steels for which no data has been found in the literature. Some beneficial effects in corrosion resistance have been reported by Ganesh et al.[32], showing that corrosion pitting resistance behaviour was found in austenitic stainless-steel specimens fabricated by direct laser deposition AM method. The influence of inclusions in high temperature water (288^0C) was investigated by Lou et al.[33] on stainless steel specimens fabricated by means of AM selective laser melting (SLM) method. The printed samples shown better corrosion resistance compared to the wrought stainless-steel specimens. Corrosion-fatigue crack growth was analysed by Lou et al.[34] in hot pressurised water 288^0C. Samples were SLM printed using stainless steel material and test specimens were examined in two different orientations. Specimens extracted from X-Z plane (load applied in X direction and crack growth along Z direction) presented higher crack growth rate. It was also observed that in both specimen orientations, a lower resistance to fatigue crack growth was observed compared to wrought stainless steel (Figure 2.6), though the stress intensity range and load ratio during tests were not identical. Similar specimens were utilised for another study on corrosion-fatigue crack growth in pure water at 288^0C by Lou et al.[35]. It was observed that longer cracks appeared in X-Z samples – along direction of the build. Corrosion-fatigue crack growth rate of the AM specimens was found higher than for the wrought counterpart (Figure 2.7). A study conducted by GE Global Research[36], has shown that fatigue and corrosion-fatigue crack growth rates in air and hot water are similar for wrought and PBF AM stainless steel specimens.

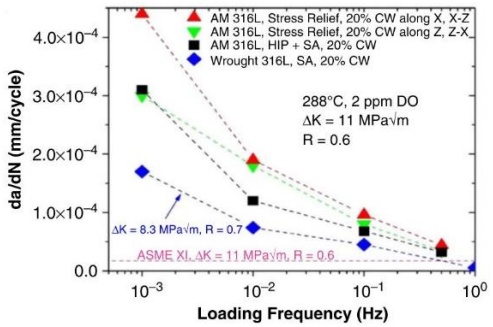

Figure 2.6: Corrosion-fatigue crack growth of AM and wrought stainless steel in hot water[34]

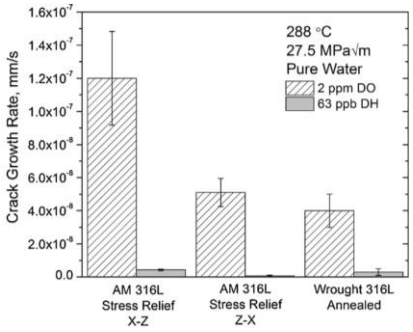

Figure 2.7: Comparison of crack growth rate of SLM and wrought stainless steel[35]

2.1.5. Conclusion and future work

Additive manufacturing has been rapidly developed for the past decade providing capability of complex shapes fabrication with less material waste and at lower cost and shorter lead times. As shown in the present literature review, printed WAAM mild steel parts have displayed similar yield and ultimate tensile strength compared with wrought material. Also, higher Charpy impact test results have been found in WAAM steel specimens compared to the wrought steel. Moreover, material properties of WAAM specimens were concluded to be relatively uniform. It was reported that fracture toughness of WAAM Ti-6Al-4V specimens is comparable or greater compared with wrought material. The experimental S-N curves for WAAM 304L stainless steel samples presented greater median number of cycles to failure than conventionally built samples. Fatigue crack growth analysis of stainless-steel samples built using the WAAM technique have shown improved fatigue crack growth resistance of the novel material compared to the conventional material. Retained residual stress was reported to influence the fatigue crack growth of the material. Extensive fatigue crack growth analysis of WAAM Ti-6Al-4V shown that fatigue crack growth rate is considerably slower than in counterpart samples. Moreover, based on examination of results for different orientation samples, the conclusion was drawn that WAAM material has isotropic fatigue crack growth rate. It has been found that AM process significantly affects the corrosion performance of the material, however very limited information is available in literature on this topic, especially for WAAM steels. The limited results in the literature on stainless steel parts built by direct laser deposition have shown better corrosion resistance in hot water, compared with wrought samples. However, some studies on similar WAAM steel samples, present higher corrosion-fatigue crack growth rate compared to counterparts. Although AM shows tremendous potential for application in offshore wind industry, the amount of data available to better characterise and implement the AM components in a new industry are very limited. A better metallurgical knowledge of AM parts needs to be developed, which requires specific and systematic experimental and numerical studies. Therefore, it is proposed to investigate in future work the fatigue crack growth behaviour of WAAM components in air and seawater to examine the applicability of WAAM technique for building structures to operate in the harsh offshore environment. It is also proposed to consider different grades of mild steel in future study and

more importantly to characterise residual stresses and surface treatment effects on the fatigue performance of WAAM built components.

2.1.6. References for paper I

1. Jacob, A., Oliveira, J., Mehmanparast, A., Hosseinzadeh, F., Kelleher, J. & Berto, F. Residual stress measurements in offshore wind monopile weldments using neutron diffraction technique and contour method. *Theor. Appl. Fract. Mech.* **96**, 418–427 (2018).
2. Sarker, B. R. & Faiz, T. I. Minimizing transportation and installation costs for turbines in offshore wind farms. *Renew. Energy* **101**, 667–679 (2017).
3. Adedipe, O., Brennan, F. & Kolios, A. Review of corrosion fatigue in offshore structures: Present status and challenges in the offshore wind sector. *Renew. Sustain. Energy Rev.* **61**, 141–154 (2016).
4. Adedipe, O., Brennan, F. & Kolios, A. Corrosion fatigue load frequency sensitivity analysis. *Mar. Struct.* **42**, 115–136 (2015).
5. Nelson, D. V. Effect of residual stress on fatigue crack propagation. *Am. Soc. Mech. Eng. Press. Vessel. Pip. Div. PVP* **304**, 172–194 (1982).
6. Baumgartner, J. Enhancement of the fatigue strength assessment of welded components by consideration of mean and residual stresses in the crack initiation and propagation phases. *Weld. World* **60**, 547–558 (2016).
7. Lott, P., Schleifenbaum, H., Meiners, W., Wissenbach, K., Hinke, C. & Bültmann, J. Design of an optical system for the in situ process monitoring of Selective Laser Melting (SLM). *Phys. Procedia* **12**, 683–690 (2011).
8. Emelogu, A., Marufuzzaman, M., Thompson, S. M., Shamsaei, N. & Bian, L. Additive manufacturing of biomedical implants: A feasibility assessment via supply-chain cost analysis. *Addit. Manuf.* **11**, 97–113 (2016).
9. Frazier, W. E. Metal additive manufacturing: A review. *Journal of Materials Engineering and Performance* **23**, 1917–1928 (2014).
10. Levy, G. N., Schindel, R. & Kruth, J. P. Rapid manufacturing and rapid tooling with layer manufacturing (LM) technologies, state of the art and future perspectives. *CIRP Ann. - Manuf. Technol.* **52**, 589–609 (2003).
11. Shamsaei, N., Yadollahi, A., Bian, L. & Thompson, S. M. An overview of Direct Laser Deposition for additive manufacturing; Part II: Mechanical behavior, process parameter optimization and control. *Addit. Manuf.* **8**, 12–35 (2015).
12. Milewski, J. O. *Additive Manufacturing of Metals*. *NDT in Progress 2017 - 9th International Workshop NDT in Progress, Proceedings* **2017-Octob**, (2017).

13. DebRoy, T., Wei, H. L., Zuback, J. S., Mukherjee, T., Elmer, J. W., Milewski, J. O., Beese, A. M., Wilson-Heid, A., De, A. & Zhang, W. Additive manufacturing of metallic components – Process, structure and properties. *Prog. Mater. Sci.* **92**, 112–224 (2018).

14. Williams, S. W., Martina, F., Addison, A. C., Ding, J., Pardal, G. & Colegrove, P. Wire + Arc Additive Manufacturing. *Mater. Sci. Technol.* **32**, 641–647 (2015).

15. Martina, F., Mehnen, J., Williams, S. W., Colegrove, P. & Wang, F. Investigation of the benefits of plasma deposition for the additive layer manufacture of Ti-6Al-4V. *J. Mater. Process. Technol.* **212**, 1377–1386 (2012).

16. Bandari, Y. K., Charrett, T. O. H., Michel, F., Ding, J., Williams, S. W. & Tatam, R. P. Compensation Strategies for Robotic Motion Errors for Additive Manufacturing. *Solid Free. Fabr.* 1–14 (2016).

17. Ding, D., Pan, Z., Cuiuri, D. & Li, H. Wire-feed additive manufacturing of metal components: technologies, developments and future interests. *Int. J. Adv. Manuf. Technol.* **81**, 465–481 (2015).

18. Xiong, J., Zhang, G., Qiu, Z. & Li, Y. Vision-sensing and bead width control of a single-bead multi-layer part: Material and energy savings in GMAW-based rapid manufacturing. *J. Clean. Prod.* **41**, 82–88 (2013).

19. Xiong, J. & Zhang, G. Adaptive control of deposited height in GMAW-based layer additive manufacturing. *J. Mater. Process. Technol.* **214**, 962–968 (2014).

20. Ding, J., Colegrove, P., Martina, F., Williams, S., Wiktorowicz, R. & Palt, M. R. Development of a laminar flow local shielding device for wire + arc additive manufacture. *J. Mater. Process. Technol.* **226**, 99–105 (2015).

21. Xiong, J., Yin, Z. & Zhang, W. Closed-loop control of variable layer width for thin-walled parts in wire and arc additive manufacturing. *J. Mater. Process. Technol.* **233**, 100–106 (2016).

22. Suryakumar, S., Karunakaran, K. P., Chandrasekhar, U. & Somashekara, M. A. A study of the mechanical properties of objects built through weld-deposition. *Proc. Inst. Mech. Eng. Part B J. Eng. Manuf.* **227**, 1138–1147 (2013).

23. Ding, J., Colegrove, P., Mehnen, J., Ganguly, S., Almeida, P. M. S., Wang, F. & Williams, S. Thermo-mechanical analysis of Wire and Arc Additive Layer Manufacturing process on large multi-layer parts. *Comput. Mater. Sci.* **50**, 3315–3322 (2011).

24. Colegrove, P. A., Coules, H. E., Fairman, J., Martina, F., Kashoob, T., Mamash, H. & Cozzolino, L. D. Microstructure and residual stress improvement in wire and arc additively manufactured parts through high-pressure rolling. *J. Mater. Process. Technol.* **213**, 1782–1791 (2013).

25. Haden, C. V., Zeng, G., Carter, F. M., Ruhl, C., Krick, B. A. & Harlow, D. G. Wire and arc additive manufactured steel: Tensile and wear properties. *Addit. Manuf.* **16**, 115–123 (2017).

26. Lu, X., Zhou, Y. F., Xing, X. L., Shao, L. Y., Yang, Q. X. & Gao, S. Y. Open-source wire and arc additive manufacturing system: formability, microstructures, and mechanical properties. *Int. J. Adv. Manuf. Technol.* **93**, 2145–2154 (2017).

27. Gordon, J., Hochhalter, J., Haden, C. & Harlow, D. G. Enhancement in fatigue performance of metastable austenitic stainless steel through directed energy deposition additive manufacturing. *Mater. Des.* **168**, 107630 (2019).

28. Waqas, A., Xiansheng, Q., Jiangtao, X., Chaoran, Y. & Fan, L. Impact toughness of components made by GMAW based additive manufacturing. *Procedia Struct. Integr.* **13**, 2065–2070 (2018).

29. Zhang, X., Martina, F., Ding, J., Wang, X. & Williams, S. W. Fracture toughness and fatigue crack growth rate properties in wire + arc additive manufactured Ti-6Al-4V. *Fatigue and Fracture of Engineering Materials and Structures* **40**, 790–803 (2017).

30. Gordon, J. V., Haden, C. V., Nied, H. F., Vinci, R. P. & Harlow, D. G. Fatigue crack growth anisotropy, texture and residual stress in austenitic steel made by wire and arc additive manufacturing. *Mater. Sci. Eng. A* **724**, 431–438 (2018).

31. Zhang, J., Wang, X., Paddea, S. & Zhang, X. Fatigue crack propagation behaviour in wire+arc additive manufactured Ti-6Al-4V: Effects of microstructure and residual stress. *Mater. Des.* **90**, 551–561 (2016).

32. Ganesh, P., Giri, R., Kaul, R., Ram Sankar, P., Tiwari, P., Atulkar, A., Porwal, R. K., Dayal, R. K. & Kukreja, L. M. Studies on pitting corrosion and sensitization in laser rapid manufactured specimens of type 316L stainless steel. *Mater. Des.* **39**, 509–521 (2012).

33. Lou, X., Andresen, P. L. & Rebak, R. B. Oxide inclusions in laser additive manufactured stainless steel and their effects on impact toughness and stress corrosion cracking behavior. *J. Nucl. Mater.* **499**, 182–190 (2018).

34. Lou, X., Othon, M. A. & Rebak, R. B. Corrosion fatigue crack growth of laser additively-manufactured 316L stainless steel in high temperature water. *Corros. Sci.* **127**, 120–130 (2017).

35. Lou, X., Song, M., Emigh, P. W., Othon, M. A. & Andresen, P. L. On the stress corrosion crack growth behaviour in high temperature water of 316L stainless steel made by laser powder bed fusion additive manufacturing. *Corros. Sci.* **128**, 140–153 (2017).

36. Rebak, R. B., Lou, X., Emigh, P. W., Othon, M. A., Andresen, P. L., Song, M. & Wang, M. *Environmental Cracking and Irradiation Resistant Stainless Steels by Additive Manufacturing Lead Organization: General Electric Company Award Number: DE-NE0008428*. (2018).

Chapter 3 : Mechanical and Fracture properties of Wire Arc Additively Manufactured Steel Components

In this chapter, mechanical and fracture properties of ER70S-6 and ER100S-1 WAAM built specimens were examined. Also included in this chapter is the fracture toughness properties of components exposed to corrosive environment. The chapter consists of the following papers:

Paper II: Investigation of mechanical and fracture properties of wire and arc additively manufactured low carbon steel components

Paper III: Corrosion effects on fracture toughness properties of wire arc additively manufactured low carbon steel specimens

3.1. Paper II: Investigation of mechanical and fracture properties of wire and arc additively manufactured low carbon steel components

Anna Ermakova[a], Ali Mehmanparast[a*], Supriyo Ganguly[b], Javad Razavi[c], Filippo Berto[c]

[a] Offshore Renewable Energy Engineering Centre, Cranfield University, England, UK

[b] Welding Engineering and Laser Processing Centre, Cranfield University, Cranfield, MK43 0AL, UK

[c] Norwegian University of Science and Technology (NTNU), Trondheim, Norway

Abstract[2]

Wire and Arc Additive Manufacturing (WAAM) technology offers efficient fabrication of large scale products and is currently being implemented across various industries. In this study, an experimental investigation has been carried out to characterise the mechanical and fracture properties of WAAM components made of ER70S-6 and ER100S-1 metal wires. Microhardness, tensile and fracture toughness tests have been performed on the specimens extracted from the WAAM built walls which were fabricated using an oscillating pattern. The specimens were extracted from different locations, at the top and bottom of the WAAM walls, in two different orientations with respect to the deposition direction. The results show that the material hardness and yield strength of ER100S-1 built wall are higher than ER70S-6 by 62% and 42%, respectively. Moreover, in the walls made with both materials, the yield and ultimate tensile strength values were found to be slightly higher in specimens extracted in deposition (horizontal) direction when compared to specimens extracted in the built (vertical) direction. The average value of fracture toughness parameter for ER70S-6 has been found to be 88% higher than ER100S-1 material. Furthermore, the results show that the specimen extraction location in ER100S-1 wall significantly influences the fracture toughness values obtained from experiments. The results from this study have been compared with those available in the literature and discussed in terms of the mechanical and fracture properties effects on structural integrity assessment of WAAM components.

Keywords: Fracture toughness; Mechanical properties; Structural Integrity; Additive manufacturing; Life assessment; Advanced manufacturing technologies.

---

[*] corresponding author

[2] *Theoretical and Applied Fracture Mechanics.* 2020; 109: 102685 (DOI: 10.1016/j.tafmec.2020.102685)

3.1.1. Introduction

Additive manufacturing (AM) brings a radically new production method that enables functionally superior designs at a lower cost with enhanced productivity, greater sustainability and is set to revolutionise many industries globally. AM can be considered as an alternative fabrication method for complicated engineering components by addressing the current manufacturing challenges and geometrical constraints. The new AM technology enables fabrication of hybrid components with several alloys, which are deposited in the form of powder or wire. Among all existing AM methods, wire and arc additive manufacturing (WAAM) is known as a relatively inexpensive technique that provides the highest deposition rates and is suitable for the fabrication of large size products[1,2]. Using this technique, the deposition process is performed in open air using a robotic arm with a localised shielded area, which indicates an alternative application of this technology for repair processes in remote areas, such as offshore plant[3].

An important challenge in the structural integrity of WAAM components is to evaluate the influence of welding processes embedded into the WAAM technique on mechanical and fracture properties, compared to those obtained from the wrought material[4]. In addition to the mechanical response, the metallurgical differences such as microstructural variations, locked-in residual stresses, phase formation processes and compositional segregation must be carefully examined and classified before employing such components in critical operational loading conditions.

Mechanical properties of WAAM mild steel specimens were investigated by Haden et al.[5] who showed that the composition of printed steel specimens is comparable with the composition of the wrought steel. Moreover, they showed that the WAAM specimens have the average hardness value of bulk steel. Another study[6] has shown a good agreement between uniaxial tensile trends in WAAM mild steel samples and the wrought low carbon steels, with similar yield strength and ultimate tensile strength (UTS) values. Suryakumar et al.[7] have concluded that tensile properties for printed mild steel specimens can differ by up to 10% for different orientations and showed that tensile strength can be improved by increasing the current of welding arc. Titanium specimens extracted from thin WAAM walls were tested by Wang et al.[8], and no correlation was found between the position of the specimen on the wall and the tensile properties. However, it was observed, that the orientation has an impact on the results, reducing yield and UTSs of the vertical specimens. Overall, tensile properties values were similar to the wrought titanium material properties. Similar trends in WAAM titanium specimens were reported by other researchers[9,10].

Fracture toughness tests were conducted on WAAM titanium specimens by Zhang et al.[11], and the results have shown similar or greater values compared with the wrought titanium samples. Moreover, it was observed that the orientation of the specimen significantly affects the fracture toughness properties, which are higher when the crack propagates perpendicular to the deposited layers.

The review of the existing data shows that the majority of the previous studies using the WAAM technique were on titanium, aluminium or stainless-steel materials and new studies are needed to comprehensively characterise the mechanical response of WAAM built wall using different steels. Moreover, while the majority of the previous studies were conducted on

microstructural and mechanical properties of WAAM built walls, there are limited data available in the literature on fracture behaviour of these components which is a crucial property for life assessment of engineering components under operational loading conditions. Therefore, to fill the gap in the knowledge, the present study investigates the mechanical and fracture properties of WAAM built walls made of two different mild steels. Also included in this study is an examination of the sensitivity of the mechanical response of the WAAM material to the built orientation, and location along the wall height. The specimen preparation process, experimental procedures and test set-up details are described below, and the presented results are discussed and compared with the existing data in the literature.

3.1.2. Material selection and fabrication process

For the current research two types of mild steel welding wires were selected that are suitable for welding low and medium tensile steels: ER70S-6 and ER100S-1. The ER70S-6 contains deoxidisers that provide better wetting, material yielding and the capacity of faster welding travel speed, which helps support higher productivity and increase consumable life[12]. This material is suitable for welding of steels with moderate amount of imperfections, which makes it a preferred material choice for marine applications[13,14]. However, these ER70S-6 wires tend to generate silicon island deposits on the weld surface that need to be removed prior to surface conditioning such as painting, which may increase the time for post-processing treatments. For the current research, Lincoln Electric ER70S-6 wire was used, with typical composition presented in Table 3.1. The second material selected for this study is the high toughness ER100S-1 low-alloy steel. This material provides an excellent welding performance and stable arc with the balanced Manganese and Silicon ensuring optimum deoxidisation and weld fluidity[15,16]. The ER100S-1 wire offers outstanding toughness of the weld metal at low temperatures and is suitable for offshore applications. The composition of ER100S-1 material used in this study is shown in Table 3.1. It is worth noting that ER100S-1 wires are around ten times more expensive than ER70S-6.

Table 3.1: Chemical composition of materials (wt.-%)

	C	*Mn*	*Cr*	*Si*	*Ni*	*Mo*	*S*	*P*	*Cu*	*V*
ER70S-6	0.09	<1.60	0.05	0.09	0.05	0.05	0.007	0.007	0.20	0.05
ER100S-1	0.08	1.70	0.20	0.60	1.50	0.50	-	-	-	-

In order to build the additively manufactured walls in this study, the Cold Metal Transfer (CMT) based WAAM process was used with the manufacturing parameters presented in Table 3.2. The same parameters were employed in fabrication of different walls for consistency and in order to minimise structural variability in the final products. The set-up and fabrication process of the WAAM walls is shown in Figure 3.1. The base plates selected for this study was the rolled structural steel EN10025 with dimensions of 420 × 200 × 12 mm^3. The deposition of the WAAM walls started at the mid-width of base plates and the layers were deposited on

top of each other using an oscillation pattern to obtain a sufficiently thick wall of approximately 24 mm. It has been found in previous studies that the oscillation pattern provides more accurate control of wall thickness compared to the parallel deposition strategy. Also, since it is a warmer process, it reduces the probability of fusion defects[3]. Moreover, it is less time consuming than depositing multiple straight wiring lines next to each other, turning the arc off and changing the location of the torch, to build a single layer[17,18].

As seen in Figure 3.1, the WAAM set-up consists of the CMT power source, a robot arm with the CMT torch feeding the wire along with the pipe that simultaneously supplies shielding gas. Samples fabrication was conducted at the ambient temperature, however, in order to draw off the heat from the sample faster, an exhaust fan was used. The base plate was attached to the working table using eight clamps (two on each side), to minimise distortion of the plate due to the thermal energy input. The clamps were released once the WAAM wall was cooled down to the ambient temperature.

Two walls were manufactured in total, one for each material. The approximate wall dimensions were 355 mm in length (i.e. X-direction in Figure 3.1(b)), 24 mm in width (Y-direction in Figure 3.1(b)) and 140 mm height (Z-direction in Figure 3.1(b))

Table 3.2: CMT-WAAM fabrication parameters

Shielding gas	Ar+20% CO_2
Gas flow rate	15 L/min
Robot travelling speed	7.33 mm/sec
Wire diameter	1.2 mm
Wire feed speed	7.5 m/min
Dwell time	120 sec

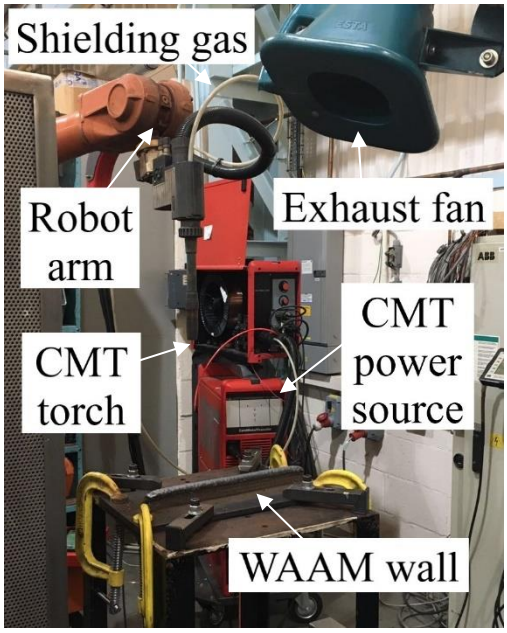

(a)

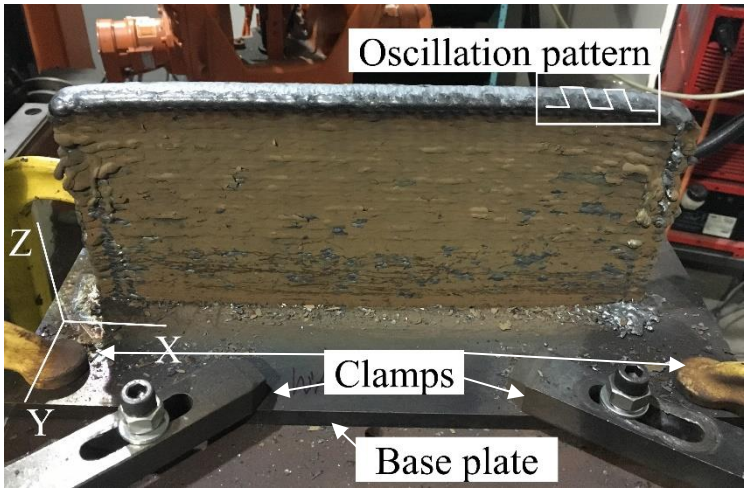

(b)

Figure 3.1: The fabrication process: (a) CMT WAAM set-up, and (b) completed wall

3.1.3. Specimen extraction

Upon completion of the WAAM walls fabrication process, compact tension, C(T), test specimens and uniaxial round bars were extracted from the walls using Electrical Discharge Machining (EDM) technique. Moreover, additional cross-sectional slices from wall sides, along the height of the walls, were extracted for microhardness measurements. For each of the materials examined in this study, four C(T) and four uniaxial cylindrical specimens were extracted along the two different orientations. As schematically shown in Figure 3.2, half of the extracted uniaxial samples had the loading direction perpendicular to the wall height axis (denoted UC-70-1 and UC-70-2), while the other half had a parallel orientation (denoted UC-70-3 and UC-70-4). Similarly, half of the extracted C(T) samples had the crack growth direction parallel to the wall height (denoted CT-70-1 and CT-70-2) while the crack plane in the other half was oriented along the X-direction (denoted CT-70-3 and CT-70-4).

As shown schematically in Figure 3.2, for each material and orientation, the C(T) specimens were extracted from the bottom and top of the wall to examine the fracture toughness properties of the WAAM walls with respect to the distance from the base plate. The C(T) specimens were extracted according to ASTM 1820 standard[19] for fracture toughness testing with the width of W = 50 mm, the height of H = 60 mm, total thickness of B = 16 mm, net thickness between the side grooves of B_n = 12 mm and initial crack length of a_0 = 17 mm before pre-fatigue cracking. The uniaxial cylindrical specimens dimensions were chosen in accordance with ASTM E8 standard[20] with the total length of L=112 mm, gauge diameter of d = 8 mm and the gripping diameter of D = 12 mm.

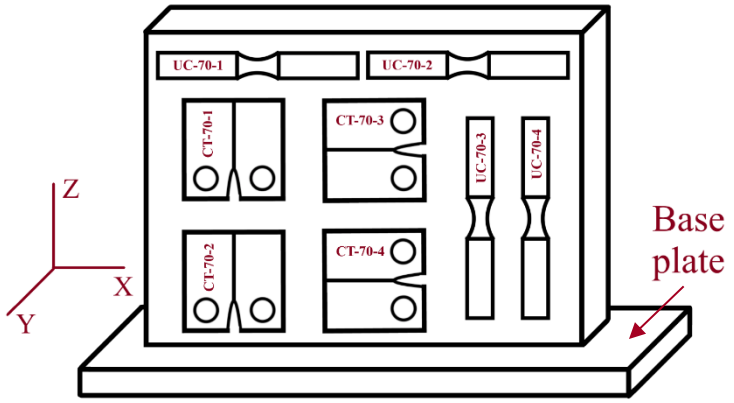

Figure 3.2: A schematic demonstration of the specimen extraction plan

3.1.4. Mechanical testing and analysis

- **Tensile properties**

Tensile tests were conducted following ASTM E8M[20] standard on four specimens for each material with two samples per orientation (i.e. vertical and horizontal), to examine the specimen orientation effects on the mechanical properties. All tests were performed under displacement control mode with the rate of 1 mm/min. The strain distribution was measured on the outer surface of the specimens using an extensometer in conjunction with the high-resolution digital image correlation (DIC) technique. It has been reported by various researches that DIC measurements provide an accurate result of local strain variations in tensile tests[21]. During the test, when the specimen is loaded and deforms, the DIC gauge measures displacement by comparing the movement of the reference points in the speckle pattern on the specimen surface. The gauge software tracks the reference points and derives the strain change from local displacement measurements. The tensile tests were carried out at the ambient temperature of around 20^0C. Upon completion of the tests, the average strain values were extracted from the software at the mid-length of the gauge region to quantify the elastic and plastic tensile properties obtained from each specimen. The average tensile curves between the repeat tests are shown in Figure 3.3 for both materials with vertical (V) and horizontal (H) orientations and the results are summarised in Table 3.3. It can be seen in Figure 3.3 and Table 3.3 that ER70S-6 material has a lower yield stress and greater tensile strain at failure compared to ER100S-1. Also seen in this figure is that for both materials the strain at failure is slightly higher in the horizontal specimen orientation (along the deposited layers) compared to vertical specimens (normal to the deposited layers).

Also included in Table 3.3 are the elastic Young's modulus, E, yield stress σ_Y (taken as 0.2% proof stress), ultimate tensile strength, σ_{UTS}, and strain at failure which has been calculated based on the axial strain $\varepsilon_{f,axial}$ and reduction of area ε_{ROA}. As seen in this table, the average value of yield stress for ER100S-1 is 42% higher than for ER70S-6 and whereas the UTS for ER100S-1 is about 56% higher. The yield stress for the vertical specimen is lower than for horizontal by 6.8% for ER70S-6 material and is very similar in both orientations for ER100S-

1. It can be seen in Table 3.3 that for both materials, the values of yield stress from both orientations are considerably lower than the values provided in the steel wire datasheets. The tensile curves show similar values of UTS for different specimen orientations though slightly lower in vertical compared to horizontal samples. The strain at failure values, calculated using the radial and axial strain measurements, show lower values for ER100S-1 material than for ER70S-6, which confirms that ER70S-6 is more ductile that ER100S-1. Also seen in the tensile test results is that both materials similar values of $\varepsilon_{f,axial}$ and ε_{ROA} are found in the horizontal and vertical specimens. Finally, the results in Table 3.3 show that the strain values at failure obtained from the reduction of area measurements are higher than axial measurements. This is due to the fact that the local deformation of the sample is accounted for in the calculation of ε_{ROA}, whereas averaged axial strains are accounted for in the calculation of $\varepsilon_{f,axial}$.

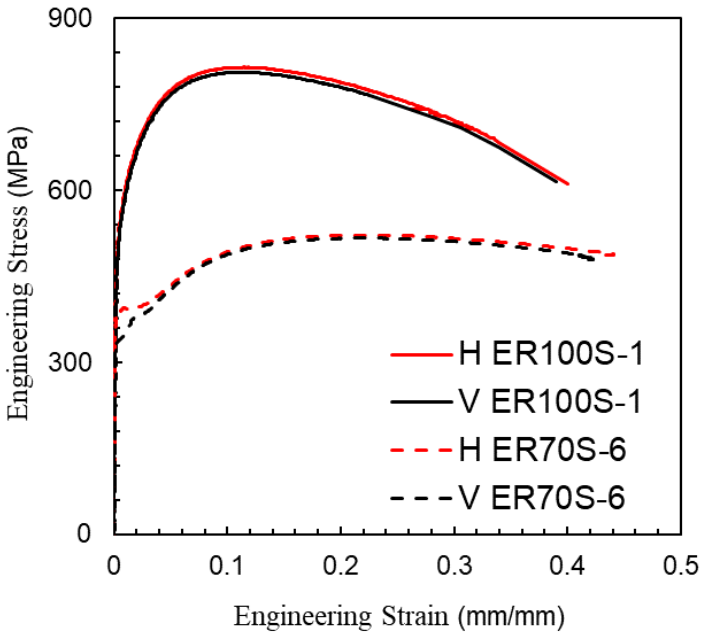

Figure 3.3: Engineering stress-strain curves for the two studied materials

Table 3.3: A summary of tensile test results

	ER70S-6			ER100S-1		
	Wire Datasheet	Orientation		Wire Datasheet	Orientation	
		Horizontal	Vertical		Horizontal	Vertical
σ_Y (MPa)	450	390	365	717	538	536
σ_{UTS} (MPa)	540	522	518	780	818	815
E (GPa)	-	209	221	-	181	155

ε_{ROA} (mm/mm)	-	0.77	0.71	-	0.62	0.65
$\varepsilon_{f,axial}$ (mm/mm)	-	0.44	0.43	-	0.40	0.39

- **Microhardness tests**

Microhardness measurements were carried out according to BS EN ISO 6507-1:1997[22]. The hardness tests were set up with a traverse along a straight line in the mid thickness of the walls, with incremental measurements of 2 mm. Figure 3.4(a) presents the macro structure of the offcut sample that was etched using 5% Nital solution, revealing the deposited layers. The microhardness tests were conducted with 500 g and 2000 g loads and the results are shown in Figure 3.4(b). Knowing that the height of individually deposited layers is on average about 3 mm (see Figure 3.4(a)), it can be observed that the hardness values vary from one layer to another. This fluctuation in hardness values is more pronounced in ER100S-1 sample and can be attributed to local variations in material properties due to the deposition process which can result in segregation of solute atoms within the deposit and lead to different phase formations (Note: ER100S-1 has much higher hardenability than ER70S-6). Also seen in the hardness results is that there is a good agreement between the observed trends obtained under 500 g and 2000 g applied loads with a slight shift to the left as the load increases. The average values of hardness for each material are calculated and summarised in Table 3.4. From the table, it can be seen that ER100S-1 material is 62% harder than ER70S-6.

The overall hardness patterns show that there is a slight hardening trend in the ER70S-6 alloy near the bottom of the wall and the hardness value increases at the top of the wall, whereas for ER100S-1 it is almost a constant trend throughout the wall height within the inherent experimental scatter. The variation in the hardness values between the middle and bottom of the ER70S-6 wall can be attributed to the effects of the thermal cycles on the mechanical behaviour of the WAAM built wall. As seen in Table 3.3, the ER70S-6 WAAM built wall demonstrates lower values of yield stress in both orientations compared to ER100S-1. Therefore, the thermal cycling has exhibited a more pronounced effect in the material with a lower yield stress. On the other hand, due to the higher yield stress in ER100S-1, there is no noticeable trend observed between the top and bottom layers on the wall made of this material. It must be noted that ER100S-1 has much higher hardenability than ER70S-6 which results in formation of martensite/bainite type structures (although not as high as medium/high carbon martensite) that would partially temper from the heat of subsequent passes – however, there is no significant hardness variation in the examined ER100S-1 WAAM wall probably because of the complex process of martensite formation and tempering occurring throughout the deposit.

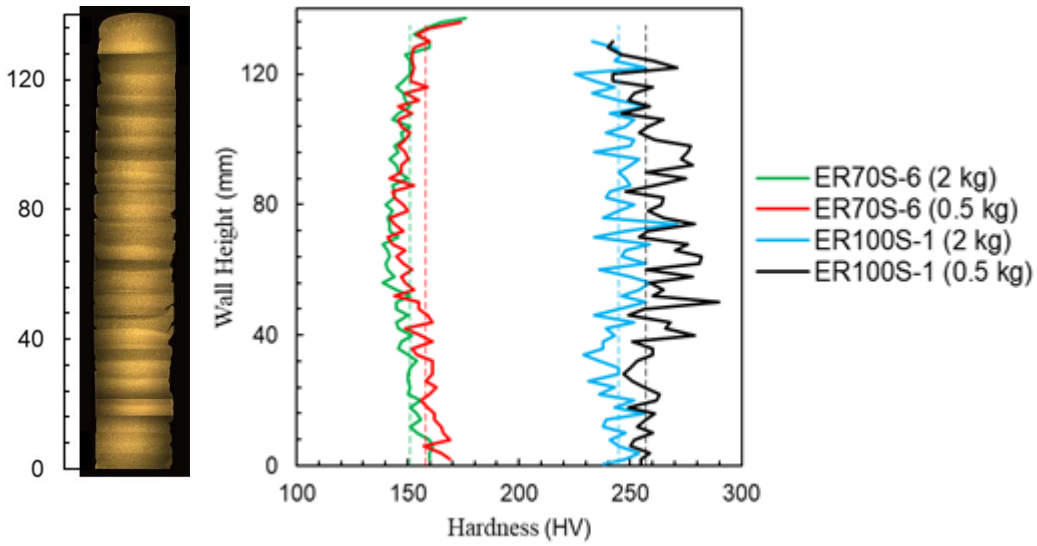

(a) (b)

Figure 3.4: (a) Macro structure of WAAM wall (b) Hardness test results for WAAM build walls

Table 3.4: Hardness values

Applied load (g)	ER70S-6	ER100S-1
500	158±14 HV	257±22 HV
2000	151±12 HV	245±18 HV

3.1.5. Fracture toughness testing and analysis

- **Specimen preparation**

Fracture toughness tests were conducted on the extracted C(T) specimens using the single specimen compliance measurement-based approach following ASTM 1820[19] standard. For each material, the tests were performed on four stepped notched specimens; two with vertical and two with horizontal orientation. For each material and orientation, one test was conducted on a sample extracted from the top of the WAAM wall (denoted by T) while the second test was performed on a sample extracted from the bottom of the wall (denoted by B). The fracture toughness specimens made of ER70S-6 and ER100S-1 materials are denoted as CT-70-1 – CT-70-4 and CT-100-1 – CT-100-4. Subsequent to specimen manufacture and prior to testing, all specimens were pre-cracked under fatigue loading using the load-decreasing approach to approximately 32 mm (a/W = 0.64) which is within the allowable range for fracture toughness testing specified in ASTM 1820[19]. The starting fatigue pre-cracking load was maintained below the maximum allowable load calculated according to Equation 3.1[19]. The purpose of fatigue pre- cracking was to introduce an infinitely sharp crack tip ahead of the machined notch without developing a significant plastic zone size ahead of the crack tip.

$$F_{\max} = \frac{0.4B(W - a_0)^2 \sigma_Y}{2W + a_0}$$ Equation 3.1

It is worth noting that ASTM 1820[19] recommends to pre-fatigue crack the plane sided samples first and then introduce the required percentage of side grooves into the test specimens. However, since the specimens were created using the WAAM technique, the trial tests on dummy samples revealed that maintaining a straight crack path during pre-fatigue cracking was highly challenging and deviations from the straight lines were observed in some dummy samples. Therefore, it was decided to side groove the specimens first and then pre-fatigue crack the samples to maintain a straight started crack and ensure that valid fracture toughness results are obtained from the experiments. The 16 mm thick C(T) specimens were side grooved from both sides by 0.25*B* (i.e. 25% of the total thickness) which resulted in a net thickness of B_n = 12 mm.

- **Crack length estimation and J parameter calculation**

The estimation of instantaneous crack length in both preliminary fatigue pre-cracking and fracture toughness testing was carried out using the compliance technique and by attaching a clip gauge onto the crack mouth of the specimen. In this approach, the load-line-displacement (LLD) is continuously monitored during the test and the instantaneous crack length is calculated using the elastic compliance measurements following Equation 3.2 – Equation 3.4 where a_i is the instantaneous crack length, C_i is the instantaneous unloading compliance, E is the elastic Young's modulus and B_e is the effective thickness which is calculated using the specimen full thickness B and net thickness value B_n.

$$\frac{a_i}{W} = 1.000196 - 4.06319u + 11.242u^2 - 106.043u^3 + 464.335u^4 - 650.677u^5$$ Equation 3.2

where

$$u = \frac{1}{\left[B_e E C_i\right]^{\frac{1}{2}}} + 1$$ Equation 3.3

$$B_e = B - (B - B_n)^2 / B$$ Equation 3.4

Fracture toughness tests were performed on a servo-hydraulic machine with the load carrying capacity of 100 kN. The tests were conducted under LLD control mode, by applying the sequences of loading and unloading with 60 seconds of hold time at each peak load followed by 20% unloading with respect to the peak load value. The loading/unloading rate in all fracture toughness tests was 1 mm/min and the sequences of unloading were conducted at LLD intervals of 0.125 mm. All tests were carried out at room temperature. In order to build up a resistance curve (i.e. *R*-curve) for fracture toughness analysis, the elastic-plastic fracture mechanics parameter *J* was calculated using Equation 3.5 that is recommended by ASTM 1820[19]. As seen in this equation, the total value of *J* is calculated by partitioning it into an elastic and a plastic term which are calculated using Equation 3.6 and Equation 3.7, respectively. In Equation 3.6 and 3.7, *K* is the stress intensity factor the solutions of which are available in the textbooks for different geometries[23], v is the Poisson's ratio, a_0 is the initial crack length, A_p is the plastic

area under the load *vs.* LLD curve and η is a geometry dependent function, the solution of which for C(T) specimen geometry is specified in Equation 3.8.

$$J = J_{el} + J_{pl} \quad \text{Equation 3.5}$$

where

$$J_{el} = \frac{K^2(1-\nu^2)}{E} \quad \text{Equation 3.6}$$

$$J_{pl} = \frac{A_p}{B_n(W-a_0)}\eta \quad \text{Equation 3.7}$$

$$\eta = 2 + 0.522(W-a_0)/W \quad \text{Equation 3.8}$$

In order to evaluate the fracture toughness value, the *R*-curve is generated for each test by plotting *J* values against the crack extension, Δa. A blunting line is then constructed (i.e. also referred to as the construction line), the slope of which is estimated using Equation 3.9. Subsequently, two exclusion lines are constructed parallel to the blunting line, offsetting the abscissa at 0.15 mm and 1.5 mm. The data points along the *R*-curve that fall in between these two exclusion lines are considered valid and a line of best fit is made to them. The intersection between the line of best fit and a 0.2 mm offset line parallel to the blunting line defines the fracture toughness value which is referred to as J_{IC}. An example of the above procedure is shown in Figure 3.8 for CT-100-3 specimen.

$$J = 2\sigma_Y \Delta a \quad \text{Equation 3.9}$$

- **Fracture toughness results**

The load *vs.* LLD data obtained from all the fracture toughness tests conducted on ER70S-6 and ER100S-1 specimens are shown in Figure 3.5 and 6, respectively. The comparison of these two figures shows that the deviation from linearity occurs at a much higher load level in ER100S-1 than ER70S-6, due to the higher yield stress. Also seen in these figures is that upon reaching the maximum load, P_{max}, for each increment of load line displacement, the reduction in the corresponding load level occurs at a much higher rate in ER100S-1 than ER70S-6. Finally seen in these figures is that while similar load *vs.* LLD trends are observed in the tests on ER70S-6 material, more noticeable differences can be observed in the test data on ER100S-1 material. It can be seen in Figure 3.6 that the sample extracted with the vertical orientation from the bottom of the wall shows the lowest load *vs.* LLD trend while the sample with horizontal orientation extracted from the top of the wall is exhibiting the highest trend. Finally, it can be seen in these figures that the specimens extracted from the bottom of the wall in both orientations generally show a lower trend compared to those of extracted from the top of the walls indicating the importance the specimens location and orientation of the fracture toughness values in WAAM build components.

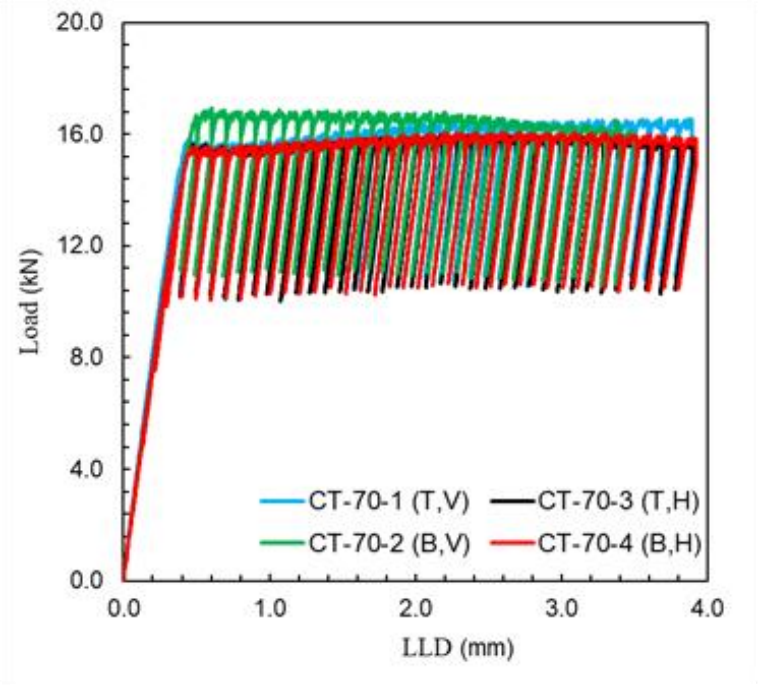

Figure 3.5: Load vs. LLD for ER70S-6 specimens

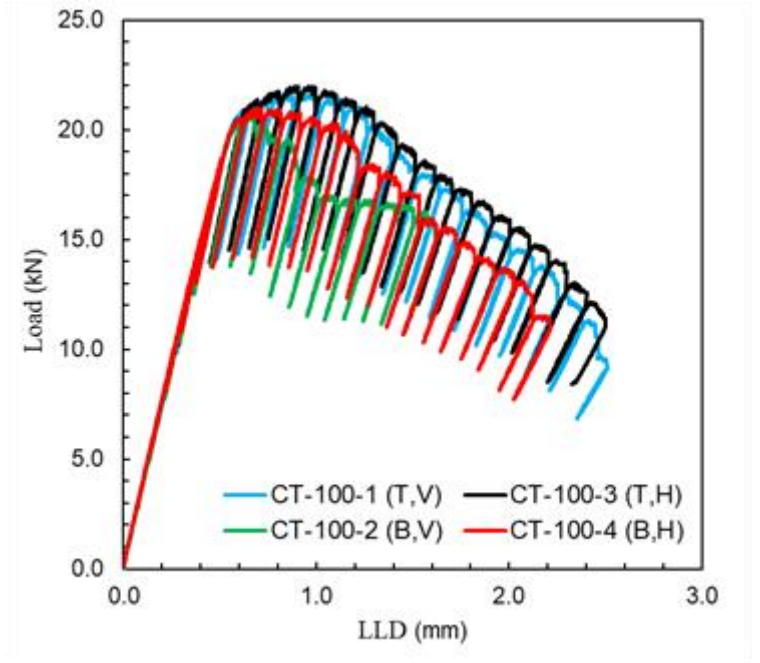

Figure 3.6: Load vs. LLD for ER100S-1 specimens

The fracture toughness *R*-curves generated for all specimens are presented in Figure 3.7, and the J_{IC} values are summarised in Table 3.5. Also, an example of the detailed fracture toughness analysis by constructing the blunting line, applying the exclusion lines and applying a line of best fit to the valid data points is given in Figure 3.7. It can be seen in Figure 3.7 that the *R*-curves for the specimens extracted from ER70S-6 show a much higher trend than ER100S-1 meaning that much more energy is required to propagate the crack in specimens made of WAAM ER70S-6 material. This observation is consistent with the fracture toughness values summarised in Table 3.5 which are on average around nine times higher in ER70S-6 material

compared to ER100S-1 (i.e. the average J_{IC} values for ER70S-6 and ER100S-1 are 420.11 kJ/m^2 and 49.19 kJ/m^2, respectively). Also seen in Figure 3.7 is that for ER100S-1 material, the specimens extracted from the bottom of the WAAM wall show noticeably lower trends than those extracted from the top of the wall. Detailed comparison of the fracture toughness values in Table 3.5 shows that for ER70S-6, all fracture toughness values are similar to each other except the vertical sample extracted from the bottom of the wall. Finally seen in Table 3.5 is that for ER100S-1, while the samples extracted from the bottom of the wall exhibit a noticeably lower fracture toughness value (48% lower), the specimens with vertical orientations have lower fracture toughness values compared to the horizontal samples. This means that similar to ER70S-6, the lowest value of fracture toughness for ER100S-1 is observed for vertical orientation at the bottom of the WAAM wall. These observations on the *R*-curves are consistent with the load *vs.* LLD trends seen in Figure 3.5 for ER70S-6 specimens and Figure 3.6 for ER100S-1.

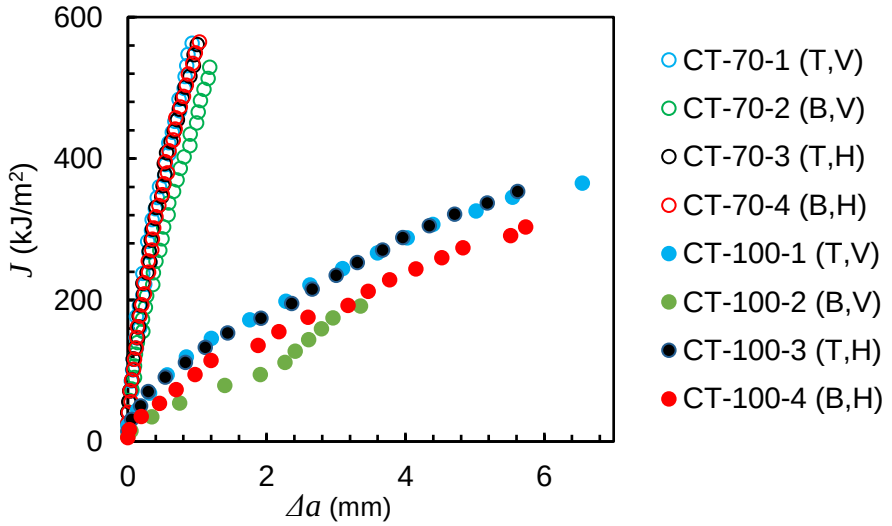

Figure 3.7: Resistance curves for ER70S-6 and ER100S-1 specimens

Table 3.5: Fracture toughness values for ER70S-6 and ER100S-1 specimens

	CT-70-1 (T, V)	CT-70-2 (B, V)	CT-70-3 (T, H)	CT-70-4 (B, H)	CT-100-1 (T, V)	CT-100-2 (B, V)	CT-100-3 (T, H)	CT-100-4 (B, H)
J_{IC} (kJ/m^2)	474.08	312.05	449.16	445.15	62.02	28.68	68.05	38.01

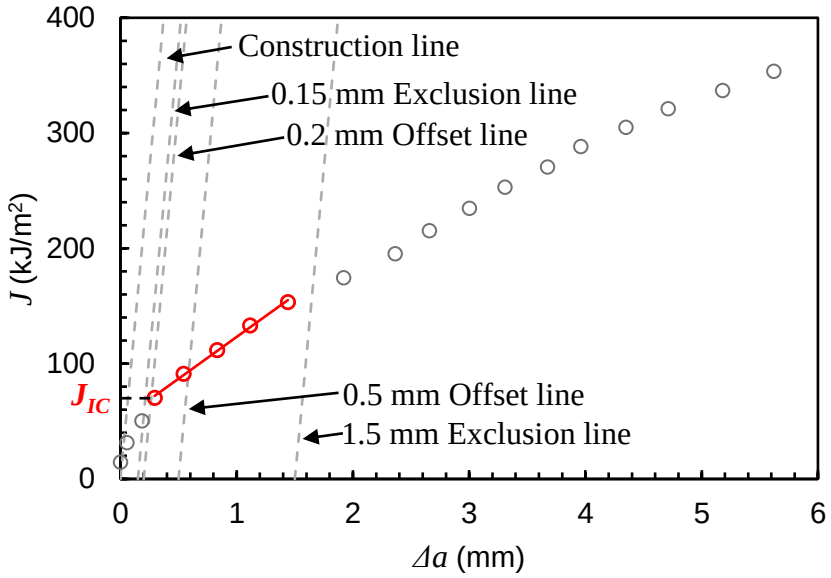

Figure 3.8: Analysis of the fracture toughness data for CT-100-3 specimen

- **Fractography**

In order to evaluate the percentage of error in crack extension values obtained using the compliance technique, post-mortem analysis was conducted on all tested fracture toughness specimens. Subsequent to completion of the fracture toughness tests, all eight specimens were placed in liquid nitrogen for 10 minutes, to facilitate the fast fracture process with minimum plastic deformation, then the specimens ends were separated by means of the hydraulic machine. High resolution macroscopic pictures of the two fracture surfaces of each specimen are shown in Figure 3.9. As shown in Figure 3.9(a), three surface areas namely 1) the pre-fatigue cracking region, 2) fracture toughness region, and 3) fast fracture region have been identified and the crack extensions in these areas have been measured for each of the test specimens.

It can be seen in Figure 3.9 that the cup and cone feature is evident in ER70S-6 specimens, whereas ER100S-1 specimens exhibit a relatively flat fracture surface. Moreover, it can be noted that vertical specimens (with the crack path going across the WAAM layers) have a wavy pre-fatigue cracking surface, which represents different layers. Also, symmetric crack propagation regions can be seen in the fractography analysis which confirms that appropriate alignment was maintained during the fracture toughness tests. The key specimen dimensions together with the machined crack length a_o, initial crack length after pre-fatigue cracking (estimated from the compliance data) $a_{i,p}$, the final crack length estimated from the compliance data $a_{f,c}$, and final crack length measured on the fracture surface, $a_{f,op}$ are summarised in Table 3.6. Also included in this table is the percentage of error between the measured and estimated final crack lengths. It can be seen in the table that the error is below 9% for all specimens, which confirms that accurate enough estimations were made using the compliance data during the fracture toughness testing process.

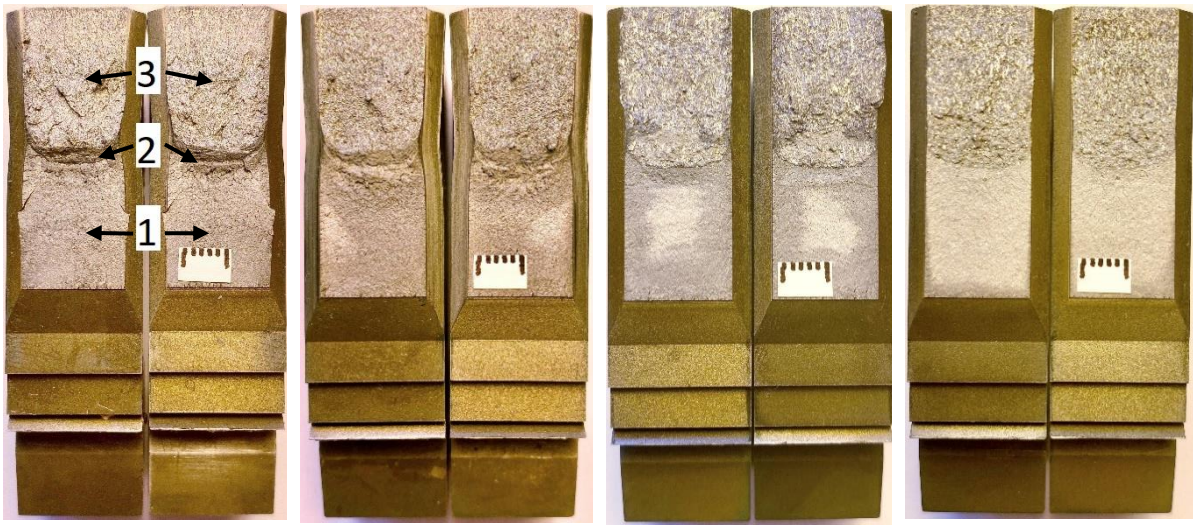

(a) (b) (c) (d)

Figure 3.9: Fracture surface for ER70S-6 specimen: (a) vertical CT-70-1, (b) horizontal CT-70-3; ER100S-1: (c) vertical CT-100-1, (d) horizontal CT-100-3

Table 3.6: Specimen dimensions and the initial and final crack lengths

Specimen ID	W (mm)	B (mm)	B_n (mm)	a_0 (mm)	$a_{i,p}$ (mm)	$a_{f,c}$ (mm)	$a_{f,op}$ (mm)	*% error in* a_f
CT-70-1	50.1	16.0	12.2	17.0	31.6	32.2	35.0	8.0
CT-70-2	50.0	16.1	12.2	17.1	30.3	32.9	33.7	2.3
CT-70-3	50.0	16.0	12.2	17.0	31.3	32.8	33.6	2.5
CT-70-4	50.0	16.0	12.2	17.2	31.5	32.8	33.8	3.0
CT-100-1	50.1	16.2	12.1	17.1	32.4	38.3	38.6	0.6
CT-100-2	50.0	16.1	12.1	17.0	31.5	35.2	35.8	1.7
CT-100-3	50.2	16.0	12.1	17.1	31.7	37.4	41.1	9.0
CT-100-4	50.0	16.2	12.1	17.0	31.5	37.6	37.1	1.2

3.1.6. Discussions

The ER70S-6 specimens examined in the present study show hardness values ranging from 137 to 180 HV, with the yield stress ranging from 365 to 390 MPa and the UTS values varied from 518 to 522 MPa. The obtained data from these experiments are in good agreement with the data provided in the literature[5,24], though some researchers have reported higher or lower values[17,25], which may be particularly because of the different WAAM parameters selected for the fabrication of the walls. Moreover, the average fracture toughness result obtained in this study on ER70S-6 is 420.11 kJ/m^2 which is slightly lower than the result found in the literature for this material[17]. The specimens made with ER100S-1 provide hardness values ranging from 222 to 290 HV, with the yield stress ranging from 536 to 538 MPa, accompanied by UTS values varying from 815 to 818 MPa. The average fracture toughness obtained for these specimens

was 49.19 kJ/m^2. No data on the mechanical or fracture toughness properties of WAAM ER100S-1 material was found in the literature for comparison.

The study of different orientations in the current research has shown that regardless of the material employed in the WAAM process, both values of yield stress and σ_{UTS} are higher for horizontal specimens than for vertical. It must be noted here that only two specimens per orientation were tested during this study, thus more tests need to be conducted to verify the preliminary result. This was also reported by several other authors[5,17,6]. Another interesting observation is that the strain at failure is similar in horizontal and vertical specimens for both materials. As for the fracture toughness results, the orientation and specimen extraction location have been found more influential on ER100S-1 than ER70S-6. The comparison of the two materials shows that ER100S-1 has more brittle behaviour compared with ER70S-6 that is more ductile. This can be concluded from the mechanical properties, along with an examination of the fracture surfaces. The fluctuation of hardness values through the WAAM layers is more pronounced for ER100S-1 offcuts. Another observation that can be made from the present study is that the yield stress and hardness values are proportional to each other, as suggested in the literature[26].

The above results were compared with characteristics of widely used wrought structural metals in Table 3.7, where the average values are presented. It can be seen from the table that with the highest values of hardness, yield and ultimate tensile stresses, ER100S-1 shows slightly higher fracture toughness results than aluminium, however this value is much less than for S355 steel. Whereas ER70S-6 values of yield and ultimate stresses are comparable with S355 and SS316, however fracture toughness is lower by 25% and 50% respectively. Hardness of ER70S-6 and SS316 is similar and the lowest among the presented materials.

Table 3.7: Comparison analysis of WAAM specimens with widely used wrought metals

Material	*E (GPa)*	σ_Y *(MPa)*	σ_{UTS} *(MPa)*	*Hardness (HV)*	J_{IC} (kJ/m^2)
S355[26]	198	446	546	198	830
SS316[27]	205	313	603	155	560
Aluminium[28]	72	503	564	175	29
ER70S-6	215	378	520	155	420
ER100S-1	168	537	817	251	49

In order to fully characterise ER70S-6 and ER100S-1 WAAM walls for various industrial applications, fatigue crack initiation and propagation tests will be performed on specimens with different orientations and extraction locations in the following chapters of the thesis. Moreover, residual stresses will be measured in the WAAM walls and extracted specimens to account for their effects on the fatigue behaviour of the WAAM walls made of both materials. Different surface treatment techniques, such as rolling or shot peening, can significantly improve the performance of WAAM specimens[29] and will also be investigated further for current materials. Comprehensive metallurgical analysis of the WAAM walls will be carried out in future work

to investigate the correlation between hardness variations and metallurgical features in the WAAM walls.

3.1.7. Conclusions

Material characterisation tests have been conducted on specimens fabricated using WAAM technique with ER70S-6 and ER100S-1 materials. The results have revealed that the average hardness value on ER70S-6 steel specimens is 155 HV which is 61% lower than the value obtained for ER100S-1. Moreover, at the top and bottom of the WAAM walls, higher hardness values are observed for ER70S-6 material, whereas the hardness values in ER100S-1 material were almost uniform. The results have also shown that lower yield stress and UTS values were observed in specimens made of ER70S-6, which have exhibited the higher average fracture toughness compared to ER100S-1 samples, confirming that the values of yield stress and hardness are proportional to each other and inversely proportional to fracture toughness. A trend was discovered for both materials that yield stress and UTS values are similar for different specimen orientations though slightly lower in vertical orientation compared to horizontal samples extracted across the WAAM layers. The specimen orientation does not significantly affect the fracture toughness results in both materials, however, for ER100S-1 the specimen extraction location has been found to have a significant effect on fracture toughness with specimens extracted from the top of the wall showing 48% higher value compared to those extracted from the bottom of the WAAM wall.

3.1.8. Acknowledgements

This work was supported by grant EP/L016303/1 for Cranfield, Oxford and Strathclyde Universities' Centre for Doctoral Training in Renewable Energy Marine Structures – REMS CDT (http://www.rems-cdt.ac.uk/) from the UK Engineering and Physical Sciences Research Council (EPSRC).

3.1.9. References for paper II

1. Williams, S. W., Martina, F., Addison, A. C., Ding, J., Pardal, G. & Colegrove, P. Wire + Arc Additive Manufacturing. *Mater. Sci. Technol.* **32**, 641–647 (2015).

2. Gordon, J. V., Haden, C. V., Nied, H. F., Vinci, R. P. & Harlow, D. G. Fatigue crack growth anisotropy, texture and residual stress in austenitic steel made by wire and arc additive manufacturing. *Mater. Sci. Eng. A* **724**, 431–438 (2018).

3. Bandari, Y. K., Charrett, T. O. H., Michel, F., Ding, J., Williams, S. W. & Tatam, R. P. Compensation Strategies for Robotic Motion Errors for Additive Manufacturing. *Solid Free. Fabr.* 1–14 (2016).

4. Zhang, M., Sun, C.-N., Zhang, X., Goh, P. C., Wei, J., Hardacre, D. & Li, H. Fatigue and fracture behaviour of laser powder bed fusion stainless steel 316L: Influence of processing parameters. *Mater. Sci. Eng. A* **703**, 251–261 (2017).

5. Haden, C. V., Zeng, G., Carter, F. M., Ruhl, C., Krick, B. A. & Harlow, D. G. Wire and arc additive manufactured steel: Tensile and wear properties. *Addit. Manuf.* **16**, 115–123 (2017).

6. Lu, X., Zhou, Y. F., Xing, X. L., Shao, L. Y., Yang, Q. X. & Gao, S. Y. Open-source wire and arc additive manufacturing system: formability, microstructures, and mechanical properties. *Int. J. Adv. Manuf. Technol.* **93**, 2145–2154 (2017).

7. Suryakumar, S., Karunakaran, K. P., Chandrasekhar, U. & Somashekara, M. A. A study of the mechanical properties of objects built through weld-deposition. *Proc. Inst. Mech. Eng. Part B J. Eng. Manuf.* **227**, 1138–1147 (2013).

8. Wang, F., Williams, S., Colegrove, P. & Antonysamy, A. A. Microstructure and mechanical properties of wire and arc additive manufactured Ti-6Al-4V. *Metall. Mater. Trans. A Phys. Metall. Mater. Sci.* **44**, 968–977 (2013).

9. Neto, L., Williams, S., Ding, J., Hönnige, J. & Martina, F. Mechanical Properties Enhancement of Additive Manufactured Ti-6Al-4V by Machine Hammer Peening. in *Lecture Notes in Mechanical Engineering* 121–132 (Springer, 2020). doi:10.1007/978-981-15-0054-1_13

10. Xu, X., Ganguly, S., Ding, J., Guo, S., Williams, S. & Martina, F. Microstructural evolution and mechanical properties of maraging steel produced by wire + arc additive manufacture process. *Mater. Charact.* (2018). doi:10.1016/j.matchar.2017.12.002

11. Zhang, X., Martina, F., Ding, J., Wang, X. & Williams, S. W. Fracture toughness and fatigue crack growth rate properties in wire + arc additive manufactured Ti-6Al-4V. *Fatigue and Fracture of Engineering Materials and Structures* **40**, 790–803 (2017).

12. ER70S-6 - Weld WireWeld Wire. Available at: http://www.weldwire.net/weld_products/ww70s-6/. (Accessed: 27th March 2020)

13. *Mild Steel Welding Alloy ER70S-6 (GMAW) (MIG) ER70S-6 (GMAW) (MIG) Mild Steel Alloy • AWS ER70S-6*.

14. Lincoln Electric Company, T. *LINCOLN ® ER70S-6 WELDING POSITIONS TYPICAL APPLICATIONS*.

15. *ER100S-G Data Sheet - Bohler Welding*. (2014).

16. *ER100S-1 Data Sheet - Pinnacle Alloys*.

17. Dirisu, P., Ganguly, S., Mehmanparast, A., Martina, F. & Williams, S. Analysis of fracture toughness properties of wire + arc additive manufactured high strength low alloy structural steel components. *Mater. Sci. Eng. A* **765**, 138285 (2019).

18. Ermakova, A., Mehmanparast, A. & Ganguly, S. A review of present status and challenges of using additive manufacturing technology for offshore wind applications. *Procedia Struct. Integr.* **17**, 29–36 (2019).

19. American Society for Testing and Materials. ASTME-1820-11: standard test method for measurement of fracture toughness. *Annu. B. ASTM Stand.* 1–55 (2011). doi:10.1520/E1820-18

20. ASTM Standard E8/E8M-13a. 'Standard Test Methods for Tension Testing of Metallic Materials'. *ASTM Int.* **i**, 1–27 (2013).

21. Acciaioli, A., Lionello, G. & Baleani, M. Experimentally achievable accuracy using a digital image correlation technique in measuring small-magnitude (< 0.1%) homogeneous strain fields. *Materials (Basel).* **11**, (2018).

22. International Standard ISO. Metallic materials - Vickers hardness test - Part 1 : Test method (ISO 6507-1 : 2018). *Int. Stand.* 1–49 (2018). doi:ISO 6507-1 : 2018

23. Anderson, T, L. *Fracture Mechanics: Fundamentals and Application*. (Taylor & Francis Group, 2005).

24. Shirizly, A. & Dolev, O. From Wire to Seamless Flow-Formed Tube: Leveraging the Combination of Wire Arc Additive Manufacturing and Metal Forming. *Jom* **71**, 709–717 (2019).

25. Ron, T., Levy, G. K., Dolev, O., Leon, A., Shirizly, A. & Aghion, E. Environmental behavior of low carbon steel produced by a wire arc additive manufacturing process. *Metals (Basel).* **9**, (2019).

26. Mehmanparast, A., Taylor, J., Brennan, F. & Tavares, I. Experimental investigation of mechanical and fracture properties of offshore wind monopile weldments: SLIC interlaboratory test results. *Fatigue Fract. Eng. Mater. Struct.* **41**, 2485–2501 (2018).

27. Mehmanparast, A. & Davies, C. M. The influence of inelastic pre-straining on fracture toughness behaviour of Type 316H stainless steel. *Eng. Fract. Mech.* **188**, 112–125 (2018).

28. Lai, M. O. & Ferguson, W. G. Fracture toughness of aluminium alloy 7075-T6 in the as-cast condition. *Mater. Sci. Eng.* **74**, 133–138 (1985).

29. Tangestani, R., Farrahi, G. H., Shishegar, M., Aghchehkandi, B. P., Ganguly, S. & Mehmanparast, A. Effects of Vertical and Pinch Rolling on Residual Stress Distributions in Wire and Arc Additively Manufactured Components. *J. Mater. Eng. Perform.* **29**, 2073–2084 (2020).

3.2. Paper III: Corrosion effects on fracture toughness properties of wire arc additively manufactured low carbon steel specimens

Anna Ermakova[a], Ali Mehmanparast[a*]

[a] Department of Naval Architecture, Ocean and Marine Engineering, University of Strathclyde, Glasgow G1 1XQ, United Kingdom

Abstract[3]

The new emerging Wire + Arc Additive Manufacturing (WAAM) technique has significant potential to improve material design as well as manufacturing cost and efficiency of the structural components, such as offshore wind turbines, and subsequently reduce the Levelised Cost of Energy (LCoE). Welded joints in offshore structures are usually considered as potential spots for crack initiation due to combination of high stress concentration at the weld toes, the residual stresses introduced by the welding process and the cyclic loading condition in harsh corrosive marine environments. The WAAM technique is a deposition method consisting of repetitive welding process, that can be used as an alternative manufacturing technique for fabrication or repair of structural components. An important issue that needs to be understood in structural integrity assessment of WAAM built components is the fracture toughness behaviour. Particularly, the sensitivity of the fracture toughness properties to corrosive environments must be understood in order to extend the application of the WAAM technique to offshore wind structures. Therefore, fracture toughness tests were conducted in this study on WAAM built compact tension specimens made of ER70S-6 and ER100S-1 steel that were initially exposed to the seawater corrosive environment prior to testing. All fracture toughness tests were performed at room temperature and the crack length was estimated using the compliance method with the clip gauge attached onto the knife edge of the specimens. The failure mechanism in the corroded specimens was observed, and the obtained results were analysed and compared with those tested in air (without any corrosion damage). The results include the comparison of load *vs.* load line displacement and *J*-integral *vs.* crack extension. The conclusions from this study contribute to the overall understanding of the design requirements for structures fabricated by means of WAAM technique for offshore applications.

Keywords: WAAM; Additive Manufacturing; Fracture; Corrosion; Offshore wind turbines.

---

[*] corresponding author

[3] *Metals* 2022, 12(2), 238; (DOI: 10.3390/met12020238)

3.2.1. Introduction

Corrosion is one of the key factors that affects the short- and long-term performance of steel structures exposed to harsh offshore environments, e.g., offshore wind turbines. The residual mechanical properties of rusty steel structures need to be assessed to ensure safety and provide further repair and reinforcement plan for the damaged structure. Fracture is a common and dangerous failure mode, especially if the behaviour is brittle or quasi-brittle, as fracture may occur suddenly without a visible warning. In ductile steels the brittle fracture can happen if concentration forces exist, for instance at the initiated fatigue crack, weld defect or geometry notch[1]. Moreover, the corrosion pits on damaged steel surface can act as stress concentrators and benefit the fracture failure mechanisms[2,3]. Therefore, it is likely that the fracture behaviour of corroded steel parts will degrade over time.

The new wire arc additive manufacturing (WAAM) technique offers a variety of benefits to various industries. Compared with other additive manufacturing (AM) techniques, such as powder-based methods, WAAM is known for lower manufacturing cost and high deposition rates for large-scale structural fabrication, which leads to reduction of manufacturing lead-time[4–7]. Nevertheless, this process consists of pure welding mechanism, depositing one metal layer on top of another, while constantly reheating and cooling down the built part. This causes uncertainties in microstructural homogeneity and mechanical properties isotropy[8,9]. Also, the inherent weld defects can be considered as potential weak spots where fracture and fatigue failure can develop[10]. Thus, in order to minimise the safety risks, the degradation mechanisms of corroded WAAM built steel components need to be carefully investigated in order to assess the suitability of this technique for offshore applications.

Great number of studies have been previously conducted to examine the corrosion effects on mechanical behaviour of conventionally built metallic specimens and welded joins. They include tensile tests performance on corroded specimens, derivation of empirical models and evaluation methods, and finally prediction of residual mechanical properties[11–18]. Moreover, some investigated the residual performance of degraded corroded steel parts[19–21]. However, only limited number of papers are available on fracture properties of corroded steel parts and there is almost no investigation on corrosion damage effects on fracture behaviour of WAAM built parts.

A research group has examined the fracture toughness performance of the corroded U-notched steel plates[22] and the results revealed significantly degraded fracture properties. According to this study, the ultimate load and fracture toughness decreased for the corroded specimens. Also, it was established that the corrosion pits increase the driving force of crack propagation. Another comprehensive test programme by Hou et al.[23] was carried out on effects of corrosion on mechanical properties of metals used for buried steel pipes, where a relationship between corrosion and deterioration of mechanical properties was developed. It was also concluded that both tensile strength and fracture toughness of corroded steel are reduced as a result of corrosion.

The intention of the present study is to investigate the effect of corrosion on fracture toughness properties of WAAM built specimens made with different grades of steel including ER70S-6 and ER100S-1. The WAAM manufacturing set-up, specimens extraction and testing procedure are described in the paper. Prior to fracture toughness testing, the specimens were soaked in

artificial seawater to assess the environmental effect on fracture properties. The test results have been analysed and compared with the previously tested WAAM built specimens without any environmental exposure (i.e., in air and in the absence of corrosion damage). The results produced in this study contribute to the overall knowledge of corrosion behaviour and its effects on fracture properties of WAAM steels to evaluate the suitability of this technique for fabrication and repair of offshore wind turbine structures.

3.2.2. Specimen fabrication and preparation process

In this study four specimens were extracted from two different WAAM walls, one made with ER70S-6 welding wire[24] and the other one with ER100S-1[25]. The chemical composition for each wire is presented in Table 3.8. Both walls were manufactured using Cold Metal Transfer (CMT) process with parameters shown in Table 3.9 and by employing an oscillation deposition method[26] which is often used for fabrication of relatively thick WAAM walls. The manufacturing set-up for the WAAM walls is demonstrated in Figure 3.10, which consists of a CMT power source, a robotic arm with a CMT torch that supplies the shielding gas and the welding wire simultaneously, and an exhaust fan that removes excessive heat and fumes from the WAAM wall. Each wall was deposited in the middle of a base plate cut from an EN10025 rolled structural steel, which was firmly attached onto the working table with eight clamps during the fabrication process to minimise any bending or distortion of the base plate and the WAAM wall as a result of high manufacturing temperatures. The clamps were removed once the deposition was completed, and the walls were cooled down to the ambient temperature.

Table 3.8: Chemical composition of the WAAM wires (wt.-%)[24,25]

	C	*Mn*	*Cr*	*Si*	*Ni*	*Mo*	*S*	*P*	*Cu*	*V*
ER70S-6	0.09	<1.60	0.05	0.09	0.05	0.05	0.007	0.007	0.20	0.05
ER100S-1	0.08	1.70	0.20	0.60	1.50	0.50	-	-	-	-

Table 3.9: CMT-WAAM fabrication parameters

Shielding gas	Ar+20% CO_2
Gas flow rate	15 L/min
Robot travelling speed	7.33 mm/sec
Wire diameter	1.2 mm
Wire feed speed	7.5 m/min
Dwell time	120 sec

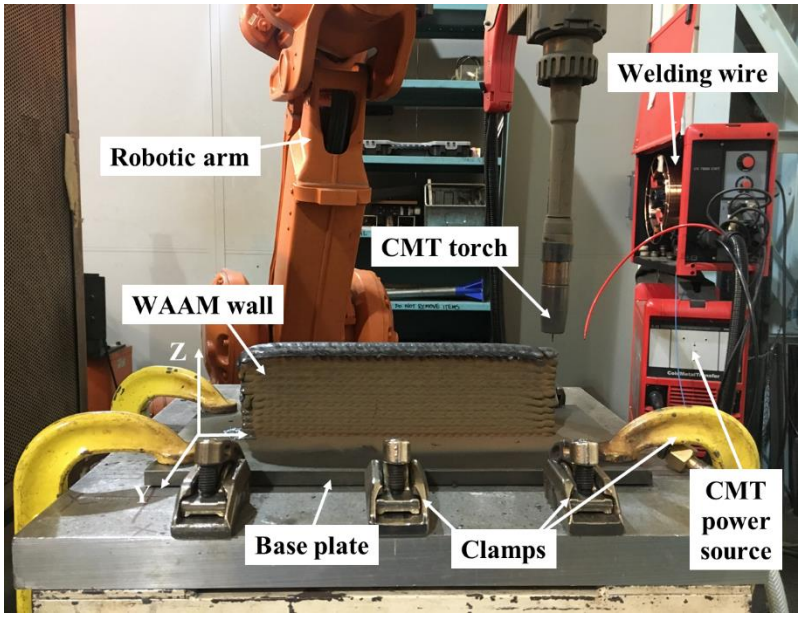

Figure 3.10: The CMT WAAM set-up

Upon completion of the wall deposition, two notched compact tension C(T) specimens from the top (T) half of each wall were extracted using Electrical Discharge Machining (EDM) method. The specimens from the bottom of the wall were used in a different study. The specimens were extracted in two different orientations with respect to the deposited AM layers: vertical (V) – with the crack growth direction perpendicular to the AM layers, and horizontal (H) – with the crack growth direction along the AM layers, as schematically presented in Figure 3.11. The specimens were designed in accordance with the ASTM 1820 standard[27] for fracture toughness testing with the width of W = 50 mm, the height of H = 60 mm, total thickness of B = 16 mm and initial crack length of a_0 = 17 mm before pre-fatigue cracking. The specimens were not side grooved (hence B_n = 16 mm) to facilitate the introduction of corrosion damage on the outer surface during exposure to seawater. The fracture toughness C(T) specimens made of ER70S-6 and ER100S-1 welding wires were denoted as C-70-1 (T, V), C-70-2 (T, H) and C-100-1 (T, V), C-100-2 (T, H), respectively. Prior to testing, all specimens were fatigue pre-cracked under cyclic loading condition using the load decreasing approach to approximately 32 mm (a/W = 0.64), as advised in the ASTM 1820 standard. The starting fatigue pre-cracking load was maintained below the maximum allowable load specified in the standard. During the pre-cracking process, an infinitely sharp crack tip is introduced ahead of the machined notch without developing a significant plastic zone ahead of the crack tip. Once the specimens were prepared for fracture toughness testing, they were immersed for 11 days in artificial seawater that was made according to the ASTM D1141-98 standard[28] using deionised water with composition shown in Table 3.10. The temperature of the artificial seawater was maintained between 8.0 and 10.0^{0}C using a chiller, and pH of 8.0 to replicate the operation conditions in the North Sea[28].

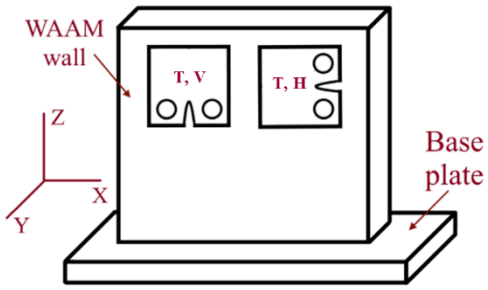

Figure 3.11: Schematic of the specimen extraction plan from the WAAM wall

Table 3.10: Chemical composition of artificial seawater

Chemical compound	Concentration (g/L)
NaCl	24.53
$MgCl_2$	5.20
Na_2SO_4	4.09
$CaCl_2$	1.16
KCl	0.695
$NaHCO_3$	0.201
KBr	1.101
H_3BO_3	0.027
$SrCl_2$	0.025
NaF	0.003

3.2.3. Crack length estimation and J parameter calculation

During fatigue pre-cracking and fracture toughness testing the estimation of instantaneous crack length was performed using the compliance method, by attaching a clip gauge onto the crack mouth of the specimen. This approach is based on constant load-line-displacement (LLD) monitoring, and calculating the instantaneous crack length using the elastic compliance measurements according to Equation 3.10 – Equation 3.12, where a_i is the instantaneous crack length, C_i is the instantaneous unloading compliance, E is the elastic Young's modulus and B_e is the effective thickness which is calculated using the specimen's full thickness B and net thickness value B_n.

$$\frac{a_i}{W} = 1.000196 - 4.06319u + 11.242u^2 - 106.043u^3 + 464.335u^4 - 650.677u^5 \quad \text{Equation 3.10}$$

where

$$u = \frac{1}{\left[B_e E C_i\right]^{\frac{1}{2}}} + 1 \qquad \text{Equation 3.11}$$

$$B_e = B - (B - B_n)^2 / B \qquad \text{Equation 3.12}$$

Fracture toughness tests were conducted at room temperature on a 100kN servo hydraulic Instron machine, under LLD control mode, by applying sequences of loading and unloading with 60 seconds of hold time at each peak load, followed by 20% unloading with respect to the peak load value. The loading-unloading rate was 1 mm/min, and the sequences of unloading were carried out at LLD intervals of 0.125 mm. To plot a resistance curve (i.e. *R*-curve) for each test, the elastic-plastic fracture mechanics parameter *J* was determined using Equation 3.13 as recommended by ASTM 1820[27]. It can be seen from the equation that the total value of *J* consists of an elastic and a plastic term which are calculated using Equation 3.14 and Equation 3.15, respectively. In these equations, *K* is the stress intensity factor, which varies for different specimen geometries[29], ν is the Poisson's ratio, a_0 is the initial crack length, A_p is the plastic area under the load *vs.* LLD curve and η is a geometry dependent function, the solution of which for C(T) specimen geometry is demonstrated in Equation 3.16.

$$J = J_{el} + J_{pl} \qquad \text{Equation 3.13}$$

where

$$J_{el} = \frac{K^2(1-\nu^2)}{E} \qquad \text{Equation 3.14}$$

$$J_{pl} = \frac{A_p}{B_n(W - a_0)}\eta \qquad \text{Equation 3.15}$$

$$\eta = 2 + 0.522(W - a_0)/W \qquad \text{Equation 3.16}$$

To establish the fracture toughness value, the *R*-curve is generated for each test by plotting *J* values against the crack extension, Δa. Then a construction line (which is also known as the blunting line) is plotted, the slope of which is calculated using Equation 3.17. In this equation, σ_Y is the yield stress of the material. Two exclusion lines are constructed parallel to the construction line, offsetting the abscissa by 0.15 and 1.5 mm. The data points along the *R*-curve that fall between two exclusion lines are considered valid data points, and a line of best fit is built to them. The intersection between the line of best fit and a 0.2 mm offset parallel to the construction line defines the fracture toughness value, denoted as J_{IC}.

$$J = 2\sigma_Y \Delta a \qquad \text{Equation 3.17}$$

3.2.4. Fracture toughness test results

The load *vs.* LLD data obtained from four fracture toughness tests performed on ER70S-6 and ER100S-1 corroded C(T) specimens are presented in Figure 3.12. Comparison of the curves for different materials shows that the deviation from linearity occurs at much higher load level in ER100S-1 than in ER70S-6 corroded specimens, due to the higher yield stress[30]. Also, it can be seen that the trends for two specimens of the same material look similar; however, for ER70S-6 material the horizontal specimen is exhibiting a higher trend compared to the vertical specimen, whereas for ER100S-1 it is the vertical specimen that shows the higher load *vs.* LLD trend compared to the horizontal specimen.

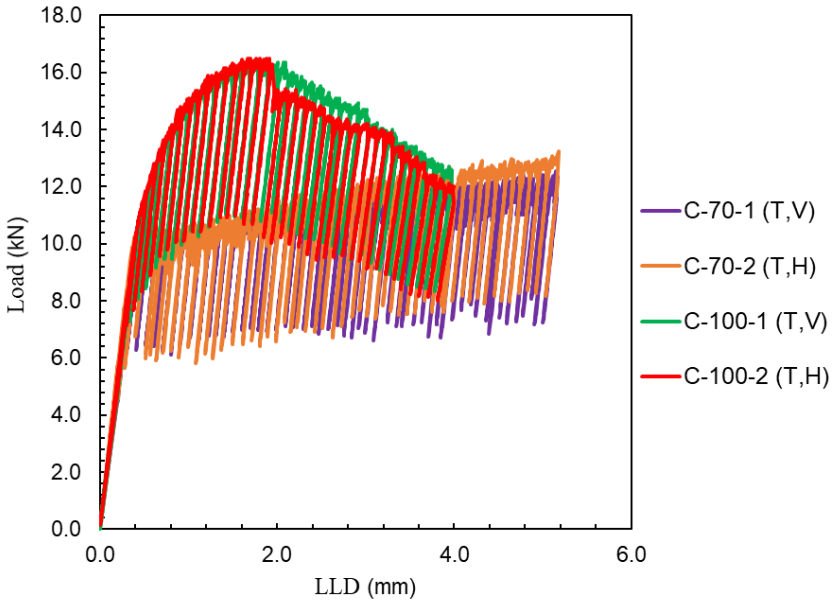

Figure 3.12: Load *vs.* LLD for both ER70S-6 and ER100S-1 corroded specimens

The results obtained in this study were further compared with the test results on similar C(T) specimens extracted from ER70S-6 and ER100S-1 WAAM walls and tested for fracture toughness in ambient conditions without any environmental exposure (denoted as A) by Ermakova et al.[30], presented in Figure 3.13. It can be seen in this figure that for both materials the obtained trends for corroded specimens are lower and longer than for the ambient tested specimens, indicating that the yield stress is reduced in corrosive environment[23]. The direct comparison of the ER70S-6 specimens extracted from the same location of the wall and with the same orientation presents that A-70-1 (T,V) and C-70-1 (T,V) have higher trends than specimens with horizontal orientation A-70-3 (T,H) and C-70-2 (T,H), hence the testing environment does not affect the orientation sensitivity of the specimens made with ER70S-6 welding wire. The scatter between ER100S-1 specimens with different orientations and the same locations is much smaller, and the results fall almost on top of each other. It must be noted here that in this study the tested corroded specimens were only extracted from the top of the wall, and in a future study, more specimens extracted from the bottom of the WAAM wall will be tested for further comparison of the obtained results with the samples tested without any prior exposure to seawater.

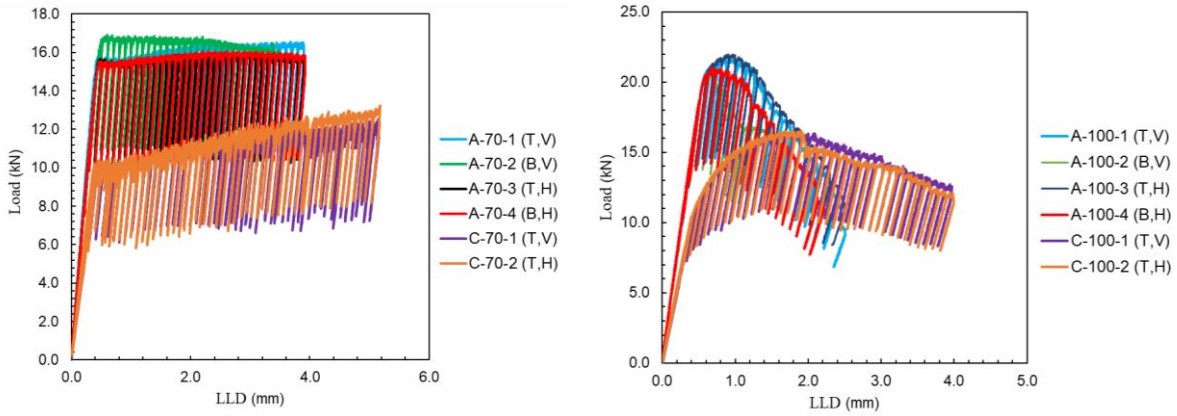

(a) (b)

Figure 3.13: Comparison of load *vs.* LLD for (a) ER70S-6 and (b) ER100S-1 specimens tested with and without corrosion exposure

The fracture toughness resistance curves were generated for four tested corroded specimens and are shown in Figure 3.14. It can be seen in this figure that the *R*-curves for the specimens extracted from ER70S-6 wall show much higher trends than ER100S-1, indicating that more energy is required to propagate the crack in specimens made of WAAM ER70S-6 material. The scatter for vertical and horizontal specimens for each material is small, and they almost overlap each other. An example of the detailed fracture toughness analysis, by plotting the blunting and exclusion lines, and the determination of J_{IC} value from the valid data points is displayed in Figure 3.15 (a) for C-100-1 specimen. The J_{IC} values for ER100S-1 corroded specimens are summarised in Table 3.11. The fracture toughness analysis of ER70S-6 corroded specimens revealed that no valid data points can be determined from the collected test data, as shown for C-70-1 specimen in Figure 3.15 (b), therefore J_{IC} values for ER70S-6 corroded specimens could not be quantified and compared in this study. However, as it was concluded above, the material properties change due to corrosion damage, therefore the slope of the blunting lines for both materials would change, as it depends on the material properties (Equation 3.17), hence the valid points and J_{IC} values will differ. In future work the tensile material properties of corroded specimens will be determined, to alter the blunting and exclusion lines for J_{IC} values quantification.

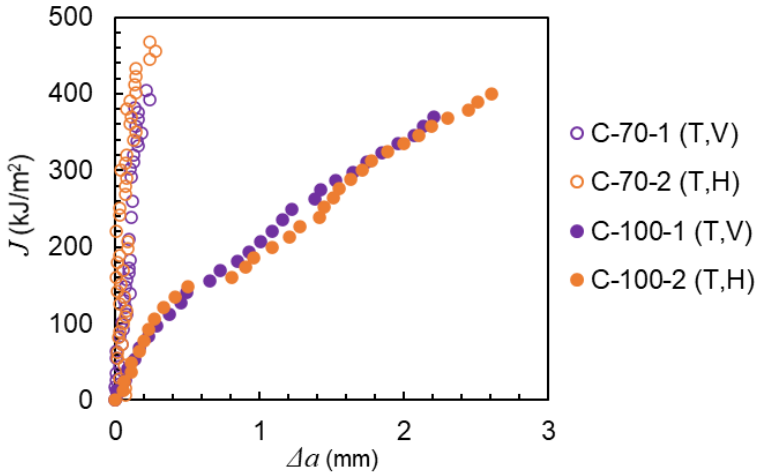

Figure 3.14: Resistance curves for ER70S-6 and ER100S-1 corroded specimens

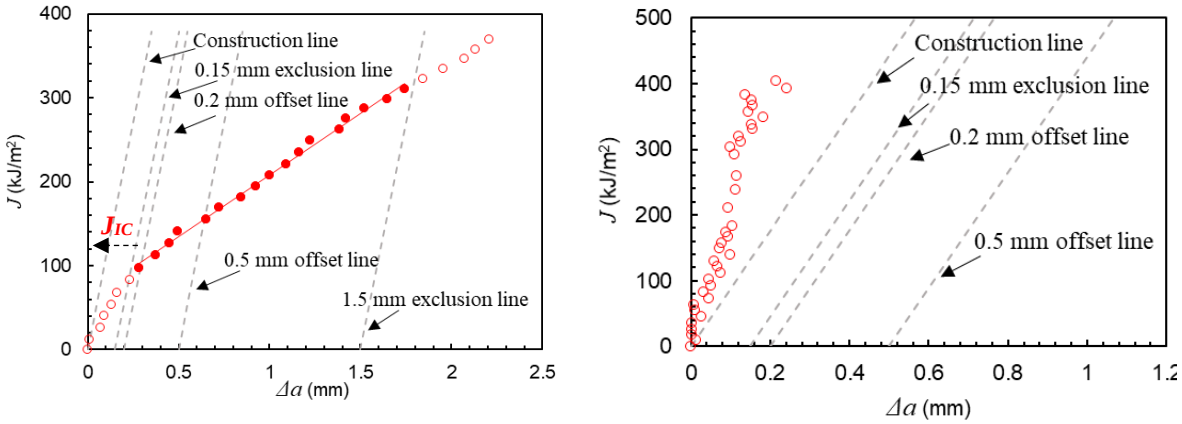

(a) (b)

Figure 3.15: Analysis of the fracture toughness data for (a) C-100-1 and (b) C-70-1 specimens

Table 3.11: Fracture toughness values for ER100S-1 corroded specimens

	C-100-1 (T, V)	C-100-2 (T, H)
J_{IC} (kJ/m^2)	104.2	109.0

Comparison of the resistance curves obtained in this study on corrosion exposed specimens with the previous study of Ermakova et al.[30] on ER70S-6 and ER100S-1 ambient specimens without any prior corrosion exposure is displayed in Figure 3.16. As seen in this figure, the slope of the curve is higher for corroded specimens for both of the WAAM built materials, indicating that a higher level of energy is required to propagate the crack in corroded specimens than in ambient specimens. As it was previously observed for ambient specimens, the *R*-curves for specimens extracted from the same location fall on top of each other, despite the orientation, and the same trend is seen for corroded specimens extracted from top of the WAAM walls. Analysis of J_{IC} values for ER100S-1 specimens demonstrates that for corroded specimens J_{IC} increased on average by 61%, compared with values for ambient specimens[30].

The higher level of fracture energy in corroded WAAM built specimens, compared to the samples without any prior exposure to seawater, can be associated with the fact that the corrosion process significantly altered not only the mechanical properties but also the sharpness of the crack tip in seawater exposed specimens. In other words, the results obtained from this study suggest that in both ER70S-6 and ER100S-1 WAAM built specimens, the exposure to seawater has resulted in significantly blunter crack tip which has subsequently elevated the R-curves in the fracture analysis. This indicates that while corrosion exposure is known to be a damaging mechanism, in the case of WAAM built components it can enhance the fracture properties by blunting the sharp fatigue crack tips created due to the cyclic loading effects exerted on the offshore structures. Therefore, the provisional results from this study show that the WAAM technique has a great potential for application in offshore wind industry; however, other design considerations such as fatigue must be investigated in more detail before

employing this efficient AM technique in fabrication or repair of offshore wind turbine structures.

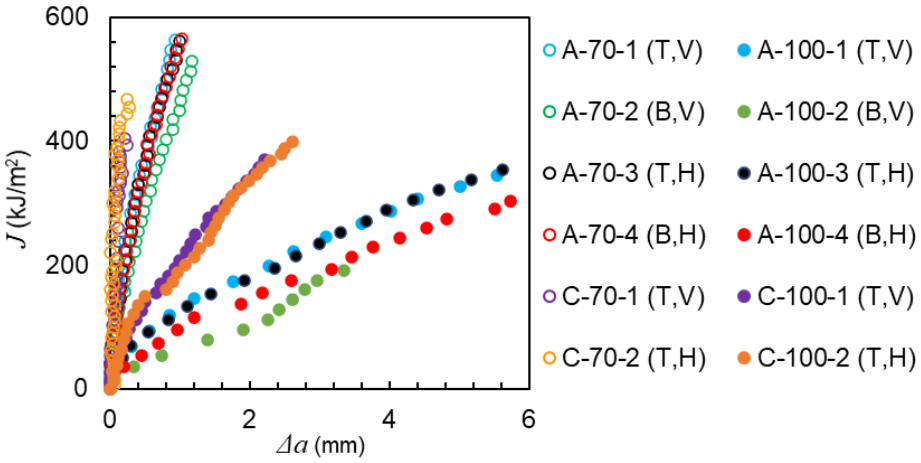

Figure 3.16: Comparison of resistance curves for ER70S-6 and ER100S-1 specimens with and without exposure to seawater

3.2.5. Conclusions

Fracture toughness tests were conducted on WAAM built specimens made with ER70S-6 and ER100S-1 welding wires. The specimens were immersed in seawater for 11 days prior to fracture testing to introduce corrosion effects in the test specimens. The results from this study were compared with those available on similar samples without exposure to seawater. The following conclusions and observations can be drawn from this study:

- The corrosive environment reduces the yield stress of the material, hence load *vs.* LLD curves show lower trends for corroded specimens for both ER70S-6 and ER100S-1 materials.
- The *R*-curves for corroded specimens fall higher than those obtained from specimens without prior corrosion exposure, thus a greater level of energy is required to propagate the crack in corroded specimens. The J_{IC} value for ER100S-1 corroded specimens is increased on average by 61% compared with J_{IC} value on the same material without corrosion exposure.
- The corrosion process does not only alter the mechanical properties in the WAAM built specimens, but also makes the fatigue cracks blunter which subsequently leads to improved fracture properties.
- The WAAM technique has demonstrated to have great potentials for employment in offshore applications, particularly manufacturing and repair of offshore wind turbine structures.
- Tensile properties of corroded specimens need to be investigated in future work, to improve the construction of the blunting and exclusion lines.

3.2.6. Acknowledgements

This work was supported by grant EP/L016303/1 for Cranfield, Oxford and Strathclyde Universities' Centre for Doctoral Training in Renewable Energy Marine Structures – REMS CDT (http://www.rems-cdt.ac.uk/) from the UK Engineering and Physical Sciences Research Council (EPSRC).

3.2.7. References for paper III

1. Berto, F. & Lazzarin, P. Recent developments in brittle and quasi-brittle failure assessment of engineering materials by means of local approaches. *Materials Science and Engineering: R: Reports* **75**, 1–48 (2014).

2. Pidaparti, R. M. & Rao, A. S. Analysis of pits induced stresses due to metal corrosion. *Corrosion Science* **50**, 1932–1938 (2008).

3. Kainuma, S., Jeong, Y. S. & Ahn, J. H. Investigation on the stress concentration effect at the corroded surface achieved by atmospheric exposure test. *Materials Science and Engineering: A* **602**, 89–97 (2014).

4. Williams, S., Martina, W. F., Addison, A. C., Ding, J., Pardal, G., & Colegrove P. Wire + Arc Additive Manufacturing. *Materials Science and Technology* **32**, 641–647 (2015).

5. Derekar, K. S. A review of wire arc additive manufacturing and advances in wire arc additive manufacturing of aluminium. *Materials Science and Technology (United Kingdom)* **34**, 895–916 (2018).

6. Haden, C., Zeng, G., Carter, F. M., Ruhl, C., Krick, B. A., & Harlow, D. G. Wire and arc additive manufactured steel: Tensile and wear properties. *Additive Manufacturing* **16**, 115–123 (2017).

7. Marinelli, G., Martina, F., Lewtas, H., Hancock, D., Ganguly, S., & Williams, S. Functionally graded structures of refractory metals by wire arc additive manufacturing. *Science and Technology of Welding and Joining* **24**, 495–503 (2019).

8. Liljedahl, C.D.M., Brouard, J., Zanellato, O., Lin, J., Tan, M.L., Ganguly, S., Irving, P.E., Fitzpatrick, M.E., Zhang, X., & Edwards, L. Weld residual stress effects on fatigue crack growth behaviour of aluminium alloy 2024-T351. *International Journal of Fatigue* **31**, 1081–1088 (2009).

9. Xu, X., Ganguly, S., Ding, J., Guo, S., Williams, S., & Martina, F. Microstructural evolution and mechanical properties of maraging steel produced by wire + arc additive manufacture process. *Materials Characterization* **143**, 152–162 (2018).

10. Seow, C. E., Zhang, J., Coules, H. E., Wu, G., Jones, C., Ding, J., & Williams, S. Effect of crack-like defects on the fracture behaviour of Wire + Arc Additively Manufactured nickel-base Alloy 718. *Additive Manufacturing* **36**, 101578 (2020).

11. Xu, S. H. & Wang, Y. de. Estimating the effects of corrosion pits on the fatigue life of steel plate based on the 3D profile. *International Journal of Fatigue* **72**, 27–41 (2015).

12. Xu, S., Wang, H., Li, A., Wang, Y. & Su, L. Effects of corrosion on surface characterization and mechanical properties of butt-welded joints. *Journal of Constructional Steel Research* **126**, 50–62 (2016).

13. Wang, Y., Xu, S., Wang, H. & Li, A. Predicting the residual strength and deformability of corroded steel plate based on the corrosion morphology. *Construction and Building Materials* **152**, 777–793 (2017).

14. Qin, G. chong, Xu, S. hua, Yao, D. qiang & Zhang, Z. xing. Study on the degradation of mechanical properties of corroded steel plates based on surface topography. *Journal of Constructional Steel Research* **125**, 205–217 (2016).

15. Kim, I. T., Dao, D. K., Jeong, Y. S., Huh, J. & Ahn, J. H. Effect of corrosion on the tension behavior of painted structural steel members. *Journal of Constructional Steel Research* **133**, 256–268 (2017).

16. Garbatov, Y., Guedes Soares, C., Parunov, J. & Kodvanj, J. Tensile strength assessment of corroded small scale specimens. *Corrosion Science* **85**, 296–303 (2014).

17. Appuhamy, J. M. R. S., Kaita, T., Ohga, M. & Fujii, K. Prediction of residual strength of corroded tensile steel plates. *International Journal of Steel Structures* **11**, 65–79 (2011).

18. Ahmmad, M. M. & Sumi, Y. Strength and deformability of corroded steel plates under quasi-static tensile load. *Journal of Marine Science and Technology* **15**, 1–15 (2010).

19. Wang, H., Xu, S., Li, A. & Kang, K. Experimental and numerical investigation on seismic performance of corroded welded steel connections. *Engineering Structures* **174**, 10–25 (2018).

20. Nakai, T., Matsushita, H. & Yamamoto, N. Effect of pitting corrosion on strength of web plates subjected to patch loading. *Thin-Walled Structures* **44**, 10–19 (2006).

21. Nakai, T., Matsushita, H. & Yamamoto, N. Effect of pitting corrosion on ultimate strength of web plates subjected to shear loading. *Key Engineering Materials* **340-341 I**, 489–494 (2007).

22. Zhang, H., Xu, S., Nie, B. & Wen, Y. Effect of corrosion on the fracture properties of steel plates. *Construction and Building Materials* **225**, 1202–1213 (2019).

23. Hou, Y., Lei, D., Li, S., Yang, W. & Li, C. Q. Experimental Investigation on Corrosion Effect on Mechanical Properties of Buried Metal Pipes. *International Journal of Corrosion* **2016**, (2016).

24. Lincoln Electric Company, T. *LINCOLN ® ER70S-6 WELDING POSITIONS TYPICAL APPLICATIONS*. www.lincolnelectric.com.

25. *ER100S-G Data Sheet - Bohler Welding*. www.voestalpine.com/welding (2014).

26. Ermakova, A., Mehmanparast, A. & Ganguly, S. A review of present status and challenges of using additive manufacturing technology for offshore wind applications. *Procedia Structural Integrity* **17**, 29–36 (2019).

27. American Society for Testing and Materials. ASTME-1820-11: standard test method for measurement of fracture toughness. *Annual book of ASTM standards* 1–55 (2011) doi:10.1520/E1820-18.

28. International, A. D1141-98 Standard Practice for the Preparation of Substitute Ocean Water. *ASTM International* **98**, 1–3 (2013).

29. Anderson, T, L. *Fracture Mechanics: Fundamentals and Application*. (Taylor & Francis Group, 2005).

30. Ermakova, A., Mehmanparast, A., Ganguly, S., Razavi, J. & Berto, F. Investigation of mechanical and fracture properties of wire and arc additively manufactured low carbon steel components. *Theoretical and Applied Fracture Mechanics* **109**, 102685 (2020).

3.3. Conclusion

In this chapter the material characterisation tests were conducted on WAAM-fabricated specimens using ER70S-6 and ER100S-1 materials. The results revealed notable differences in hardness, yield stress, and UTS between the two materials, with ER70S-6 exhibiting lower hardness but higher average fracture toughness compared to ER100S-1. The orientation of specimens had minor effects on yield stress and UTS, while the extraction location significantly influenced fracture toughness in ER100S-1, with top-wall specimens exhibiting a 48% higher value compared to bottom-wall specimens.

Additionally, fracture toughness tests were performed on WAAM built specimens made with ER70S-6 and ER100S-1, both exposed to seawater and unexposed. The corrosive environment reduced yield stress in both materials, resulting in lower load vs. LLD curves for corroded specimens. However, the R-curves of corroded specimens showed higher values, indicating improved crack propagation resistance. The corrosion process not only altered mechanical properties but also led to blunter fatigue cracks, contributing to enhanced fracture properties.

Overall, the research demonstrated the potential of WAAM for offshore applications, particularly in the manufacturing and repair of offshore wind turbine structures. Further investigations on tensile properties of corroded specimens are recommended for better understanding and optimising blunting and exclusion lines in future work.

Chapter 4 : Assessment of Fatigue Crack Growth Behaviour in WAAM Steel Components

In this chapter, fatigue crack growth tests were conducted on ER70S-6 and ER100S-1 WAAM built specimens. The sensitivity of results to extraction location and orientation of the specimens was discussed. The chapter consists of the following papers:

Paper IV: Fatigue crack growth behaviour of wire and arc additively manufactured ER70S-6 low carbon steel components

Paper V: Experimental investigation of the fatigue crack growth behaviour in wire arc additively manufactured ER100S-1 steel specimens

4.1. Paper IV: Fatigue crack growth behaviour of wire and arc additively manufactured ER70S-6 low carbon steel components

Anna Ermakova[a], Ali Mehmanparast[a*], Supriyo Ganguly[b], Javad Razavi[c], Filippo Berto[c]

[a] Offshore Renewable Energy Engineering Centre, Cranfield University, England, UK

[b] Welding Engineering and Laser Processing Centre, Cranfield University, Cranfield, MK43 0AL, UK

[c] Norwegian University of Science and Technology (NTNU), Trondheim, Norway

Abstract[4]

The new emerging Wire and Arc Additive Manufacturing (WAAM) technology has significant potential to improve material design and efficiency for structural components as well as reducing manufacturing costs. Due to repeated and periodic melting, solidification, and reheating of the layers, the WAAM deposition technique results in some elastic, plastic and viscous deformations that can affect material degradation and crack propagation behaviour in additively manufactured components. Therefore, it is crucial to characterise the cracking behaviour in WAAM built components for structural design and integrity assessment purposes. In this work, fatigue crack growth tests have been conducted on compact tension specimens extracted from ER70S-6 steel WAAM built components. The crack propagation behaviour of the specimens extracted with different orientations (i.e., horizontal and vertical with respect to the deposition direction) has been characterised under two different cyclic load levels. The obtained fatigue crack growth rate data have been correlated with the linear elastic fracture mechanics parameter ΔK and the results are compared with the literature data available for corresponding wrought structural steels and the recommended fatigue crack growth trends in BS7910 standard. The obtained results have been found to fall below the recommended trends in BS7910 standard and above the data points obtained from S355 wrought material. The obtained fatigue growth trends and Paris law constants from this study contribute to the overall understanding of the design requirements for the new optimised functionally graded structures fabricated using WAAM technique.

[*] corresponding author

[4] *International Journal of Fracture*. 235, 47–59 (2022). (DOI: 10.1007/s10704-021-00545-8)

4.1.1. Introduction

The wire and arc additive manufacturing (WAAM) method creates multi-layer components by melting a wire at a controlled rate using an electric or plasma arc[1,2]. Compared with powder based additive manufacturing techniques, WAAM has a key advantage of relatively high deposition rate, depositing several kilograms of metal per hour, resulting in lower cost and reasonably short fabrication time[3,4]. Additionally, using wire as the feeding material brings fewer safety issues compared to powders[2,5]. However, as-deposited WAAM parts may require post processing due to surface roughness and inaccuracies involved in exact dimensions[6,7]. This technique has been already adopted by the aerospace industry and is now finding its applications in other industrial sectors[8]. One of the major constraints for widespread application of WAAM in industries is limited knowledge of mechanical properties of such components, particularly the fatigue behaviour under different loading and environmental conditions, which is a key requirement for further product design and certification. Moreover, previous studies have shown that additive manufacturing process due to repeated melting, solidification, and reheating, introduces changes to the microstructure and residual stresses that would have an impact on mechanical and fatigue properties, hence have to be examined carefully for more accurate interpretation of the WAAM built components.

The majority of the published work on WAAM built components reported in the literature are on the parts made of titanium and stainless-steel alloys particularly for application in the aerospace industry; however, there is an essential need to examine the fatigue and fracture behaviour of other WAAM built materials, e.g., ferritic steel, to explore the suitability of this AM technology for other high production rate industries such as offshore wind. Experimental evaluation of fatigue behaviour of WAAM titanium alloy compact tension, C(T), samples by Zhang et al.[5,9] revealed considerably lower fatigue crack growth (FCG) rates of the WAAM material compared to the wrought counterpart. Therefore, WAAM technique was recommended as a strong candidate for manufacturing damage tolerance driven designs. Moreover, different sample orientations were investigated by Zhang et al.[5,9] and it was found that the FCG rate is slightly faster when the crack propagates across the WAAM layers, compared to the crack that propagates along the layers. Similar results were reported by Zhang et al.[10]. Gordon et al.[11] performed FCG tests on 304L stainless steel WAAM built SEN(B) specimens and observed favourable behaviour in the Paris region compared to the conventional wrought stainless steel. It was also reported that as-built parts offer higher FCG resistance. Further observed in their study was some degree of variability in the crack growth rates of different sample orientations, with the lowest rates observed in samples with multi-layer crack paths. 17-4 PH stainless steel WAAM built C(T) specimens were tested by Nezhadfar et al.[12] and the results showed lower FCG rates compared to the specimens made of the wrought material.

The preliminary test results reported in the literature on titanium and stainless steel WAAM components show that relatively lower FCG rates were observed in the multi-layer deposited specimens compared to the conventional parts made from the wrought material. However, there is generally limited experimental data available on FCG behaviour of the WAAM built components for a wide range of materials. Therefore, further experimental studies are needed to inform decisions for material selection in fabrication of future WAAM built components based on the fatigue resistance observed in fatigue crack growth tests. To fill in the gap in the

knowledge, the present study examines the FCG behaviour of WAAM built specimens made with ER70S-6 mild steel wire. Also included in this study is the sensitivity analysis of the fatigue response to the built orientation and applied cyclic load level. The manufacturing process of the WAAM walls, specimen extraction strategy, experimental set-up and the results obtained FCG test are presented below, along with discussions and comparison with the existing data in the literature. The results presented in this study provide an insight into extension of the application of WAAM technology to other industries, such as offshore wind, where a significant number of large-scale components must be fabricated within limited timeframes.

4.1.2. Material selection and specimen extraction

The material used in this study is ER70S-6 copper coated carbon steel welding wire. It is suitable for automatic welding and is well-known for excellent welding properties, stable arc, high deposition efficiency and low spatter. Typical applications for this wire are in repair of a variety of mild and low alloy steels, small diameter pipes and tubing, sheet metal applications, and root pass pipe welding[13]. Moderate amount of rust is acceptable during the welding process which makes this wire a preferable choice for marine applications[14]. However, some post-processing is usually required subsequent to fabrication to remove the generated silicon island deposits. In this study, Lincoln electric ER70S-6 wire[15] was used with the chemical composition summarised in Table 4.1.

Table 4.1: Chemical composition of ER70S-6 material (wt.-%)[15]

	C	*Mn*	*Cr*	*Si*	*Ni*	*Mo*	*S*	*P*	*Cu*	*V*
ER70S-6	0.09	<1.60	0.05	0.09	0.05	0.05	0.007	0.007	0.20	0.05

Two additively manufactured walls were built using the Cold Metal Transfer (CMT) based WAAM process, with manufacturing parameters shown in Table 4.2. In order to minimise the structural variability of different walls, all the parameters were kept constant during the fabrication process. The manufacturing set-up and an example of the completed wall are displayed in Figure 4.1. As shown in the figure, the WAAM set-up consists of the CMT power source, a robot arm with the torch feeding the wire and simultaneous shielding gas supply. An exhaust fan was also used to draw off the generated fume and heat from the wall.

Each WAAM wall was built in the middle of the base plate that was made of EN10025 rolled structural steel with the plate dimensions of 420 × 200 × 12 mm^3. The base plate was fixed on the working table using eight clamps (two for each corner). The clamps helped to prevent the plate from bending due to the thermal energy input and were released once the completed WAAM wall cooled down to the ambient temperature. Additive layers were deposited on top of each other using an oscillation pattern, the details of which can be found in the work by Ermakova et al.[16], to create relatively thick walls of approximately 24 mm in thickness (Y-direction in Figure 4.1 (b)), 355 mm in length (X-direction) and 140 mm in height (Z-direction).

Table 4.2: CMT-WAAM fabrication parameters

Shielding gas	Ar+20% CO_2
Gas flow rate	15 L/min
Wire diameter	1.2 mm
Robot travelling speed	7.33 mm/sec
Wire feed speed	7.5 m/min
Dwell time	120 sec

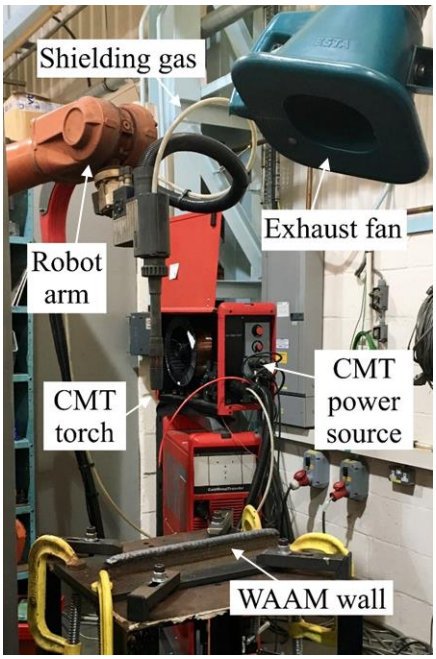

(a)

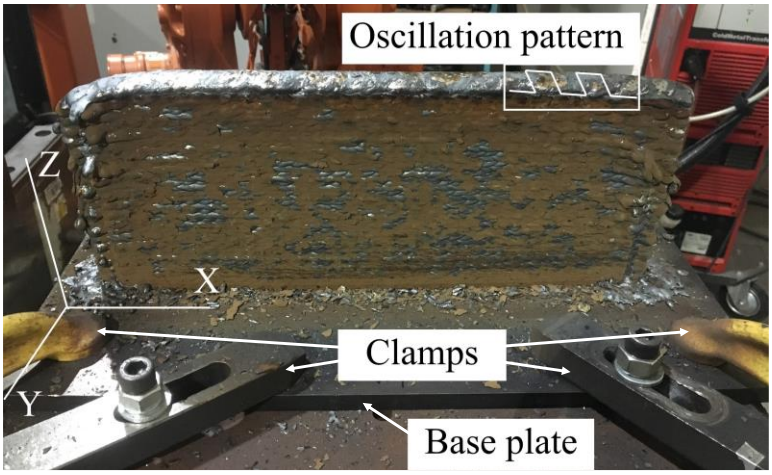

(b)

Figure 4.1: The fabrication process: (a) CMT WAAM set-up, (b) completed wall

Once the fabrication of the WAAM walls was completed, tests specimens were extracted from each wall using the Electrical Discharge Machining (EDM) technique. Twelve stepped notched compact tension, C(T), specimens were extracted along two different orientations: vertical (V) – with the crack plane perpendicular to the deposited layers, and horizontal (H) – with the crack plane parallel to the deposited layers. As schematically shown in Figure 4.2, specimens denoted CT-V-1 and CT-V-2 are vertically oriented, whereas CT-H-1 and CT-H-2 have horizontal orientation. The C(T) specimens were extracted in accordance with ASTM E647[17] standard with the width W = 50 mm, the height of H = 60 mm, total thickness of B = 16 mm and initial crack length of a_0 = 17 mm before pre-fatigue cracking. Also, in order to enable compliance measurements for crack growth monitoring during FCG tests, knife edges were machined at the crack mouth following the instructions provided in E1820[18] to accommodate a clip gauge for compliance measurements throughout the tests.

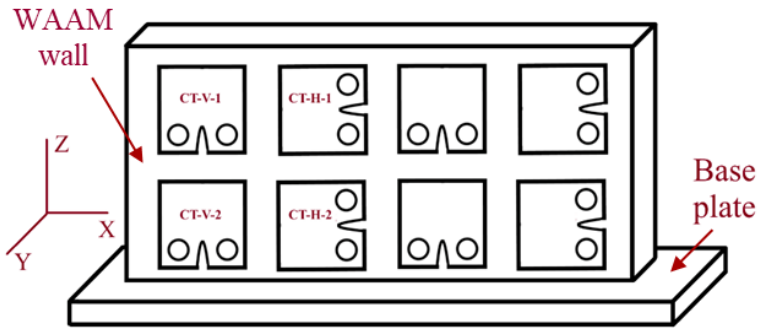

Figure 4.2: A schematic demonstration of the specimen extraction plan

4.1.3. Fatigue crack growth test set-up and data analysis

FCG tests were conducted on a 100 kN servo-hydraulic machine under Mode I fracture mechanics loading conditions in accordance with the ASTM E647[17] standard. All tests were performed under load control mode at room temperature in air and with the load ratio of R = 0.1. The fatigue load cycles were applied using a constant amplitude sinusoidal cyclic waveform at 5 Hz frequency. Six specimens were tested with the maximum applied load of P_{max} = 10 kN, with another six samples tested under P_{max} = 11 kN. For each of the load levels examined in this study, half of the specimens (i.e., 3 C(T) specimens) were selected with vertical orientation and the other half with horizontal orientation, to examine crack path effects with respect to the deposited layers in the WAAM walls on the FCG behaviour of the material. Prior to testing, all specimens were pre-cracked under fatigue loading conditions using the load decreasing approach to approximately 20 mm ($a_{i,p}/W$ = 0.4), to introduce an infinitely sharp crack tip ahead of the machined notch. During the pre-cracking process, it was ensured that the final value of maximum stress intensity factor K_{max} does not exceed the initial K_{max} at the beginning of the actual FCG test, according to the test requirements listed in ASTM E647.

The estimated values of crack length during the pre-cracking phase and the main FCG tests were monitored using the unloading compliance technique[19], by attaching a clip gauge onto the crack mouth of the specimen. The crack path was carefully observed using high resolution cameras located in front of and behind the test specimens to ensure that the crack propagates

straight without any major deviation from the symmetry line in the C(T) test specimens. Moreover, the cameras were used to cross check the crack growth readings obtained from the compliance technique by measuring the crack lengths at the outer surface of the C(T) specimens. The tests were terminated once the crack length, estimated using the compliance technique, reached approximately 35 mm ($a_{f,c}/W$ = 0.7). The fatigue test set-up and the crack growth monitoring tool employed in this study are presented in Figure 4.3.

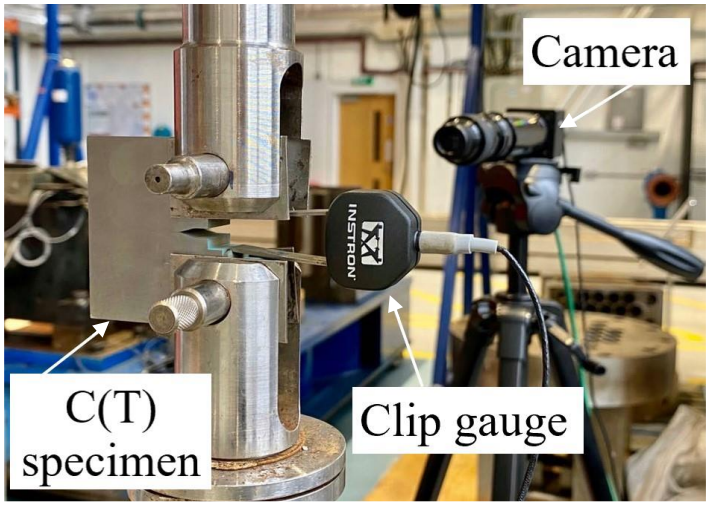

Figure 4.3: Fatigue crack growth test set-up

The instantaneous crack length and number of cycles were continuously recorded throughout the tests. The FCG rate, *da/dN*, was then calculated using the secant method for the first and the last three data points, and seven-point incremental polynomial technique for the rest of the data points. As suggested by ASTM E647, the stress intensity factor (SIF) range, *ΔK*, for C(T) specimen geometry can be obtained using Equation 4.1:

$$\Delta K = \frac{\Delta P}{B\sqrt{W}} \cdot \frac{(2+\alpha)}{(1-\alpha)^{\frac{3}{2}}} \cdot (0.886 + 4.64\alpha - 13.32\alpha^2 - 14.72\alpha^3 - 5.6\alpha^4) \quad \text{Equation 4.1}$$

where ΔP is the applied cyclic load range, and $\alpha = a/W$ is the normalised crack length.

However, due to the validity limitation of this equation for C(T) specimens with shallow crack lengths, a new shape function equation was developed based on numerical analysis in a previous study by Mehmanparast et al.[20] and incorporated in calculation of the SIF for C(T) specimens which is shown in Equation 4.2. It was reported by Mehmanparast et al.[20] that *ΔK* values obtained using Equation 4.2 are more accurate for a wider range of normalised crack lengths ranging from *a*/*W* = 0.2 to *a*/*W* = 0.7.

$$\Delta K = \frac{\Delta P}{BW} \cdot \sqrt{a} \cdot (-372.12\alpha^6 + 1628.60\alpha^5 - 2107.46\alpha^4 + 1304.65\alpha^3 - 391.20\alpha^2 + 54.81\alpha + 7.57) \quad \text{Equation 4.2}$$

4.1.4. Fatigue crack growth test results and discussion

The FCG test data, which include the instantaneous crack lengths a and number of cycles, collected during the tests on all specimens are presented and compared with each other in Figure 4.4. As seen in this figure, the initial crack length (after pre-cracking) for all FCG tests was approximately 20 mm, with the exception of two specimens CT-V-1 and CT-V-2 that were pre-cracked to slightly higher values, resulting in shorter FCG test durations in these two test specimens. The comparison of the crack growth trends observed in specimens tested under different loading conditions shows that by increasing P_{max} from 10 kN to 11 kN, the test duration on average decreased by approximately 2.3 times for horizontal specimens and 1.5 times for vertical specimens. The results show that under P_{max} =10 kN, on average around twice longer fatigue life is generally observed in horizontal specimens, compared to vertical specimens. However, when the applied load level was increased to P_{max} =11 kN an opposite trend is observed with the vertical specimens having on average around 1.3 times longer fatigue life compared to horizontal samples. This trend can be caused due to the microstructural effects, which are discussed next, or induced residual stresses that need to be examined in the future work. Finally seen in Figure 4.4 is that while the short-term repeat tests under P_{max} =11 kN exhibit similar trends with relatively small level of scatter, the deviation in the test results enlarges in longer-term tests under P_{max} =10 kN particularly in the horizontal specimens. This indicates that the fatigue test duration and the level of scatter in the test data strongly dependents on the applied load level in the tests on ER70S-6 WAAM built specimens.

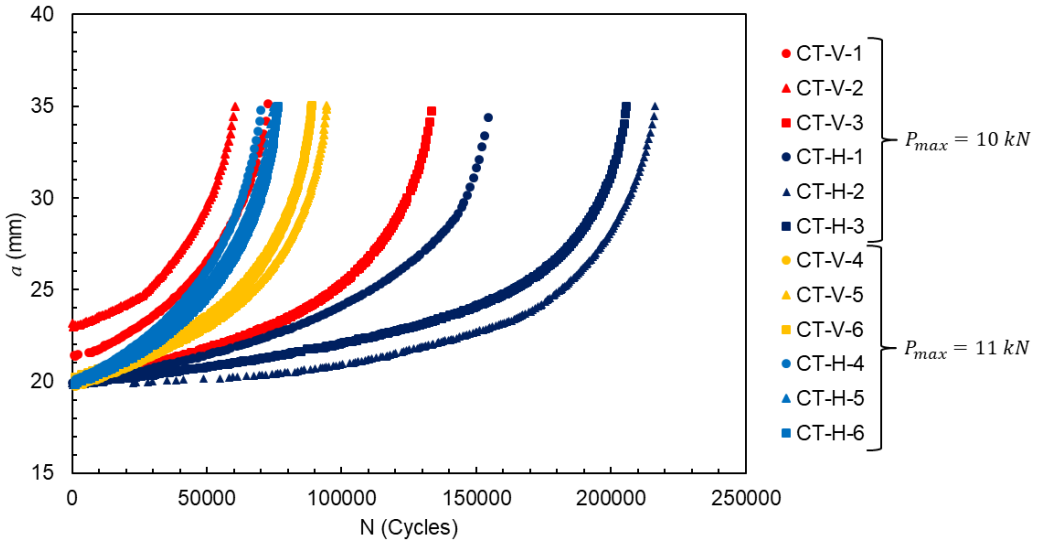

Figure 4.4: Fatigue crack growth trends in the tests on ER70S-6 WAAM built specimens with different orientations under different applied load levels

The FCG rates, *da/dN*, obtained from the tests on C(T) specimens have been correlated with the linear elastic fracture mechanics parameter, ΔK, and the results are presented in Figure 4.5. It can be seen in this figure that for a given loading condition, the experimental data obtained from the tests on each specimen orientation fall upon each other, showing four distinguished clouds of data and indicating good repeatability for each four datasets at two different load levels and on two different specimen orientations. It can be seen in this figure that the FCG results show a higher trend in the tests performed at P_{max} =11 kN, particularly at greater values

of ΔK towards the end of the tests. The comparison of the results obtained from different orientations shows that under the cyclic applied load of P_{max} =10 kN the vertical specimens exhibit a higher FCG rate compared to the horizontal specimens throughout the tests, including the near threshold region and the Paris region. For the tests performed under P_{max} =11 kN, it can be seen that while the horizontal specimens demonstrate a higher FCG rate in the near threshold region at low values of ΔK, this trend switches at larger crack lengths with the vertical specimens showing a higher FCG rate towards the end of the Paris region. Comparing the experimental clouds in Figure 4.5 it can be seen that the lowest FCG rates are observed in horizontal specimens tested under P_{max} =10 kN.

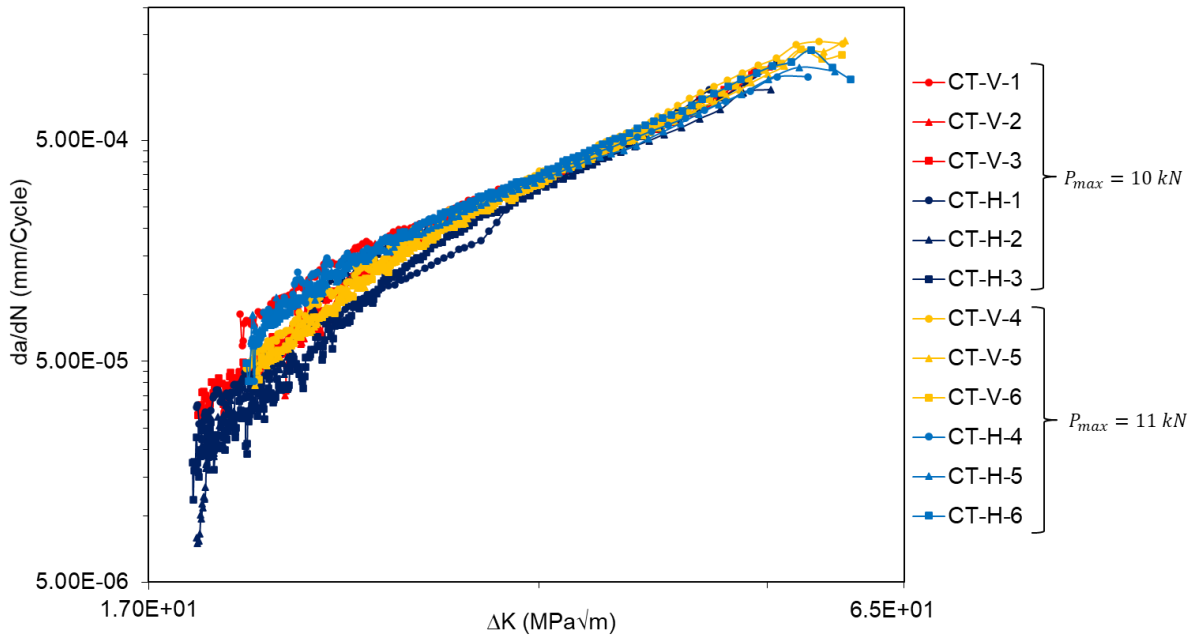

Figure 4.5: Analysis of the fatigue crack growth rates in ER70S-6 WAAM built specimens with different orientations under different applied load levels

For each FCG dataset presented in Figure 4.5, the material constants C and m in the Paris region with intermediate values of ΔK (Equation 4.3) were obtained by plotting the line of best fit to the data and determining the power-law constants, which are summarised in

Table 4.3. Also included in Table 4.3 are the values of the coefficient of determination, R^2, which have been found to be close to 1 indicating that the lines of best fit made to the data accurately describe the realistic behaviour of the material. It can be seen in this table that the values of the stress intensity factor range exponent, m, are within the established range of 2 to 4 which is typically observed in the FCG tests on wrought materials in the absence of corrosive environment[21]. The information on the extraction location of each C(T) specimen with respect to the height (i.e. top (T) and bottom (B) regions) of the WAAM walls (see Figure 4.2) is also reported in Table 4.3. Comparing the test results in Figure 4.5 and Table 4.3, it was concluded that the extraction location of the C(T) specimen does not have any major impact on the FCG behaviour of the ER70S-6 steel WAAM specimens, and within the inherent experimental scatter the *da/dN vs.* ΔK trends from specimens extracted at the top and bottom of the WAAM walls fall close to or upon each other.

$$da/dN = C\Delta K^m \quad \text{Equation 4.3}$$

Table 4.3: Paris law constants for the fatigue crack growth tests on ER70S-6 WAAM built specimens

Specimen ID	Orientation	Location	P_{max} (kN)	C	m	R^2
CT-V-1	V	T	10	7.51×10^{-8}	2.39	0.993
CT-V-2	V	B	10	7.37×10^{-8}	2.39	0.997
CT-V-3	V	B	10	8.34×10^{-9}	2.99	0.995
CT-H-1	H	T	10	4.29×10^{-9}	3.11	0.996
CT-H-2	H	B	10	3.37×10^{-8}	2.59	0.989
CT-H-3	H	T	10	2.80×10^{-9}	3.28	0.991
CT-V-4	V	B	11	6.64×10^{-9}	3.08	0.993
CT-V-5	V	B	11	1.32×10^{-8}	2.86	0.995
CT-V-6	V	B	11	9.09×10^{-9}	2.97	0.997
CT-H-4	H	B	11	5.20×10^{-8}	2.49	0.995
CT-H-5	H	B	11	3.94×10^{-8}	2.56	0.996
CT-H-6	H	B	11	2.46×10^{-8}	2.72	0.997

Furthermore, the Paris law constants were determined for each set of specimens with the same orientation (i.e., vertical and horizontal) and under a given loading condition (P_{max} of 10 kN and 11 kN). The results obtained from the line of best fit (i.e., mean line) for each dataset are presented in Figure 4.6 and summarised in Table 4.4. As seen in Figure 4.6 and Table 4.4, the R^2 values are found to be slightly higher for specimens tested under P_{max} =11 kN, indicating less scatter in these datasets, compared to those tested at P_{max} =10 kN, which is consistent with observations made in Figure 4.4. Lower values of R^2 for specimens tested under P_{max} =10 kN suggests more scattered results. To further analyse the level of scatter in each of the obtained datasets, the upper bound trends were calculated based on +2 standard deviation (SD) by assuming the same slope as the mean line. The Power-law constants for the upper bound FCG trends (mean+2SD) in the Paris region for each of the four datasets are reported in Table 4.4.

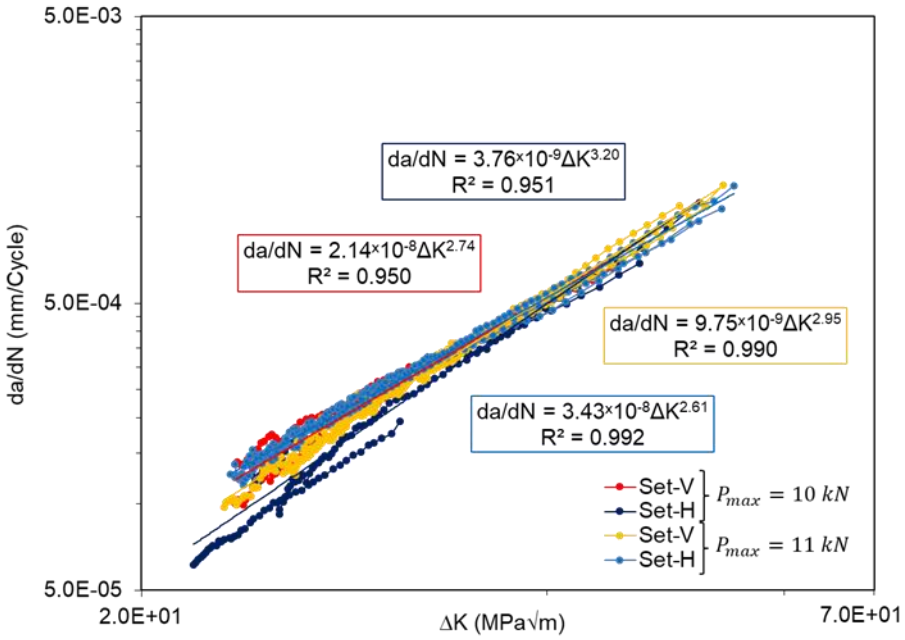

Figure 4.6: The lines of best fit made to the fatigue crack growth data in the Paris region for different specimen orientations and load levels

Table 4.4: Power-law constants for the mean curves and upper bound trends in the Paris region for different orientations and load levels

Datasets	Orientation	P_{max} (kN)	Mean			Mean+2SD	
			C	m	R^2	C	m
Set-V	V	10	2.14×10^{-8}	2.74	0.950	2.61×10^{-8}	2.74
Set-H	H	10	3.76×10^{-9}	3.20	0.951	4.95×10^{-9}	3.20
Set-V	V	11	9.75×10^{-9}	2.95	0.990	1.09×10^{-8}	2.95
Set-H	H	11	3.43×10^{-8}	2.61	0.992	3.79×10^{-8}	2.61

The mean+ 2SD lines for four sets of experiments on different specimen orientations and load levels are plotted and compared with each other in Figure 4.7. Also included in this figure are the BS7910 recommended fatigue crack growth trends[22] (i.e. upper bound trends) for welded joints in air based on the simplified law and 2-stage law. From the figure it can be seen that all four lines describing the upper bound FCG behaviour of ER70S-6 WAAM specimens fall below the simplified and 2-stage FCG trends recommended in BS7910 standard. This indicates that the FCG rates in ER70S-6 WAAM built components can be conservatively predicted by the recommended trends in BS7910 standard. It can be seen in Figure 4.7 that the upper bound FCG lines for the vertical specimens at 10 kN and horizontal specimens at 11 kN have similar slopes to the 2-stage law recommended in BS7910, while the other two datasets (i.e. horizontal specimens at 10 kN and vertical specimens at 11 kN) have similar slopes to BS7910 simplified law.

Furthermore, the FCG data obtained from this study have been compared with the fatigue test data in air on S355G+10M structural steel C(T) specimens extracted from the heat affected zone (HAZ) tested by Jacob et al.[23] and S355G8+M steel C(T) specimens on HAZ and base metal (BM) tested by Mehmanparast et al.[20], both sets of specimens have been prepared replicating the existing welds in offshore wind turbine monopile structures using the multi-pass butt-welding and no post-weld heat treatment was performed on the welded specimens. All tests have been conducted under similar loading conditions of P_{max} =10 kN, 5Hz frequency and R=0.1, and the results are presented in Figure 4.7. The comparison of the experimental data in this figure shows that the upper bound FCG trends from ER70S-6 WAAM specimens fall slightly above the experimental data band from S355G8+M BM specimens. Also seen in this figure is that the upper bound FCG rates in ER70S-6 WAAM specimens are on average around three and four times higher than S355G8+M and S355G+10M HAZ specimens, respectively. Knowing that S355G8+M and S355G+10M are widely used in fabrication of offshore structures which are subjected to severe cyclic loading conditions during their lifespan[24,25,26], the comparison of results in Figure 4.7 shows that the WAAM technology can be potentially employed in fabrication of less critical components and parts of offshore structures using low carbon steel wires, though the fatigue crack growth rates are expected to be higher than the S355 weldments but still lower than the recommended FCG trends provided in BS7910 standard.

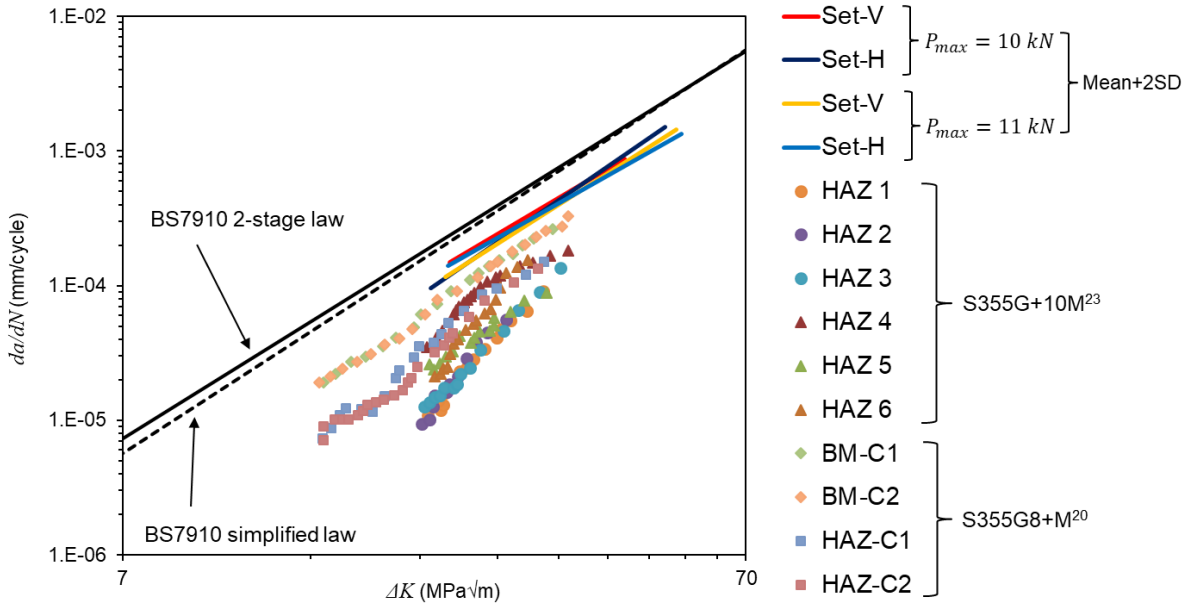

Figure 4.7: Comparison of the upper bound fatigue crack growth trends on ER70S-6 WAAM specimens to BS7910 curves and literature data on S355

4.1.5. Fractography

Upon completion of FCG tests, post-mortem analysis was conducted on all specimens to evaluate the percentage of error in crack length estimations using the compliance technique. In order to do this, the tested specimens were initially soaked in liquid nitrogen for 10 minutes to

increase the brittleness of the material and facilitate the fast fracture opening process with minimum plastic deformation. Examples of fracture surfaces are shown in Figure 4.8 for different specimen orientations and loading conditions. As seen in Figure 4.8(a), three surface areas were identified on the fracture surface: (1) fatigue pre-cracking, (2) fatigue crack growth, and (3) fast fracture (i.e., specimen fracture opening). The crack extension was measured in the first two regions for all twelve specimens tested in this study. The fractography analysis of the tested specimens shows that the crack propagation regions are quite symmetric for each specimen, which confirms that perfect appropriate alignment was maintained during the FCG tests. It can be also observed that the macroscopic fatigue crack growth regions are very smooth for all specimen orientations without any evidence of significant defects or crack deviation from the straight line on the fracture surface.

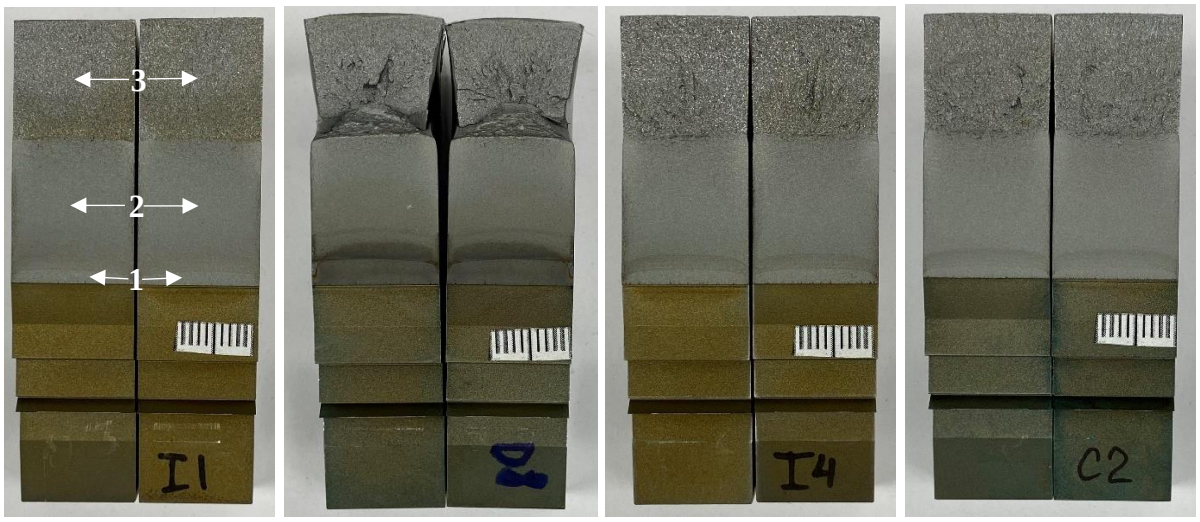

(a) (b) (c) (d)

Figure 4.8: Fracture surface of ER70S-6 WAAM specimens tested under P_{max} = 10kN: (a) CT-V-3 vertical, (b) CT-H-2 horizontal; and under P_{max} =11kN: (c) CT-V-6 vertical, (d) CT-H-4 horizontal

The information on the key specimen dimensions, the machined crack length a_o, the crack length after pre-cracking process estimated using the compliance method $a_{i,p}$, the final crack length after FCG test estimated using the compliance method $a_{f,c}$, and the final crack length measured on the fracture surfaces using optical imaging $a_{f,op}$ is summarised in Table 4.5. As seen in this table, the percentage of error between the estimated (using the compliance technique) and measured (using optical imaging on the fracture surface) final crack lengths is less than 2.2% confirming that the crack lengths were accurately estimated during FCG tests using the compliance technique.

Table 4.5: Specimen dimensions, loading condition, initial and final crack lengths

Specimen ID	P_{max} (kN)	W (mm)	B (mm)	a_0 (mm)	$a_{i,p}$ (mm)	$a_{f,c}$ (mm)	$a_{f,op}$ (mm)	% error in a_f
CT-V-1	10	50.1	16.0	17.0	21.9	35.0	35.8	2.2
CT-V-2	10	50.0	16.1	17.1	23.2	35.0	34.7	0.8
CT-V-3	10	50.0	16.0	17.0	20.1	35.0	34.8	0.7
CT-H-1	10	50.0	16.0	17.2	19.7	35.0	34.9	0.2

CT-H-2	10	50.1	16.2	17.1	19.9	35.0	35.7	2.0
CT-H-3	10	50.0	16.1	17.0	19.5	35.0	35.0	0.2
CT-V-4	11	50.2	16.0	17.1	19.9	35.0	35.2	0.5
CT-V-5	11	50.0	16.2	17.0	20.1	35.0	35.3	0.7
CT-V-6	11	50.1	16.0	17.0	20.2	35.0	35.2	0.5
CT-H-4	11	50.1	16.0	17.0	20.3	35.0	35.4	1.0
CT-H-5	11	50.0	16.1	17.2	20.3	35.0	35.4	1.0
CT-H-6	11	50.0	16.0	17.1	20.1	35.0	35.1	0.2

In order to examine the FCG rate differences observed in Figure 4.5, further microstructural analysis has been conducted on the broken-open specimens using TESCAN VEGA 3 Scanning Electron Microscope (SEM) with high 5kx magnification and the results are presented in Figure 4.9. Since the largest difference in FCG rates took place at lower ΔK values and became almost negligible towards the end of the tests, the microstructural analysis was performed on the area corresponding to the beginning of the test (approximately 2 mm ahead of the pre-cracked region). The fracture surface analysis on the horizontal specimen tested at P_{max} =10 kN (Figure 4.9 (a)), revealed dimpled rapture characteristics and large secondary cracks, which is compelling evidence of the ductile fracture mechanism. On the other hand, the fracture surface of the vertical specimen tested at P_{max} =10 kN (Figure 4.9 (b)) consists of nearly flat regions, in the absence of secondary cracks, where relatively fast cleavage fracture occurs during the crack propagation process confirming brittle fracture in the vertical specimen. Similar observations were reported by several researchers[27,28,29]. Based on the microstructural analysis it can be concluded that the specimen orientation plays a significant role in microstructural deformation and subsequently the FCG behaviour of WAAM ER70S-6 specimens, and the horizontal specimen orientation which requires a higher amount of energy for crack propagate due to the ductile cracking mode, exhibits a lower FCG rate compared to the vertical specimen tested under the same cyclic loading condition (see Figure 4.5).

To examine the influence of plasticity on the FCG behaviour of specimens with different orientations, further microstructural analyses were conducted on the horizontal and vertical specimens tested at P_{max} =11 kN (see Figure 4.9 (c) and (d)). Comparison of the microstructural deformation in the horizontal specimens tested at P_{max} =10 kN in Figure 4.9 (a) and at P_{max} =11 kN in Figure 4.9 (c) shows that increasing the load level on this specimen orientation has resulted in shallower dimples and lower density of secondary cracks indicating a less ductile fracture behaviour in the test conducted at a higher load. This means that in the horizontal specimen orientation, an increase in the cyclic load level leads to higher FCG rates, in the absence of significant plasticity effects, which is consistent with the FCG trends observed in Figure 4.5. Comparison of the microstructural deformation in the vertical specimens tested at P_{max} =10 kN in Figure 4.9 (b) and at P_{max} =11kN in Figure 4.9 (d) shows that increasing the load on this specimen orientation results in dimpled features and small secondary cracks, as a result of plasticity, which would subsequently decrease the FCG rates. This observation is consistent with the results shown in Figure 4.5 where the FCG rates in the vertical specimens tested at a higher load fall below or upon those obtained at a lower load. This confirms that under the cyclic loading conditions examined in this study the vertical specimens are more sensitive to plastic deformation, therefore an increase in the maximum fatigue load from 10 kN to 11 kN reduces the FCG trend due to formation of dimpled regions and secondary cracks which increase the resistance of the material to crack propagation.

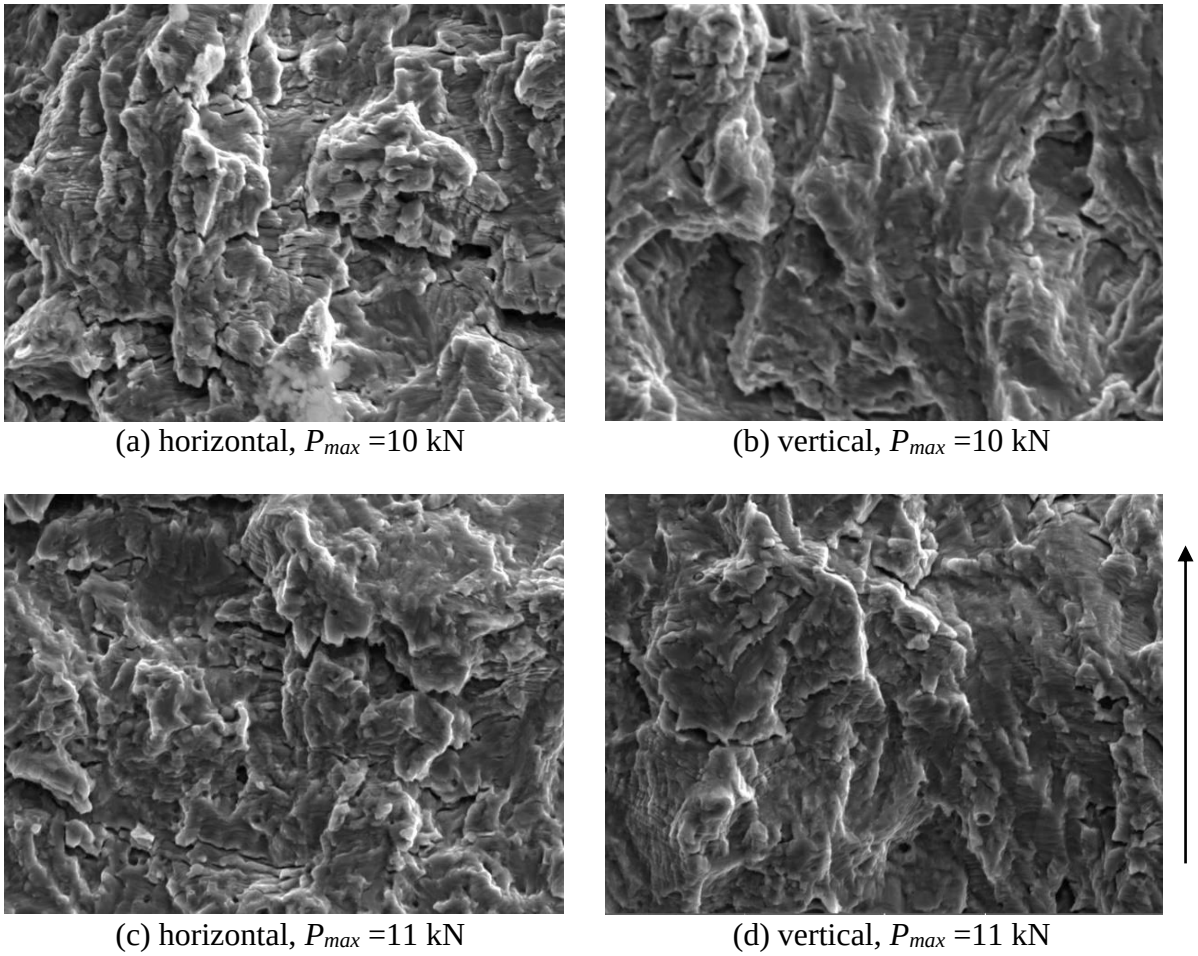

(a) horizontal, P_{max} =10 kN (b) vertical, P_{max} =10 kN

(c) horizontal, P_{max} =11 kN (d) vertical, P_{max} =11 kN

Figure 4.9: Fracture surface of the FCG specimens with 5.0 kx magnification (arrow on the right shows the crack propagation direction)

The grain size is known to be an important microstructural characteristic that determines the mechanical behaviour of the metal[28]. In order to analyse the grain size distribution in the test specimens, a vertical slice of the WAAM wall was examined under the optical microscope and the results are shown in Figure 4.10 (a) and (b). As seen in this figure, the grain coarsening feature in the heat affected zone (HAZ) of the previously deposited WAAM layer is clearly visible, whereas the area of the melt pool consists of relatively smaller grains. Knowing that the nature of the WAAM process is layer-by-layer deposition, depositing every new layer reheats the previous layer and the temperature increase in the previously solidified layer initiates the grain boundaries migration and causes grain growth near each melt pool boundary. These microstructural inhomogeneities in the WAAM manufactured components cause anisotropic mechanical properties. According to Figure 4.10 (b), the mechanical properties of the vertical specimens could change up to four times during the FCG test, as the crack propagated for around 15 mm, hence through multiple WAAM layers. It was previously suggested by Rafieazad et al.[27] that the presence of the coarse grains in the HAZ could be one of the main weakening mechanisms in WAAM ER70S-6 alloy, which deteriorates the ductility of the material. Thus, in addition to the microstructural deformation characteristics the variation in mechanical properties could also influence the FCG behaviour in vertical

specimens at different applied load levels. Further examination of the changes in mechanical properties in vertical samples will be conducted in future work.

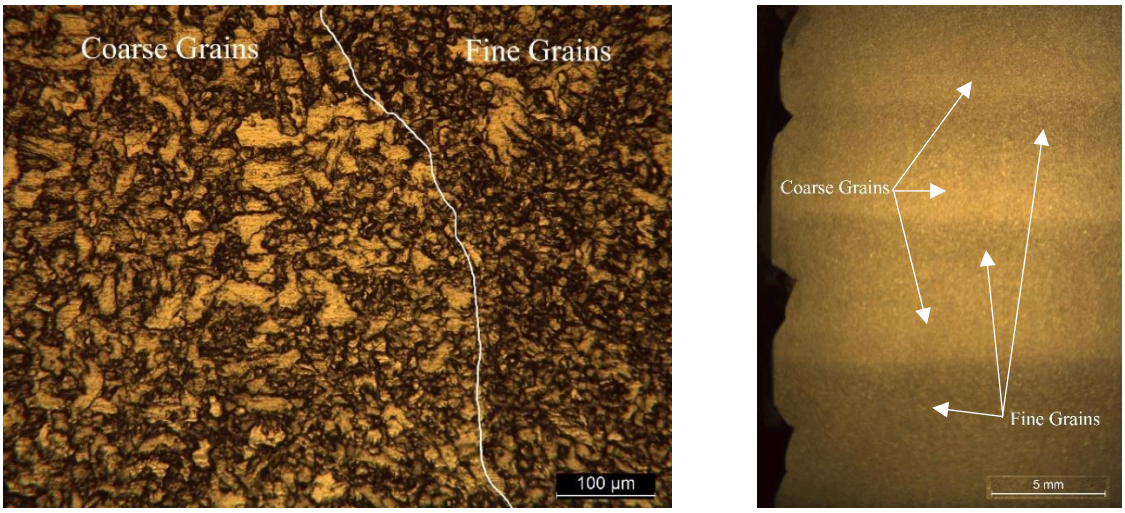

(a) (b)

Figure 4.10: Optical microscopy analysis (a) after etching and (b) before etching on a vertical slice of the WAAM built wall

4.1.6. Conclusions

Fatigue crack growth tests were conducted in air on standard tension C(T) specimens extracted from ER70S-6 WAAM built walls. All tests were performed at room temperature, with R = 0.1, frequency of 5 Hz, at two different load levels of P_{max} =10 kN and 11 kN. The following conclusions and observations have been made from this study:

- The specimen extraction location with respect to the WAAM wall does not have any major effect on the FCG behaviour of specimens.
- Depending on the applied load level, different specimen orientations may introduce some variation in the test results. Under P_{max} =10 kN the horizontal specimens showed twice longer fatigue life, while vertical specimens exhibited 1.3 times longer fatigue life under 11 kN.
- The lowest fatigue crack growth rate was observed in horizontal specimens tested at P_{max} =10 kN and the highest in horizontal specimens tested under P_{max} =11 kN.
- The mean + 2SD lines obtained from the fatigue crack growth test data on ER70S-6 WAAM specimens with different orientations and tested at different load levels fall below the recommended trends by BS7910 standard.
- Comparison of the FCG data on ER70S-6 WAAM specimens with HAZ S355 steels, shows that higher fatigue crack growth rates are observed in WAAM built components while the results fall close to the upper bound data band on S355G8+M base metal.
- The fractography analysis confirmed the accuracy of the compliance method for crack length estimation in WAAM built samples.
- Analysis of the fracture surfaces showed that the microstructural deformation mechanism significantly depends on the specimen orientation and is found to be ductile in horizontal and brittle in vertical specimens tested at P_{max} =10 kN.

- The vertical specimens are more sensitive to material inhomogeneity and also plasticity effects at higher load levels which would cause dimpled ductile fracture regions and reduced FCG trends.

4.1.7. Acknowledgments

This work was supported by grant EP/L016303/1 for Cranfield, Oxford and Strathclyde Universities' Centre for Doctoral Training in Renewable Energy Marine Structures – REMS CDT (http://www.rems-cdt.ac.uk/) from the UK Engineering and Physical Sciences Research Council (EPSRC).

4.1.8. References for paper IV

1. Williams, S. W. *et al.* Wire + Arc Additive Manufacturing. *Mater. Sci. Technol.* **32**, 641–647 (2015).
2. Martina, F., Mehnen, J., Williams, S. W., Colegrove, P. & Wang, F. Investigation of the benefits of plasma deposition for the additive layer manufacture of Ti-6Al-4V. *J. Mater. Process. Technol.* **212**, 1377–1386 (2012).
3. Brandl, E., Baufeld, B., Leyens, C. & Gault, R. Additive manufactured Ti-6A1-4V using welding wire: Comparison of laser and arc beam deposition and evaluation with respect to aerospace material specifications. *Phys. Procedia* **5**, 595–606 (2010).
4. Wang, F., Williams, S. & Rush, M. Morphology investigation on direct current pulsed gas tungsten arc welded additive layer manufactured Ti6Al4V alloy. *Int. J. Adv. Manuf. Technol.* **57**, 597–603 (2011).
5. Zhang, X., Martina, F. & Syed, A. K. Fatigue Crack Growth in Additive Manufactured Titanium: Residual stress control and life evaluation method development Corrosion fatigue: pit-to-cracking transition-experimental and numerical modelling View project "Modelling Applications of Additive Manu. 7–9 (2017) doi:10.13140/RG.2.2.29032.16643.
6. Greitemeier, D., Dalle Donne, C., Syassen, F., Eufinger, J. & Melz, T. Effect of surface roughness on fatigue performance of additive manufactured Ti–6Al–4V. *Mater. Sci. Technol. (United Kingdom)* **32**, 629–634 (2016).
7. Pegues, J., Roach, M., Scott Williamson, R. & Shamsaei, N. Surface roughness effects on the fatigue strength of additively manufactured Ti-6Al-4V. *Int. J. Fatigue* **116**, 543–552 (2018).
8. Ding, D., Pan, Z., Cuiuri, D. & Li, H. Wire-feed additive manufacturing of metal components: technologies, developments and future interests. *Int. J. Adv. Manuf. Technol.* **81**, 465–481 (2015).
9. Zhang, X., Martina, F., Ding, J., Wang, X. & Williams, S. W. Fracture toughness and fatigue crack growth rate properties in wire + arc additive manufactured Ti-6Al-4V. *Fatigue and Fracture of Engineering Materials and Structures* vol. 40 790–803 (2017).

10. Zhang, J., Wang, X., Paddea, S. & Zhang, X. Fatigue crack propagation behaviour in wire+arc additive manufactured Ti-6Al-4V: Effects of microstructure and residual stress. *Mater. Des.* **90**, 551–561 (2016).

11. Gordon, J. V., Haden, C. V., Nied, H. F., Vinci, R. P. & Harlow, D. G. Fatigue crack growth anisotropy, texture and residual stress in austenitic steel made by wire and arc additive manufacturing. *Mater. Sci. Eng. A* **724**, 431–438 (2018).

12. Nezhadfar, P. D. *et al.* Fatigue crack growth behavior of additively manufactured 17-4 PH stainless steel: Effects of build orientation and microstructure. *Int. J. Fatigue* **123**, 168–179 (2019).

13. *Mild Steel Welding Alloy ER70S-6 (GMAW) (MIG) ER70S-6 (GMAW) (MIG) Mild Steel Alloy • AWS ER70S-6*. www.mathesongas.com.

14. ER70S-6 - Weld WireWeld Wire. http://www.weldwire.net/weld_products/ww70s-6/.

15. Lincoln Electric Company, T. *LINCOLN ® ER70S-6 WELDING POSITIONS TYPICAL APPLICATIONS*. www.lincolnelectric.com.

16. Ermakova, A., Mehmanparast, A. & Ganguly, S. A review of present status and challenges of using additive manufacturing technology for offshore wind applications. *Procedia Struct. Integr.* **17**, 29–36 (2019).

17. ASTM E647−13. Standard Test Method for Measurement of Fatigue Crack Growth Rates. *Am. Soc. Test. Mater.* 1–50 (2014) doi:10.1520/E0647-15E01.2.

18. American Society for Testing and Materials. ASTME-1820-11: standard test method for measurement of fracture toughness. *Annu. B. ASTM Stand.* 1–55 (2011) doi:10.1520/E1820-18.

19. Ermakova, A., Mehmanparast, A., Ganguly, S., Razavi, J. & Berto, F. Investigation of mechanical and fracture properties of wire and arc additively manufactured low carbon steel components. *Theor. Appl. Fract. Mech.* **109**, 102685 (2020).

20. Mehmanparast, A., Brennan, F. & Tavares, I. Fatigue crack growth rates for offshore wind monopile weldments in air and seawater: SLIC inter-laboratory test results. *Mater. Des.* **114**, 494–504 (2017).

21. Anderson, T, L. *Fracture Mechanics: Fundamentals and Application*. (Taylor & Francis Group, 2005).

22. BS 7910. BSI Standards Publication Guide to methods for assessing the acceptability of flaws in metallic structures. *BSI Stand. Publ.* 490 (2015).

23. Jacob, A. *et al.* Residual stress measurements in offshore wind monopile weldments using neutron diffraction technique and contour method. *Theor. Appl. Fract. Mech.* **96**, 418–427 (2018).

24. Jacob, A., Mehmanparast, A., D'Urzo, R. & Kelleher, J. Experimental and numerical investigation of residual stress effects on fatigue crack growth behaviour of S355 steel weldments. *Int. J. Fatigue* **128**, 105196 (2019).

25. Igwemezie, V., Mehmanparast, A. & Kolios, A. Current trend in offshore wind energy sector and material requirements for fatigue resistance improvement in large wind turbine support structures – A review. *Renew. Sustain. Energy Rev.* **101**, 181–196

(2019).

26. Jacob, A. & Mehmanparast, A. Crack growth direction effects on corrosion-fatigue behaviour of offshore wind turbine steel weldments. *Mar. Struct.* **75**, 102881 (2021).

27. Rafieazad, M., Ghaffari, M., Vahedi Nemani, A. & Nasiri, A. Microstructural evolution and mechanical properties of a low-carbon low-alloy steel produced by wire arc additive manufacturing. *Int. J. Adv. Manuf. Technol.* **105**, 2121–2134 (2019).

28. Rafieazad, M., Nemani, A. V., Ghaffari, M. & Nasiri, A. On Microstructure and Mechanical Properties of a Low-Carbon Low-Alloy Steel Block Fabricated by Wire Arc Additive Manufacturing. *J. Mater. Eng. Perform.* (2021) doi:10.1007/s11665-021-05568-9.

29. Xu, X. *et al.* Microstructural evolution and mechanical properties of maraging steel produced by wire + arc additive manufacture process. *Mater. Charact.* **143**, 152–162 (2018).

4.2. Paper V: Experimental investigation of the fatigue crack growth behaviour in wire arc additively manufactured ER100S-1 steel specimens

Anna Ermakova[a], Supriyo Ganguly[b], Javad Razavi[c], Filippo Berto[c], Ali Mehmanparast[a*]

[a] Offshore Renewable Energy Engineering Centre, Cranfield University, Cranfield, MK43 0AL, UK

[b] Welding Engineering and Laser Processing Centre, Cranfield University, Cranfield, MK43 0AL, UK

[c] Norwegian University of Science and Technology (NTNU), Trondheim, Norway

Abstract[5]

Wire arc additive manufacturing (WAAM) is an advanced fabrication technology for the rapid and efficient production of large-scale engineering structures. In order to design WAAM components for a given loading condition, it is essential to characterise the mechanical and failure behaviour of the parts. In this study the performance of ER100S-1 low carbon steel has been investigated by performing fatigue crack growth tests on compact tension specimens extracted from a WAAM built wall. The experimental results have been compared with the recommended trends in the BS7910 standard and with data available in the literature. Metallurgical investigations have been carried out to explore the microstructural effects on the fatigue behaviour of the WAAM built components. The specimen location and orientation effects were comprehensively examined**,** and the results are discussed in terms of the influence of macro- and microscopic deformation on the global response of the WAAM built components under fatigue loading conditions.

* corresponding author

[5] *Fatigue & Fracture of Engineering Materials & Structures*. 45 (2021), 371-385. (DOI: 10.1111/ffe.13598)

4.2.1. Introduction

Additive Manufacturing (AM) technology is a layer-by-layer manufacturing technique that enables the fabrication of complex shapes in a continuous production process without an expensive conventional set-up and tools. The AM technology is rapidly evolving from simple prototyping to fabrication and repairing of critical large-scale industrial parts[1,2,3]. The AM components generally do not show isotropic behaviour due to the layer-wise nature of the AM process and continuous melting and solidification of the material, which induces residual stresses and microstructural changes. Depending on the AM process conditions, the parts may have a high likelihood of porosity and internal defects, which would subsequently influence the mechanical response and failure behaviour of the AM parts.

Wire arc additive manufacturing (WAAM) is a direct energy deposition technique that combines an electric arc as a heat source and a wire as feedstock and provides the highest deposition rates among all AM techniques[4], which makes it suitable for the production of large-scale structures. Moreover, compared to the powder-based AM techniques, using wire as a feedstock reduces the level of safety-related risks in the course of the manufacturing process. The WAAM technique can be utilised for the fabrication of simple and complex parts by employing a wide range of alloys such as aluminium, steels and titanium, as well as functionally graded materials[5]. In addition to the fabrication of new parts, the WAAM technique also facilitates the repair of damaged structures, as an alternative to the replacement of the entire component[6,7]. Similarly, to all AM techniques, as well as all the advantages mentioned for WAAM, this technique may also involve some disadvantages. The main disadvantage of such a fabrication method is the possibility of relatively high roughness on the outer surface of the as-built parts and dimensional inaccuracies that may impose the requirement of further post-deposition treatments such as surface machining, high pressure rolling, etc. The WAAM technique has been developed and investigated since the 1990s and is currently adopted by several industries such as aerospace and automotive for the fabrication of industrial-scale components [8,9]. Further developments have been carried out in recent years to increase the scale of the WAAM built parts from component size to the structural level by printing a large-scale bridge[10]. In order to explore the suitability of the WAAM technique for low-cost fabrication of large-scale structures, the WAAM built parts made of conventional steels (i.e., which are relatively cheap) must be fully characterised under various loading conditions and in different environments.

For industrial applications where the engineering component or structure is subjected to repetitive load cycles during service, such as marine structures, fatigue assessment is a critical consideration at the design and life assessment stages[11,12,13]. Particularly for life prediction purposes, it is crucial to investigate the fatigue behaviour of the material to better understand the damage evolution and failure behaviour in such components. Therefore, feasibility studies must be performed on the fatigue behaviour of WAAM built components made of various alloys to examine the suitability of the WAAM technique and particular alloys for consideration in industrial applications where the component or structure is subjected to repeated cyclic stresses. While there are some limited fatigue crack growth (FCG) data available in the literature on WAAM built parts made of titanium[14,15] and occasionally stainless steel[16,17], the fatigue response of more effective low carbon steels is yet to be explored for application in less safety-critical industries such as offshore wind. Knowing that steel alloys

are the most common types of material utilised in the fabrication of metallic structures in offshore applications, further research into the FCG behaviour of WAAM built parts made of steel alloys would rapidly expand the extent of application of this efficient AM technology and enable this technology to be considered for low-cost fabrication of offshore renewable energy structures.

The fatigue crack propagation behaviour of WAAM built parts using titanium Ti-6Al-4V alloy was examined by Zhang et al.,[18] where compact tension C(T) specimens were extracted from WAAM walls. The specimens had different orientations with the crack initiation region in substrate or the WAAM built area. The maximum load, load ratio and frequency in these tests were 5 kN, 0.1 and 10 Hz, respectively. It was reported that the crack propagated along straight and smooth lines in the wrought part of the specimen and in tortuous paths in the WAAM built region, due to different microstructural characteristics and lamellar structure of the WAAM part. Furthermore, lower crack propagation rates were observed in the WAAM specimens compared to the wrought substrate. Similar observations were reported by the same authors in further analysis of such C(T) specimens[19]. Gordon et al.[20] examined the fatigue behaviour of WAAM built parts using 304L stainless steel by performing fatigue tests on single edge notched bend, SEN(B), thin specimens extracted from different wall locations and in two different orientations with respect to the building direction. The experiments were conducted at a constant load range of 0.7 kN, load ratio of 0.1 and frequency of 10 Hz. The results show that as-printed WAAM specimens have improved the FCG resistance compared to the conventional wrought 304L stainless steel. In addition, it was observed that the vertical WAAM specimens displayed lower fatigue propagation rates compared to the horizontal specimens, which can be due to the long columnar grains and strong texture in the WAAM built direction. A set of WAAM built Ti-6Al-4V titanium alloy specimens were tested under fatigue loading conditions by Zhang et al. [14,21]. Thicker C(T) specimens were also extracted with two different crack orientations with respect to the WAAM deposited layers. The FCG rates in WAAM specimens were found to be lower than the wrought counterpart. Moreover, the crack growth rate was found to be lower in specimens with the propagating path across the AM layers, compared to those where the crack was growing along the layers. These findings suggest that the WAAM process can be considered as an alternative technology for manufacturing purposes.

The experimental results reported in previous studies have shown that the FCG behaviour of the WAAM built parts strongly depend on the material and crack orientation. In this study, the FCG behaviour of WAAM built parts made of ER100S-1 steel has been investigated to explore the suitability of this material for the WAAM production of offshore structures which are subjected to cyclic loading conditions. Also included in this study is a sensitivity analysis of the specimen orientation and extraction location, with respect to the WAAM built wall, on the fatigue performance of the extracted specimens. Details of the manufacturing process of the WAAM walls, specimen extraction plan and geometry, the test set-up and data analysis procedure and obtained test results are presented below. The results obtained from this study have been discussed in terms of the material microstructure effects on the cracking behaviour of ER100S-1 WAAM built parts. Furthermore, the obtained results from this study have been compared with the recommended FCG trends available in standards and also the existing test data on wrought steels in order to critically assess the fatigue performance of WAAM built parts compared to conventional welded structures.

4.2.2. Manufacturing set-up and specimen extraction

A high strength metal wire ER100S-1 with low carbon and high manganese was used in this study. This material is normally used for shielded arc welding on a variety of steels employed in critical applications, such as mining, pressure vessels, shipbuilding, military equipment and high strength products. The yield stress of ER100S-1 is equal to or greater than 690 MPa with the ultimate tensile strength (UTS) of 760 MPa[22]. This material offers excellent toughness; however, its mechanical properties significantly depend on the level of preheating, interpass temperature, and post-weld heat treatment. A spool of Böhler Welding ER100S-1 wire[23] was used in this study with the chemical composition listed in Table 4.6.

Table 4.6: Chemical composition of ER100S-1 material (wt.-%)[23]

	C	*Mn*	*Cr*	*Si*	*Ni*	*Mo*
ER100S-1	0.08	1.70	0.20	0.60	1.50	0.50

A Cold Metal Transfer (CMT) based WAAM process, with the manufacturing parameters summarised in Table 4.7, was used to produce an additively manufactured wall for this study. The WAAM set-up consists of the CMT power source, and a robot arm with the torch that feeds the wire and supplies shielding gas simultaneously. An exhaust fan draws off the generated fumes and heat in the course of the WAAM process. The manufacturing set-up and completed wall are shown in Figure 4.11 (a). The WAAM deposition process was started in the middle of the base plate which was cut from EN10025 rolled structural steel with dimensions of 420 × 200 × 12 mm^3. Each side of the base plate was fixed onto the working table with two clamps to prevent any bending and movement due to the thermal energy input. Once the fabrication of the WAAM wall was completed and the part was cooled down to the ambient temperature, the clamps were removed. The additive layers in the WAAM wall were deposited on top of each other in an oscillating manner[24] in order to create a relatively thick wall with approximately 355 mm length (X-direction in Figure 4.11 (b)), 24 mm thickness (Y-direction) and 140 mm height (Z-direction).

Table 4.7: CMT-WAAM fabrication parameters

Shielding gas	Ar+20% CO_2
Gas flow rate	15 L/min
Wire diameter	1.2 mm
Wire feed speed	7.5 m/min
Robot travelling speed	7.33 mm/sec
Dwell time	120 sec

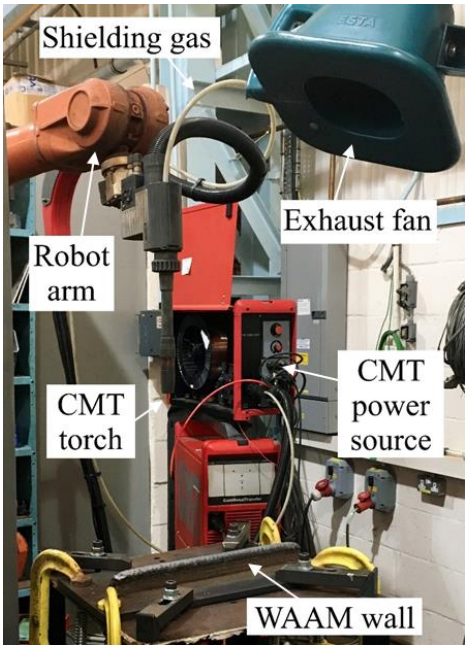

(a)

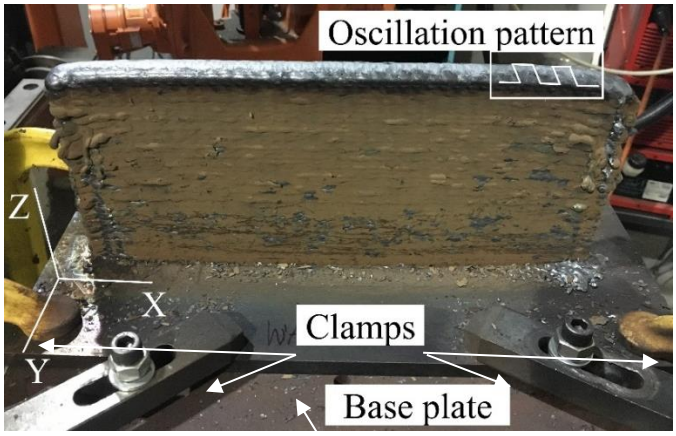

(b)

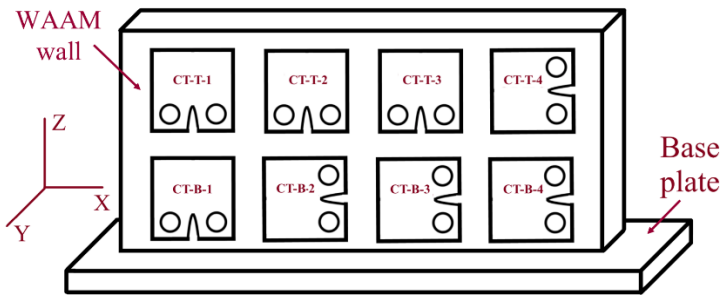

(c)

Figure 4.11: The fabrication process: (a) CMT WAAM set-up, (b) completed wall, and (c) schematic demonstration of the specimen extraction plan

Upon completion of the WAAM wall fabrication, eight stepped notched C(T) specimens were extracted using the Electrical Discharge Machining (EDM) technique. Four of the specimens

were extracted from the bottom of the wall (near the base plate), and four from the top of the WAAM wall. As shown in Figure 4.11 (c), specimens denoted CT-T-1 – CT-T-4 were located at the top of the wall, whereas CT-B-1 – CT-B-4 were from the bottom. Moreover, the specimens were extracted with two different crack orientations; half of them had vertical (V) orientation – with the crack plane perpendicular to the deposition direction (for example CT-T-1 or CT-B-1), and the other half had horizontal (H) orientation – with the crack plane parallel to the AM layers (for example CT-T-4 or CT-B-2). The geometry of C(T) specimens was selected in accordance with the ASTM E647[25] standard with the width of W = 50 mm, height of H = 60 mm, total thickness of B = 16 mm and the initial crack length a_0 = 17 mm (before pre-fatigue cracking). Knife edges were machined at the crack mouth of the C(T) specimens following the instructions provided in the E1820[26] standard in order to accommodate a clip gauge for crack growth monitoring using the compliance measurements throughout the tests[27].

4.2.3. Fatigue crack growth test set-up and data analysis

FCG tests were performed on a 100 kN servo hydraulic Instron machine under Mode I fracture mechanics loading conditions according to the ASTM E647[25] standard. All tests were conducted in air at room temperature with the load ratio (i.e., the ratio of minimum to maximum load P_{min}/P_{max}) of R = 0.1 and maximum applied load of P_{max} = 10 kN. The fatigue cycles were introduced using a constant amplitude sinusoidal cyclic waveform at 5 Hz frequency. Prior to FCG testing, all specimens were pre-fatigue cracked to approximately 20 mm ($a_{i,p}/W$ = 0.4) under fatigue loading conditions using the load decreasing approach, to introduce an infinitely sharp crack tip ahead of the machined notch. During the fatigue pre-cracking phase, it was ensured that the final value of maximum stress intensity factor K_{max} did not exceed the initial K_{max} in the actual FCG tests.

The instantaneous crack lengths, a_i, during the pre-cracking phase and FCG tests were estimated using the unloading compliance method, by attaching a clip gauge onto the knife edges located at the crack mouth of the specimens. Moreover, two high resolution cameras were placed at the back and in front of the set-up to monitor the crack growth on each side of the specimen and capture the crack paths throughout the tests. The crack lengths were measured at the outer surfaces of the C(T) specimens using the cameras to validate the data obtained from the compliance method. All C(T) specimens were tested until the value of the crack length estimated by the compliance technique reached 35 mm ($a_{f,c}/W$ = 0.7). The fatigue test set-up and crack growth monitoring tools are demonstrated in Figure 4.12.

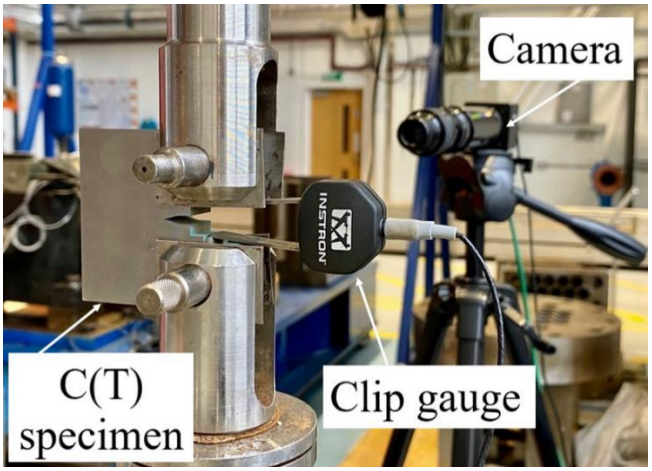

Figure 4.12: Fatigue crack growth test set-up

The number of cycles and the instantaneous crack lengths were continuously captured during the fatigue tests and the FCG rates, *da/dN*, were subsequently calculated using a combination of the secant method for the first and last three data points, and the seven-point incremental polynomial method for the rest of the data points. The stress intensity factor (SIF) range, ΔK, was obtained according to the shape function equation shown in Equation 4.4, developed by Mehmanparast et al.[28] which provides accurate solutions of the shape function for a wider range of crack lengths, $0.2 \leq a/W \leq 0.7$, in a C(T) specimen compared to that available in ASTM E647[25] which involves a relatively large percentage of error at shorter crack lengths. In Equation 4.4, α is the normalised crack length a/W and ΔP is the load range which is defined as the difference between P_{max} and P_{min}.

$$\Delta K = \frac{\Delta P}{BW} \cdot \sqrt{a} \cdot (-372.12\alpha^6 + 1628.60\alpha^5 - 2107.46\alpha^4 + 1304.65\alpha^3 - 391.20\alpha^2 + 54.81\alpha + 7.57) \quad \text{Equation 4.4}$$

4.2.4. Test results and discussion

The recorded data during the FCG tests, which comprised the crack length *a* and the number of cycles *N*, are shown for each specimen and compared with each other in Figure 4.13. As seen in this figure, the initial crack length after fatigue pre-cracking was approximately 20 mm for all specimens, except for the CT-T-4 specimen which had a longer starting crack and therefore exhibited a shorter FCG test duration. The comparison of the crack growth trends in Figure 4.13 shows that the duration of the fatigue tests performed on specimens extracted from the top of the WAAM wall was on average approximately 3.9 times longer, compared to those extracted from the bottom of the wall. Moreover, it can be observed in Figure 4.13 that the FCG trends obtained from the bottom specimens are consistently similar, whilst the specimens extracted from the top of the wall exhibited some noticeable levels of inconsistency in the FCG trends. The obtained FCG results in Figure 4.13 show that, for the material examined in this study, the FCG test duration and trend strongly depend on the location at which the specimens were extracted from the ER100S-1 WAAM wall.

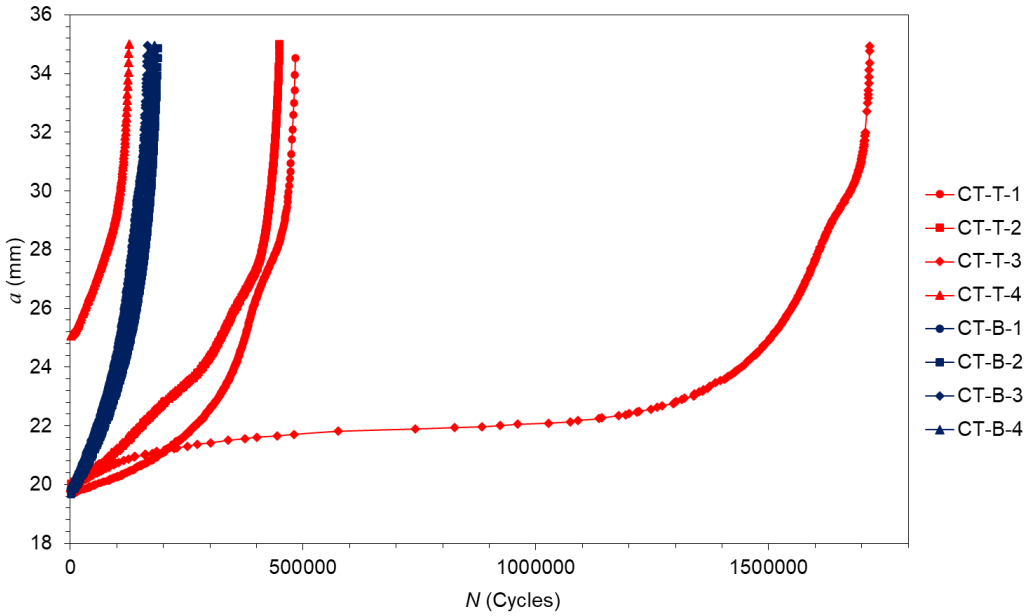

Figure 4.13: Fatigue crack growth trends in ER100S-1 WAAM built specimens extracted from different locations

The FCG rate, *da/dN*, obtained from the tests on C(T) specimens were correlated with the SIF range, *ΔK*, and the results are presented in Figure 4.14 (a). It can be seen in this figure that for the given loading condition, the FCG results on the specimens extracted from the bottom of the WAAM wall show a higher crack growth rate at the low and intermediate values of *ΔK* compared to those extracted from the top of the wall. However, at larger values of *ΔK*, the difference between the FCG rates in the bottom and top specimens decreases and eventually diminishes. The results in Figure 4.14 (a) show that the FCG trends obtained from horizontally oriented specimens extracted from the bottom of the WAAM wall (CT-B-2, CT-B-3 and CT-B-4) fall upon each other indicating a good repeatability in those tests from horizontal specimens while the vertically oriented specimen from the bottom of the wall (CT-B-1) initially followed the same trend as the horizontal specimens in the low *ΔK* region but subsequently showed a reduction followed by an increase in *da/dN* in the high *ΔK* region. The results for the top specimens present a higher level of scatter with a strong dependency on the specimen orientation. The FCG data for the specimens extracted from the top of the wall show an irregular wavy behaviour in the vertical specimens (CT-T-1, CT-T-2, CT-T-3), with at least one drop point, as depicted in Figure 4.14 (b), whereas the horizontal specimen (CT-T-4) exhibits a relatively straight crack growth trend in log-log axes. It can be seen in Figure 4.14 (b) that in the vertical specimens, the FCG rates reduce by up to 17 times at the drop points while the horizontal specimens show a relatively smooth FCG behaviour in specimens extracted both from the top and bottom of the wall (see Figure 4.14 (c)). This can be due to the fact that in vertical specimens the crack grows throughout different AM deposited layers, hence the local material properties may vary which subsequently influence the FCG behaviour of the material.

It is worth noting that the WAAM built wall was not subjected to any heat treatment. This was to replicate the realistic conditions where AM technology is used to repair a damaged/cracked component and also in the case of large-scale, additively manufactured built structures, which cannot be heat treated in an oven due to their large size, and therefore high costs are involved

in this process[29]. Although some residual stress profiles are expected to exist in the WAAM built wall before removing the base plate, the separation of the base plate from the additively manufactured wall followed by C(T) specimen extraction would significantly relax the initial residual stresses[30]. Therefore, it has been assumed in this study that the remaining residual stresses in extracted C(T) specimens are insignificant and as such the applied loading condition has been employed in the analysis of the FCG behaviour of the material. Further investigations will be conducted in future work to evaluate the influence of significant residual stress profiles on the subsequent fatigue behaviour of large-scale WAAM built structures.

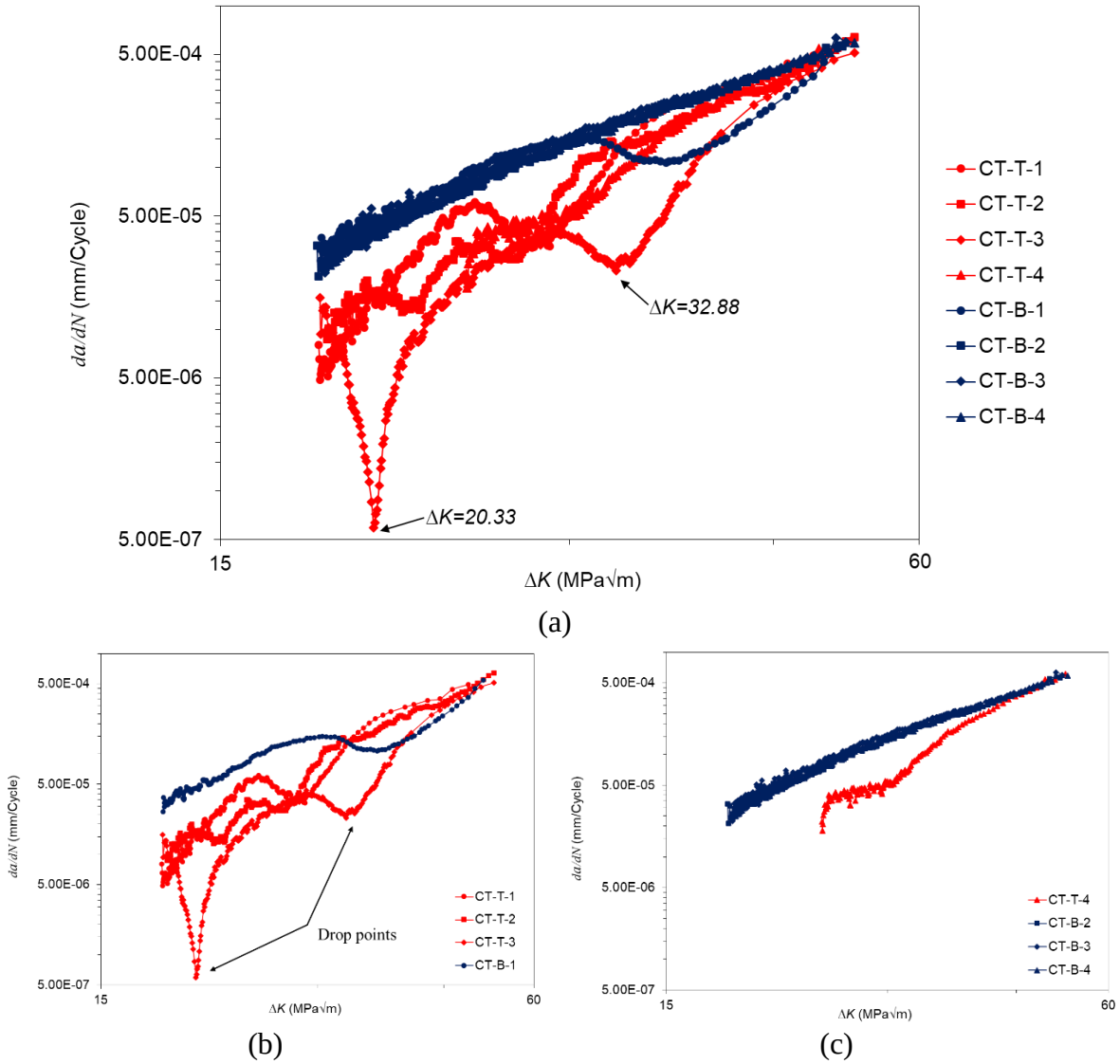

(a)

(b)

(c)

Figure 4.14: Fatigue crack growth rates results for ER100S-1 WAAM built specimens extracted from different locations: (a) all specimens, (b) vertical specimens, and (c) horizontal specimens

For all eight FCG datasets, the lines of best fit within the Paris region were plotted to work out the power law constants C and m (see Equation 4.5), which are summarised in Table 4.8. Additionally, the coefficient of determination, R^2, is included in the table for each dataset which has been found close to 1 for all horizontal specimens, indicating that the lines of best fit accurately describe the behaviour of the material, and approximately 0.87 for vertical specimens due to the waviness of the obtained FCG curves. Typical values of the stress

intensity factor range exponent, *m*, for FCG tests on wrought steel materials in air are within the range of 2 to 4[31]; however, only for three tested ER100S-1 WAAM specimens in this study has the *m* value been found within this range, and for the rest of the specimens the *m* value is found to be between 4.10 and 5.56. Consequently, comparing the fatigue test results in Figure 4.14 and Table 4.8, it can be concluded that the extraction location (i.e. top and bottom) has a major impact on the *da/dN vs.* ΔK trends of the ER100S-1 WAAM built specimens, whereas the orientation of the extracted specimens mostly affects the shape and level of scatter in the fatigue data.

$$da/dN = C\Delta K^m \qquad \text{Equation 4.5}$$

Table 4.8: Paris law constants obtained from the tests performed on ER100S-1 WAAM built specimens (*da/dN* in mm/Cycle and ΔK in MPa$\sqrt{m}$)

Specimen ID	Orientation	Location	P_{max} (kN)	C	m	R^2
CT-T-1	Vertical	Top	10	4.08×10^{-11}	4.24	0.85
CT-T-2	Vertical	Top	10	4.85×10^{-11}	4.17	0.96
CT-T-3	Vertical	Top	10	1.52×10^{-12}	4.95	0.80
CT-T-4	Horizontal	Top	10	3.20×10^{-13}	5.56	0.98
CT-B-1	Vertical	Bottom	10	1.23×10^{-7}	1.99	0.86
CT-B-2	Horizontal	Bottom	10	8.87×10^{-10}	3.63	0.99
CT-B-3	Horizontal	Bottom	10	2.40×10^{-10}	4.10	0.99
CT-B-4	Horizontal	Bottom	10	2.76×10^{-9}	3.27	0.99

Subsequent to quantification of the Paris law constants for each of the tests performed in this study, the data were re-analysed based on the specimen extraction location by plotting a line of best fit to all top and all bottom specimens, and the obtained results are summarised in Table 4.9. The results show that the value of R^2 is higher for the specimens extracted from the bottom, (Set-B), indicating less scatter in this dataset compared to the top specimens dataset, (Set-T), which is consistent with observations previously made in Table 4.8. The level of scatter in the obtained FCG data was further analysed by calculating the upper bound trends based on 2 standard deviation (SD), assuming the same slope as the mean line. The values of the power law constants for the upper bound FCG trends (mean+2SD) within the Paris region are reported in Table 4.9 for each dataset.

Table 4.9: Power law constants for the mean curves and upper bound trends in the Paris region for different specimen locations

Datasets	Location	P_{max} (kN)	Mean			Mean+2SD	
			C	m	R^2	C	m
Set-B	Bottom	10	1.00×10^{-8}	2.73	0.95	1.69×10^{-8}	2.73
Set-T	Top	10	3.00×10^{-11}	4.20	0.77	1.05×10^{-10}	4.20

The mean+2SD FCG lines for the top (set-T) and bottom (set-B) specimen datasets are plotted in Figure 4.15 and compared with the recommended FCG trends in the BS7910 standard for welded joints, made of a wide range of wrought metals, in air, and based on the simplified law and 2-stage law[32]. It can be seen in this figure that the upper bound lines for the Set-B and Set-T specimens extracted from the ER100S-1 WAAM built wall fall below the trends recommended in the BS7910 standard, indicating that the FCG behaviour of ER100S-1 WAAM components can be conservatively predicted by the trends specified in the BS7910 standard. Moreover, it can be observed that the slope of the upper bound FCG line for Set-B is similar to the BS7910 2-stage law, whilst the slope of the Set-T upper bound line is much steeper than both trends recommended in the standard.

In addition to comparison of the results with BS7019 recommended trends, the FCG data obtained from this study were compared with the FCG data in air on wrought structural steels available in the literature. A set of C(T) specimens extracted from the heat affected zone (HAZ) for S355G+10M structural steel was tested by Jacob et al.[33] under similar loading conditions with P_{max} =10 kN, 5Hz frequency and R=0.1. The same loading conditions were used to conduct the FCG test in air on S355G8+M steel C(T) specimens extracted from HAZ and base metal (BM) by Mehmanparast et al.[28] The results from these studies are presented in Figure 4.15 for comparison purposes and show that the upper bound FCG line for Set-B falls upon or above all the experimental data points obtained from S355G8+M and S355G+10M steel BM and HAZ specimens. The slope of the Set-T upper bound FCG line is similar to the experimental results from S355G+10M and S355G8+M HAZ specimens. Both wrought steels taken for comparison are widely used for the fabrication of offshore structures that are subjected to severe cyclic loading conditions during their lifetime[34,35,36]. Hence, this comparison shows that ER100S-1 steel can be potentially considered for the WAAM fabrication of critical parts of offshore structures, demonstrating similar performance to the wrought steels currently used in conventional fabrication processes.

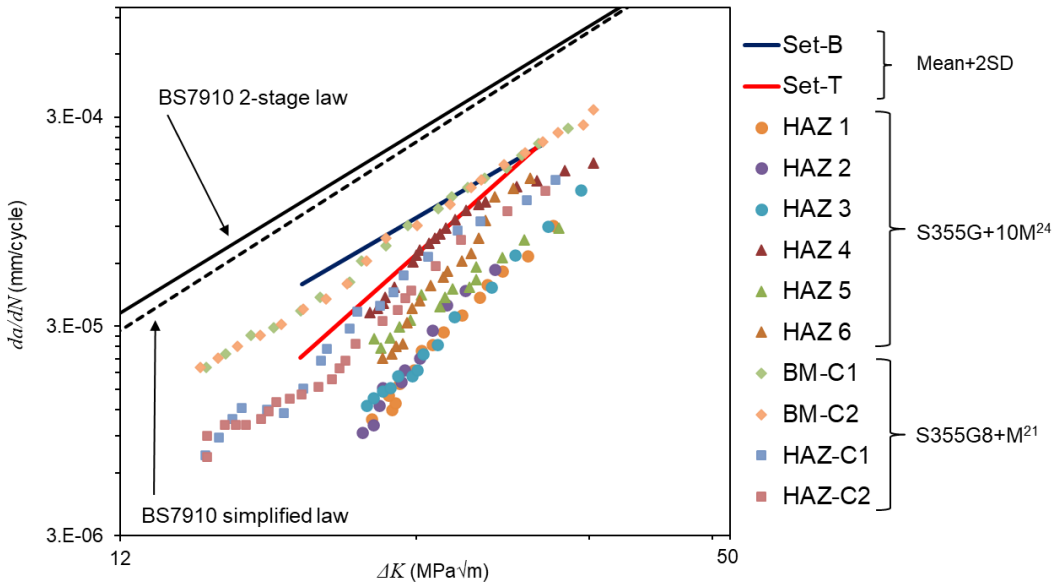

Figure 4.15: Comparison of the upper bound fatigue crack growth trends for ER100S-1 WAAM specimens with BS7910 curves and literature data on structural steels

4.2.5. Microstructural analysis

- **Fractography**

After the FCG experiments were completed, all specimens were broken into halves for the post-mortem analysis in order to evaluate the accuracy of crack length estimation in fatigue tests using the compliance method. Prior to the break open, the specimens were soaked in liquid nitrogen for a few minutes to embrittle the material and then pulled under tension using the servo-hydraulic machine for fast fracture opening with minimum plastic deformation on the fracture surface. Two examples of the fracture surfaces are shown in Figure 4.16 for each of the top and bottom specimens extracted from the WAAM wall. Three areas are highlighted on the fracture surface of the FCG specimens in Figure 4.16: (1) pre-fatigue cracking, (2) fatigue crack growth, and (3) fast fracture. The crack extension in the first two regions was measured on all eight specimens. The fracture surface analysis reveals a symmetric crack propagation behaviour with respect to the mid-thickness plane, indicating acceptable alignment in the test set-up during the FCG tests. Further examination of the fracture surfaces shows that the fatigue regions are smooth on the fracture surface of all specimens without any evidence of significant WAAM fabrication defects or any deviation of the crack from the straight plane. Moreover, it can be observed that the fracture surface of the vertical specimens (Figure 4.16 (a), (b) and (c)) exhibited some waviness representing different AM layers of the WAAM wall, where the height of one layer was approximately 3 mm, whereas the fracture surface of the horizontal specimen (Figure 4.16 (d)) is fairly flat, as the crack was propagating along a single AM layer. Additionally, the entire fracture surface of the vertical specimens, including the area of fast fracture, reveals a columnar texture with the lines perpendicular to the AM layers, and parallel to the WAAM deposition direction, which is absent on the horizontal specimen's fracture surface.

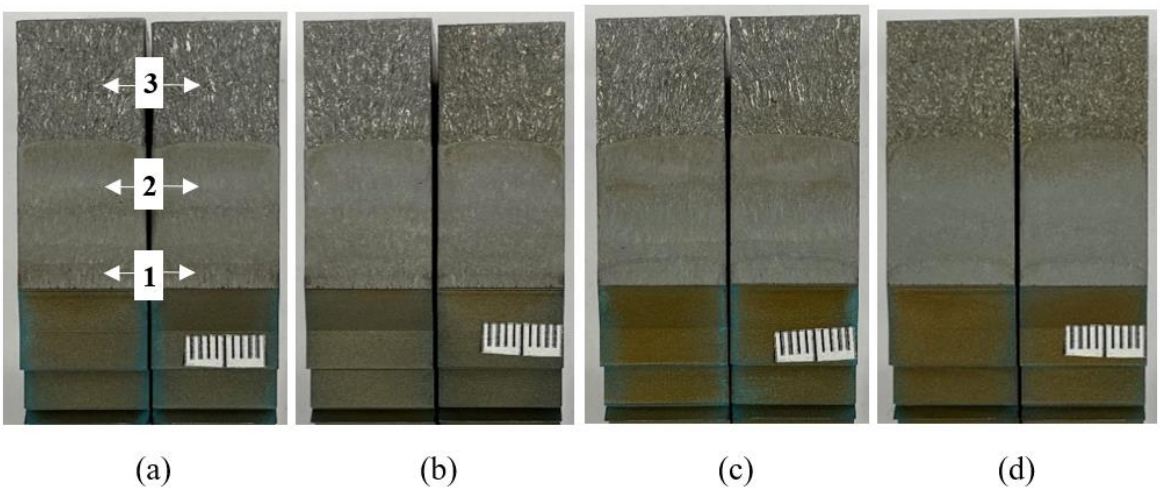

Figure 4.16: Fracture surface of WAAM built ER100S-1 specimens extracted from the top: (a) CT-T-1, (b) CT-T-2; and from the bottom of the wall: (c) CT-B-1, (d) CT-B-3.

Some key specimen dimensions such as the machined crack length a_o, the crack length after the fatigue pre-cracking process (estimated from the compliance method) $a_{i,p}$, the final crack length after the FCG test (estimated from the compliance method) $a_{f,c}$, and the final crack length measured on the fracture surfaces (using optical imaging on the fracture surface) $a_{f,op,}$ are

presented in Table 4.10. It can be seen in this table that the percentage of error in the estimated crack lengths using the compliance method, in comparison with the measured crack lengths from optical imaging, is equal to or less than 1.3%. This implies that the compliance technique provides an accurate estimation of the crack length during the FCG experiments on WAAM built specimens.

Table 4.10: Specimen dimensions, initial and final crack lengths

Specimen ID	W (mm)	B (mm)	a_0 (mm)	$a_{i,p}$ (mm)	$a_{f,c}$ (mm)	$a_{f,op}$ (mm)	% error in a_f
CT-T-1	50.1	16.0	17.0	19.7	35.0	35.5	1.3
CT-T-2	50.0	16.0	17.0	20.0	35.0	35.3	0.7
CT-T-3	50.0	16.1	17.0	19.8	35.0	35.4	1.2
CT-T-4	50.0	16.0	17.1	25.0	35.0	35.1	0.2
CT-B-1	50.1	16.0	17.0	19.8	35.0	35.3	0.8
CT-B-2	50.0	16.0	17.0	19.7	35.0	35.0	0.1
CT-B-3	50.0	16.2	17.1	19.8	35.0	34.7	0.8
CT-B-4	50.2	16.0	17.0	19.9	35.0	34.6	1.1

- **SEM analysis on fracture surface**

Once all specimens were broken-open, the microscopy analysis was conducted on vertical specimens using a TESCAN VEGA 3 Scanning Electron Microscope (SEM), to examine the fracture surface areas of the vertical specimens corresponding to the FCG regions where the curve showed significant drops, such as areas A and C on the FCG curve for CT-T-3 in Figure 4.17. Area B between the two drop points was also selected to investigate any noticeable microstructural differences. Moreover, for comparison purposes the fracture surface of a horizontal specimen, CT-T-4, extracted from the top of the WAAM wall was also examined. Since the obtained FCG trend of the horizontal specimen is relatively straight in log-log axes, areas of interest were selected with the same ΔK values that correspond to the vertical specimen, as depicted in Figure 4.17 (a).

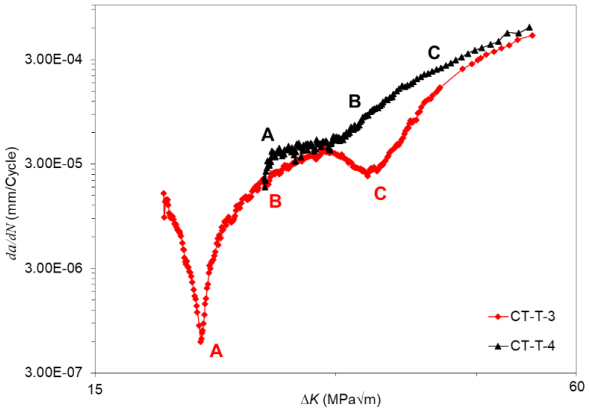

(a)

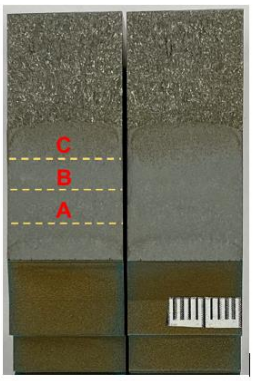

(b)

Figure 4.17: (a) Areas of interest for SEM analysis on vertical specimen CT-T-3 and horizontal specimen CT-T-4, (b) demonstration of the investigated areas on the fracture surface

The SEM analysis of the three areas of interest for the horizontal and vertical specimens are shown in Figure 4.18, with a magnification of 5000. Fracture surfaces of both vertical and horizontal specimens revealed transgranular cup and cone features, suggesting a ductile fracture mechanism. However, these ductile fracture features of the vertical specimen are smaller and with higher density, whilst for the horizontal specimen there are fewer of them and with a larger size. Additionally, the microstructural analysis of the fracture surface of the horizontal specimen CT-T-4 reveals the presence of large horizontal secondary cracks that lead to higher FCG rates, compared with the vertically oriented specimen CT-T-3, which is consistent with the FCG trends observed in Figure 4.17 (a). Furthermore, there are elongated dimples on the vertical specimen with different orientations, compared to the horizontal specimen. In areas A and C, where the drop of FCG rate is visible, the orientation of the dimples on the vertical CT-T-3 specimen is upwards and parallel to the crack propagation direction, whereas in area B, the orientation of rupture changes and inclines to approximately 55^0 with respect to the crack propagation direction, which accelerates the cracking rate compared to areas A and C. These observations are consistent with the observed FCG trend seen in Figure 4.17 (a). The microstructural difference of areas A and C, along with the drop of the FCG rates, can happen when the crack tip is encountering the re-melted zone between two WAAM layers; however, to confirm this fact, further hardness mapping and microstructural investigation was conducted.

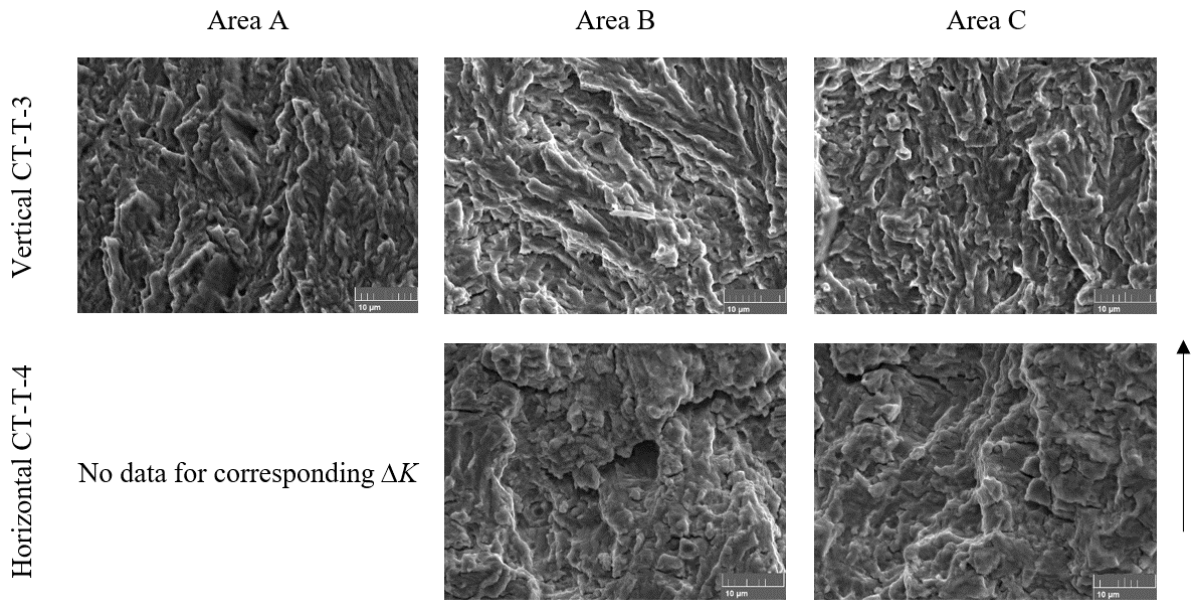

Figure 4.18: SEM fractographs of three areas on vertical (CT-T-3) and horizontal (CT-T-4) specimens with 5000 magnification (the scale bar is 10 µm, and the right-hand side arrow shows the direction of the crack propagation)

- **Microhardness mapping**

The same vertical specimen (CT-T-3) was taken for further microhardness analysis to examine how the hardness changes along the crack propagation path. As depicted in Figure 4.19 (a), hardness values were measured on the front face of the specimen from the initial crack tip location, towards the end of the specimen, with the same direction as the crack propagation path during FCG test, at approximately 0.2 mm from the edge of the specimen. Measurements were carried out according to BS EN ISO 6507-1:1997[37] using a 0.5 kg load, in which the applied load was held for 15 seconds, and the indentations were conducted at 2 mm intervals. The hardness results are presented in Figure 4.19 (b). The areas of interest were also marked in the figure and show that area A corresponds to the lowest hardness value of the tested plane (approximately 235HV), whereas area C lays in the region with the highest hardness at about 258HV; hardness value in area B is 248HV. This confirms that the drops in the FCG rates do not depend on the microhardness of ER100S-1 material for WAAM components.

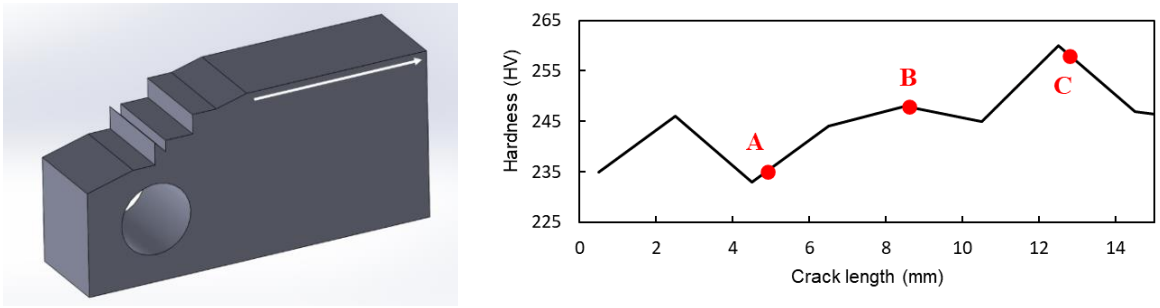

(a) (b)

Figure 4.19: (a) Microhardness mapping path, (b) Hardness test results along the crack path for the vertical specimen CT-T-3

- **Optical microscopy analysis**

A thin slice of the fracture surface, which was approximately 1.5 mm thick, was cut off from the vertical specimen's fracture surface of CT-T-3 using the EDM technique. The sample was then hot-mounted in mould, ground (with final grinding step of 2500 grit), polished using DiaPro Dac 3 µm diamond suspension, final polished using OP-S colloidal silica suspension with a grain size of about 0.04 µm, and then etched using 2% Nital solution in accordance with ASTM E407-07[38]. This etchant reveals alpha grain boundaries and constituents. The microstructures of the etched specimen were observed using a digital microscope HIROX, MXB-2500REZ, at the exact areas A, B and C specified in Figure 4.17 and the results are presented in Figure 4.20.

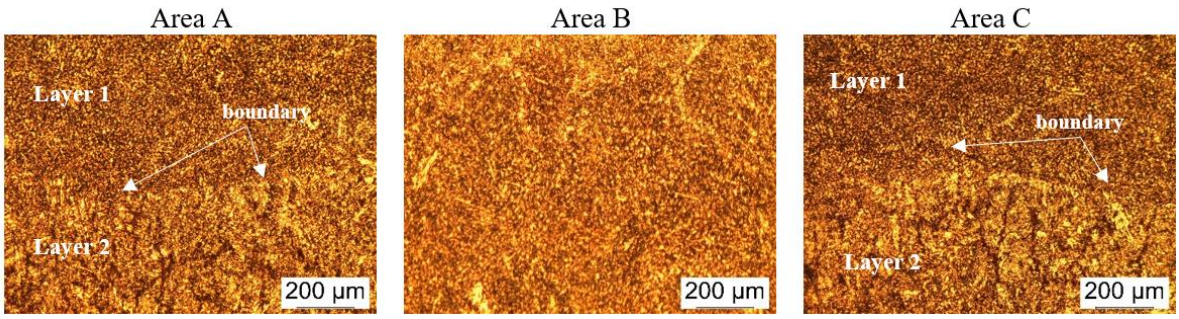

Figure 4.20: Optical microscopy analysis of vertical specimen CT-T-3 at three different areas of interest

The material microstructures in areas A and C in Figure 4.20 demonstrate that the crack is travelling between two WAAM layers, hence why a reduction in the FCG rate is observed at the ΔK values corresponding to these regions. On the other hand, the microscopical analysis of area B shows a region with a single WAAM layer that does not affect the FCG behaviour. Based on this analysis it can be concluded that the specimen orientation plays a significant role in microstructural variations along the crack path and consequently the FCG behaviour of WAAM ER100S-1 specimens. The microstructural observations also confirm that the vertical specimen orientation requires a higher amount of energy for a crack to propagate at the boundaries between two consecutive WAAM layers and exhibits a lower FCG rate in such regions, compared to the horizontal specimens where the crack propagates throughout only a single WAAM layer and does not require extra amounts of energy for crack propagation (Figure 4.17 (a)).

- **Defects**

The WAAM technique is a continuous welding process. During the fabrication of WAAM components, the quality of the metal deposition depends on the process parameters (CMT power, layer thickness, deposition rate, etc.) and can be unstable due to complex mass and heat transfer, which leads to variety of defects, such as porosity, lack-of-fusion, distortion or cracking[39,40]. The embedded defects or flaws can affect the mechanical behaviour of the WAAM component and significantly reduce its fatigue life[39]. Previous analysis of the fracture surfaces in Figure 4.16 did not indicate any visible defects at low magnifications, therefore in order to examine the existence of potential defects in more detail, all polished specimens were inspected with an SEM, and some key observations are presented in Figure 4.21. As can be seen, porosity defects are observed in all three images, with the maximum diameter of approximately 5 µm. Moreover, a combination of a keyhole and gas-entrapped pores porosity defect is visible in Figure 4.21 (c). The typical pore size reported for WAAM built components in the literature varies from 10 to <100 µm[41,42,43], therefore due to the small size of the discovered defects, the manufactured ER100S-1 WAAM part produced for this study can be considered as a low level defects component.

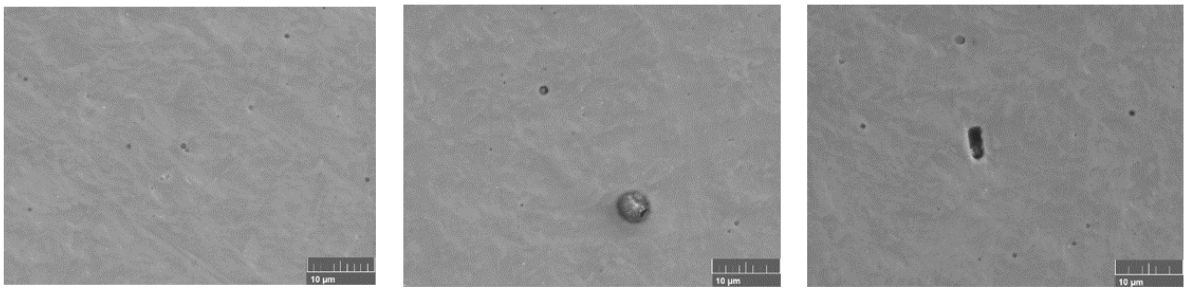

(a) (b) (c)

Figure 4.21: SEM fractographs of polished ER100S-1 specimens with defects (a) and (b) gas-entrapped pores, (c) pores and a keyhole porosity defect (the scale bar is 10 μm).

4.2.6. Conclusions

The FCG behaviour of ER100S-1 WAAM built specimens was investigated in this study. Based on the observations and analysis of the collected data the following conclusions can be drawn:

- The duration of the experiments on the C(T) specimens extracted from the top of the WAAM built walls is on average 3.9 times longer than for the bottom specimens.
- At the beginning of the Paris region the specimens extracted from the top of the WAAM wall exhibit slower FCG rates; however, at higher ΔK values all specimens extracted from both top and bottom show similar trends.
- The specimen orientation affects the shape of the FCG trends and the level of scatter, with wavy FCG data patterns and high level of scatter observed in the vertical specimens.
- The mean+2SD FCG lines for both top and bottom sets of specimens fall below the recommended FCG trend in BS7910.
- The upper bound trend for Set-B lies upon or above the FCG data points obtained from S355G8+Mand S355G+10M BM and HAZ specimens, whilst the slope of the upper bound line for Set-T aligns with S355G8+M and S355G+10M HAZ specimens.
- The SEM analysis of fracture surfaces revealed the ductile fracture mechanism for both horizontal and vertical specimens. However, the presence of large secondary cracks perpendicular to the crack propagation direction in the horizontal specimens accelerates the FCG rate compared to the vertical specimens.
- Optical microscopy analysis demonstrated that the drops in FCG rates in vertical specimens occur when the crack propagates through the boundary between two consecutive WAAM layers.
- Examination of polished ER100S-1 WAAM specimens under SEM confirmed a low level of defects, with the maximum pore diameter of approximately 5 μm.

4.2.7. Acknowledgements

This work was supported by grant EP/L016303/1 for Cranfield, Oxford and Strathclyde Universities' Centre for Doctoral Training in Renewable Energy Marine Structures – REMS CDT (http://www.rems-cdt.ac.uk/) from the UK Engineering and Physical Sciences Research Council (EPSRC).

4.2.8. References for paper V

1 Frazier WE. Metal additive manufacturing: A review. *Journal of Materials Engineering and Performance*. 2014;23: 1917–1928.

2 Selcuk C. Laser metal deposition for powder metallurgy parts. *Powder Metallurgy*. 2011;54: 94–99.

3 Berto F, Razavi SMJ, Torgersen J. Frontiers of fracture and fatigue: Some recent applications of the local strain energy density. *Frattura ed Integrita Strutturale*. 2018;12: 1–32.

4 Martina F, Ding J, Williams S, Caballero A, Pardal G, Quintino L. Tandem metal inert gas process for high productivity wire arc additive manufacturing in stainless steel. *Additive Manufacturing*. 2019;25: 545–550.

5 Marinelli G, Martina F, Lewtas H, Hancock D, Ganguly S, Williams S. Functionally graded structures of refractory metals by wire arc additive manufacturing. *Science and Technology of Welding and Joining*. 2019;24: 495–503.

6 Balit Y, Joly LR, Szmytka F, Durbecq S, Charkaluk E, Constantinescu A. Self-heating behavior during cyclic loadings of 316L stainless steel specimens manufactured or repaired by Directed Energy Deposition. *Materials Science and Engineering A*. 2020;786: 139476.

7 Li Y, Han Q, Horváth I, Zhang G. Repairing surface defects of metal parts by groove machining and wire + arc based filling. *Journal of Materials Processing Technology*. 2019;274: 116268.

8 Thapliyal S. Challenges associated with the wire arc additive manufacturing (WAAM) of aluminum alloys. *Materials Research Express*. 2019;6: 112006.

9 Najmon JC, Raeisi S, Tovar A. Review of additive manufacturing technologies and applications in the aerospace industry. In: *Additive Manufacturing for the Aerospace Industry*. Elsevier Inc.; 2019:7–31.

10 Gardner L, Kyvelou P, Herbert G, Buchanan C. Testing and initial verification of the world's first metal 3D printed bridge. *Journal of Constructional Steel Research*. 2020;172.

11 Mehmanparast A, Taylor J, Brennan F, Tavares I. Experimental investigation of mechanical and fracture properties of offshore wind monopile weldments: SLIC

interlaboratory test results. *Fatigue and Fracture of Engineering Materials and Structures*. 2018;41: 2485–2501.

12 Jacob A, Mehmanparast A, D'Urzo R, Kelleher J. Experimental and numerical investigation of residual stress effects on fatigue crack growth behaviour of S355 steel weldments. *International Journal of Fatigue*. 2019;128: 105196.

13 Anandavijayan S, Mehmanparast A, Braithwaite J, Brennan F, Chahardehi A. Material pre-straining effects on fatigue behaviour of S355 structural steel. *Journal of Constructional Steel Research*. 2021;183: 106707.

14 Zhang X, Martina F, Ding J, Wang X, Williams SW. Fracture toughness and fatigue crack growth rate properties in wire + arc additive manufactured Ti-6Al-4V. *Fatigue and Fracture of Engineering Materials and Structures*. 2017;40: 790–803.

15 Zhang X, Martina F, Syed AK, Wang X, Ding J, Williams SW. Fatigue Crack Growth in Additive Manufactured Titanium: Residual stress control and life evaluation method development. *29 th ICAF Symposium-Nagoya*. 2017: 7–9.

16 Smith TR, Sugar JD, Schoenung JM, San Marchi C. Relationship between manufacturing defects and fatigue properties of additive manufactured austenitic stainless steel. *Materials Science and Engineering A*. 2019;765: 138268.

17 Gordon J, Hochhalter J, Haden C, Harlow DG. Enhancement in fatigue performance of metastable austenitic stainless steel through directed energy deposition additive manufacturing. *Materials and Design*. 2019;168: 107630.

18 Zhang J, Wang X, Paddea S, Zhang X. Fatigue crack propagation behaviour in wire+arc additive manufactured Ti-6Al-4V: Effects of microstructure and residual stress. *Materials & Design*. 2016;90: 551–561.

19 Zhang J, Zhang X, Wang X, et al. Crack path selection at the interface of wrought and wire + arc additive manufactured Ti–6Al–4V. *Materials & Design*. 2016;104: 365–375.

20 Gordon JV., Haden CV., Nied HF, Vinci RP, Harlow DG. Fatigue crack growth anisotropy, texture and residual stress in austenitic steel made by wire and arc additive manufacturing. *Materials Science and Engineering A*. 2018;724: 431–438.

21 Zhang X, Martina F, Syed AK, Ding J. Fatigue Crack Growth in Additive Manufactured Titanium: Residual stress control and life evaluation method development. 2017: 7–9.

22 *ER100S-1 Data Sheet - Pinnacle Alloys*. Washington D.C.

23 *ER100S-G Data Sheet - Bohler Welding*.2014.

24 Ermakova A, Mehmanparast A, Ganguly S. A review of present status and challenges of using additive manufacturing technology for offshore wind applications. *Procedia Structural Integrity*. 2019;17: 29–36.

25 ASTM E647−13. Standard Test Method for Measurement of Fatigue Crack Growth Rates. *American Society for Testing and Materials*. 2014: 1–50.

26 American Society for Testing and Materials. ASTME-1820-11: standard test method for measurement of fracture toughness. *Annual book of ASTM standards*. 2011: 1–55.

27 Ermakova A, Mehmanparast A, Ganguly S, Razavi J, Berto F. Investigation of mechanical and fracture properties of wire and arc additively manufactured low carbon steel components. *Theoretical and Applied Fracture Mechanics*. 2020;109: 102685.

28 Mehmanparast A, Brennan F, Tavares I. Fatigue crack growth rates for offshore wind monopile weldments in air and seawater: SLIC inter-laboratory test results. *Materials & Design*. 2017;114: 494–504.

29 Wang Z, Stoica AD, Ma D, Beese AM. Stress relaxation behavior and mechanisms in Ti-6Al-4V determined via in situ neutron diffraction: Application to additive manufacturing. *Materials Science and Engineering A*. 2017;707: 585–592.

30 Hönnige JR, Colegrove PA, Ahmad B, et al. Residual stress and texture control in Ti-6Al-4V wire + arc additively manufactured intersections by stress relief and rolling. *Materials and Design*. 2018;150: 193–205.

31 Anderson, TL. *Fracture Mechanics: Fundamentals and Application*. 3rd ed. Boca Raton: Taylor & Francis Group; 2005.

32 BS 7910. BSI Standards Publication Guide to methods for assessing the acceptability of flaws in metallic structures. *BSI Standards Publication*. 2015: 490.

33 Jacob A, Oliveira J, Mehmanparast A, Hosseinzadeh F, Kelleher J, Berto F. Residual stress measurements in offshore wind monopile weldments using neutron diffraction technique and contour method. *Theoretical and Applied Fracture Mechanics*. 2018;96: 418–427.

34 Adedipe O, Brennan F, Kolios A. Review of corrosion fatigue in offshore structures: Present status and challenges in the offshore wind sector. *Renewable and Sustainable Energy Reviews*. 2016;61: 141–154.

35 Lotsberg I, Sigurdsson G, Fjeldstad A, Moan T. Probabilistic methods for planning of inspection for fatigue cracks in offshore structures. *Marine Structures*. 2016;46: 167–192.

36 Jacob A, Mehmanparast A. Crack growth direction effects on corrosion-fatigue behaviour of offshore wind turbine steel weldments. *Marine Structures*. 2021;75: 102881.

37 International Standard ISO. Metallic materials - Vickers hardness test - Part 1 : Test method (ISO 6507-1 : 2018). *International Standard*. 2018: 1–49.

38 Practice S. Standard Practice for Microetching Metals and Alloys ASTM E-407. 2016;07: 1–22.

39 Wu B, Pan Z, Ding D, et al. A review of the wire arc additive manufacturing of metals: properties, defects and quality improvement. *Journal of Manufacturing Processes*. 2018;35: 127–139.

40 Javadi Y, MacLeod CN, Pierce SG, et al. Ultrasonic phased array inspection of a Wire + Arc Additive Manufactured (WAAM) sample with intentionally embedded defects. *Additive Manufacturing*. 2019;29: 100806.

41 Derekar KS. A review of wire arc additive manufacturing and advances in wire arc additive manufacturing of aluminium. *Materials Science and Technology (United Kingdom)*. 2018;34: 895–916.

42 Al-Nabulsi Z, Mottram JT, Gillie M, Kourra N, Williams MA. Mechanical and X ray computed tomography characterisation of a WAAM 3D printed steel plate for structural engineering applications. *Construction and Building Materials*. 2021;274: 121700.

43 Xiong J, Zhang G, Zhang W. Forming appearance analysis in multi-layer single-pass GMAW-based additive manufacturing. *International Journal of Advanced Manufacturing Technology*. 2015;80: 1767–1776.

4.3. Conclusion

The research investigated the fatigue crack growth behaviour of WAAM built specimens using ER70S-6 and ER100S-1 materials. From the study on ER70S-6 specimens, it was observed that the specimen extraction location had minimal impact on FCG performance, while different load levels and specimen orientations introduced variations in fatigue life and crack growth rates. The FCG data fell below the recommended trends in the BS7910 standard. Comparisons with HAZ S355 steels showed higher fatigue crack growth rates in WAAM built components.

For ER100S-1 specimens, experiments revealed longer durations for top-extracted specimens, and at higher ΔK values, both top and bottom specimens exhibited similar trends. Specimen orientation influenced FCG trends and scatter, with vertical specimens showing wavy FCG patterns and higher scatter. The mean+2SD FCG lines were found below the recommended FCG trend in BS7910. Fracture surface analysis indicated ductile fracture mechanisms for both horizontal and vertical specimens, with additional cracks in horizontal specimens accelerating FCG rates. Examination of ER100S-1 WAAM specimens confirmed a low level of defects.

Overall, these findings provide valuable insights into the fatigue crack growth behaviour of WAAM built components, on their mechanical performance and fracture mechanisms. These results are crucial for the advancement of WAAM technology in practical applications, particularly in offshore structures, where the FCG performance of these materials is a significant consideration.

Chapter 5 : Corrosion-fatigue Crack Growth Performance of WAAM Steel Components

In this chapter, corrosion-fatigue crack growth characteristics of ER70S-6 and ER100S-1 WAAM built components were examined. The chapter consists of the following papers:

Paper VI: Corrosion-fatigue crack growth behaviour of wire arc additively manufactured ER70S-6 steel parts in marine environments

Paper VII: Corrosion-fatigue crack growth behaviour of wire arc additively manufactured ER100S-1 steel specimens

5.1. Paper VI: Corrosion-fatigue crack growth behaviour of wire arc additively manufactured ER70S-6 steel parts in marine environments

Anna Ermakova[a], Supriyo Ganguly[b], Javad Razavi[c], Filippo Berto[c], Ali Mehmanparast[a*]

[a] Offshore Renewable Energy Engineering Centre, Cranfield University, Cranfield, MK43 0AL, UK

[b] Welding Engineering and Laser Processing Centre, Cranfield University, Cranfield, MK43 0AL, UK

[c] Department of Mechanical and Industrial Engineering, Norwegian University of Science and Technology (NTNU), Trondheim, Norway

Abstract[6]

A crucial part of the structural integrity assessment of marine structures is the analysis of the fatigue crack growth behaviour of the welded joints in seawater environments, where the cracks often initiate and propagate under corrosion-fatigue loading conditions. In recent years, technological developments have facilitated the fabrication of steel components and structures using additive manufacturing technologies. Among the existing technologies, the Wire Arc Additive Manufacturing (WAAM) technique has proven to offer great potentials for fabrication of large-scale structures. The present study investigates the corrosion-fatigue crack growth (CFCG) behaviour of the WAAM parts fabricated using ER70S-6 low carbon steel wire to assess the suitability of this technology for future marine structures. In this experimental study, the cracking behaviour and test duration in corrosion-fatigue tests were investigated and analysed in conjunction with the microstructural examinations on the tested specimens. Moreover, the obtained results were compared with the recommended trends available in BS7910 standard for conventional welded joints and the data available in the literature on widely used offshore structural steel weldments. The CFCG results obtained from this study contribute to the overall knowledge and design requirements for the new optimised functionally graded structures made with WAAM technology for marine applications.

---

[*] corresponding author

[6] *European Journal of Mechanics - A/Solids*. 96 (2022), 104739. (DOI: 10.1016/j.euromechsol.2022.104739)

5.1.1. Introduction

Offshore wind turbine foundations, which are fabricated using conventional welding techniques, experience millions of load cycles during their service life in highly corrosive environments. Therefore, under corrosion-fatigue loading conditions the welded joints in these marine structures are often found to be the potential areas for crack initiation and propagation which can eventually lead to catastrophic failure of the structure[1]. Moreover, the phase changes in metal, induced during the welding process can change the pattern of crack growth mechanisms, introducing crack branching[2]. Some studies on the heat affected zones (HAZ) of welded wrought steels confirm that the fatigue crack growth (FCG) rates strongly depend on the welding procedure, alloy composition, crack growth region, residual stress magnitude and distribution, and service environment[3–6]. These studies suggest that the material selection and fabrication technology have a significant impact on the design life of the marine structures and the fatigue life of these structures can be considerably enhanced by employing more damage tolerant materials and appropriate manufacturing techniques.

Wire arc additive manufacturing (WAAM) technique is a relatively new additive manufacturing (AM) technology that enables the production process by feeding a wire of metal into an electric arc to melt the material on top of the previously deposited layers at a controlled rate. The key advantages of this method compared with widely used powder-based AM methods, are large-scale near net shape parts that can be fabricated at acceptable cost, in reasonable time with deposition rates of several kilograms per hour[7–9]. However, as the WAAM process consists of complex welding thermal cycles, it will lead to microstructural variations and introduce a complex and variably distributed residual stress state. This will have profound influence on the overall mechanical behaviour of a WAAM built part[10,11]. While the employment of the WAAM technique in some industries, such as aerospace, has been widely investigated in recent years, the great potentials that this AM technique offers make it a suitable manufacturing technology for many other industrial sectors such as renewable energy marine structures. In order to investigate the suitability of the WAAM technique for employment in fabrication and repair of renewable energy marine structures, the corrosion-fatigue crack growth (CFCG) behaviour of a WAAM built steel part needs to be accurately characterised and compared to the conventional welded joints. This will provide an insight into the estimation of the remaining lifetime and development of efficient inspection plans for future WAAM built marine structures and components.

The environmental behaviour of low carbon steel ER70S-6 specimens produced by means of WAAM was examined by Ron et al.[12], where general corrosion performance was evaluated by salt spray testing, immersion testing, potentiodynamic polarization analysis, and electrochemical impedance spectroscopy. The stress corrosion performance was also assessed by slow strain testing. The results have shown that the general and stress corrosion resistance of WAAM specimens was similar with the ST-37 steel counterparts. Therefore, it was concluded that the WAAM process does not cause any further deterioration in corrosion performance when compared with the conventional wrought alloy. A similar research study was conducted on austenitic stainless steel WAAM built parts[13], which also showed that electrochemical performance and stress corrosion susceptibility of the parts were similar with the wrought counterparts, despite differences in microstructure and mechanical properties. Moreover, the effect of microstructure imperfections on corrosion-fatigue performance of the

material was evaluated for ER70S-6 WAAM parts in a 3.5% NaCl solution[14]. The results presented a reduction in fatigue strength of WAAM specimens, compared to the wrought ST-37 counterparts, due to porosity, impurities and lack of fusion defects that are imposed during WAAM production process and promote corrosion attacks and consequently stimulate fatigue cracking.

It is evident from previous studies that the WAAM process introduces microstructural variation in additively built parts compared with wrought steel. These changes directly affect the behaviour of WAAM built steel parts, including their corrosion characteristics, hence require additional in-depth studies. Although some limited studies were previously performed on the structural response of the WAAM built parts in corrosive environments, no trends nor comprehensive studies on the CFCG of the WAAM built parts are currently available in the literature. Therefore, the present study focuses on the investigation of the CFCG behaviour of ER70S-6 low carbon steel WAAM built specimens in seawater. Moreover, an experimental sensitivity analysis has been conducted on the corrosion-fatigue response of the material to the build location and cracking orientation. The WAAM strategy adopted in this study, the CFCG test set-up, the crack growth monitoring method employed in this study, data collection process and analysis, and comparison with the existing data in the literature are presented and discussed in the following sections. The results presented in this study demonstrate the possibility of employment of the WAAM process for offshore structures with harsh environmental conditions such as offshore wind, where the structures experience severely high number of cycles in corrosive environments.

5.1.2. Manufacturing set-up and specimen extraction

For this study a WAAM wall was manufactured with Lincoln electric ER70S-6 welding filler wire with the chemical composition specified in Table 5.1, using the Cold Metal Transfer (CMT) process. The fabrication parameters for the WAAM wall are shown in Table 5.2. The full manufacturing set-up and the completed WAAM wall are shown in Figure 5.1. It can be seen in this figure that the set-up comprises of a CMT power source, a robotic arm with the torch that is feeding the wire and supplying the shielding gas at the same time. An exhaust fan was used to remove any fume and cool the wall from the excessive heat generated during the manufacturing process.

The WAAM wall was built on top of a base plate, which was made of EN10025 rolled structural steel, with dimensions of $420 \times 200 \times 12$ mm^3. The deposition was carried out in the middle of the base plate using an oscillation deposition pattern[15,16]. The wall was built with the following dimensions: thickness of 24 mm (Y-axis Figure 5.1 (b)), length of 355 mm (X-axis) and height of 140 mm (Z-axis). The base plate was rigidly fixed on the worktable with eight clamps, to prevent bending and distortions of the base plate due to the increased temperature. The clamps were released once the WAAM wall deposition was completed, and it was cooled down to the ambient temperature.

Table 5.1: Chemical composition of ER70S-6 material (wt.-%)[17]

	C	*Mn*	*Cr*	*Si*	*Ni*	*Mo*	*S*	*P*	*Cu*	*V*
ER70S-6	0.09	<1.60	0.05	0.09	0.05	0.05	0.007	0.007	0.20	0.05

Table 5.2: CMT-WAAM fabrication parameters

Shielding gas	Ar+20% CO_2
Gas flow rate	15 L/min
Wire diameter	1.2 mm
Wire feed speed	7.5 m/min
Robot travelling speed	7.33 mm/sec
Dwell time	120 sec

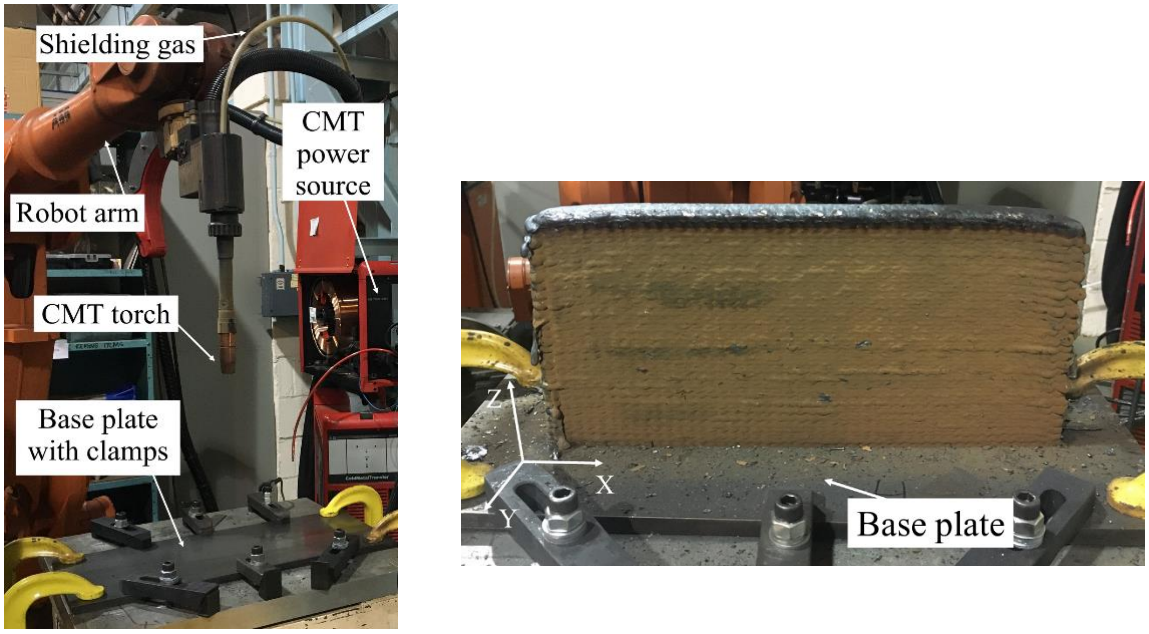

(a) (b)

Figure 5.1: Fabrication process (a) CMT WAAM set-up, (b) completed WAAM wall

Upon completion of the WAAM wall, four notched compact tension, C(T), specimens were extracted using Electrical Discharge Machining (EDM) technique. The specimens were extracted from two locations: top (T) and bottom (B), and in two orientations: vertical (V) – with crack plane perpendicular to the additive layers, and horizontal (H) – with crack plane parallel to deposited layers. These four combinations provided specimens denoted CT-VT, CT-VB, CT-HT and CT-HB as schematically shown in Figure 5.2 (a). The C(T) specimens were designed according to ASTM E647 standard[18] with a width of W = 50 mm, height of H = 60 mm, total thickness of B = 16 mm and initial crack length of a_0 = 17 mm. Knife edges were

machined at the crack mouth of the C(T) specimens following the guidelines in ASTM E1820 standard[19] to accommodate a clip gauge for compliance measurements during fatigue pre-cracking, which is required to introduce an infinitely sharp crack tip ahead of the machined notch prior to CFCG testing. All four specimens were pre-cracked under fatigue loading conditions using the load decreasing approach to approximately 20 mm ($a_{i,p}/W$ = 0.4). It is worth noting that the final value of maximum stress intensity factor K_{max} at the end of pre-cracking did not exceed the initial K_{max} at the beginning of the actual CFCG test. During the main CFCG tests, the crack growth monitoring was performed using the back face strain measurement technique (see Figure 5.2 (b)) the details of which are described in Section 5.1.3.

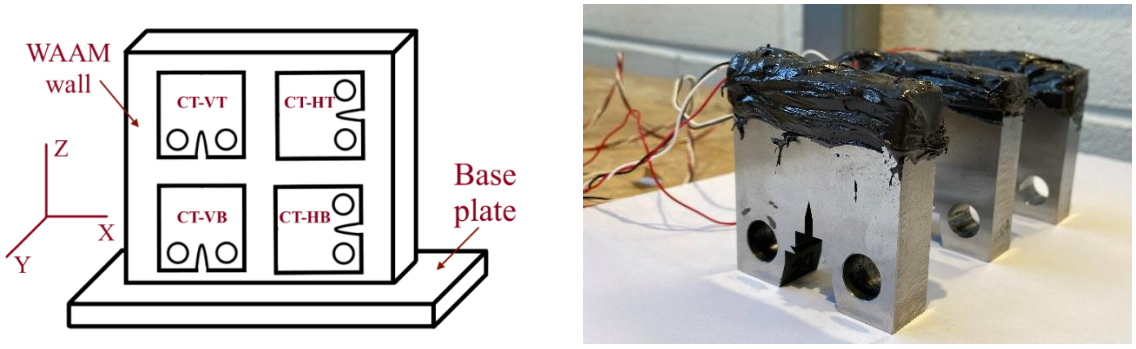

(a) (b)

Figure 5.2: Specimens (a) extraction plan from the WAAM wall, (b) in protective coating after strain gauging

5.1.3. Corrosion-fatigue crack growth test set-up and data analysis

- **Test set-up**

CFCG tests were performed on C(T) specimens under load-controlled mode using a 100 kN servo hydraulic Instron machine. The sinusoidal cyclic load was applied under a constant amplitude with the maximum load of P_{max} = 10 kN, the load ratio of R = 0.1, and frequency of f = 0.3 Hz, which is the typical frequency used in corrosion-fatigue analysis for offshore structures[20,21]. To simulate free-corrosion conditions for the tests, 60 L of artificial seawater was prepared according to ASTM D1141-98[22], using deionised water and chemicals shown in Table 5.3. The pH level of seawater was maintained at 8.0-8.2 during the tests, and once it dropped below 8.0 the seawater was subsequently replaced. The full CFCG test set-up is shown in Figure 5.3 (a). The test specimen was placed in an environmental water chamber that was attached onto the machine, with the area of interest within the crack path immersed in seawater throughout the test (Figure 5.3 (b)). The created artificial seawater stored in a tank was running through the water chamber using pumps at a continuous rate of 4 L/min to create a circulation of simulated seawater during the test. The seawater temperature was controlled using a chiller and varied between 8.0 and 10.0°C to replicate the operation conditions in the North Sea.

Table 5.3: Chemical composition of artificial seawater[22]

Chemical compound	Concentration (g/L)
$NaCl$	24.53
$MgCl_2$	5.20
Na_2SO_4	4.09
$CaCl_2$	1.16
KCl	0.695
$NaHCO_3$	0.201
KBr	1.101
H_3BO_3	0.027
$SrCl_2$	0.025
NaF	0.003

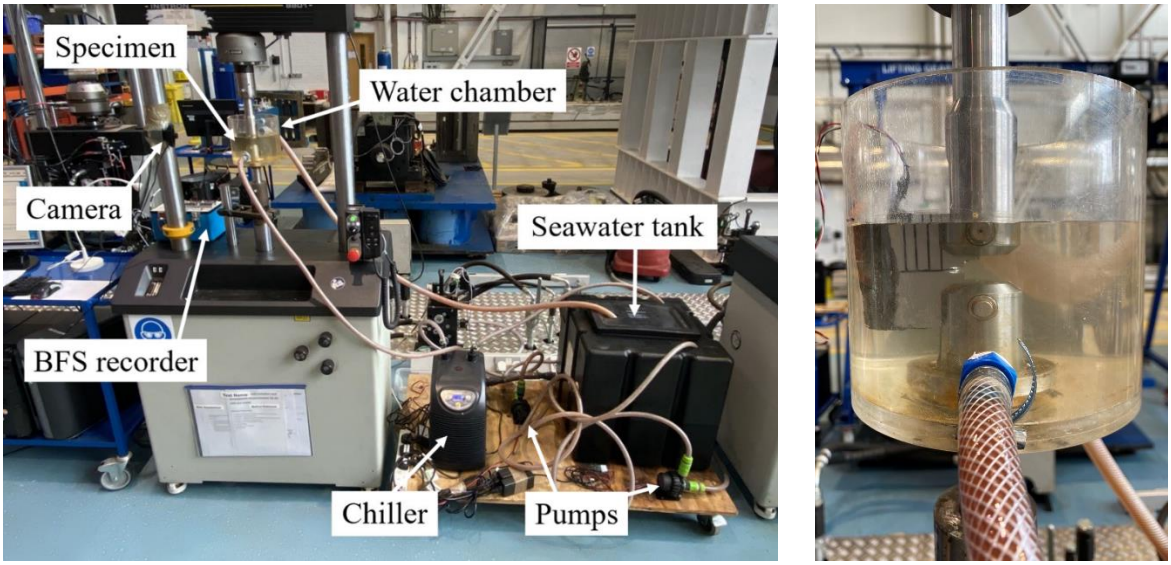

(a) (b)

Figure 5.3: CFCG test (a) full set-up, (b) specimen in the water chamber

- **Crack growth monitoring methods**

An efficient crack growth monitoring technique that is suitable for corrosion-fatigue tests, where the specimen is soaked in seawater with limited direct access to it, is the back face strain (BFS) method[23,24]. The main idea in this approach, which is originally designed for CFCG testing on C(T) specimens, is to correlate the BFS variations with the crack length. These empirical correlations, which are generally referred to as BFS calibration curves, are initially developed in air for a given loading condition and then used in CFCG tests in seawater to estimate the instantaneous crack length throughout the test using the collected BFS data. The BFS values are recorded from the strain gauge attached to the back of the C(T) specimens at the mid-height and mid-width. The basis of this approach is similar to the compliance measurement technique in FCG tests in air where the instantaneous crack length is estimated using the crack mouth displacement data. Therefore, for a given material, specimen geometry and testing condition, the BFS and crack mouth displacement (hence compliance) data are directly correlated, and the instantaneous crack length can be estimated using the data which

can be collected from the test depending on the access limitations to the test specimen (i.e. immersed specimen in seawater).

After attaching strain gauges onto the C(T) specimens in the present study, a polysulfide coating was applied to protect the specimens against seawater damage (Figure 5.2 (b)) and then the specimens were soaked in seawater for approximately 24 hours prior to testing, as recommended by ASTM D1141[22]. The BFS values from the strain gauge attached to the back of the specimen were recorded with a strain recorder every second and the maximum magnitude of compressive strain values were captured with a camera every minute (Figure 5.3 (a)). Prior to CFCG testing, four calibration tests were performed in air on C(T) specimens with the same dimensions and extraction orientations/locations (VT, HT, VB, HB), under loading conditions presented in Table 5.4, to generate empirical BFS calibration curves for each of the four ER70S-6 WAAM specimens. It can be noted here, that due to dependency of BFS calibration curves on the load level, the applied loads for the calibration tests in air and CFCG tests in seawater were the same. The tests in air were conducted using a clip gauge attached to the knife edges at the crack mouth of the C(T) specimens for instantaneous crack length measurements, which were then correlated with the maximum magnitude of compressive BFS value (hence maximum crack mouth opening). Four calibration curves were derived by applying cubic polynomial lines of best fit to the data and then used to correlate the BFS recordings from seawater tests with the estimated instantaneous crack lengths for each case.

Moreover, beach markings (BM) were carried out at different intervals throughout the tests to cross-check the accuracy of the estimated crack length from the BFS technique[25]. In this method, the maximum cyclic fatigue load and frequency are decreased for a limited period of time to introduce thin marks on the fracture surface, so called beach marks. By recording the BFS value at which the beach marking process was applied, the estimated crack lengths can be verified through comparison with the experimentally measured crack length on the fracture surface subsequent to completion of the test. In order to apply the BM in these tests, the loading conditions were changed to P_{max} = 8 kN with the load ratio of R = 0.125 and frequency of f = 0.1 Hz for one hour to perform beach marking in the absence of noticeable crack growth (this was confirmed by ensuring that the BFS values remained constant during beach marking procedure). For each CFCG test, this process was performed three times to introduce multiple BM data for further validation of the calibration curves. The BM approach was initially employed in BFS calibration tests in air on nominally identical C(T) specimens to verify the accuracy of crack length estimations, the results and loading conditions of which are presented in Figure 5.4 and Table 5.4, respectively. For the CFGC tests in seawater, to make beach marks more visible and keep them at sufficient distance from each other, every specimen was marked prior to testing, dividing the required 15 mm of the crack length into three regions (5 mm each) as shown in Figure 5.3(b). Crack length was visually inspected throughout the test and when it was approximately in the middle of each marked region, BM was employed. The CFCG tests were terminated once the crack length reached 15 mm ($a_{f,c}/W$ = 0.7).

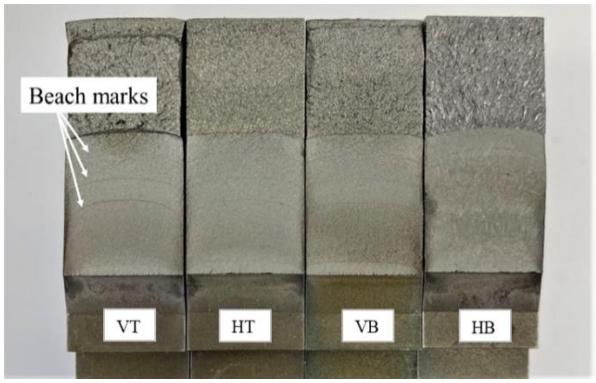

Figure 5.4: The beach marks on fracture surface of WAAM ER70S-6 C(T) specimens tested in air

Table 5.4: Beach marking loading conditions for the tests in air and seawater

Test environment	The main test condition			Beach marking loading condition		
	P_{max} (kN)	R	f (Hz)	P_{max} (kN)	R	f (Hz)
Air	10	0.1	5	8	0.125	3
Seawater	10	0.1	0.3	8	0.125	0.1

After completion of the CFCG tests, all four C(T) specimens were broken open to measure the actual crack lengths on the fracture surface and verify the accuracy of the estimated crack lengths from the BFS data. In order to break open the specimens post-testing, the specimens were initially soaked in liquid nitrogen for 5 minutes to induce brittleness in the specimens (thereby minimising any deformation during the breaking process) and then pulled in tension using a servo hydraulic Instron machine. The fracture surfaces of all four CFCG specimens are displayed in Figure 5.5. It is worth noting here that due to the corroded fracture surface the beach marks were not very clear (see Figure 5.5) compared with the specimens tested in air (see Figure 5.4), so some level of error in measurements might be expected when the beach marks are measured in corrosion-fatigue test specimens. In Figure 5.5, three distinct areas corresponding to different stages of the test can be clearly identified on the fracture surfaces: (1) fatigue pre-cracking, (2) fatigue crack growth, and (3) fast fracture (i.e., specimen fracture opening). Also, from Figure 5.5 it can be concluded that the crack propagation regions are symmetric in all four C(T) specimens, indicating good alignment during the CFCG tests. An example of the calibration curve for CT-HB specimen tested in seawater, plotted using the empirical correlation from the air test, is shown in Figure 5.6. It can be seen in Figure 5.6 that the calibration curve and beach marking results are in good agreement, hence the estimated crack lengths using the BFS data are fairly reliable.

(a) (b) (c) (d)

Figure 5.5: Fracture surface of WAAM built ER70S-6 specimens after CFCG test (a) CT-VT, (b) CT-VB, (c) CT-HT, (d) CT-HB (each division on the scale bars indicates a distance of 1 mm)

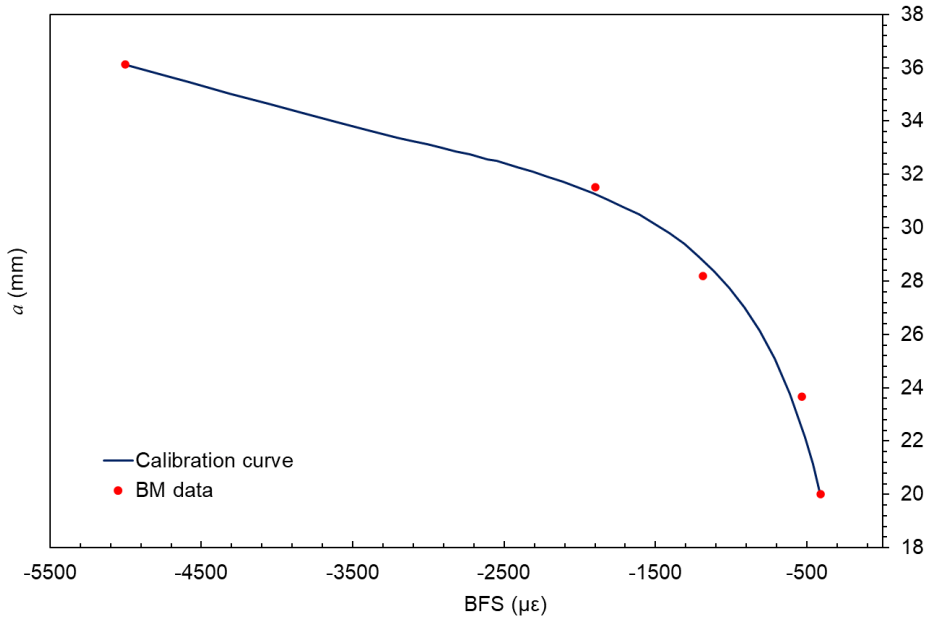

Figure 5.6: Crack length vs. BFS values for CT-HB specimen tested in seawater, and the comparison with the beach marking data

- **Data analysis**

The CFCG rate, *da/dN*, was calculated using the estimated crack lengths and the number of cycles, using the secant method for the first and the last three data points, and seven-point incremental polynomial technique for the rest of the data points. The stress intensity factor (SIF) was determined using the shape function equation developed by Mehmanparast et al.[26], Equation 5.1, that offers accurate solutions for a wider range of crack length in a C(T) specimen, $0.2 \leq a/W \leq 0.7$, compared with the original shape function equation available in ASTM E647 standard. In the SIF calculation shown in Equation 5.1, α is the normalised crack length a/W and ΔP is the load range which is defined as the difference between the maximum load P_{max} and the minimum load P_{min}.

$$\Delta K = \frac{\Delta P}{BW} \cdot \sqrt{a} \cdot (-372.12\alpha^6 + 1628.60\alpha^5 - 2107.46\alpha^4 + 1304.65\alpha^3 - 391.20\alpha^2 + 54.81\alpha + 7.57)$$ Equation 5.1

5.1.4. Test results and discussion

The estimated crack lengths for each tested specimen were plotted against the number of cycles and the results are shown in Figure 5.7. It can be observed in this figure that the longest fatigue life (i.e. largest number of cycles) was experienced in the vertical specimen that was extracted from top of the WAAM wall CT-VT. Figure 5.7 shows that this specimen endured approximately 1.5-1.7 times more cycles to reach 15 mm of crack extension compared to other specimen locations/orientations. Another observation that can be made from this figure is that the test durations for the two specimens extracted from the top of the wall, regardless of their orientation, is the longest compared to the specimens from the bottom of the wall. The longer fatigue life in the specimens extracted from the top of the WAAM wall would have been caused by the microstructural variations caused by different thermal effects and presumably the residual stresses induced during WAAM fabrication process which are expected to have higher magnitudes of compressive residual stress in the bottom layers compared to the top layers due to the greater number of repeated thermal cycles. The two specimens extracted from the bottom part of the WAAM wall show similar results with the average number of cycles of around 49,000 to reach 15 mm of crack extension. Comparison of CFCG behaviour of ER70S-6 WAAM walls with the FCG test results in air conducted in a previous study by Ermakova et al[27] shows that whilst the fatigue life is more dependent on the orientation of the specimens in air tests, for seawater tests the extraction location has a more pronounced effect on the fatigue life of the test specimens. These observations indicate that the fatigue test duration of ER70S-6 WAAM built specimens strongly depends on the test environment.

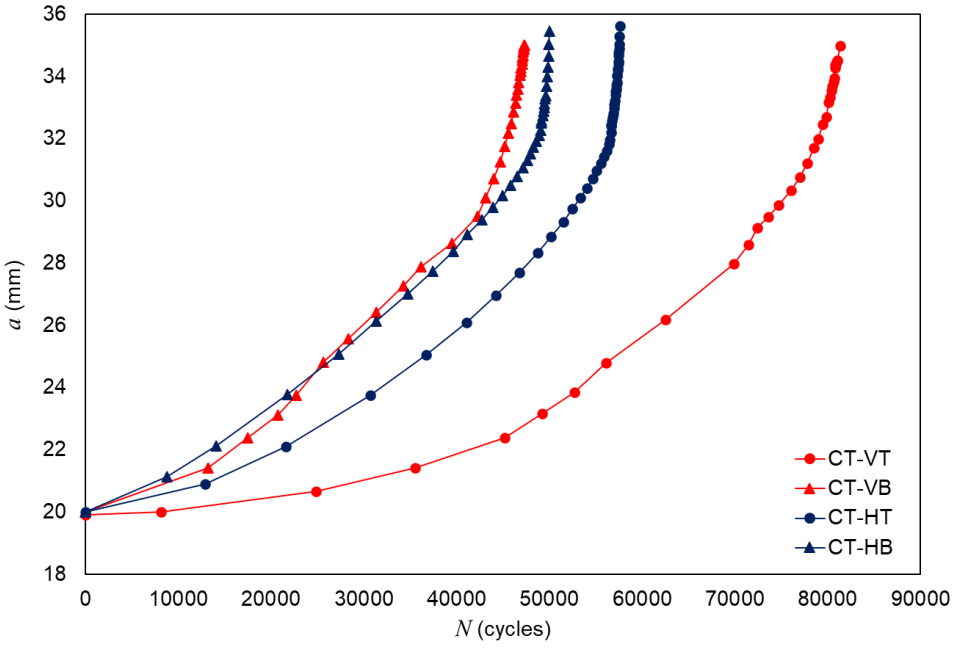

Figure 5.7: Corrosion-fatigue crack growth trends in ER70S-6 WAAM built specimens

The CFCG rates, *da/dN*, for all C(T) specimens have been then correlated with the linear elastic fracture mechanic parameter, *ΔK*, and the results are displayed in Figure 5.8. This figure illustrates the typical environmental crack growth behaviour, where the crack growth rate, *da/dN*, is highly sensitive to the applied *K* in Stage I and Stage III. It can be observed in this figure that while in Stage II the crack growth rate increases with an increase in *ΔK*, the slope of the *da/dN* versus *ΔK* curve in this stage is much lower than in Stage I and III. Moreover, it can be seen that the slope of CT-VB specimen in Stage II is almost insensitive to the applied *ΔK* and the *da/dN* for this specimen is almost constant in Stage II. Further observed in Figure 5.8 is that in Stage I and II, the CFCG data for the same specimen extraction locations (Top or Bottom) fall close to each other within the inherent experimental scatter; however, towards the end of the test (i.e. in Stage III) the vertical specimens have noticeably lower crack growth rates than the horizontal specimens, regardless of their extraction locations. It is worth noting here that the lowest CFCG rates in Stage I and III are obtained from the vertical specimen extracted from the top of the wall, CT-VT; however, in Stage II, all four datasets fall close to each other with the specimens with the same extraction locations falling almost upon each other. Comparison of the CFCG results in seawater from the present study with the results from the air tests reported by Ermakova et al[27] shows that under similar loading conditions the specimen orientation has a higher impact on the crack growth behaviour of the material in the air tests, with vertical specimens presenting higher trends throughout the test than the horizontal specimens. Whereas in seawater environment the crack growth behaviour changes depending on the stage of the test. Since only four CFCG specimens were tested in this study, with four different combinations of extraction locations and orientations, further tests must be conducted in future work to confirm the provisional trends presented in this study and evaluate the level of scatter for each specimen. Moreover, the residual stresses need to be measured to evaluate their effects on the crack growth behaviour for each specimen location/orientation.

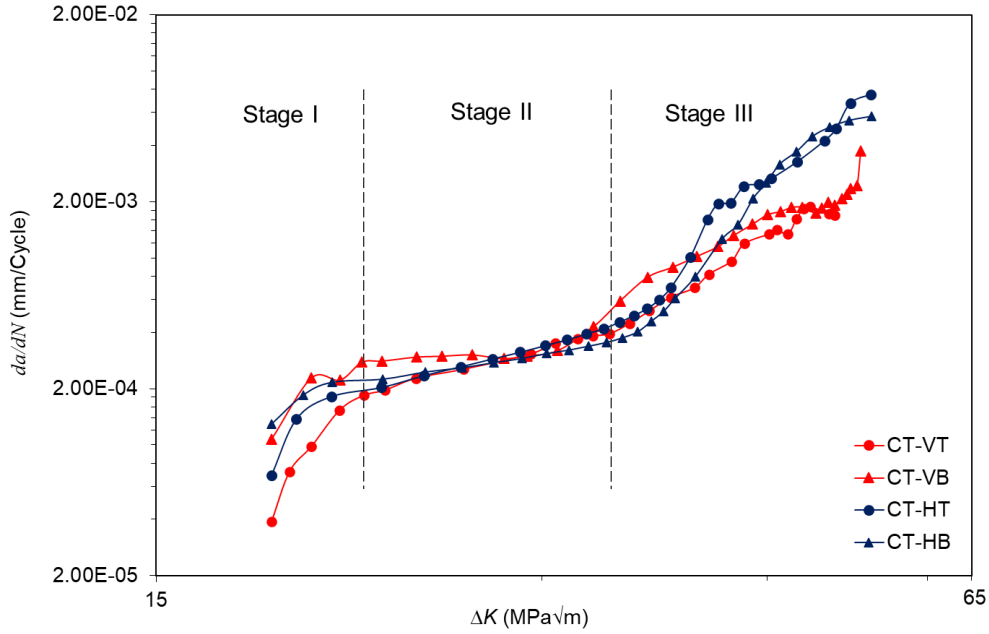

Figure 5.8: Corrosion-fatigue crack growth rates for ER70S-6 WAAM built specimens

Further analysis was carried out on Stage II (Paris region) data points obtained from all four tests, and the material constants *C* and *m* (see Equation 5.2) were determined for each dataset

by plotting the line of best fit and extracting the power-law constants. The Paris law constants obtained from each data set are summarised in Table 5.5. In addition to *C* and *m* constants, the values of the coefficient of determination, R^2, were also calculated to examine how accurately the lines of best fit describe the material behaviour. As seen in Table 5.5 the R^2 values for all tests are close to 1 except CT-VB specimen where the crack growth rate is almost constant during Stage II (see Figure 5.8).

$$da/dN = C\Delta K^m \qquad \text{Equation 5.2}$$

Table 5.5: Paris law constants obtained from the CFCG tests performed on ER70S-6 WAAM built specimens (*da/dN* in mm/Cycle and *ΔK* in MPa$\sqrt{m}$)

Specimen ID	Orientation	Location	P_{max} (kN)	*C*	*m*	R^2
CT-VT	Vertical	Top	10	7.85×10^{-7}	1.77	0.994
CT-VB	Vertical	Bottom	10	1.13×10^{-4}	0.296	0.679
CT-HT	Horizontal	Top	10	5.89×10^{-7}	1.87	0.993
CT-HB	Horizontal	Bottom	10	5.15×10^{-6}	1.21	0.983

Additionally, the Paris law constants were obtained for specimens with the same extraction location (top or bottom) and the results are shown in Figure 5.9 and Table 5.6. With closer look in Figure 5.9, a difference in slopes for Set-T (all specimens extracted from the top of the wall) and Set-B (all specimens extracted from the bottom of the wall) can be observed, where Set-B is less sensitive to the applied *ΔK*. Also, Set-B has higher level of scatter between two sets of data, which is confirmed by R^2 values from the table. The level of scatter was further analysed by calculating the upper bound trends for two location datasets, based on +2 standard deviation (SD), the material constants for which were added into Table 5.6.

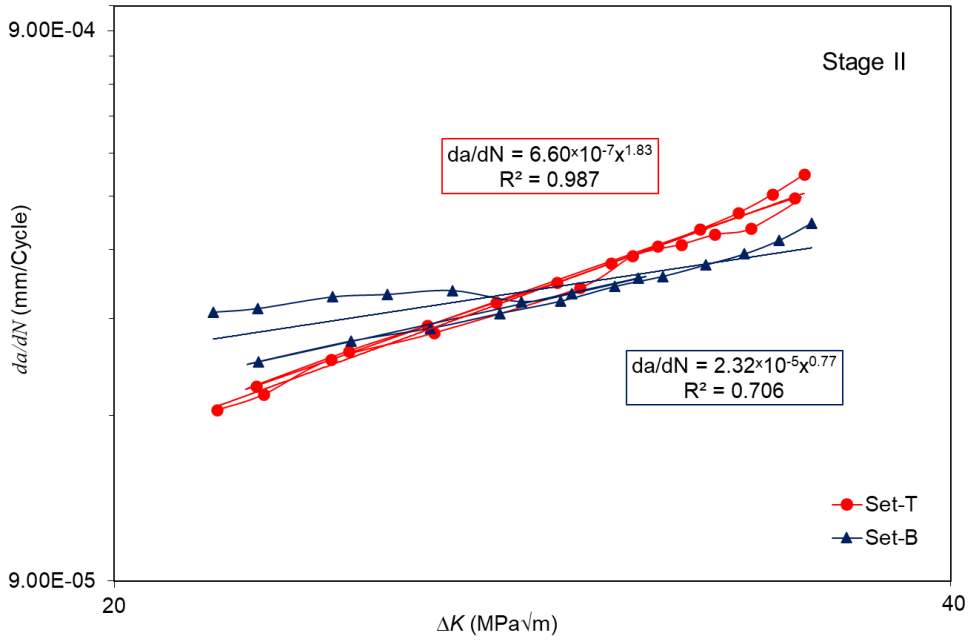

Figure 5.9: Lines of best fit made to the CFCG data in Stage II region for different specimen locations (Set-T for top specimens and Set-B for bottom specimens)

Table 5.6: Power law constants for the mean curves and upper bound trends in Stage II region for different specimen location datasets

Datasets	Location	P_{max} (kN)	Mean			Mean + 2SD	
			C	m	R^2	C	m
Set-T	Top	10	6.60×10^{-7}	1.83	0.987	7.06×10^{-7}	1.83
Set-B	Bottom	10	2.32×10^{-5}	0.77	0.706	2.71×10^{-5}	0.77

The mean + 2SD lines for two datasets of top and bottom specimens are plotted in Figure 5.10, along with the BS7910 recommended upper bound trends for welded joints tested in seawater[28], based on the simplified law and the 2-stage law. It can be seen from this figure that both upper bound lines describing the behaviour of tested specimens fall below the BS7910 recommended lines, indicating that the CFCG rates of WAAM ER70S-6 components can be conservatively predicted by the recommended trends in the standard.

Moreover, the CFCG rates obtained in this study have been compared with the experimental data available on welded steel specimens tested in seawater, such as: S355G10+M structural steel C(T) specimens extracted from the heat affected zone (HAZ)[29], S355G8+M steel C(T) specimens extracted from HAZ and base metal[1], S355J2+N steel C(T) specimens extracted from HAZ[2] and weld areas and X70 pipeline steel specimens[30]. All tests were carried out under similar loading conditions as summarised in Table 5.4 and are presented in Figure 5.10. Comparison of all experimental curves shows that the upper bound lines obtained from this study for WAAM ER70S-6 specimens fall slightly above the experimental trends for

S355G10+M, S355G8+M and S355J2+N HAZ specimens; however, they are below the curve for X70. The slope for ER70S-6 Set-T specimens replicates the slopes for curves representing the behaviour of S355G10+M HAZ specimens. Since S355G10+M, S355G8+M and S355J2+N steels are widely used in fabrication of offshore structures, which are subjected to severe cyclic loads in harsh marine environments, the comparison from the Figure 5.10 confirms that the WAAM technology and ER70S-6 steels can be potentially considered for fabrication of offshore structures, even though its corrosion-fatigue cracking resistance is slightly less than S355 welded steels, but the crack growth rates are still below the recommended CFCG trends provided in BS7910 standard. In addition to the fracture mechanics studies performed in this study, S-N fatigue tests will also need to be conducted in future work to assess the design requirements of WAAM built components for operation under cyclic loading marine conditions. Further comparison of the test duration from this study to four tests on S355G10+M HAZ specimens performed by Jacob et al.[29] shows that on average it takes three times longer to propagate the crack to 15 mm in WAAM ER70S-6 specimens than in the wrought counterparts.

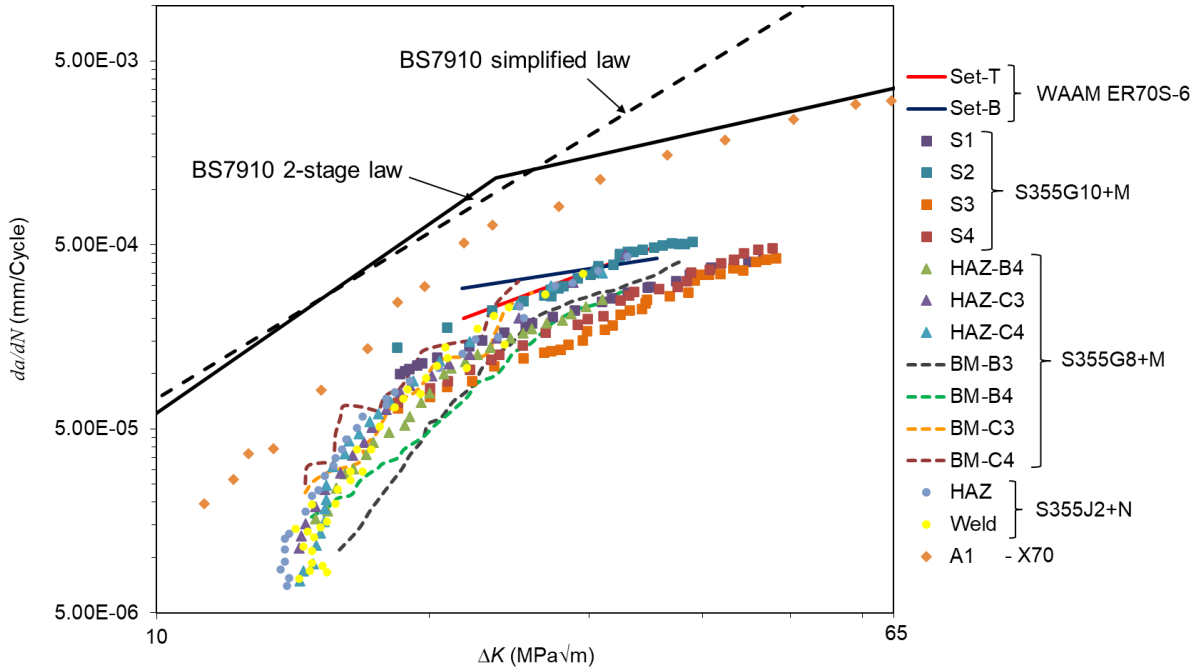

Figure 5.10: Comparison of the upper bound CFCG trends for ER70S-6 WAAM specimens with BS7910 curves and the literature data on structural steels

5.1.5. Microstructural examinations

Due to the severe level of corrosion developed on the fracture surface of the specimens during the CFCG tests (see Figure 5.5), microscopical examination of fracture mechanisms was not possible for the specimens tested in this study. However, a thin slice of approximately 1.5 mm thickness was removed from the fracture surface using EDM technique to examine the microstructure of each specimen underneath the fracture surface. Each specimen slice was prepared for microstructural analysis according to ASTM E407-07 standard[31] by hot-mounting

in a mould, followed by grinding, polishing and finally etching using 2% Nital solution for 10 seconds. Then the microstructures of the specimens in the areas corresponding to the middle of Paris regions were examined using a HIROX RH-2000 digital microscope, and the results are presented in Figure 5.11. These figures reveal a typical microstructure for low carbon steel that consists of a ferrite matrix and reduced amount of a secondary pearlite phase due to low amount of carbon in metal composition (Table 5.1) and rapid solidification process of WAAM. Similar results were presented in several research studies by Ron et al [12,14]. Comparison of the micrographs for four specimens in Figure 5.11 shows that no distinct difference can be observed in the grain structure of the specimens tested in this study.

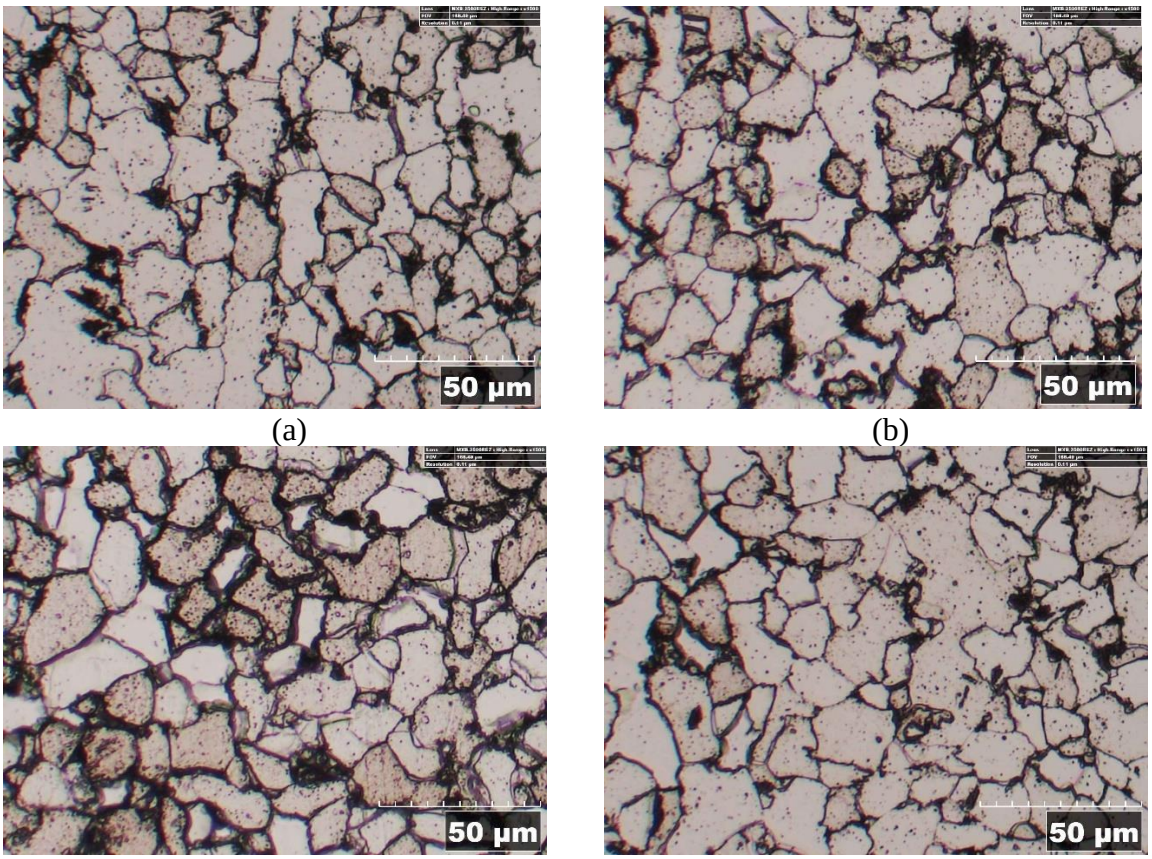

(a) (b) (c) (d)

Figure 5.11: Typical microstructures of ER70S-6 WAAM specimens in the middle of Paris region: (a) CT-VT, (b) CT-VB, (c) CT-HT, and (d) CT-HB.

The general microstructure, at lower magnification, for vertical and horizontal specimens captured from the extracted slice underneath the fracture surface is shown in Figure 5.12. As seen in this figure, the microstructure of the horizontal specimens with the crack path located within a single deposited layer is relatively uniform as expected (Figure 5.12 (b)) compared to the non-uniform grain structure of the vertical specimens with multiple deposited layers (Figure 5.12 (a)), where clear boundaries can be observed between AM layers. It can be clearly seen in Figure 5.12 (a) that a grain size variation is present along the crack path which can subsequently influence the cracking behaviour of the vertical specimens. It was previously reported that the grain refinement, shown in vertical specimens, can result in toughness improvement and hence the material can be expected to have higher cracking resistance through the weld region, affecting the crack growth rates in that region[2].

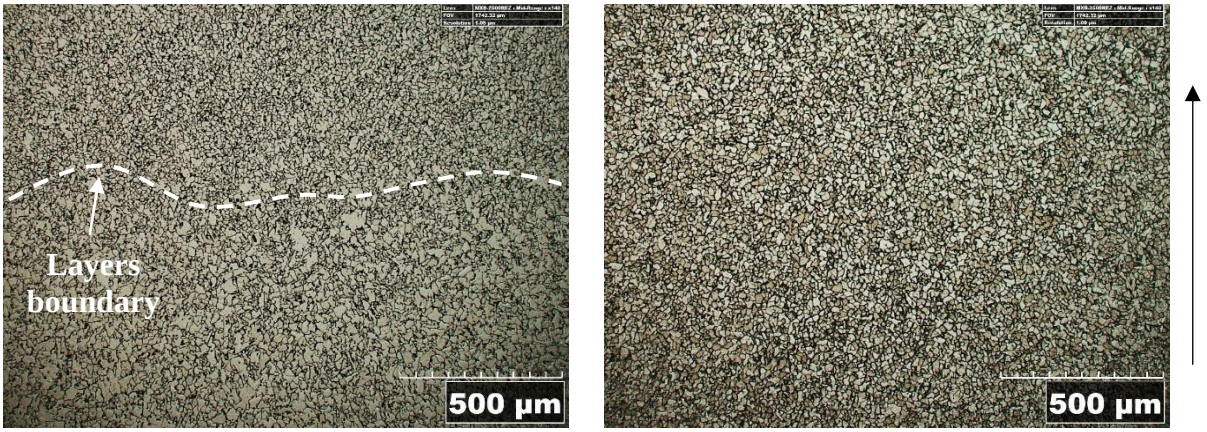

(a) (b)

Figure 5.12: Comparison of the microstructures for (a) vertical and (b) horizontal specimens (arrow on the right indicates the crack growth direction)

5.1.6. Conclusions

Corrosion-fatigue crack growth tests were carried out in artificial seawater on standard C(T) specimens extracted from WAAM built walls made with ER70S-6 wire low carbon steel. All tests were conducted at load level of P_{max} =10 kN, with R = 0.1, and frequency of 0.3 Hz. The following observations and conclusions can be made from this study:

- The specimen extraction location with respect to the WAAM wall affects the duration of the test and the CFCG rates particularly in Stages I and II. The specimens extracted from the top of the WAAM wall required on average 1.4 times more cycles to reach 15 mm of crack extension compared to those from the bottom of the wall.
- The orientation of the extracted specimens may have minor effects on the CFCG rates towards the end of the test in Stage III.
- The lowest CFCG rates in Stage I and III were exhibited in the vertical C(T) extracted from the top of the wall while in Stage II all four results fall close to each other.
- The mean + 2SD lines for top and bottom specimen datasets fall below the BS7910 recommended fatigue crack growth trends, slightly higher than S355G8+M and S355G10+M HAZ data sets but below X70.
- The ER70S-6 WAAM built specimens require on average three times greater number of cycles to propagate the crack to 15 mm compared to the wrought counterparts extracted from S355G10+M HAZ steel.
- Further tests need to be examined in future work to evaluate the level of scatter in the data. Moreover, the influence of the residual stresses in C(T) specimens on the CFCG behaviour of the WAAM built specimens need to be considered and analysed in future work.

5.1.7. Acknowledgments

This work was supported by grant EP/L016303/1 for Cranfield, Oxford and Strathclyde Universities' Centre for Doctoral Training in Renewable Energy Marine Structures – REMS

CDT (http://www.rems-cdt.ac.uk/) from the UK Engineering and Physical Sciences Research Council (EPSRC).

5.1.8. References for paper VI

1. Mehmanparast, A., Brennan, F. & Tavares, I. Fatigue crack growth rates for offshore wind monopile weldments in air and seawater: SLIC inter-laboratory test results. *Materials and Design* **114**, 494–504 (2017).

2. Adedipe, O., Brennan, F., Mehmanparast, A., Kolios, A. & Tavares, I. Corrosion fatigue crack growth mechanisms in offshore monopile steel weldments. *Fatigue and Fracture of Engineering Materials and Structures* **40**, 1868–1881 (2017).

3. Burnside, O. H., Hudak, S. J., Jr., Oelkers, E., Chan, K. & Dexter, R. J. Long-Term Corrosion Fatigue of Welded Marine Steels. (1984).

4. Adedipe, O., Brennan, F. & Kolios, A. Review of corrosion fatigue in offshore structures: Present status and challenges in the offshore wind sector. *Renewable and Sustainable Energy Reviews* **61**, 141–154 (2016).

5. Fatigue behaviour of high-strength steel-welded joints in offshore and marine systems (FATHOMS) - Publications Office of the EU. https://op.europa.eu/en/publication-detail/-/publication/52679314-1c6d-41d6-9d70-19711b29427f.

6. Bertini, L. Influence of seawater and residual stresses on fatigue crack growth in CMn steel weld joints. *Theoretical and Applied Fracture Mechanics* **16**, 135–144 (1991).

7. Zhang, X., Martina, F., Syed, A. K. & Ding, J. Fatigue Crack Growth in Additive Manufactured Titanium: Residual stress control and life evaluation method development. 7–9 (2017) doi:10.13140/RG.2.2.29032.16643.

8. Martina, F., Mehnen, J., Williams, S. W., Colegrove, P. & Wang, F. Investigation of the benefits of plasma deposition for the additive layer manufacture of Ti–6Al–4V. *Journal of Materials Processing Technology* **212**, 1377–1386 (2012).

9. Williams, S., W. Martina, F., Addison, A. C., Ding, J., Pardal, G., and Colegrove, P. Wire + Arc Additive Manufacturing. *Materials Science and Technology* **32**, 641–647 (2015).

10. Liljedahl, C. D. M., Brouard, J., Zanellato, O., Lin, J., Tan, M.L., Ganguly, S., Irving, P.E., Fitzpatrick, M.E., Zhang, X., and Edwards, L. Weld residual stress effects on fatigue crack growth behaviour of aluminium alloy 2024-T351. *International Journal of Fatigue* **31**, 1081–1088 (2009).

11. Xu, X., Ganguly, S., Ding, J., Guo, S., Williams, S., and Martina, F. Microstructural evolution and mechanical properties of maraging steel produced by wire + arc additive manufacture process. *Materials Characterization* **143**, 152–162 (2018).

12. Ron, T., Levy, G. K., Dolev, O., Leon, A., Shirizly, A., and Aghion, E. Environmental behavior of low carbon steel produced by a wire arc additive manufacturing process. *Metals* **9**, (2019).

13. Ron, T., Dolev, O., Leon, A., Shirizly, A. & Aghion, E. Effect of phase transformation on stress corrosion behavior of additively manufactured austenitic stainless steel produced by directed energy deposition. *Materials* **14**, 1–12 (2021).

14. Ron, T., Levy, G. K., Dolev, O., Leon, A., Shirizly, A., and Aghion, E. The effect of microstructural imperfections on corrosion fatigue of additively manufactured ER70S-6 alloy produced by wire arc deposition. *Metals* **10**, (2020).

15. Ermakova, A., Mehmanparast, A., Ganguly, S., Razavi, J. & Berto, F. Investigation of mechanical and fracture properties of wire and arc additively manufactured low carbon steel components. *Theoretical and Applied Fracture Mechanics* **109**, 102685 (2020).

16. Ermakova, A., Mehmanparast, A. & Ganguly, S. A review of present status and challenges of using additive manufacturing technology for offshore wind applications. *Procedia Structural Integrity* **17**, 29–36 (2019).

17. Lincoln Electric Company, T. *LINCOLN ® ER70S-6 WELDING POSITIONS TYPICAL APPLICATIONS*. www.lincolnelectric.com.

18. ASTM E647−13. Standard Test Method for Measurement of Fatigue Crack Growth Rates. *American Society for Testing and Materials* 1–50 (2014) doi:10.1520/E0647-15E01.2.

19. American Society for Testing and Materials. ASTME-1820-11: standard test method for measurement of fracture toughness. *Annual book of ASTM standards* 1–55 (2011) doi:10.1520/E1820-18.

20. Henderson, A. Hydrodynamic Loading of Offshore Wind Turbines. (2003).

21. Jacob, A., Mehmanparast, A., D'Urzo, R. & Kelleher, J. Experimental and numerical investigation of residual stress effects on fatigue crack growth behaviour of S355 steel weldments. *International Journal of Fatigue* **128**, 105196 (2019).

22. International, A. D1141-98 Standard Practice for the Preparation of Substitute Ocean Water. *ASTM International* **98**, 1–3 (2013).

23. Adedipe, O., Brennan, F. & Kolios, A. Corrosion fatigue load frequency sensitivity analysis. *Marine Structures* **42**, 115–136 (2015).

24. Newman, J. C., Yamada, Y. & James, M. A. Back-face strain compliance relation for compact specimens for wide range in crack lengths. *Engineering Fracture Mechanics* **78**, 2707–2711 (2011).

25. Hou, C. Y. Fatigue analysis of welded joints with the aid of real three-dimensional weld toe geometry. *International Journal of Fatigue* **29**, 772–785 (2007).

26. Mehmanparast, A., Taylor, J., Brennan, F. & Tavares, I. Experimental investigation of mechanical and fracture properties of offshore wind monopile weldments: SLIC interlaboratory test results. *Fatigue and Fracture of Engineering Materials and Structures* **41**, 2485–2501 (2018).

27. Ermakova, A., Mehmanparast, A., Ganguly, S., Razavi, J. & Berto, F. Fatigue crack growth behaviour of wire and arc additively manufactured ER70S-6 low carbon steel

components. *International Journal of Fracture* (2021) doi:10.1007/s10704-021-00545-8.

28. BS 7910. BSI Standards Publication Guide to methods for assessing the acceptability of flaws in metallic structures. *BSI Standards Publication* 490 (2015).

29. Jacob, A. & Mehmanparast, A. Crack growth direction effects on corrosion-fatigue behaviour of offshore wind turbine steel weldments. *Marine Structures* **75**, 102881 (2021).

30. Vosikovsky, O. Effects of Stress Ratio on Fatigue Crack Growth Rates in X70 Pipeline Steel in Air and Saltwater. *Journal of Testing and Evaluation, JTEVA* **8**, (1980).

31. Practice, S. Standard Practice for Microetching Metals and Alloys ASTM E-407. **07**, 1–22 (2016).

5.2. Paper VII: Corrosion-fatigue crack growth behaviour of wire arc additively manufactured ER100S-1 steel specimens

Anna Ermakova[a], Supriyo Ganguly[b], Javad Razavi[c], Filippo Berto[c], Ali Mehmanparast[a*]

[a] Department of Naval Architecture, Ocean and Marine Engineering, University of Strathclyde, Glasgow G1 1XQ, United Kingdom

[b] Welding Engineering and Laser Processing Centre, Cranfield University, Cranfield, MK43 0AL, UK

[c] Norwegian University of Science and Technology (NTNU), Trondheim, Norway

Abstract[7]

Crack initiation and propagation in welded joints is one of the main failure mechanisms in offshore structures which operate in harsh marine environment under severe cyclic loading conditions. As an essential part of the design and structural integrity assessment of such joints, corrosion-fatigue crack growth needs to be characterised and accounted for. The wire arc additive manufacturing (WAAM) technology is a promising fabrication technique which has been proven to have many advantages for producing large structures; however, the fatigue and corrosion-fatigue performance of WAAM steel components for application in the marine environments is still unexplored. In this study, the WAAM technique was employed to fabricate four specimens made of ER100S-1 low carbon steel, which were then tested under cyclic loading conditions in seawater to assess the corrosion-fatigue crack growth (CFCG) behaviour and hence suitability of this fabrication technology for offshore renewable energy applications. The test duration, cracking mechanisms and CFCG rate were investigated for each specimen and the material's behaviour was investigated by considering the microstructural examinations. Furthermore, the obtained results were compared with the BS7910 standard recommended trends and experimental data available in the literature for conventionally built weldments made of different grades of steel which are commonly used for offshore applications.

Keywords: Corrosion-fatigue; WAAM; Additive manufacturing; Offshore structures; Structural Integrity.

---

* corresponding author

7 *Engineering Failure Analysis*. 138 (2022), 106362. (DOI: 10.1016/j.engfailanal.2022.106362)

5.2.1. Introduction

Offshore structures are commonly manufactured onshore by welding steel sections and then transported to marine environments for installation and operation. The welded joints in offshore structures are considered as potential weak spots which are prone to crack initiation and propagation due to high stress concentration and residual stresses effects introduced during the welding process. These structures experience millions of load cycles during their operation in highly corrosive environments, which can lead to corrosion-fatigue failures if suitable inspection and maintenance strategies are not carefully implemented. Furthermore, the welding process causes phase changes in metal that affect the microstructure and crack growth patterns, by introducing crack branching[1]. Previous studies on welded wrought steel specimens extracted from the heat affected zone (HAZ) exhibit a strong dependence of fatigue crack growth (FCG) rates on the welding parameters, metal composition, crack growth region, residual stress magnitude and distribution pattern, and testing environment[2–6]. These studies suggest that the fatigue life of marine structures can be significantly improved by selecting more appropriate materials and manufacturing techniques.

Wire arc additive manufacturing (WAAM) is a rapidly developing technique that has gained substantial attention for fabrication of large-scale components employed in structural applications. Compared with other additive manufacturing (AM) methods, such as powder-based techniques, WAAM is known to be substantially beneficial for lower manufacturing cost, unlimited build envelope, and significantly high deposition rates (3-8 kg/h), which results in reduction of manufacturing lead-time[7–10]. Despite the advantages of this method, the high heat input and nonuniform solidification rates during the WAAM fabrication process lead to microstructural inhomogeneity and mechanical properties anisotropy[11,12]. Nevertheless, WAAM has been already adopted by many industries, including aerospace and automotive, and offers a great potential for other industrial sectors such as offshore renewable energy and particularly offshore wind turbines. However, in order to investigate the suitability of this technique for manufacturing and repair of renewable energy marine structures, the corrosion-fatigue crack growth (CFCG) performance of WAAM built steel components has to be closely examined and compared with the conventionally welded joints. This will help to estimate the remaining lifetime and develop efficient inspection plans for future WAAM built marine structures and components.

The environmental behaviour of ER70S-6 low carbon WAAM built specimens was investigated by Ron et al.[13], which included the corrosion behaviour assessment in salt spray testing, immersion testing, potentiodynamic polarization analysis, and electrochemical impedance spectroscopy. The obtained results from this study showed that the general and stress corrosion resistance of WAAM specimens were comparable with conventional wrought ST-37 steel counterparts, which led to a conclusion that the WAAM process does not cause any weakening in corrosion performance for the considered application. Another study was conducted on austenitic stainless steel WAAM specimens with a similar analysis procedure[14], which confirmed that despite the microstructural differences and variations in mechanical properties, electrochemical performance and stress corrosion susceptibility of the parts were similar to the wrought counterparts. Additionally, some ER70-6 WAAM built specimens were tested in a 3.5% NaCl solution to investigate the effect of microstructure imperfections on corrosion-fatigue performance[15]. The results revealed a reduction in fatigue strength of WAAM

specimens, compared with wrought ST-37 specimens, due to the existence of defects that are imposed during WAAM fabrication process, and stimulate corrosion attacks and accelerate fatigue cracking process.

Previous studies demonstrated that corrosion characteristics of WAAM built specimens may differ compared to the wrought counterparts, due to evident microstructural differences imposed by specific manufacturing process. However, the data available in the literature are very limited and do not show any CFCG rates trends for WAAM built low carbon steels, which is required for in-depth analysis and comprehensive comparison for considering the use of this technology in marine structures. Thus, the present study investigates the CFCG behaviour of ER100S-1 low carbon steel WAAM built specimens in seawater. This research includes the manufacturing of a WAAM wall, CFCG testing on extracted specimens, crack growth monitoring, data collection and analysis, and comparison of the obtained results with the existing data on wrought steels. Moreover, a sensitivity analysis of the corrosion-fatigue response to the built orientation and location of the specimens was conducted and presented in this study, along with the microstructural analysis. The observations from this study prove the suitability of WAAM technique with ER100S-1 steel wires for offshore applications.

5.2.2. Material and specimen preparation

One WAAM wall was manufactured for this study using Cold Metal Transfer (CMT) process with Böhler welding ER100S-1 wire[16], the typical composition for which is presented in Table 5.7. The detailed parameters for CMT-WAAM fabrication process are shown in Table 5.8. The manufacturing set-up is demonstrated in Figure 5.13 in which a CMT power source, a robotic arm, a CMT torch that is supplying the shielding gas and feeding the metal wire, an exhaust fan to remove any generated fumes and excessive heat are demonstrated. The WAAM wall was deposited in the middle of a base plate that was cut from an EN10025 rolled structural steel plate, with dimensions of 420 × 200 × 12 mm^3. The completed WAAM wall is shown in Figure 5.13. An oscillation process was selected[17,18] for fabricating a relatively thick wall with dimensions of length of 355 mm (X-axis in Figure 5.13), thickness of 24 mm (Y-axis) and height of 140 mm (Z-axis). The base plate was fixed onto the working table with eight clamps before starting the deposition process, to prevent any bending and distortion of the plate due to the high manufacturing temperatures. These clamps were removed once the WAAM wall was completed and cooled down to the ambient temperature.

Table 5.7: Chemical composition of ER100S-1 material (wt.-%)[16]

	C	*Mn*	*Cr*	*Si*	*Ni*	*Mo*
ER100S-1	0.08	1.70	0.20	0.60	1.50	0.50

Table 5.8: CMT-WAAM fabrication parameters

Shielding gas	Ar+20% CO_2
Gas flow rate	15 L/min
Wire diameter	1.2 mm
Wire feed speed	7.5 m/min
Robot travelling speed	7.33 mm/sec
Dwell time	120 sec

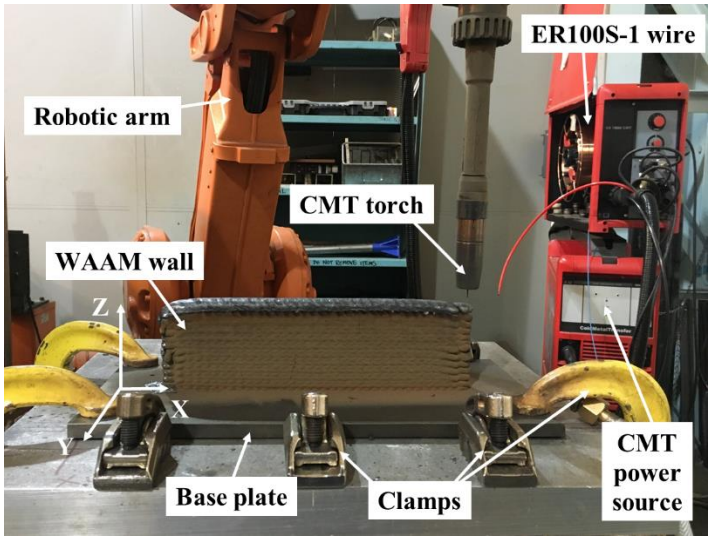

Figure 5.13: Fabrication process including the CMT WAAM set-up and completed WAAM wall

After completing the deposition of the WAAM wall, four notched compact tension, C(T), specimens were extracted using Electrical Discharge Machining (EDM) method. The specimens were designed in accordance[19] standard with the width of W = 50 mm, height of H = 60 mm, total thickness of B = 16 mm and initial crack length of a_0 = 17 mm. The specimens were extracted from two different locations; top (T) and bottom (B) of the wall, and along two different orientations; vertical (V) – where the crack plane is perpendicular to the deposited layers, and horizontal (H) – where the crack plane is parallel to the deposited layers. All four combinations of specimens are presented schematically in Figure 5.14 (a). For example, the specimen denoted CT-VT, is a C(T) specimen with vertical orientation, from top of the wall. Knife edges were machined at the crack mouth of the specimens as per ASTM 1820 stndard[20] to attach a clip gauge for compliance measurements during fatigue pre-cracking that is required prior to CFCG testing to introduce an infinitely sharp crack tip ahead of the machined notch. All four specimens were pre-cracked to approximately 20 mm ($a_{i,p}/W$ = 0.4) using the load-decreasing approach. The final value of maximum stress intensity factor K_{max} at the end of pre-cracking did not exceed the initial K_{max} at the beginning of the main CFCG tests. For the CFCG tests performed in seawater, the crack was measured using the back face strain measurement technique, which is explained in Section 5.2.3. Some examples of the specimens prepared for CFCG testing are displayed in Figure 5.14 (b).

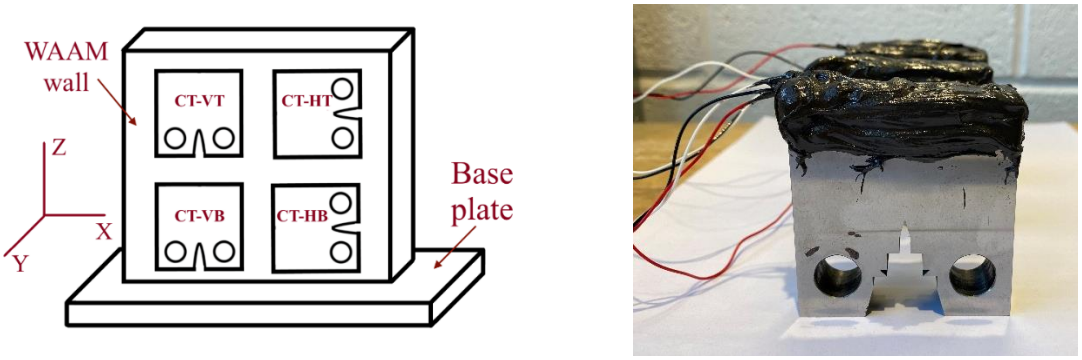

(a) (b)

Figure 5.14: (a) Specimen extraction plan from the WAAM wall, (b) specimens with protective coating after strain gauging

5.2.3. Corrosion-fatigue crack growth test

- **Test set-up**

CFCG tests were conducted under load-controlled mode using a 100 kN servo hydraulic Instron machine. A sinusoidal cyclic load wave was applied with a constant amplitude of the maximum load P_{max} = 10 kN, the load ratio of R = 0.1, and frequency of f = 0.3 Hz, which is the typical frequency used in corrosion-fatigue analysis for offshore wind turbine structures[21,22]. To imitate free-corrosion condition for testing, 60 L artificial seawater was made according to according to the ASTM D1141-98 standard[23] using deionised water and a set of chemicals presented in Table 5.9. During the CFCG tests, the pH level of seawater was constantly monitored and maintained between 8.0 and 8.2, and fresh water was made once the level dropped below 8.0. The full CFCG test set-up is shown in Figure 5.15. An environmental seawater chamber was attached onto the Instron machine, and the specimen was immersed in artificial seawater with the crack path located below the waterline throughout the tests (Figure 5.15). The prepared seawater was stored in a water tank and circulated in the environmental chamber by means of a pump at a constant rate of 4 L/min. The seawater temperature was controlled with a chiller and maintained between 8.0 and 10.0^{0}C, to replicate the operation conditions in the North Sea[3].

Table 5.9: Chemical composition of artificial seawater[23]

Chemical compound	Concentration (g/L)
$NaCl$	24.53
$MgCl_2$	5.20
Na_2SO_4	4.09
$CaCl_2$	1.16
KCl	0.695
$NaHCO_3$	0.201
KBr	1.101
H_3BO_3	0.027
$SrCl_2$	0.025
NaF	0.003

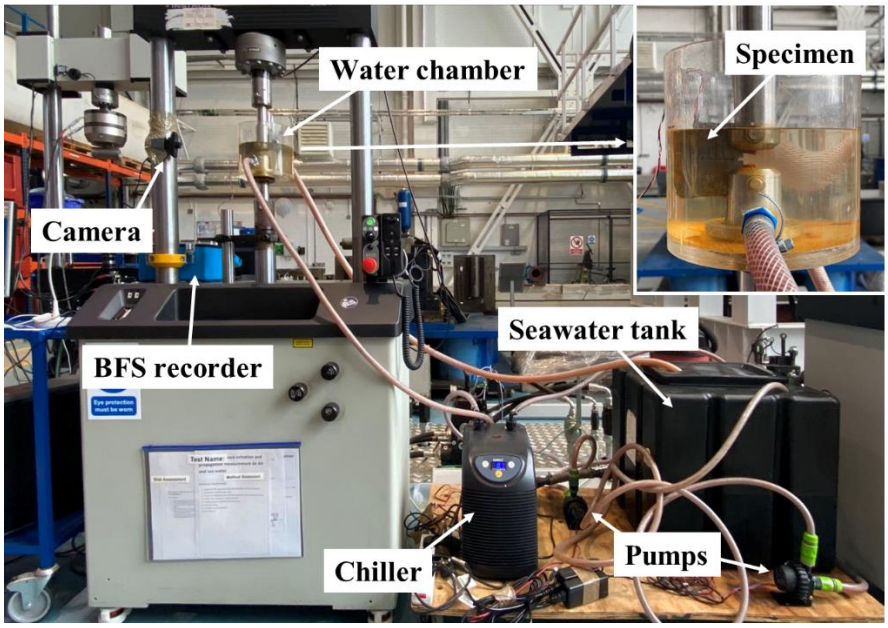

Figure 5.15: CFCG test set-up

- **Crack growth estimation method**

During corrosion-fatigue tests, the specimens are immersed in seawater with limited direct access; therefore, the crack growth monitoring becomes challenging. One of the existing well-known and efficient crack growth monitoring techniques which is suitable for the CFCG testing is the back face strain (BFS) method that was designed for C(T) specimens[24,25]. The main idea for this approach is to correlate the BFS variations with the crack length of the specimen. The BFS calibration curve is initially developed under the same loading conditions during the FCG tests in air, where it is possible to measure the instantaneous crack length using the optical and compliance techniques. This calibration curve will be valid for the considered C(T) specimen geometry, material and loading conditions. Therefore, the same empirical correlation from FCG tests in air is used to estimate the crack lengths from the BFS measurements in CFCG tests in seawater.

The BFS values are recorded from the strain gauge attached to the back face of the C(T) specimen, at mid-height and mid-width. In this study, strain gauges were initially attached to the back face of C(T) specimens and then covered with a layer of a polysulfide coating to protect them against seawater damage (Figure 5.14 (b)). Prior to testing all the specimens were soaked in artificial seawater for approximately 24 hours, as recommended in the ASTM D1141[23] standard. The BFS values were recorded from the strain gauges every second by a strain recorder during the CFCG tests, and the maximum magnitude of compressive strain values were captured and stored on a memory card (see BFS recorder in Figure 5.15).

In order to produce unique BFS calibration curves for each specimen, four fatigue tests in air were carried out on C(T) specimens with the same geometry and extraction orientation/locations (VT, HT, VB, and HB), with the exact same loading conditions as the CFCG tests as shown in Table 5.10. As the BFS calibration curves depend on the load level applied on the specimen during the test, the calibration test in air and the main CFCG test in

seawater were performed at the same loading conditions. The instantaneous crack growth during the FCG test in air was measured using a clip gauge attached to the knife edges at the crack mouth of the C(T) specimens, and then correlated with the corresponding maximum magnitude of compressive BFS value (hence maximum crack mouth opening). Four calibration curve equations were derived by applying cubic polynomial lines of best fit to the experimental data, and then were used to estimate the crack length from the BFS measurements collected during each of the CFCG tests.

Additionally, to cross-check the accuracy of the estimated values of the crack length from the BFS method, the beach marking (BM) technique was employed in crack growth tests[26]. For this purpose, the maximum cyclic fatigue load and the frequency were decreased for a short period of time to introduce a thin mark on the fracture surface, which is called a beach mark. The duration of BM process was selected in such a way that it is performed without a noticeable crack growth, to keep the BFS value unchanged. By recording the BFS value at which the BM process was implemented, the estimated crack length from BFS method can be verified against the experimentally measured crack length at the BM line on the fracture surface of the opened C(T) specimen upon completion of the test. The BM loading conditions for seawater tests are presented in Table 5.10. For each CFCG test, the BM process was repeated three times at various stages of the test to build extra confidence in the developed BFS calibration curves. The BM method was first applied during the FCG tests in air on nominally identical C(T) specimens, to verify the accuracy of the crack length estimations, an example of the fracture surface and loading conditions are shown in Figure 5.16 and Table 5.10 respectively. Satisfactory results from the air tests confirmed the accuracy of the compliance approach which was then implemented in CFCG tests.

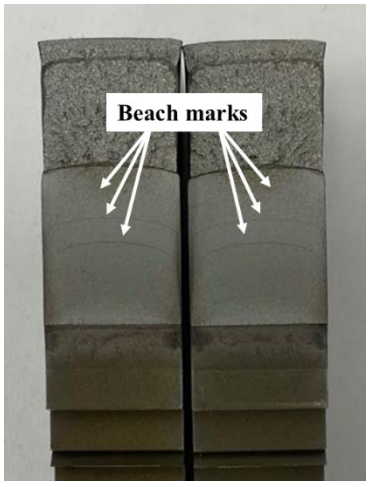

Figure 5.16: The beach marks on fracture surface of WAAM ER100S-1 C(T) specimen tested in air for development of BFS calibration curves

Table 5.10: The loading condition during the main phase and beach marking phase of the calibration tests in air and CFCG tests in seawater

Test environment	The main test condition			Beach marking loading condition		
	P_{max} (kN)	R	f (Hz)	P_{max} (kN)	R	f (Hz)
Air	10	0.1	5	8	0.125	3
Seawater	10	0.1	0.3	8	0.125	0.1

Upon completion of the CFCG tests, all C(T) specimens were broken open to measure the actual crack length at BM lines on the fracture surfaces and verify the accuracy of the estimated crack lengths obtained from the BFS calibration curves. The fracture surfaces of four CFCG test specimens are presented in Figure 5.17. It is worth noting here, that due to corroded fracture surface of the C(T) specimens tested in seawater, the beach marks were not very clear with the naked eye, compared with the fracture surfaces of the specimens tested in air (see Figure 5.16), therefore high magnification optical microscopy was used to find the exact location of the BM lines. It can be seen in Figure 5.17 that the crack propagation regions are symmetric in all CFCG specimens, indicating good alignment in the test set-up.

CT-VT CT-VB CT-HT CT-HB

Figure 5.17: Fracture surface of WAAM built ER100S-1 specimens after CFCG test in seawater

An example of the calibration curve for CT-VT specimen, plotted using the empirical correlation equation from the air test is presented in Figure 5.18. Also included in this figure are the BM data points obtained at different stages of the test which indicate the actual crack lengths observed on the fracture surface upon the test completion and specimen fracture open. A very good agreement between the BFS calibration curve derived from the test in air and the BM data obtained from the CFCG test in seawater can be seen in this figure. Similar level of agreement between the calibration curves and the BM data points from the CFCG tests were obtained from the other three specimens (CT-VB, CT-HT, CT-HB). Hence the estimated crack lengths using the BFS data in CFCG tests are found to be very reliable.

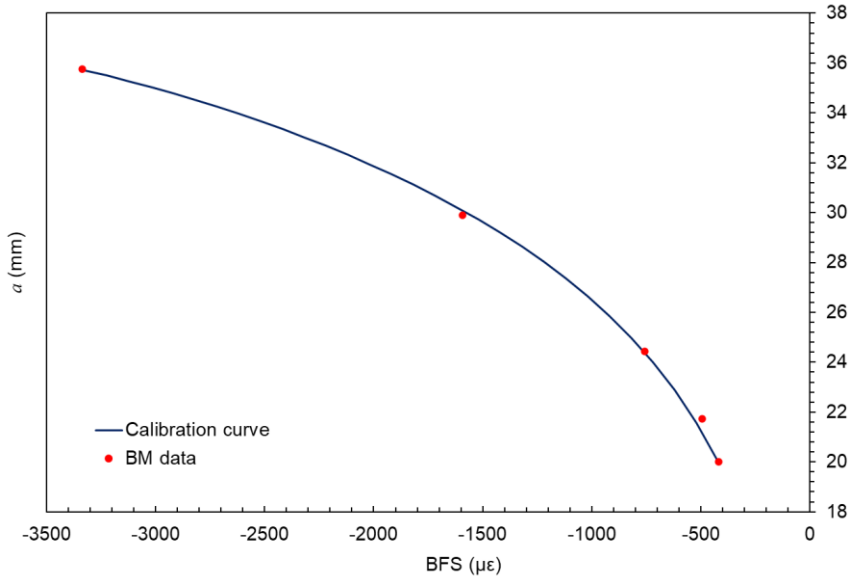

Figure 5.18: Crack length vs. BFS correlation for CT-VT specimen, and its comparison with the BM data points

- **Data analysis**

The CFCG rates, *da/dN*, were determined using the estimated crack lengths and the experimental number of cycles for each specimen, by applying the secant method for the first and the last three data points, and seven-point incremental polynomial method for the rest of the data points. Subsequently, the stress intensity factor (SIF) was calculated using the shape function equation introduced by Mehmanparast et al.[27], Equation 5.3, which provides accurate solutions for a wider range of crack lengths in a C(T) specimen ranging between *a/W* of 0.2 and 0.7, compared with the original shape function equation from the ASTM E647 standard. In Equation 5.3, α is the normalised crack length *a*/*W* and ΔP is the load range which is defined as the difference between the maximum load P_{max} and the minimum load P_{min}.

$$\Delta K = \frac{\Delta P}{BW} \cdot \sqrt{a} \cdot (-372.12\alpha^6 + 1628.60\alpha^5 - 2107.46\alpha^4 + 1304.65\alpha^3 - 391.20\alpha^2 + 54.81\alpha + 7.57) \quad \text{Equation 5.3}$$

5.2.4. Experimental results and discussion

To assess and compare the duration of each test, the estimated crack lengths are plotted against the number of fatigue cycles for each specimen, and the results are displayed in Figure 5.19. According to this figure, the longest fatigue life was experienced by the vertical specimen extracted from the top of the WAAM wall, CT-VT. This specimen required 1.5 to 2.6 times more cycles to propagate the crack by 15 mm than the other three specimens. Also seen in this figure is that the two specimens extracted from the top of the wall with two different orientations had the longest fatigue lives compared to specimens extracted from the bottom of the WAAM wall. For both locations of the WAAM wall considered in this study (i.e. top and bottom), the test duration for the vertical specimens is higher than the horizontal specimens extracted from the same location. Based on these experimental observations, the horizontal specimen extracted from the bottom of the wall, CT-HB, has the shortest fatigue life. These variations in the test duration are expected to have been caused by microstructural differences due to the thermal effects and possibly the remnant residual stresses which might have remained in the C(T) specimens after extraction. Additive layers at the bottom of the wall experience a greater number of repeated thermal cycles; therefore, it is expected that the magnitude of residual stress is generally lower at the bottom compared to the top of the WAAM wall. Comparison of the CFCG data obtained from this study with the FCG results in air previously conducted on WAAM ER100S-1 specimens by Ermakova et al.[28] shows that in both test environments the crack growth results are sensitive to the extraction location, with a longer fatigue life experienced by the specimens extracted from the top of the WAAM wall.

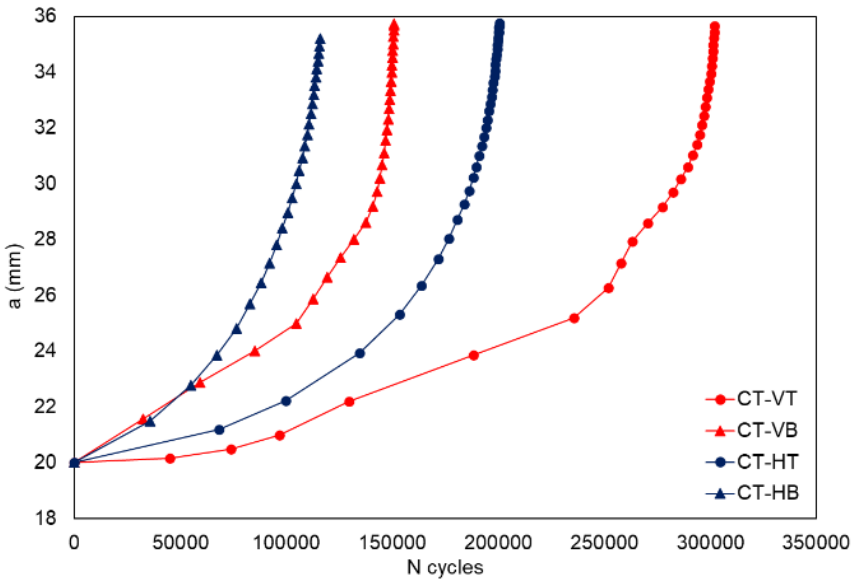

Figure 5.19: Corrosion-fatigue crack growth trends in ER100S-1 WAAM built C(T) specimens

The CFCG rates, *da/dN*, were calculated and plotted against the linear elastic fracture mechanic parameter, *ΔK*, as shown in Figure 5.20. It can be observed in this figure that at the low values of *ΔK*, the crack growth rate is higher in horizontal specimens regardless of the extraction location; however, towards the end of the test, at larger values of *ΔK*, vertical specimens exhibit higher crack growth rates. In general, the lowest CFCG trend observed throughout the entire range of *ΔK* values is found to be obtained from CT-VT vertical specimen extracted from the top of the wall, indicating the highest level of corrosion-fatigue resistance across all four specimens considered in this study. Also seen in Figure 5.20 is that within the inherent experimental scatter similar slopes are found in the CFCG trends from specimens with the same orientation. Moreover, the crack growth rates for vertical specimens show higher scatter than horizontal specimens, and display wavy patterns, similar to the observations reported by Ermakova et al.[28] for FCG tests on the same material and the same specimen orientation in air. It was also seen that the FCG rates from air test are location dependant, with the lowest crack growth rates observed in specimen extracted from the top of the wall. Thus, a conclusion can be made that for ER100S-1 WAAM built specimens, regardless of the testing environment, FCG and CFCG rates and test duration strongly depend on the extraction location. Having said that, considering that only four specimens were tested in seawater in the present study, more tests need to be conducted in future work to confirm the provisional results presented in this paper and assess the level of scatter for each specimen orientation and location. Furthermore, the remaining residual stresses in the C(T) specimens extracted from the WAAM wall must be measured in future work to evaluate their possible effects on the CFCG behaviour of ER100S-1 WAAM built specimens.

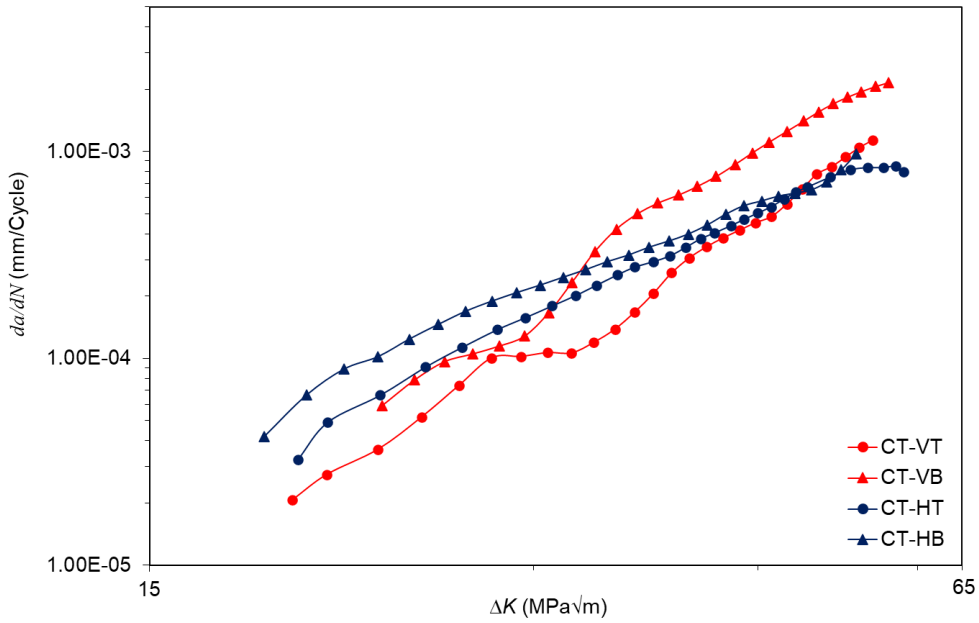

Figure 5.20: Corrosion-fatigue crack growth results for ER100S-1 WAAM built specimens

The CFCG test data were further analysed to evaluate the material constants, *C* and *m* (see Equation 5.4), in the secondary Paris region for each dataset by plotting the lines of best fit to the experimental data and finding the corresponding power-law constants. The *C* and *m* values obtained from the regression analyses are presented in Table 5.11. Also included in this table are the values of coefficient of determination, R^2, to examine the level of scatter in each of the data sets. As seen in Table 5.11, the R^2 values for all specimens are close to 1, although a marginally higher level of scatter is generally observed in vertical specimens compared to the horizontal specimens.

$$da/dN = C\Delta K^m \qquad \text{Equation 5.4}$$

Table 5.11: Paris-law constants obtained from the CFCG test data on ER100S-1 WAAM built specimens (*da/dN* in mm/Cycle and *ΔK* in MPa$\sqrt{m}$)

Specimen ID	Orientation	Location	*Pmax* (kN)	*C*	*m*	R^2
CT-VT	Vertical	Top	10	2.89×10^{-10}	3.76	0.988
CT-VB	Vertical	Bottom	10	1.33×10^{-10}	4.15	0.987
CT-HT	Horizontal	Top	10	1.07×10^{-8}	2.82	0.995
CT-HB	Horizontal	Bottom	10	5.28×10^{-8}	2.44	0.994

Furthermore, the power-law constants were determined for specimens with the same orientations (vertical or horizontal) and the results are presented in Table 5.12. Moreover, the upper bound trends for the vertical data set (Set-V) and horizontal data set (Set-H), based on +2 standard deviation (2SD), were calculated, and added to Table 5.12 and plotted in Figure 5.21. Also shown in Figure 5.21 is the comparison of the results obtained from this study with the recommended trends provided in the BS7910 standard for welded joints in seawater, based on the simplified law and the 2-stage law[29]. It can be seen in Figure 5.21 that the upper bound

trends for Set-V and Set-H from the CFCG tests on ER100S-1 WAAM built specimens both fall below the BS7910 recommended lines, except the very end of the Set-V, which crosses the 2-stage law at large values of ΔK. This indicates that the CFCG rates for ER100S-1 WAAM built specimens can be conservatively predicted by the simplified law provided in BS7910 standard.

Table 5.12: Power-law constants associated with the mean curves and upper bound trends for different specimen orientation datasets

Datasets	Orientation	P_{max} (kN)	Mean			Mean+2SD	
			C	m	R^2	C	m
Set-V	Vertical	10	1.49×10^{-10}	4.03	0.913	3.09×10^{-10}	4.03
Set-H	Horizontal	10	2.91×10^{-8}	2.58	0.972	3.77×10^{-8}	2.58

Furthermore, the obtained CFCG results in this study have been compared with the experimental data available in the literature on conventionally built welded steel specimens tested in seawater, including: S355G8+M C(T) specimens extracted from HAZ and base metal[6], S355G10+M C(T) specimens extracted from HAZ[30], S355J2+N C(T) specimens extracted from HAZ and weld metal[1], and X70 pipeline steel specimens[31]. All specimens were tested under similar loading conditions as the samples tested in this study (see Table 5.10), and their trends are depicted in Figure 5.21. Comparison of all considered datasets shows that the upper bound CFCG data obtained on ER100S-1 WAAM built specimens from the present study begins at approximately the same ΔK value as experimental data for S355G10+M specimens, though with a longer fatigue life, continuing to the higher values of ΔK. For the ΔK values of between approximately 19 and 35 MPa$\sqrt{m}$, the upper bound lines for ER100S-1 WAAM built specimens fall upon the test data on S355G10+M and S355G8+M, which are the subgrades of S355 structural steel that are widely used in fabrication of offshore renewable energy structures. Further comparison of the test durations for the specimens from this study and S355G+10M HAZ specimens tested by Jacob et al.[30] shows that on average it takes 9.7 times longer to propagate a crack in WAAM ER100S-1 specimens than in conventionally welded S355 counterpart. Therefore, this comparison confirms that ER100S-1 steel and WAAM technology can be potentially considered for manufacturing of offshore renewable energy structures. Nevertheless, the S-N fatigue tests will need to be conducted in future work to fully assess the design requirements for WAAM built components operating under cyclic loading conditions in marine environments.

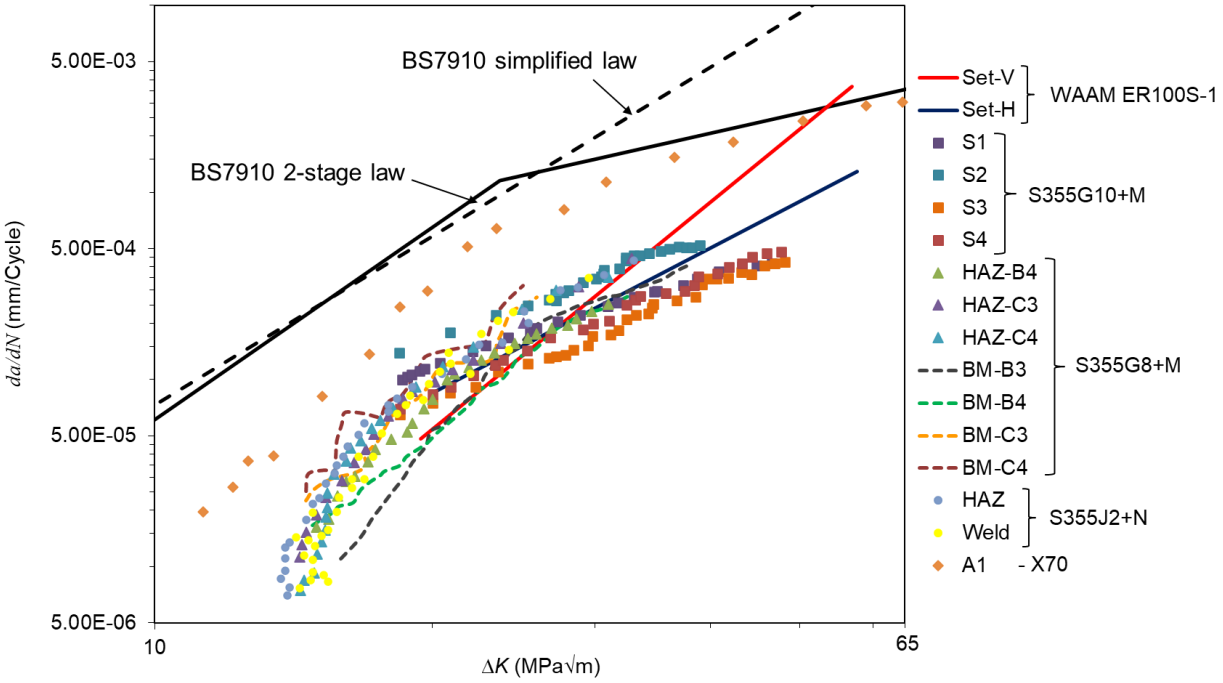

Figure 5.21: Comparison of the upper bound CFCG trends for ER100S-1 WAAM built specimens with BS7910 curves and the literature data on structural steels

5.2.5. Fractography

Once four test specimens were broken-open, their fracture surfaces were examined using a TESCAN VEGA 3 Scanning Electron Microscope (SEM) with a magnification of 5000. According to Figure 5.20, at lower values of ΔK the CFCG rates demonstrate higher level of scatter; therefore, the microstructural analysis was conducted on the area corresponding to the beginning of the test (ΔK of approximately 23 MPa√m), and the results are shown in Figure 5.22. The fracture surface examination in the regions shown in Figure 5.22 demonstrates the existence of transgranular tortuous features for all specimens extracted with different orientations and locations, indicating a ductile fracture mechanism. Moreover, the general observation across various regions on the fracture surface shows that tortuosity of the vertical specimens is more pronounced, and deeper and larger in size, compared to the horizontal specimens which have smoother surface with shallower features. This indicates that at a given value of ΔK the CFCG would be higher in the horizontal specimens than the vertical samples. This conclusion is consistent with the trends presented in Figure 5.20. Similar to the observations in the previous study on the FCG behaviour of WAAM built ER100S-1 specimens in air[28], elongated fracture features, which are marked with red dashed lines in Figure 5.22, can be found in the vertical CFCG test specimens examined in this study both at the top and bottom locations (CT-VT and CT-VB). It was reported in the previous study [28] that once the orientation of these elongated fracture features changes, which appears with an increase in the inclination angle from the crack growth propagation plane, the FCG rate simultaneously increases. It is seen in Figure 5.22 that the elongated fracture features in CT-VB have higher inclination angle, and hence higher CFCG rate than in CT-VT, where the feature is nearly parallel to the crack

propagation direction, resulting in lower CFCG rate at a given value of ΔK as seen in Figure 5.20. Comparison of two fracture surfaces of horizontal specimens shows that the specimen extracted from the bottom of the WAAM wall has shallower ductile features with higher density of small secondary cracks (shown with yellow arrows), whereas the fracture surface of the specimen extracted from the top of the wall exhibits deeper dimples and larger secondary cracks with lower density, which results in lower CFCG rates in CT-HT sample compared to CT-HB, which is confirmed by the trends observed in Figure 5.20. Therefore, it can be concluded that for a given specimen orientation, the sample extracted from the bottom of the ER100S-1 WAAM wall exhibits less ductile fracture features which result in higher CFCG rates compared to the top specimens.

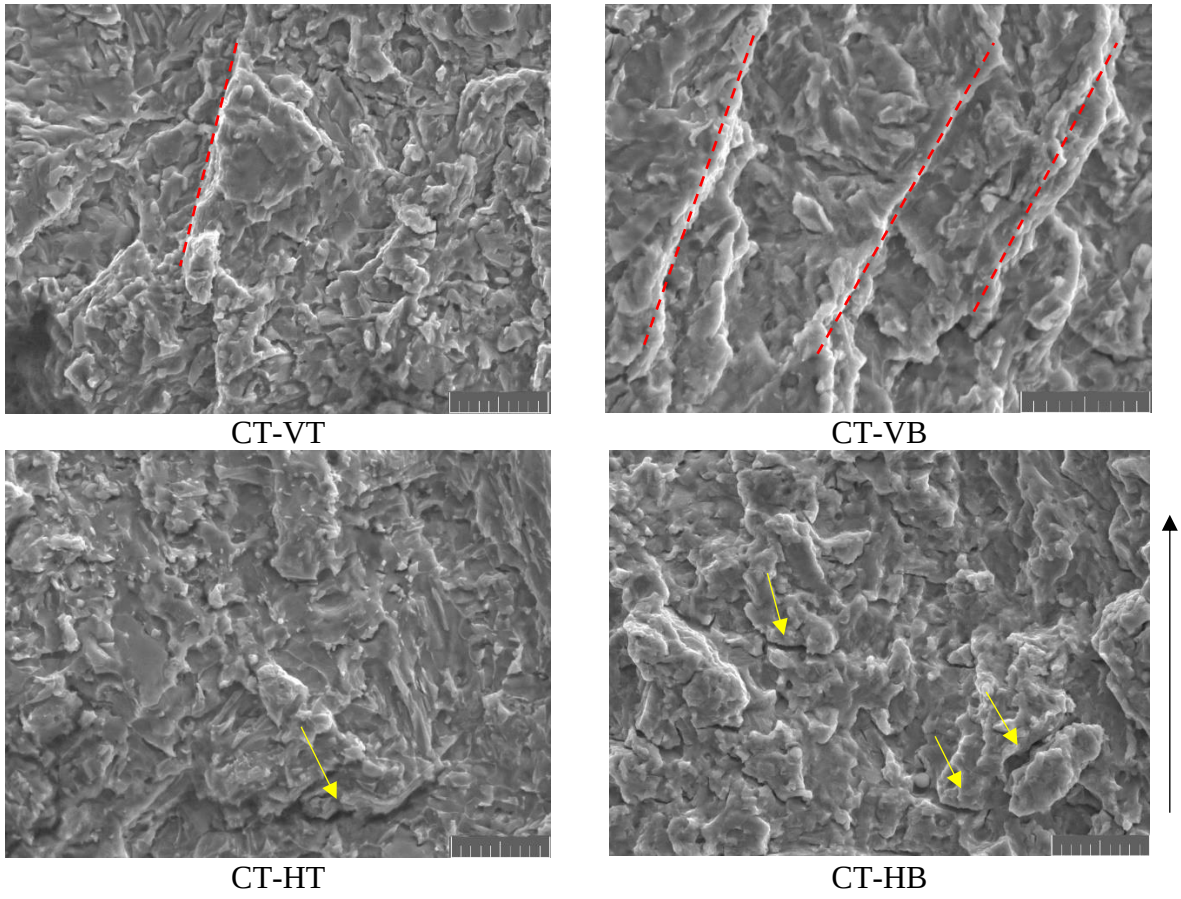

Figure 5.22: SEM images of fracture surfaces for four test specimens at ΔK=23 MPa√m (the scale bar is 10 µm, and the right-hand side arrow shows the direction of the crack propagation)

5.2.6. Conclusions

The CFCG behaviour of ER100S-1 WAAM built specimens was investigated in the present study, the following conclusions and observations were made:

- The specimen extraction location with respect to the WAAM wall height has a major effect on the test duration and CFCG rates. Specimens extracted from the top of the

wall require a greater number of cycles to propagate and they also demonstrate lower CFCG rates.

- Vertical specimens show a longer test duration compared to horizontal specimens extracted from the same location of WAAM wall, and on average they present lower CFCG rates.
- The upper bound lines for CFCG trends fall below BS7910 recommended crack growth trends, and also on top of the existing test data on S355G10+M and S355G8+M.
- The ER100S-1 WAAM built specimens require on average 9.7 times greater number of cycles to propagate the crack by 15 mm compared to the wrought counterparts extracted from S355G10+M HAZ steel.
- Bottom portion of ER100S-1 WAAM steel wall represented a lower ductility which subsequently results in higher CFCG rates.
- The fracture surface of the vertical WAAM built ER100S-1 specimens demonstrates elongated failure features. The higher inclination angle from the crack propagation plane results in a higher CFCG rate.
- Repeat tests are required in future work to evaluate the level of scatter for each specimen extraction location and orientation. Also, the remnant residual stresses in WAAM built C(T) specimens need to be measured to assess their potential effects on CFCG behaviour of ER100S-1 WAAM specimens.

5.2.7. Acknowledgements

This work was supported by grant EP/L016303/1 for Cranfield, Oxford and Strathclyde Universities' Centre for Doctoral Training in Renewable Energy Marine Structures – REMS CDT (http://www.rems-cdt.ac.uk/) from the UK Engineering and Physical Sciences Research Council (EPSRC).

5.2.8. References for paper VII

1. Adedipe, O., Brennan, F., Mehmanparast, A., Kolios, A. & Tavares, I. Corrosion fatigue crack growth mechanisms in offshore monopile steel weldments. *Fatigue and Fracture of Engineering Materials and Structures* **40**, 1868–1881 (2017).

2. Burnside, O. H., Hudak, S. J. , Jr., Oelkers, E., Chan, K. & Dexter, R. J. Long-Term Corrosion Fatigue of Welded Marine Steels. (1984).

3. Adedipe, O., Brennan, F. & Kolios, A. Review of corrosion fatigue in offshore structures: Present status and challenges in the offshore wind sector. *Renewable and Sustainable Energy Reviews* **61**, 141–154 (2016).

4. Fatigue behaviour of high-strength steel-welded joints in offshore and marine systems (FATHOMS) - Publications Office of the EU. https://op.europa.eu/en/publication-detail/-/publication/52679314-1c6d-41d6-9d70-19711b29427f.

5. Bertini, L. Influence of seawater and residual stresses on fatigue crack growth in CMn steel weld joints. *Theoretical and Applied Fracture Mechanics* **16**, 135–144 (1991).

6. Mehmanparast, A., Brennan, F. & Tavares, I. Fatigue crack growth rates for offshore wind monopile weldments in air and seawater: SLIC inter-laboratory test results. *Materials and Design* **114**, 494–504 (2017).

7. Zhang, X. *et al.* Fatigue Crack Growth in Additive Manufactured Titanium: Residual stress control and life evaluation method development. *29 th ICAF Symposium-Nagoya* 7–9 (2017).

8. Martina, F., Mehnen, J., Williams, S. W., Colegrove, P. & Wang, F. Investigation of the benefits of plasma deposition for the additive layer manufacture of Ti–6Al–4V. *Journal of Materials Processing Technology* **212**, 1377–1386 (2012).

9. Williams, S. W. *et al.* Wire + Arc Additive Manufacturing. *Materials Science and Technology* **32**, 641–647 (2015).

10. Rafieazad, M., Nemani, A. V., Ghaffari, M. & Nasiri, A. On Microstructure and Mechanical Properties of a Low-Carbon Low-Alloy Steel Block Fabricated by Wire Arc Additive Manufacturing. *Journal of Materials Engineering and Performance* (2021) doi:10.1007/s11665-021-05568-9.

11. Liljedahl, C. D. M. *et al.* Weld residual stress effects on fatigue crack growth behaviour of aluminium alloy 2024-T351. *International Journal of Fatigue* **31**, 1081–1088 (2009).

12. Xu, X. *et al.* Microstructural evolution and mechanical properties of maraging steel produced by wire + arc additive manufacture process. *Materials Characterization* **143**, 152–162 (2018).

13. Ron, T. *et al.* Environmental behavior of low carbon steel produced by a wire arc additive manufacturing process. *Metals* **9**, (2019).

14. Ron, T., Dolev, O., Leon, A., Shirizly, A. & Aghion, E. Effect of phase transformation on stress corrosion behavior of additively manufactured austenitic stainless steel produced by directed energy deposition. *Materials* **14**, 1–12 (2021).

15. Ron, T. *et al.* The effect of microstructural imperfections on corrosion fatigue of additively manufactured ER70S-6 alloy produced by wire arc deposition. *Metals* **10**, (2020).

16. *ER100S-G Data Sheet - Bohler Welding*. www.voestalpine.com/welding (2014).

17. Ermakova, A., Mehmanparast, A. & Ganguly, S. A review of present status and challenges of using additive manufacturing technology for offshore wind applications. *Procedia Structural Integrity* **17**, 29–36 (2019).

18. Ermakova, A., Mehmanparast, A., Ganguly, S., Razavi, J. & Berto, F. Investigation of mechanical and fracture properties of wire and arc additively manufactured low carbon steel components. *Theoretical and Applied Fracture Mechanics* **109**, 102685 (2020).

19. ASTM E647−13. Standard Test Method for Measurement of Fatigue Crack Growth Rates. *American Society for Testing and Materials* 1–50 (2014) doi:10.1520/E0647-15E01.2.

20. American Society for Testing and Materials. ASTME-1820-11: standard test method for measurement of fracture toughness. *Annual book of ASTM standards* 1–55 (2011) doi:10.1520/E1820-18.

21. Henderson, A. Hydrodynamic Loading of Offshore Wind Turbines. (2003).

22. Jacob, A., Mehmanparast, A., D'Urzo, R. & Kelleher, J. Experimental and numerical investigation of residual stress effects on fatigue crack growth behaviour of S355 steel weldments. *International Journal of Fatigue* **128**, 105196 (2019).

23. International, A. D1141-98 Standard Practice for the Preparation of Substitute Ocean Water. *ASTM International* **98**, 1–3 (2013).

24. Adedipe, O., Brennan, F. & Kolios, A. Corrosion fatigue load frequency sensitivity analysis. *Marine Structures* **42**, 115–136 (2015).

25. Newman, J. C., Yamada, Y. & James, M. A. Back-face strain compliance relation for compact specimens for wide range in crack lengths. *Engineering Fracture Mechanics* **78**, 2707–2711 (2011).

26. Hou, C. Y. Fatigue analysis of welded joints with the aid of real three-dimensional weld toe geometry. *International Journal of Fatigue* **29**, 772–785 (2007).

27. Mehmanparast, A., Taylor, J., Brennan, F. & Tavares, I. Experimental investigation of mechanical and fracture properties of offshore wind monopile weldments: SLIC interlaboratory test results. *Fatigue and Fracture of Engineering Materials and Structures* **41**, 2485–2501 (2018).

28. Ermakova, A., Ganguly, S., Razavi, J., Berto, F. & Mehmanparast, A. Experimental investigation of the fatigue crack growth behavior in wire arc additively manufactured ER100S-1 steel specimens. *Fatigue & Fracture of Engineering Materials & Structures* (2021) doi:10.1111/FFE.13598.

29. BS 7910. BSI Standards Publication Guide to methods for assessing the acceptability of flaws in metallic structures. *BSI Standards Publication* 490 (2015).

30. Jacob, A. & Mehmanparast, A. Crack growth direction effects on corrosion-fatigue behaviour of offshore wind turbine steel weldments. *Marine Structures* **75**, 102881 (2021).

31. Vosikovsky, O. Effects of Stress Ratio on Fatigue Crack Growth Rates in X70 Pipeline Steel in Air and Saltwater. *Journal of Testing and Evaluation* **8**, 68–73 (1980).

5.3. Conclusion

The corrosion-fatigue crack growth behaviour was examined in WAAM built specimens using ER70S-6 and ER100S-1 materials. For ER70S-6 specimens, the extraction location relative to the WAAM wall influenced test duration and CFCG rates in Stages I and II, with top-extracted specimens requiring more cycles to reach 15 mm crack extension. Orientation had minor effects on CFCG rates in Stage III. ER70S-6 WAAM specimens showed lower CFCG rates in Stage I and III for vertical C(T) specimens extracted from the top of the wall.

Similarly, ER100S-1 WAAM specimens demonstrated significant variations in test duration and CFCG rates based on extraction location within the WAAM wall. Top-extracted specimens required more cycles to propagate the crack and exhibited lower CFCG rates. Vertical specimens showed longer test durations and lower CFCG rates compared to horizontal specimens from the same wall location. Fracture surfaces of vertical ER100S-1 WAAM specimens exhibited elongated failure features, leading to higher CFCG rates.

The CFCG trends for both ER70S-6 and ER100S-1 WAAM specimens fell below the recommended fatigue crack growth trends in BS7910. The ER70S-6 specimens required three times more cycles to propagate the crack to 15 mm compared to wrought counterparts, while ER100S-1 specimens required 9.7 times more cycles.

Future work should focus on evaluating data scatter and residual stresses in WAAM built specimens to better understand and analyse their influence on CFCG behaviour. These findings contribute valuable insights into the CFCG performance of WAAM materials, critical in the assessment and application of these components in various industries, particularly in harsh environments like offshore structures.

Chapter 6 : Uniaxial, Torsion and Multiaxial Fatigue Assessment of Wire Arc Additively Manufactured Mild Steels

In this chapter, uniaxial, torsion and multiaxial behaviour of ER70S-6 and ER100S-1 WAAM built components was investigated. The chapter consists of the following papers:

Paper VIII: Uniaxial and multiaxial fatigue behaviour of wire arc additively manufactured ER70S-6 low carbon steel components

Paper IX: Fatigue life assessment of wire arc additively manufactured ER100S-1 steel parts

6.1. Paper VIII: Uniaxial and multiaxial fatigue behaviour of wire arc additively manufactured ER70S-6 low carbon steel components

Anna Ermakova[a], Javad Razavi[b], Filippo Berto[b], Ali Mehmanparast[a*]

[a] Department of Naval Architecture, Ocean and Marine Engineering, University of Strathclyde, Glasgow G1 1XQ, United Kingdom

[b] Norwegian University of Science and Technology (NTNU), Trondheim, Norway

Abstract[8]

Wire arc additive manufacturing (WAAM), also known as directed energy deposition (DED) process, is an efficient additive manufacturing technology, offers high potential to rapidly fabricate large-scale parts with complex geometries layer-by-layer. However, the fundamental understanding of the fatigue behaviour of such parts and the material requirements need to be significantly improved at all levels before this unique technology can be implemented for critical applications. This work aims to investigate the fatigue behaviour of WAAM built ER70S-6 steel under uniaxial, torsion and multiaxial loading conditions. Specimens were extracted in two different orientations: vertical and horizontal, to explore if the orientation direction has any effect on the fatigue results. Scanning Electron Microscopy (SEM) was conducted to examine the fracture surface of broken specimens and identify crack initiation regions and fracture mechanisms. The obtained results were compared with the fatigue data available in the literature on common structural steels fabricated using conventional welding and WAAM technique, showing similar fatigue behaviour with wrought S355 specimens. Moreover, the uniaxial data set on ER70S-6 WAAM specimens was evaluated according to the DNV RP-C203 standard for continuous welds, demonstrating advantageous fatigue resistance in the examined material.

[*] corresponding author

[8] *International Journal of Fatigue*. 166(2023), 107283. (DOI: 10.1016/j.ijfatigue.2022.107283)

6.1.1. Introduction

Additive manufacturing (AM) is a process of joining material layer by layer to produce objects from a three-dimensional model, using a combination of the energy source and material deposition. This manufacturing process offers some advantages compared to the conventional production techniques, for instance, more design freedom, material waste reduction, shorter lead-time, near net shape fabrication without expensive production moulds and tools. On the other hand, AM parts may contain defects related to the welding manufacturing process (lack of fusion, trapped gas bubbles, etc)[1], locked in residual stresses and rough surfaces[2]. Moreover, due to repeating heating and cooling processes during production, the material can experience different thermal histories and hence different microstructures, resulting in highly anisotropic behaviour which would subsequently affect the fatigue strength, wear, and corrosion resistance[3–5].

Development of more powerful and economical manufacturing processes enables the rapid production of larger components using common engineering materials, such as structural steels, for various industrial applications[6]. Wire arc additive manufacturing (WAAM) technique is a type of the directed energy deposition (DED) AM process, which meets the requirements for the large-scale component production offering the highest deposition rates among all AM methods: 5-8 kg/h compared with 55 g/h for the powder-based techniques[7]. With comparatively easy deposition process completed in open air, WAAM can be used for alternative re-manufacturing and repair applications in various industries such as offshore structures operating in remote areas[8].

It has been estimated that fatigue contributes to approximately 90% of all mechanical service failures; therefore, fatigue analysis is an essential part of any structural design assessment and inspection planning, especially for AM built components, in which welding defects and tensile residual stresses are detrimental for fatigue characteristics[9]. Thus, for future structural applications the uncertainty of the fatigue performance of AM components must be fully characterised and new test data need to be generated for structural durability predictions. Due to the increasing interest by aerospace and nuclear industries in AM technologies, a significant majority of the existing experimental fatigue data in the literature are available on AM built titanium Ti-6Al-4V specimens[2,10–14] and stainless steel SS316[15,16]; however, only a limited number of the available data sets are on fatigue behaviour of WAAM built steels for application in other industries, such as offshore renewable energy in which the structures are commonly made of structural steels. Among the limited data available on WAAM built steels in the literature, a study was carried out by Dirisu et al.[17] on the fatigue performance of ER70S-6 alloy. Flat dog bone specimens were extracted from the WAAM walls in horizontal orientation (i.e. parallel to the deposition direction) and three specimen types were examined: as-built, as-built rolled and machined. All specimens were tested under uniaxial fatigue loading condition with the load ratio of R=0.1. The test results demonstrated an improvement in the fatigue strength for the machined specimens with smooth surface compared to other specimen types. It has been also reported that rolling of the as-built wavy surfaces was found beneficial to enhance the fatigue performance of the WAAM built components compared to as-built specimens. These findings confirmed that wall waviness, which is in fact naturally occurred notches during manufacturing process, acts as a stress riser and therefore reduces the fatigue strength of the as-built components. Another study was conducted by Bartsch et al.[6] on as-built

WAAM G3Si1, a copper coated steel, specimens. Dog bone specimens with two different lengths were tested under uniaxial fatigue loading conditions with the load ratio of R=0.1 The presented experimental and numerical results revealed that the surface roughness was the main influencing factor in fatigue life analysis of the examined specimens.

A review of the existing works available in the literature shows that only a few fatigue data sets were generated for WAAM built structural steels, which only included uniaxial fatigue loading conditions. The lack of wider range of fatigue data for WAAM built steel components restricts the industry's access to the full range of advantages that the WAAM technology offers to a wide range of industries and limits the implementation of this powerful technology into new manufacturing procedures. In this context, the current work aims to contribute to the fundamental understanding of the fatigue and cracking behaviour of additively manufactured ER70S-6 specimens subjected to uniaxial, torsion and multiaxial fatigue loading conditions. The experimental data obtained from this study was compared with the existing fatigue data for wrought structural steels and also with limited data available on WAAM built components. Also included in this study is the sensitivity analysis of the fatigue behaviour to the specimen extraction orientation (parallel or perpendicular) with respect to the deposition direction. Last yet importantly, the presented results from this study were interpreted by conducting complementary microscopic analysis of the fracture surfaces to better understand the failure mechanism under different type of fatigue loading conditions.

6.1.2. Specimen manufacturing process

For conducting fatigue tests in the present study, four WAAM walls were built using Lincoln Electric ER70S-6 welding wire[18], with the chemical composition summarised in Table 6.1. The Cold Metal Transfer (CMT) based WAAM process was implemented, with manufacturing process parameters summarised in Table 6.2. To minimise the microstructural variability of different WAAM walls, all manufacturing parameters were kept the same for all four walls. Each WAAM wall was built in the middle of the base plate, made of EN10025 rolled structural steel, with dimensions of approximately 420 × 200 × 12 mm^3. As shown in Figure 6.1, the base plate was rigidly fixed onto the working table using eight clamps (two on each side of the base plate). This helped to minimise bending and distortion of the base plate and WAAM wall due to high manufacturing temperatures. The clamps were released once the wall was completed and cooled down to the ambient temperature. Additive layers were deposited on top of each other using an oscillation pattern[8], in order to produce relatively thick walls of approximately 24 mm in thickness (Y-direction in Figure 6.1), 355 mm in length (X-direction) and 140 mm in height (Z-direction). As shown in Figure 6.1, the WAAM fabrication set-up consisted of the CMT power source, a robotic arm with the torch feeding the wire and supplying shielding gas simultaneously. An exhaust fan was set above the WAAM wall to remove the generated heat and fumes.

Upon completion of the WAAM walls fabrication process, sixty smooth round bar (SB) specimens were extracted using the Electrical Discharged Machining (EDM) technique. Specimens were extracted along two different orientations: vertical (V) – perpendicular to the AM layers, and horizontal (H) – oriented along the deposited layers. An example of the schematic extraction plan for one of the WAAM walls is displayed in Figure 6.2 (a), where

specimens denoted B-1 – B-6 have horizontal and B-7 – B-16 have vertical orientations. The round bar specimens were designed in accordance with the ASTM E466 standard[19], and the key dimensions are presented in Figure 6.2 (b).

Table 6.1: Chemical composition of ER70S-6 material (wt.-%)[18]

	C	*Mn*	*Cr*	*Si*	*Ni*	*Mo*	*S*	*P*	*Cu*	*V*
ER70S-6	0.09	<1.60	0.05	0.09	0.05	0.05	0.007	0.007	0.20	0.05

Table 6.2: CMT-WAAM fabrication process parameters

Shielding gas	Ar+20% CO_2
Gas flow rate	15 L/min
Wire diameter	1.2 mm
Robot travelling speed	7.33 mm/sec
Wire feed speed	7.5 m/min
Dwell time	120 sec

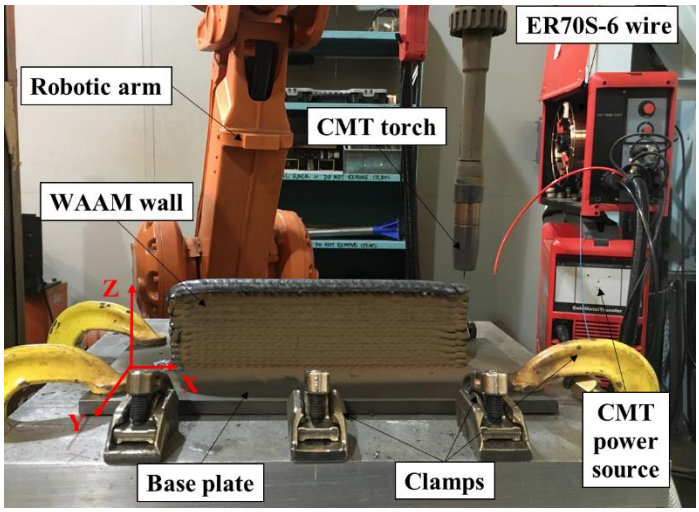

Figure 6.1: CMT system set up and the WAAM deposition process

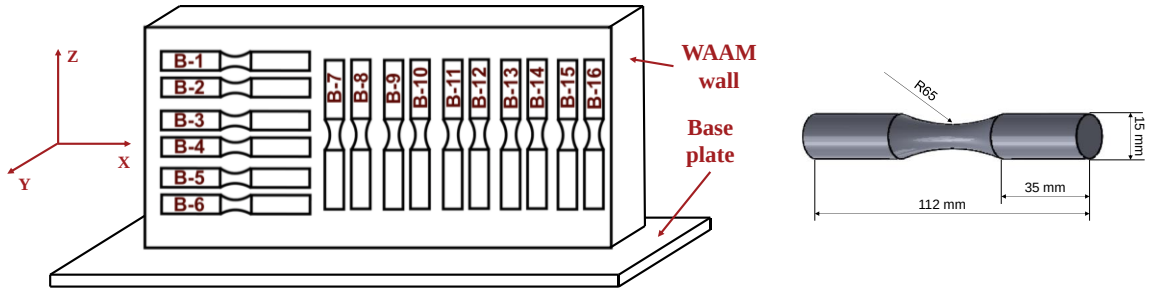

(a) (b)

Figure 6.2: (a) Schematic extraction plan for a WAAM wall, and (b) cylindrical specimen dimensions

6.1.3. Testing and data analysis methodology

- **Fatigue tests**

All fatigue tests under uniaxial, torsion, and multiaxial loading conditions were performed using an MTS landmark servo-hydraulic test machine with the load cell capacity of 100 kN, under load control mode with a frequency of 20 Hz and the load ratio of R=0.01. The test machine was accurately tuned prior to the start of the testing phase to ensure that the intended load levels were precisely applied on the test specimens. Moreover, alignment checks were conducted to ensure that the fatigue response of the WAAM built material is examined in the absence of any bending stresses. For multiaxial fatigue tests, a biaxiality ratio of λ = 1 was used, with phase angle $\Phi = 0^0$ (in phase loading). The stress-fatigue life diagrams were obtained separately for vertical and horizontal specimens, to capture the sensitivity of the fatigue behaviour to specimen extraction orientation. On average around 10 specimens were tested for each fatigue loading condition (uniaxial, torsion and multiaxial) and specimen orientation (vertical and horizontal). In this experimental test programme, specimens that endured 2×10^6 cycles were considered as run-out. The obtained fatigue data were analysed using 10% (upper bound), 50% (mean curve) and 90% (lower bound) probability of failure bands according to procedure described in the BS ISO 12107:2003[20] and ASTM E739-10[21] standards, and the data were plotted to obtain the inverse slope, k, of the Wöhler curves and scatter index, T_σ, in the fatigue data analysis. In this assessment, T_σ is the ratio between the stress level corresponding to 10% and 90% of survival probability. The calculated stresses for uniaxial loading were the nominal stress at the net section of the specimen. In case of torsion loading, the presented stresses were the maximum values in the cross section (the stress at the surface). As for the multiaxial loading, since the biaxiality ratio was λ = 1, only one of the stresses (tension or torsion) was used for illustration.

According to the procedure given in the literature, the uniaxial fatigue data can be analysed using the following equation, which is often referred to as Basquin relationship.

$$N_f = A(\Delta\sigma)^B \qquad \text{Equation 6.1}$$

Equation 6.1 shows that the number of cycles to failure N_f can be correlated with the cyclic stress range $\Delta\sigma$ using a power-law equation. The power-law constants in this equation, A and

B, are material dependent and can be obtained using a line of best fit made to the data. In this research, a similar approach has been adopted by plotting the maximum applied stress against the number of cycles to failure in uniaxial fatigue tests. The inverse slope obtained from this analysis is: $k = 1/B$. Similar power-law relationships have been employed to correlate torsion and multiaxial fatigue stresses with the number of cycles to failure.

- **Fractography analysis**

Upon completion of the fatigue tests, six specimens were selected for post-mortem microscopy analysis to study the failure mechanisms in the specimens subjected to different type of fatigue load (uniaxial, torsion and multiaxial) and oriented along different directions (vertical and horizontal). The fractography analysis was carried out using the FEI Quanta 650 FEG scanning electron microscope (SEM). In order to directly compare the observations on the fracture surfaces, the specimens subjected to the same fatigue load level with different orientations and fatigue load types were selected for the SEM analysis. The results obtained from the post-mortem analysis were implemented in conjunction with the experimental data in order to provide an accurate interpretation of the fatigue behaviour of the WAAM built specimens under different fatigue load types and for different specimen orientations.

6.1.4. Experimental results and discussions

- **Fatigue test results**

The fatigue test data for WAAM built ER70S-6 specimens for different specimen orientations and different loading types are shown in Figure 6.3 in log-log axes. These data were analysed following the procedure detailed in Section 6.1.3, by plotting the maximum stress against the number of cycles to failure, and the resulting fatigue properties are summarised in Table 6.3. In this table, $\Delta\sigma_{50\%}$ is the fatigue strength at 2×10^6 cycles, T_σ is the scatter index, and k is the inverse slope factor. The experimental data from uniaxial fatigue tests on vertical and horizontal specimens are presented in Figure 6.3 (a) and (b), respectively, with the obtained trends directly compared with each other in Figure 6.3 (c). It can be observed in Figure 6.3 (a-c) that under uniaxial loading condition the fatigue strength of 436 MPa and 384 MPa was obtained for vertical and horizontal specimens, respectively, indicating that the fatigue strength of the vertical specimens was higher than the horizontal. Comparison of the S-N data sets for different specimens orientations in Figure 6.3 (c) shows that a much steeper slope can be observed for the horizontal specimens, which is also indicated by the inverse slope factor that is 2.6 times higher for the vertically oriented specimens compared to the horizontal samples reported in Table 6.3. As it was previously reported by Ermakova et al.[22], WAAM built ER70S-6 specimens with horizontal orientation have a higher yield strength (390 MPa) than the vertical (365 MPa), hence it is expected that the material with higher yield strength (horizontal orientation) will have a lower fatigue life[23], confirming the trends observed in Figure 6.3 (a-c). Moreover, having higher value of yield strength along with higher elongation at failure (higher ductility), possibly resulting in higher fatigue strength at high load level for horizontal specimens (0.77 mm/mm), compared with the vertical (0.71 mm/mm)[22]. It also can be noted here that the fatigue strengths obtained in the study for the horizontal and vertical specimens are close to and above the orientation-specific yield stress of the material, respectively. As seen

in Table 6.3 the analysis of the test results show that the scatter index observed in uniaxial fatigue data is comparable for both specimen orientations and differs only by 2%. Finally observed in the uniaxial fatigue data is that while the fatigue life in horizontal specimens is generally lower than the vertical specimens at low stress levels, this trend can be switched at higher stress levels if the obtained trend from horizontal specimens is extrapolated to the high stress region.

The fatigue data from torsion tests on vertical and horizontal specimens are presented in Figure 6.3 (d) and (e), respectively, with the obtained trends directly compared with each other in Figure 6.3 (f). As seen in Figure 6.3 (d-f), the fatigue strengths of vertical and horizontal specimens are found to be 324 MPa and 355 MPa, respectively, indicating similar, though slightly higher, fatigue strength in horizontal specimens compared to the vertical. This increase in the fatigue strength of horizontal specimens tested under torsion can be attributed to the higher ductility of this orientation resulting in higher stress shielding in the specimen. As seen in Table 6.3 the analysis of the torsion test results show that the scatter index is similar for both orientations with 1.19 for vertical against 1.16 for horizontal specimens. Moreover, the inverse slope factor has been found to be higher for horizontally oriented specimens compared to vertical by 43%, with a steeper slope for the vertical specimens data set.

The fatigue data from multiaxial fatigue tests on vertical and horizontal specimens are presented in Figure 6.3 (g) and (h), respectively, with the obtained trends directly compared with each other in Figure 6.3 (i). It can be observed in Figure 6.3 (g) and (h) that the fatigue strengths obtained from vertical and horizontal specimens under multiaxial loading condition are 229 MPa and 245 MPa, respectively, indicating 6.5% higher value of fatigue strength for the horizontal specimens compared to the vertical. Analysing the experimental data from multiaxial tests shows that the values for the scatter index in vertical and horizontal data sets are comparable within 0.8% for specimens with different orientations. Finally observed in the results from multiaxial fatigue test data is that the difference in the inverse slope factors for specimens with different orientations drops to 16.6%, with slightly higher value (hence lower slope) observed for the horizontal specimens compared to the vertical data set (see Table 6.3). It should be noted here that the presented preliminary trends in this study are indicative representation of the fatigue behaviour of WAAM built ER70S-6 specimens, hence further repeat tests are required for design curves development for the material.

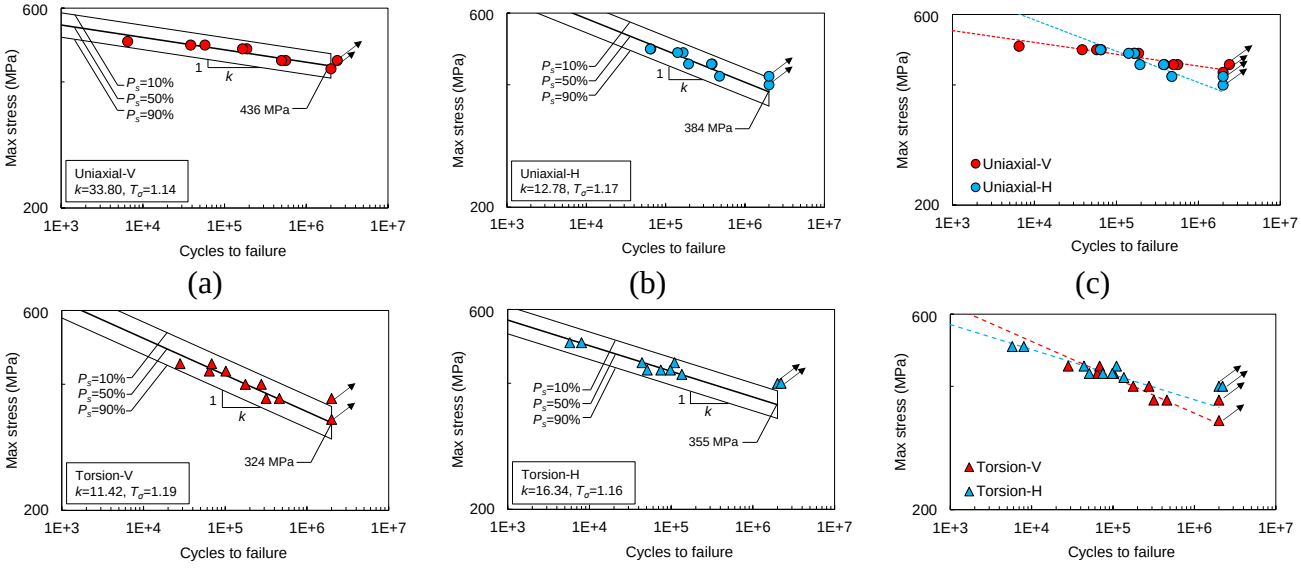

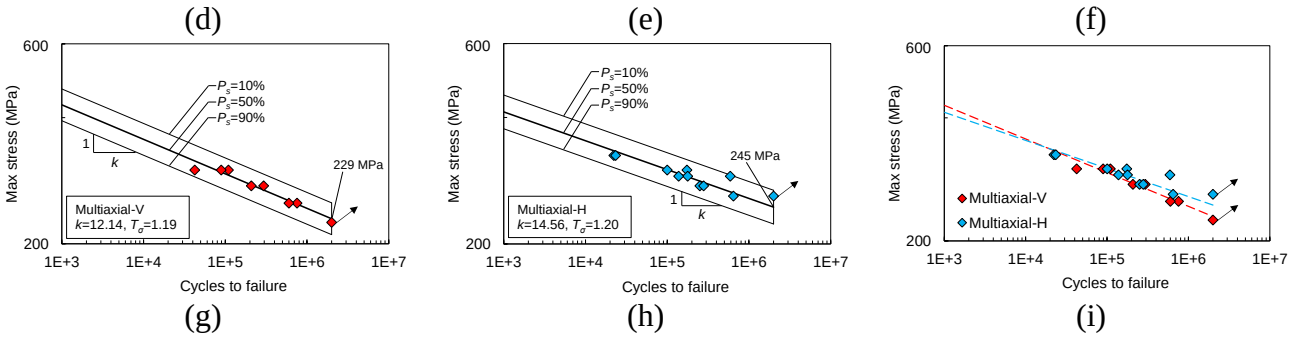

Figure 6.3: Fatigue test data for ER70S-6 specimens under (a-c) uniaxial, (d-f) torsion, and (g-i) multiaxial loading conditions

Table 6.3: Fatigue behaviour of tested ER70S-6 specimens

Test	Orientation	$\Delta\sigma_{50\%}$ [MPa]	T_σ	k
Uniaxial	V	436	1.14	33.80
	H	384	1.17	12.78
Torsion	V	324	1.19	11.42
	H	355	1.16	16.34
Multiaxial	V	229	1.19	12.14
	H	245	1.20	14.56

Further comparison of all fatigue data obtained from the current study is presented in Figure 6.4. This figure shows that a decreasing overall trend in fatigue strength can be observed from uniaxial fatigue to torsion and further to multiaxial fatigue tests. The analysis of the presented results in Figure 6.4 and Table 6.3 reveals that compared to the uniaxial test results the average fatigue strength of the material (i.e. the mean value between fatigue strength of vertical and horizontal specimens) drops by 15% for specimens tested under torsion and by 42% for specimens tested under multiaxial loading condition considering solely the tension or torsion applied stress. This observation confirms that the fatigue strength of the ER70S-6 WAAM built specimens is sensitive to the fatigue loading type, as expected. Moreover, the experimental data obtained from specimens with different orientations indicates that in addition to the type of the fatigue loading (i.e. uniaxial, torsion and multiaxial), the results are also sensitive to the specimen orientation. Comparison of the fatigue strengths in vertical and horizontal specimens tested under different fatigue loading types shows that highest difference, which is 12%, is observed in specimens tested under pure uniaxial loading condition, whereas this difference gradually reduces to 9% in torsion fatigue tests and 6.5% in multiaxial fatigue tests. It is also worth noting that due to varying inverse slope factors for data sets with different specimen orientations obtained under different fatigue load types, the data sets intersect when the observed trends are extrapolated to lower number of cycles. This suggests that the performance of one specimen orientation is better at lower number of cycles and then gradually deteriorates at higher number of cycles, and vice versa. The general observation in Figure 6.4 shows that under torsion and multiaxial loads, horizontal specimens display higher fatigue strengths at 2 million cycles (run-out limit) than vertical, whereas for uniaxial load, the vertical orientation exhibits a higher fatigue strength than the horizontal.

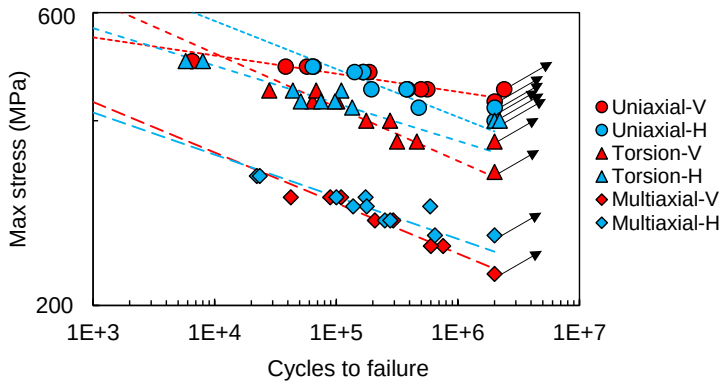

Figure 6.4: Comparison of all experimental data for ER70S-6 WAAM specimens under different fatigue load types

- **Comparison with the literate data and design curves**

In order to assess the fatigue performance of ER70S-6 WAAM built specimens for fatigue design and life assessment of offshore structures, the obtained fatigue data from this study have been compared with the S-N fatigue design curve recommended for the continuous welds (C1) by the DNV RP-C203 standard[24], and with available data in the literature on uniaxial, torsion and multiaxial fatigue for structural steels. It is known that the fatigue behaviour of engineering materials is dependent on the load ratio and specimen design[25,26]; however, due to the limited data available in the literature some of the data presented in this section are for specimen designs that differ from the ones employed in this study. In order to normalise the fatigue data under various stress ratios collected form the literature into a single fatigue plot, the effective stress model was employed, using the following Equation 6.2. The concept of the effective stress was introduced by Li et al.[27] and is used for direct comparison of fatigue data from different studies. This model does not consider the effect of loading frequency, therefore limited effect of different loading frequencies is expected.

$$\sigma_{eff} = \sigma_{max}\left(\frac{1-R}{2}\right)^{0.28} \qquad \text{Equation 6.2}$$

It can be seen in Figure 6.5 that the obtained experimental data for ER70S-6 WAAM built specimens from this study fall ahead of the C1 design curve from the DNV standard for horizontal specimens above 10,000 cycles, and for vertical specimens above 39,500 cycles, indicating that with the exception of extremely high stress range values the DNV recommended C1 design curve provides a conservative estimate of the fatigue life in ER70S-6 WAAM built specimens. Having said that, it can be seen that the slopes for the experimental S-N curves are lower compared with the standard curve.

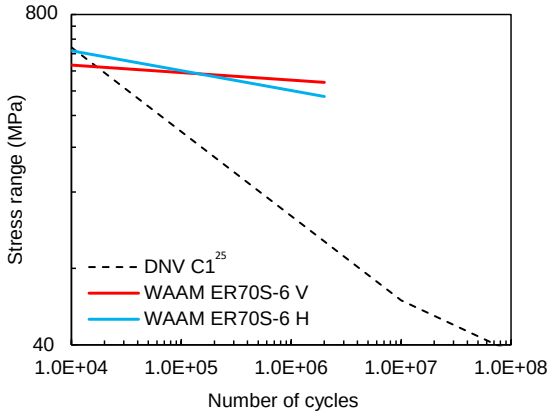

Figure 6.5: Comparison of uniaxial fatigue data for ER70S-6 WAAM specimens with the DNV C1 standard

Along with the C1 S-N fatigue design curve provided by DNV standard, the 50% uniaxial fatigue failure bands (i.e. mean curves) for ER70S-6 WAAM built specimens were also compared with a series of S-N curves obtained from S355 wrought steel specimens. S355 structural steel is commonly used in offshore structure and marine renewable energy applications, hence the results were compared with this material to assess the suitability of WAAM built steel structure for offshore applications[28,29]. Large dog bone S355 specimens tested at R=0.1 by Anandavijayan et al.[23], smaller flat dog bone specimens assessed at R=-1 by Corigliano et al.[30], cylindrical specimens tested at R=0.01 by Dantas et al.[31], and at R=-1 by Aeran et al.[32], fillet welded cruciform specimens examined at R=0 by Berto et al.[33], and S-N curves for wrought C40 carbon steel cylindrical specimens generated at R=-1 by Atzori et al.[34] were considered for comparison with the results obtained from the present study. Moreover, the uniaxial fatigue data available on ER70S-6 WAAM built flat dog bone specimens tested at R=0.1 by Dirisu et al.[17] and G3Si1 WAAM as built flat dog bone specimens (with rough surface) tested at R=0.1 for two different specimen designs by Bartsch et al.[6] were used for comparison purposes. All experimental uniaxial data from the literature are summarised and presented in Figure 6.6 (a) as effective stress versus number of cycles.

Comparison of the obtained data from the present study with the S-N curves literature data on S355 steel specimens reveals that the uniaxial data for ER70S-6 WAAM built specimens overlap with the upper bound for the S355 cloud, suggesting generally higher fatigue life compared to the wrought material. The direct comparison with the results on S355 specimens with similar design and tested with the same stress ratio R=0.01[31] demonstrates that the higher fatigue life was exhibited in WAAM specimens, where S355 S-N curve has similar slope with the vertical WAAM specimens. It can be seen in Figure 6.6 (a) that a different specimen design from an independent study on ER70S-6 WAAM specimens tested under different loading conditions[17] resulted in S-N curve slightly below the horizontal and vertical curves obtained from this study, confirming the general trend for the WAAM specimens made with ER70S-6 steel and highlighting the sensitivity to the test frequency and specimen design. The above observations lead to a conclusion that ER70S-6 steel parts produced by means of WAAM technology can be considered for manufacturing or repair of offshore structures and an alternative to conventional structural steels and manufacturing technologies.

Due to the limited data available on torsion and multiaxial fatigue for steels in the literature, only a few curves were found and presented for comparison with the experimental data from

this study in Figure 6.6 (b) and (c), data is also presented as effective stress versus number of cycles. One source presents the behaviour of cylindrical C40 carbon steel specimens tested with loading ratio of R=-1 for torsion and R=0 for multiaxial tests by Atzori et al.[34], and another source covers cylindrical 39NiCrMo3 steel specimens examined under R=-1 by Berto et al.[35] Additional data set was found and displayed for multiaxial fatigue comparison on wrought cylindrical S355 specimens tested under R=0.01[31], hence valid for the direct comparison with the data obtained from the present study. For presented multiaxial fatigue data a biaxiality ratio was λ = 1, with in phase loading angle $\Phi = 0^0$. It can be seen in Figure 6.6 (b) that the torsion fatigue trends for WAAM ER70S-6 specimens fall close to the 39NiCrMo3 steel specimens, and above C40 carbon steel. With regards to multiaxial fatigue behaviour, the results for WAAM tested specimens in Figure 6.6 (c) are above those obtained for C40 carbon steel specimens with shallower slope, but lower than S355 and 39NiCrMo3 steel. The slope for S355 specimens is similar to the data obtained from this study, and the data set falls slightly above the ER70S-6 WAAM built specimens data, suggesting similar but slightly higher fatigue life under multiaxial loading in S355 specimens.

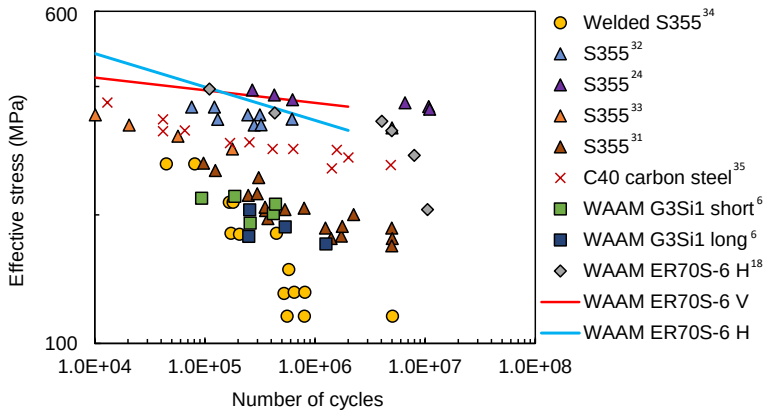

(a)

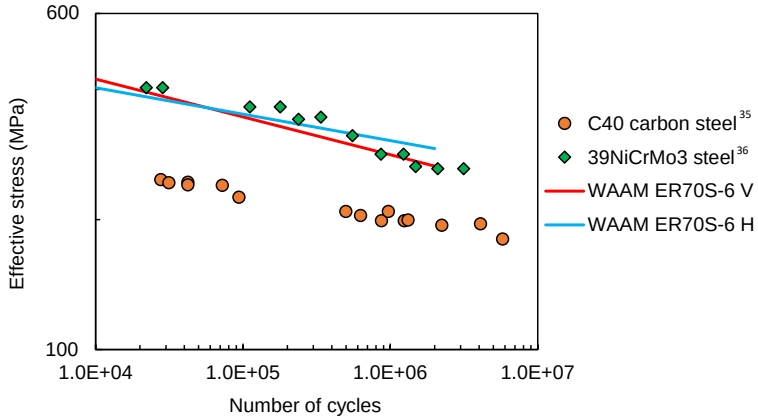

(b)

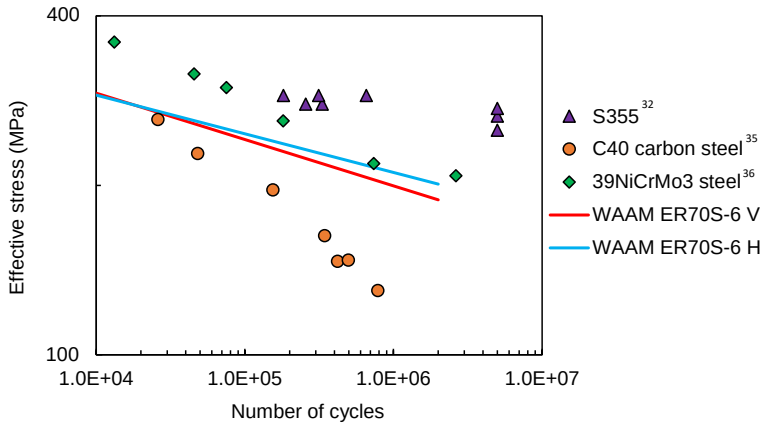

(c)

Figure 6.6: Comparison of the obtained fatigue data from ER70S-6 WAAM specimens with the literature data on: (a) uniaxial, (b) torsion and (c) multiaxial fatigue tests

- **Fractography analysis**

The microstructural investigation by means of SEM showed an almost defect-free material in all ER70S-6 WAAM built specimens with some occasional defects with dimensions of less than 30 μm. The fractography analysis was performed on fatigue tested specimens to examine differences in failure mechanisms in specimens with different orientations under different types of fatigue loading condition (uniaxial, torsion and multiaxial). Examples of fracture surfaces obtained from uniaxial fatigue tests under 480 MPa are shown in Figure 6.7 (a) for vertical and Figure 6.7 (b) for horizontal ER70S-6 WAAM built specimens. Four distinct crack growth stages are indicated in both figures, starting with the crack initiation in area 1, crack growth in area 2 (where white arrows show the direction of the crack growth propagation), and ductile failure in region 3 due to unstable fatigue crack growth, followed by the ductile failure in region 4 due to fast fracture. The presented fracture surface for the horizontal specimen consists of two crack initiation sites (Figure 6.7 (b)), in which cracks started simultaneously in two parallel planes and subsequently merged into one in the crack growth area 2. In both cases the crack nucleated from the surface irregularities. In the crack growth region for both vertical and horizontal specimens the fatigue striations can be observed, which are perpendicular to the crack growth plane (marked with yellow arrows). Also observed in the figures are the elongated fracture features parallel to the crack growth direction (shown in yellow dashed lines). The fracture surface in regions 1 and 2 for the vertical specimens indicates shallower ductile features, whereas the fracture surface of horizontal specimen in the same regions exhibits deeper dimples. This is in good agreement with slightly higher ductility of the horizontal specimens. Lastly, it can be observed that even though both specimens were tested under the same loading condition uniaxial fatigue load, the areas for first three crack growth stages 1-3 are larger for the vertical specimen, which resulted in longer performance of the specimen under this load level. The shorter fatigue life of the horizontal specimen in this case can also be affected by two independent crack planes contributing to the final failure of the specimen.

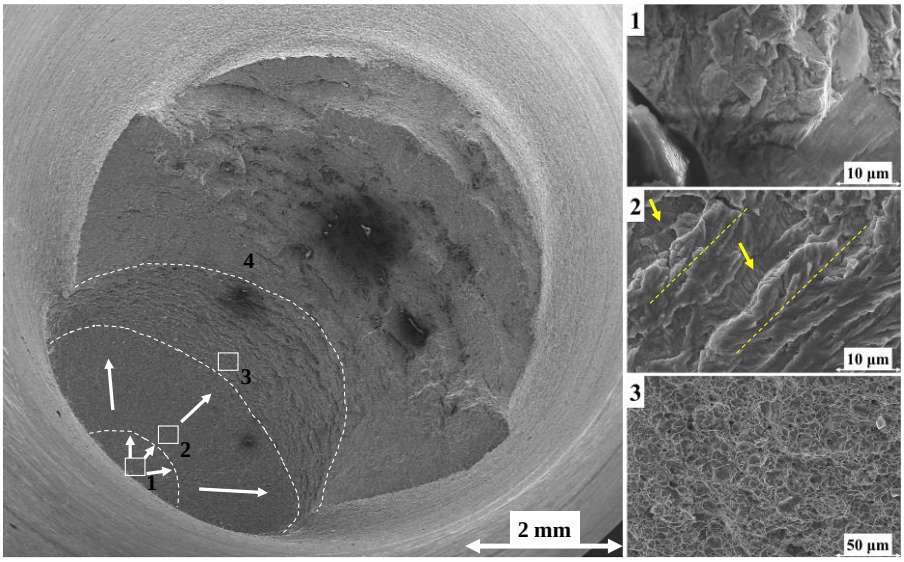

(a)

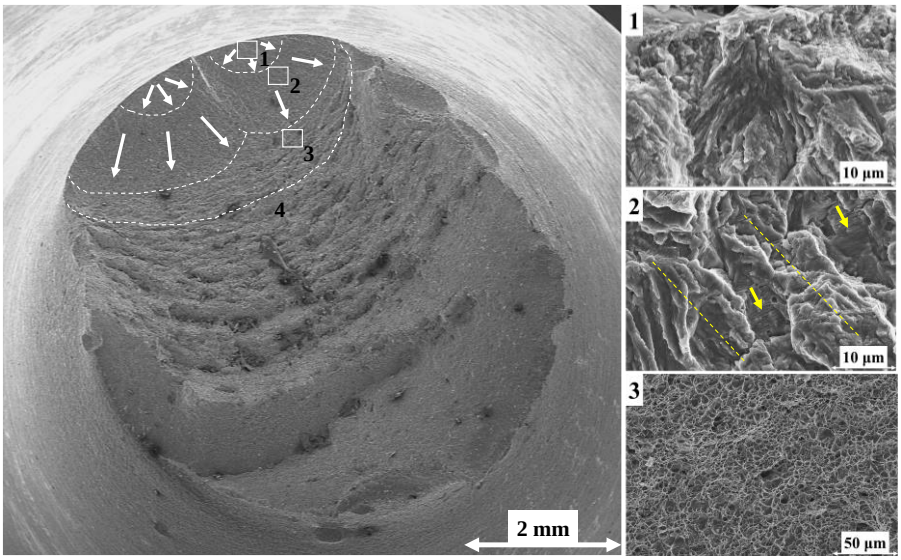

(b)

Figure 6.7: Fracture surface of ER70S-6 WAAM built specimens tested under uniaxial loading condition (a) for vertical, and (b) for horizontal specimens, presenting crack initiation region (1), crack propagation region (2), and ductile fracture region (3), and fast fracture region (4)

The failure surfaces of vertical and horizontal specimens tested under 448 MPa torsion fatigue load are shown in Figure 6.8 (a) and (b), respectively. It can be seen in this figure that the outer diameter of the fracture surface is flat in both specimens, suggesting the contact of the two faces of initiated crack under mode III loading condition in these test specimens. The larger area of fracture surface in both cases indicates the evidence of abrasion, demolishing all fracture features under out-of-plane shear, by rubbing the fracture surfaces against each other. Only 18% of the fracture surface of vertical specimen and 28.5% of horizontal specimens retained fatigue fracture features. This was also reflected in exhibited number of cycles, which

is 1.6 times higher for the vertical specimen compared to the horizontal specimen. The remaining fatigue fracture area is due to the final specimen failure under mode I fracture mechanics condition, resulting in cascade of several fatigue fracture planes with visible boundaries of ductile fracture between them (marked with white arrows), which is also referred to as 'factory roof' morphology[35,36]. The ductile cup and cone features are more pronounced for horizontally oriented specimen, which failed at lower number of cycles. Fatigue striations can be observed on the fracture surface of both specimens and highlighted with yellow arrows. Although the abrasion of crack planes eliminated some of the fracture features under torsion loading, by comparing fracture surfaces of the specimens tested under uniaxial and torsion fatigue it can be seen that the surface area after uniaxial testing is approximately two times smaller, due to ductile elongation of the specimen under pure mode I fracture mechanics condition.

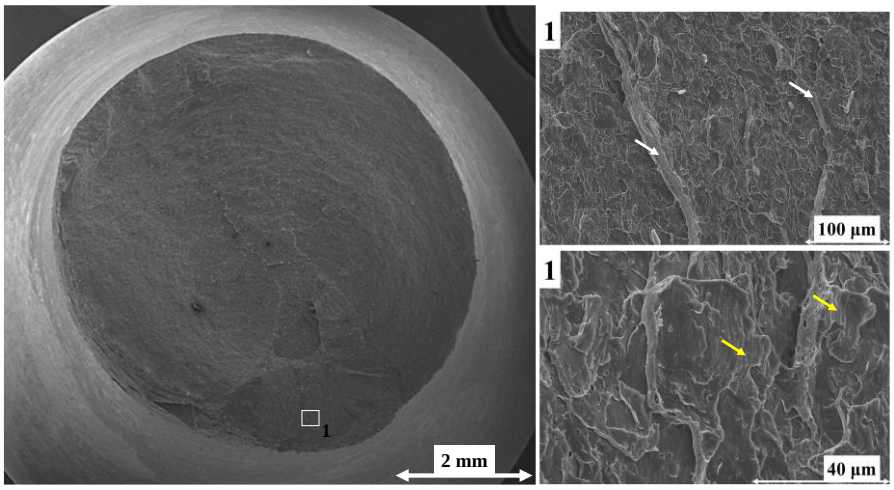

(a)

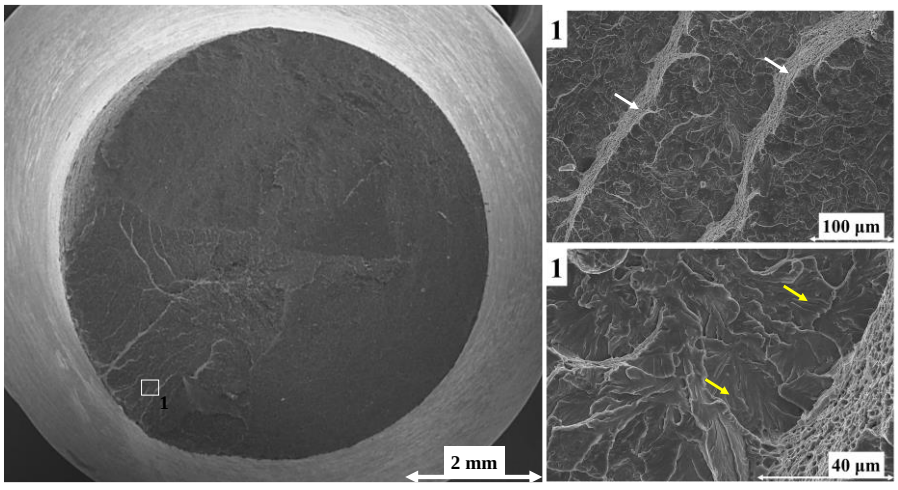

(b)

Figure 6.8: Fracture surface of ER70S-6 WAAM built specimens tested under torsion loading condition (a) for vertical, and (b) for horizontal specimens

Fracture surfaces of the specimens tested under multiaxial fatigue load of 300 MPa are shown in Figure 6.9 (a) for vertical and (b) for horizontal specimens. Comparable features of 'factory roof' can be observed on both specimen surfaces, which are located in central part of the

fracture area and indicated as region A. Similar to the fracture surfaces after torsion fatigue failure a considerable proportion (40-45%) of the two broken specimens has been found to be flat and consists of evidence of wear and abrasion, suggesting mode III fracture mechanics condition in region B. In this area two main fatigue features were observed and marked with yellow arrows: 1 – fatigue striations, and 2 – colonies of flat 'fish-bone' features indicating large striations near the specimen surface and parallel to it. The remaining cone surface is corresponding to the fast fracture which is shown as region C. As expected, due to combination of tension and torsion loading conditions the fracture surface area after multiaxial fatigue testing is larger than for pure uniaxial load (on average by 35%) and smaller than for pure torsion load (on average by 23%).

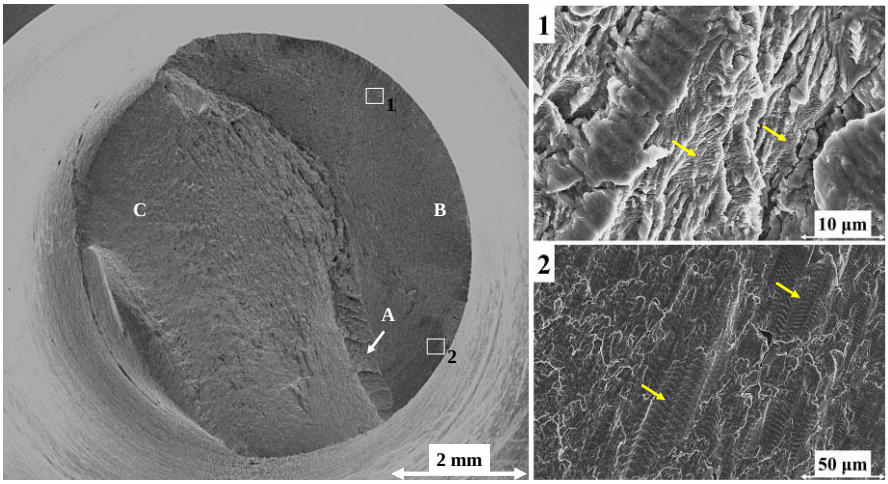

(a)

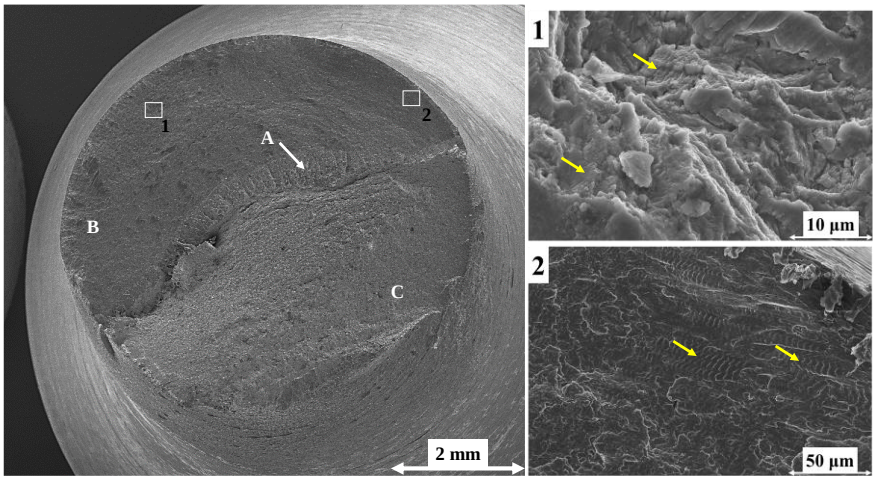

(b)

Figure 6.9: Fracture surface of ER70S-6 WAAM built specimens tested under multiaxial loading condition (a) for vertical, and (b) for horizontal specimens, presenting fatigue (1) and fishbone (2) features

6.1.5. Conclusions

Fatigue tests were conducted on sixty ER70S-6 WAAM built specimens to examine the uniaxial, torsion and multiaxial fatigue properties. Specimens were extracted from the WAAM walls in two distinct orientations: vertical and horizontal. The main conclusions and observations from this study are summarised below:

- Sensitivity of the fatigue results to the specimen orientation was observed during this study. Higher fatigue strength was found for vertical specimens tested under uniaxial load, however, under torsion and multiaxial load, the horizontal specimens exhibited higher fatigue strength.
- The difference between fatigue strength for specimens with different orientations dropped for results obtained from torsion fatigue tests and further reduced for multiaxial fatigue compared with uniaxial test results.
- The S-N data show that material with the higher yield stress (horizontal orientation) exhibited lower fatigue life. The yield stress of vertical specimens is 16% lower than the uniaxial fatigue strength.
- Comparison of the obtained fatigue data for ER70S-6 WAAM built specimens with the existing fatigue data on structural steels in the literature revealed that the S-N data from this study overlap with the upper bound of the fatigue results for wrought S355 steel.
- The S-N fatigue data from this study exhibited a higher trend compared to the recommended DNV C1 design curve. This suggests that the tested material and WAAM technique can be considered to be used for fabrication of offshore structures.
- Analysis of the fatigue data on torsion and multiaxial fatigue available in the literature demonstrated similar trends with C40 carbon steel and S355 steel.
- Fracture surfaces of six specimens (two orientations for each fatigue load type) were analysed with SEM and fracture mechanisms and features were compared for different types of loading. The WAAM built material employed in this study was found to be almost defect-free with some minor defects of smaller than 30 μm.

6.1.6. Acknowledgements

This work was supported by grant EP/L016303/1 for Cranfield, Oxford and Strathclyde Universities' Centre for Doctoral Training in Renewable Energy Marine Structures – REMS CDT (http://www.remscdt.ac.uk/) from the UK Engineering and Physical Sciences Research Council (EPSRC). Special thanks to the NTNU structural integrity research group for conducting the fatigue testing in their laboratory.

6.1.7. References for paper VIII

1. Razavi, S. M. J., Ferro, P. & Berto, F. Fatigue assessment of Ti–6Al–4V circular notched specimens produced by selective laser melting. *Metals (Basel).* **7**, 1–10 (2017).

2. Fotovvati, B., Namdari, N. & Dehghanghadikolaei, A. Fatigue performance of selective laser melted Ti6Al4V components: State of the art. *Mater. Res. Express* **6**, (2019).

3. Lee, Y. S. & Zhang, W. Modeling of heat transfer, fluid flow and solidification microstructure of nickel-base superalloy fabricated by laser powder bed fusion. *Addit. Manuf.* **12**, 178–188 (2016).

4. Domashenkov, A., Plotnikova, A., Movchan, I., Bertrand, P., Peillon, N., Desplanques, B., Saunier, S. & Desrayaud, C. Microstructure and physical properties of a Ni/Fe-based superalloy processed by Selective Laser Melting. *Addit. Manuf.* **15**, 66–77 (2017).

5. Todai, M., Nakano, T., Liu, T., Yasuda, H. Y., Hagihara, K., Cho, K., Ueda, M. & Takeyama, M. Effect of building direction on the microstructure and tensile properties of Ti-48Al-2Cr-2Nb alloy additively manufactured by electron beam melting. *Addit. Manuf.* **13**, 61–70 (2017).

6. Bartsch, H., Kühne, R., Citarelli, S., Schaffrath, S. & Feldmann, M. Fatigue analysis of wire arc additive manufactured (3D printed) components with unmilled surface. *Structures* **31**, 576–589 (2021).

7. Seow, C. E., Zhang, J., Coules, H. E., Wu, G., Jones, C., Ding, J. & Williams, S. Effect of crack-like defects on the fracture behaviour of Wire + Arc Additively Manufactured nickel-base Alloy 718. *Addit. Manuf.* **36**, 101578 (2020).

8. Ermakova, A., Mehmanparast, A. & Ganguly, S. A review of present status and challenges of using additive manufacturing technology for offshore wind applications. *Procedia Struct. Integr.* **17**, 29–36 (2019).

9. ASM. ASM International Fatigue. *Elem. Metall. Eng. Alloy.* 243–265 (2008).

10. Pegues, J., Roach, M., Scott Williamson, R. & Shamsaei, N. Surface roughness effects on the fatigue strength of additively manufactured Ti-6Al-4V. *Int. J. Fatigue* **116**, 543–552 (2018).

11. Syed, A. K., Zhang, X., Caballero, A., Shamir, M. & Williams, S. Influence of deposition strategies on tensile and fatigue properties in a wire + arc additive manufactured Ti-6Al-4V. *Int. J. Fatigue* **149**, 106268 (2021).

12. Springer, S., Leitner, M., Gruber, T., Oberwinkler, B., Lasnik, M. & Grün, F. Fatigue Assessment of Wire and Arc Additively Manufactured Ti-6Al-4V. *Met. 2022, Vol. 12, Page 795* **12**, 795 (2022).

13. Biswal, R., Zhang, X., Shamir, M., Al Mamun, A., Awd, M., Walther, F. & Khadar Syed, A. Interrupted fatigue testing with periodic tomography to monitor porosity defects in wire + arc additive manufactured Ti-6Al-4V. *Addit. Manuf.* **28**, 517–527 (2019).

14. Shamir, M., Syed, A. K., Janik, V., Biswal, R. & Zhang, X. The role of microstructure and local crystallographic orientation near porosity defects on the high cycle fatigue life of an additive manufactured Ti-6Al-4V. *Mater. Charact.* **169**, 110576 (2020).

15. Shrestha, R., Simsiriwong, J. & Shamsaei, N. Fatigue behavior of additive manufactured 316L stainless steel under axial versus rotating-bending loading: Synergistic effects of stress gradient, surface roughness, and volumetric defects. *Int. J. Fatigue* **144**, 106063 (2021).

16. Zulić, S., Rostohar, D., Kaufman, J., Pathak, S., Kopeček, J., Böhm, M., Brajer, J. & Mocek, T. Fatigue life enhancement of additive manufactured 316l stainless steel by LSP using a DPSS laser system. *https://doi.org/10.1080/02670844.2022.2060463* (2022). doi:10.1080/02670844.2022.2060463

17. Dirisu, P., Supriyo, G., Martina, F., Xu, X. & Williams, S. Wire plus arc additive manufactured functional steel surfaces enhanced by rolling. *Int. J. Fatigue* **130**, 105237 (2020).

18. Lincoln Electric Company, T. *LINCOLN ® ER70S-6 WELDING POSITIONS TYPICAL APPLICATIONS*.

19. Standard Practice for Conducting Force Controlled Constant Amplitude Axial Fatigue Tests of Metallic Materials. Available at: https://www.astm.org/e0466-21.html. (Accessed: 5th July 2022)

20. BS ISO 12107-2003--[2022-07-06--10-12-27 AM].pdf.

21. Testing, F. Standard Practice for Statistical Analysis of Linear or Linearized Stress-Life (. *Stat. Anal. Fatigue Data* **91**, 129-129–9 (2009).

22. Ermakova, A., Mehmanparast, A., Ganguly, S., Razavi, J. & Berto, F. Investigation of mechanical and fracture properties of wire and arc additively manufactured low carbon steel components. *Theor. Appl. Fract. Mech.* **109**, 102685 (2020).

23. Anandavijayan, S., Mehmanparast, A., Braithwaite, J., Brennan, F. & Chahardehi, A. Material pre-straining effects on fatigue behaviour of S355 structural steel. *J. Constr. Steel Res.* **183**, 106707 (2021).

24. (DNV) Det Norske Veritas. Fatigue Design of Offshore Steel Structures. *Recomm. Pract. DNV-RPC203* 126 (2005).

25. Razavi, S. M. J., Van Hooreweder, B. & Berto, F. Effect of build thickness and geometry on quasi-static and fatigue behavior of Ti-6Al-4V produced by Electron Beam Melting. *Addit. Manuf.* **36**, 101426 (2020).

26. Berto, F., Campagnolo, A. & Lazzarin, P. Fatigue strength of severely notched specimens made of Ti-6Al-4V under multiaxial loading. *Fatigue Fract. Eng. Mater. Struct.* **38**, 503–517 (2015).

27. Li, P., Warner, D. H., Fatemi, A. & Phan, N. Critical assessment of the fatigue performance of additively manufactured Ti-6Al-4V and perspective for future research. *Int. J. Fatigue* **85**, 130–143 (2016).

28. Mehmanparast, A., Taylor, J., Brennan, F. & Tavares, I. Experimental investigation of mechanical and fracture properties of offshore wind monopile weldments: SLIC interlaboratory test results. *Fatigue Fract. Eng. Mater. Struct.* **41**, 2485–2501 (2018).

29. Mehmanparast, A., Brennan, F. & Tavares, I. Fatigue crack growth rates for offshore wind monopile weldments in air and seawater: SLIC inter-laboratory test results. *Mater. Des.* **114**, 494–504 (2017).

30. Corigliano, P., Cucinotta, F., Guglielmino, E., Risitano, G. & Santonocito, D. Fatigue assessment of a marine structural steel and comparison with Thermographic Method and Static Thermographic Method. *Fatigue Fract. Eng. Mater. Struct.* **43**, 734–743 (2020).

31. Dantas, R., Correia, J., Lesiuk, G., Rozumek, D., Zhu, S. P., de Jesus, A., Susmel, L. & Berto, F. Evaluation of multiaxial high-cycle fatigue criteria under proportional loading for S355 steel. *Eng. Fail. Anal.* **120**, 105037 (2021).

32. Aeran, A., Acosta, R., Siriwardane, S. C., Starke, P., Mikkelsen, O., Langen, I. & Walther, F. A nonlinear fatigue damage model: Comparison with experimental damage evolution of S355 (SAE 1020) structural steel and application to offshore jacket structures. *Int. J. Fatigue* **135**, 105568 (2020).

33. Berto, F., Mutignani, F. & Pittarello, L. Effect of hot-dip galvanization on the fatigue behaviour of welded structural steel. *Procedia Struct. Integr.* **2**, 1813–1820 (2016).

34. Atzori, B., Berto, F., Lazzarin, P. & Quaresimin, M. Multi-axial fatigue behaviour of a severely notched carbon steel. *Int. J. Fatigue* **28**, 485–493 (2006).

35. Berto, F., Lazzarin, P. & Yates, J. R. Multiaxial fatigue of V-notched steel specimens: A non-conventional application of the local energy method. *Fatigue Fract. Eng. Mater. Struct.* **34**, 921–943 (2011).

36. Berto, F., Lazzarin, P. & Marangon, C. Fatigue strength of notched specimens made of 40CrMoV13.9 under multiaxial loading. *Mater. Des.* **54**, 57–66 (2014).

6.2. Paper IX: Fatigue life assessment of wire arc additively manufactured ER100S-1 steel parts

Anna Ermakova[a], Javad Razavi[b], Rocco Crescenzo[b], Filippo Berto[b], Ali Mehmanparast[a*]

[a] Department of Naval Architecture, Ocean and Marine Engineering, University of Strathclyde, Glasgow G1 1XQ, United Kingdom

[b] Norwegian University of Science and Technology (NTNU), Trondheim, Norway

Abstract[9]

The aim of this work was to examine uniaxial, torsion, and multiaxial fatigue characteristics of ER100S-1 low carbon steel specimens fabricated with wire arc additive manufacturing (WAAM) technique a subcategory of directed energy deposition (DED). Two distinct specimen orientations were tested; vertical and horizontal, extracted perpendicular and parallel to the WAAM deposited layers, respectively. Fracture surfaces of the tested specimens were analysed under Scanning Electron Microscope (SEM) to observe fracture mechanisms corresponding to different specimen orientations, different fatigue loading conditions, and to interpret the fatigue results obtained from the tests. Finally, the obtained stress-life results were compared with the fatigue data available in the literature for a series of wrought and WAAM built structural steel specimens. Moreover, the S-N curves obtained in this study were evaluated against the fatigue design curve recommended for offshore marine welded structures in DNV standard. Test results have shown advantageous characteristics of WAAM built ER100S-1 specimens compared with behaviour of other structural steels and conservative prediction of its fatigue life by the design curve available in DNV standard.

[*] corresponding author

[9] Submitted manuscript in *Progress in Additive Manufacturing*. September 2022

6.2.1. Introduction

Additive manufacturing (AM) is a comparatively new method of fabricating a product directly from a 3D computer model by adding material in layers, where each layer is a thin cross-section from the corresponding 3D model[1]. This technique does not require any expensive moulds and production planning associated with conventional manufacturing procedures. Hence, it offers fabrication freedom, where the complexity of the final product form does not affect the manufacturing process. Since this process is based on adding material layer by layer rather than removing or subtracting it from a block of material, it is more sustainable and dramatically decreases the material waste. Even though all AM machines use a layer-based approach, the final product characteristics will depend on the deposition process, layer thickness, the employed material, etc. Such differences will affect the dimensional accuracy, material properties and mechanical behaviour[2].

Directed energy deposition (DED) process, which is often referred to as 'metal deposition' technology, enables parts fabrication by melting material as it is being deposited. Wire arc additive manufacturing (WAAM) is a type of DED process that feeds and melts metal wire for deposition. It allows fabrication of functionally graded components by melting and mixing wires with different composition. Fully dense parts are achievable by WAAM technique, with controllable microstructural features[3]. WAAM is most effective for simpler and bulky structures, without many thickness variations and with lower accuracy requirements, compared with powder-based techniques. WAAM provides the highest deposition rates among all AM methods (up to 5-8 kg/h depending on the employed material), whereas powder-based process can only offer up to 55 g/h[3,4]. Hence, it reduces the manufacturing time by 40-60% as well as post-machining time by 20% compared with the conventional manufacturing methods[3]. Moreover, the WAAM process is designed to be pore-free, sacrificing the dimensional accuracy[5]. On the other hand, all the advantages of the new technique are balanced with the following common defect characteristics due to the welding nature of the process: locked-in residual stresses, poor surface finish, deformations, delamination, etc[6]. Thus, some post-processing is usually required to address the above issues, such as machining, heat treatment and mechanical treatment on the WAAM wall surfaces. Also, the repetitive cycles of heating and cooling during the manufacturing process can lead to microstructural variations and anisotropic behaviour of the WAAM part[7–10].

The majority of failures in engineering structures and machinery are caused by fatigue[11]. Such failures usually happen with little warning, thus may bring catastrophic consequences. Therefore, fatigue of materials is an essential study for any new material and manufacturing technique in modern industries. This includes a broad variety of complex mechanical testing, investigating different stages of fatigue damage, to control nucleated cracks and prevent the final fatigue failure[12]. Having said that, fatigue assessment becomes crucial for AM built components that consist of welding defects and tensile residual stresses – two major factors contributing to the fatigue failures[13]. Some industries, such as aerospace and automotive, have already introduced and are widely implementing AM processes, thus the majority of reported data on fatigue performance of AM (and WAAM in particular) are for titanium[6,14–17] and stainless steel[18,19]. However, only limited information is available on structural steels, which is required for promoting AM techniques in other industrial sectors, including civil engineering and renewable energy and offshore structures.

In previous work carried out by Dirisu et al.[20] fatigue experiments were conducted to investigate the failure behaviour of ER70S-6 WAAM built flat dog bone specimens extracted in horizontal orientation (i.e. along deposited layers). Three different specimen types were examined: as-built, as-built with rolling surface treatment applied, and machined. All specimens were subjected to pure uniaxial loading conditions with the load ratio of R=0.1. The experimental results revealed the higher fatigue strength of the machined specimens compared with other two types of as-built specimens with poor surface finishes, confirming that smooth surface prolongates the fatigue life. However, rolling surface treatment was also found to be an effective method for fatigue life enhancement of the specimens when compared with just as-built specimens. Another study was carried out by Bartsch et al.[13] on G3Si1WAAM as-built dog bone specimens. Two different specimen lengths were examined under uniaxial fatigue loading with the load ratio of R=0.1. Similarly, it was discovered that the surface waviness acts as the stress riser and is the main influencing factor affecting the life span of the tested specimens.

It can be seen from the above literature review that only a few data sets on fatigue performance were generated for WAAM built structural steel specimens, covering only uniaxial fatigue loading condition. In order to fill the gap in the knowledge, the present study was conducted, investigating the fatigue behaviour of ER100S-1 WAAM built specimens under different cyclic loading conditions. The current study includes a broad fatigue analysis under uniaxial, torsion and multiaxial loading conditions, generating stress-life plots. Moreover, the sensitivity of the fatigue life to the specimen extraction orientation was examined for each of the cyclic loading conditions considered in this study. Furthermore, the obtained data from this study were compared with the existing fatigue data for conventionally built structural steel specimens and with the recommended design curve for welded structures in international standards. Finally, the fracture surfaces of the broken specimens were carefully observed under microscope to better understand the failure mechanisms inherent in specimens with different orientations tested under different fatigue loading conditions.

6.2.2. Specimen preparation process

The fatigue tests were conducted on the specimens that were produced by means of WAAM process. Four WAAM walls were manufactured using Böhler Welding ER100S-1[21] low carbon steel wire, with the chemical composition presented in Table 6.4. The Cold Metal Transfer (CMT) based WAAM system was employed with the fabrication parameters highlighted in Table 6.5, which were maintained during the manufacturing process, in order to minimise the microstructural variabilities throughout deposited layers and among all of the built walls. The automatic WAAM-CMT system set up is displayed in Figure 6.10 (a), which consists of the CMT power source with a mounted wire spool, a pre-programmed robotic arm that supplies both wire and shielding gas through the torch simultaneously, a workbench on which the base plate was clamped to, and an exhaust fan positioned above the manufacturing area to remove the excess of the heat and fumes generated during the process. The base plate was cut from a plate of the wrought EN10025 rolled structural steel, with dimensions of 420 × 200 × 12 mm^3. It was fixed onto the working table with eight clamps, to minimise bending and distortion of the plate and hence the WAAM wall due to high fabrication temperatures. Prior to releasing

the clamps and upon completion of the wall deposition, the time was allowed for the wall to cool down to the ambient temperature. Additive layers were deposited in the middle of the base plate, in oscillation manner[22] to attain the desired thickness of 24 mm (Y-axis in Figure 6.10 (a)), the wall length of approximately 355 mm (X-axis) and height of 140 mm (Z-axis).

Sixty smooth round bar (SB) specimens were extracted from the manufactured ER100S-1 WAAM walls using Electrical Discharged Machining (EDM) process. The round bar specimens were designed in accordance with the ASTM E466 standard[23] with the dimensions presented in Figure 6.10 (b). A schematic of the extraction plan for one wall is shown in Figure 6.10 (a), where it can be seen that the specimens were cut in two different orientations: vertical (V) – along Z-axis and perpendicular to the deposited AM layers, and horizontal (H) – along X-axis and deposited layers, to conduct the sensitivity analysis of the fatigue response to the built orientation.

Table 6.4: Chemical composition of ER100S-1 material (wt.-%)[21]

	C	*Mn*	*Cr*	*Si*	*Ni*	*Mo*
ER100S-1	0.08	1.70	0.20	0.60	1.50	0.50

Table 6.5: CMT-WAAM fabrication parameters

Shielding gas	Ar+20% CO_2
Gas flow rate	15 L/min
Wire diameter	1.2 mm
Robot travelling speed	7.33 mm/sec
Wire feed speed	7.5 m/min
Dwell time	120 sec

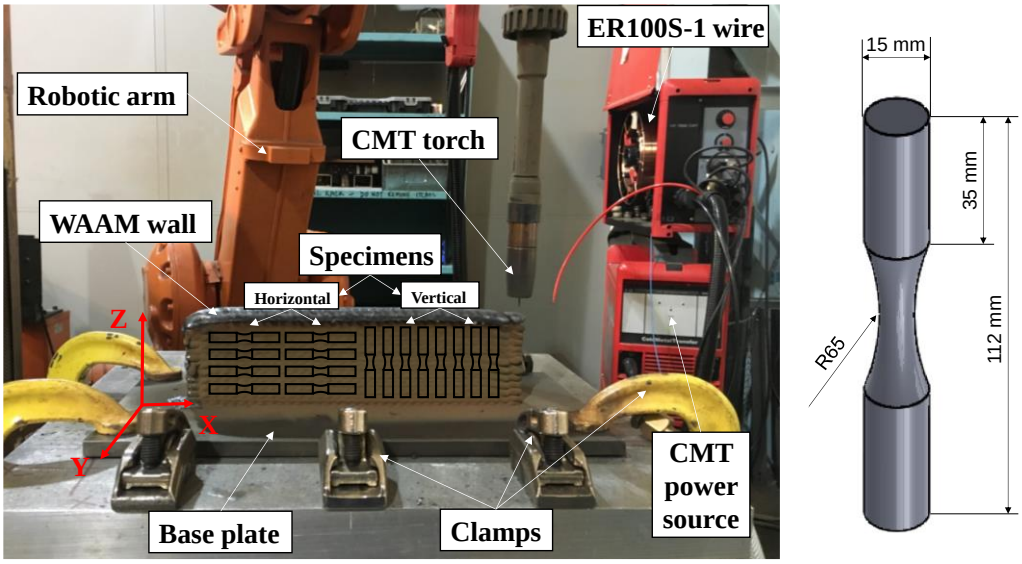

(a) (b)

Figure 6.10: (a) WAAM-CMT system set up with schematic extraction plan for specimens from a built wall, and (b) cylindrical specimen dimensions

6.2.3. Experimental and Analysis Procedures

- **Fatigue tests**

Three types of fatigue tests were conducted in this study: uniaxial, torsion, and multiaxial. All tests were performed using an MTS landmark servo-hydraulic machine with the maximum load capacity of 100 kN, under load control mode. The test parameters in all experiments were as follows: frequency of 20 Hz and the load ratio of R=0.01. For multiaxial fatigue tests, in phase loading was applied, $\Phi = 0^0$, with the biaxiality ratio of $\lambda = 1$. The Wöhler curves were obtained separately for vertical and horizontal specimens, testing on average 10 specimens for each loading type (uniaxial, torsion and multiaxial), recording the maximum stress σ_{max} and number of cycles at failure N_f for each test case. In this study the specimens that endured 2×10^6 cycles, were considered as run-outs. The collected test data were then analysed using the Basquin relationship, correlating the number of cycles to failure N_f with the cyclic stress range $\Delta\sigma$ using a power-law expression of $N_f = A(\Delta\sigma)^B$. In this equation A and B are the material-dependent coefficients that can be obtained from a line of best fit made to the experimental data.

The fatigue data were subsequently analysed by plotting 10% (upper bound), 50% (mean curve) and 90% (lower bound) probability of survival bands based on the procedure defined in ASTM E739-10[24] and BS ISO 12107:2003[25] standards. the inverse slope $k = 1/B$, scatter index T_σ and the fatigue strength were identified for each stress-fatigue life diagram. In this analysis T_σ was computed as a ratio between the stress levels corresponding to the 10% and 90% survival probabilities.

- **Fractography**

Failure mechanisms were examined by conducting the microscopy analysis on specimens with different orientations subjected to different fatigue load conditions (uniaxial, torsion and multiaxial). The fractography examination was performed using the FEI Quanta 650 FEG scanning electron microscope (SEM). For direct comparison of the fracture surfaces after fatigue testing in specimens with different orientations, specimens subjected to the similar load levels were selected for post-mortem analysis. The recorded observations from the fractography analysis were then correlated with the experimental fatigue data for an accurate interpretation of fatigue life assessment of WAAM built ER100S-1 specimens with different orientations tested under different fatigue load types.

6.2.4. Tests results and discussions

- **Fatigue test results**

The obtained fatigue data from ER100S-1 WAAM specimens for different loading types and specimen orientations were analysed according to the procedure described in Section 6.2.3, by plotting the maximum stress against number of cycles to failure in log-log axes presented in Figure 6.11, and by determining the fatigue properties: fatigue strength at 2×10^6 cycles, $\Delta\sigma_{50\%}$, the scatter index T_σ, and the inverse slope factor k, which were are summarised in Table 6.6. The fatigue data from the uniaxial tests are shown in Figure 6.11 (a) for vertical specimens, Figure 6.11 (b) for horizontal and Figure 6.11 (c) direct comparison of two trends. The run-out data for both specimen orientations suggest that the alloy exhibits a plateau at the low stress values in the stress-life plot, known as the endurance limit, σ_e. Based on the obtained experimental data the endurance limit for the vertical specimens is found to be between 600 and 575 MPa, and for the horizontal specimens between 575 and 550 MPa. Hence, both vertical and horizontal specimen orientations have similar endurance limit within 4.1%, with slightly higher value for the vertically oriented specimens. Based on the previous study by Ermakova et al.[26], different orientations of WAAM built ER100S-1 specimens have very similar yield and ultimate tensile strength values (under 1% difference), hence the obtained trend is confirmed and reflected in values of uniaxial fatigue endurance limits in this study. It is also worth noting that the obtained endurance limits for the vertical and horizontal specimens are above the yield strength of the material, which is 536 MPa and 538 MPa, respectively. Comparison of the maximum stress against number of cycles to failure curves for different specimens orientations in Figure 6.11 (c) shows that the slope for the vertical specimens curve is steeper than for horizontal, this is also indicated by the inverse slope factor that is 1.2 times higher for the horizontally oriented specimens, presented in Table 6.6. Also seen in the table, the scatter index for the obtained data sets from uniaxial test is comparable for the specimens with different orientations and only differ by 2.3%. Finally, the plotted data display that at lower cycles both specimen orientations exhibit similar behaviour under uniaxial fatigue loading condition; however, the trend changes with the increase in the number of cycles.

Assessment of the torsion fatigue results demonstrated in Figure 6.11 (d-f) reveals that the trends are independent of the specimen orientation and fall on top of each other, with identical torsion fatigue strength of 457 MPa. The slope of the two curves only differs by 1.3%, with the

data points falling slightly apart at higher stress values and converging towards the lower stress values. However, the scatter index (Table 6.6) is 11.4% higher for the horizontal specimens than for vertical. Comparable torsion fatigue behaviour for two specimen orientations can also be attributed to the similar tensile characteristics of the material, including its ductility[26].

The multiaxial fatigue results for WAAM built ER100S-1 specimens are shown in Figure 6.11 (g-i). From the figures it can be seen that the 50% survival probability lines of the data sets for vertical and horizontal specimens are almost parallel to each other, with the vertical curve falling above the horizontal. The inverse slope factors for two trends differ by 5.7%, and similar to the pattern observed in torsion fatigue results, two curves are converging towards low stress (high cycle) fatigue results. The multiaxial fatigue strength for vertical specimens is 356 MPa and is 3.9% higher than for horizontal specimens, with fatigue strength of 342 MPa. The scatter for the obtained data sets is 3.8% higher for the horizontal specimens than for vertical as seen by the scatter index summarised in Table 6.6.

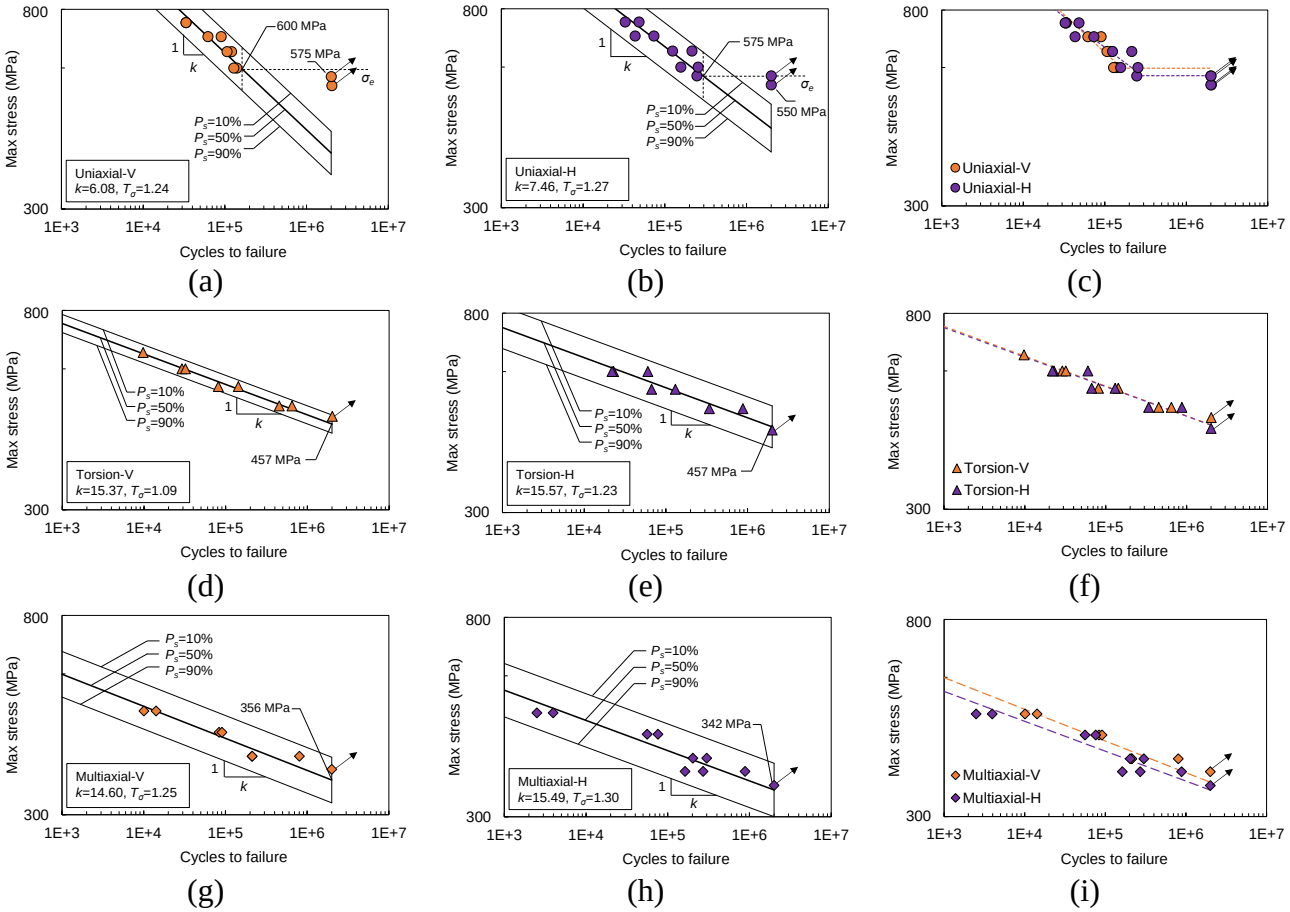

Figure 6.11: Fatigue data for ER100S-1 specimens (a-c) axial, (d-f) torsion, (g-i) multiaxial tests

Table 6.6: Fatigue properties of tested ER100S-1 specimens

Test	Orientation	$\Delta\sigma_{50\%}$ [MPa]	T_σ	k
Uniaxial	V	600	1.24	6.08
	H	575	1.27	7.46
Torsion	V	457	1.09	15.37
	H	457	1.23	15.57
Multiaxial	V	356	1.25	14.60
	H	342	1.30	15.49

The obtained data sets for all fatigue tests for vertical and horizontal specimens were then compared with each other in Figure 6.12. As expected, it is seen from this figure that the overall fatigue strength of material is decreasing from uniaxial fatigue to torsion and, similarly, from torsion to multiaxial fatigue test results. Considering the values summarised in Table 6.6, the average fatigue strength of ER100S-1 WAAM components (i.e., the mean value between fatigue strength of vertical and horizontal specimens) drops by 22.2% for torsion tests compared with the average endurance limit obtained in uniaxial tests, and further by 23.6% for results obtained under multiaxial applied stress. This leads to a conclusion that the fatigue strength of WAAM built ER100S-1 specimens strongly depends on the type of the applied fatigue loading condition, as expected. Another observation can be made from Figure 6.12 is that the slope for the data from torsion and multiaxial fatigue tests are almost parallel to each other, while for uniaxial fatigue it is approximately 2 times steeper. Thus, the reduction of the applied stress values towards the high cycle fatigue region is more pronounced in tests under pure uniaxial loading condition. Furthermore, analysis of the data obtained from different specimen orientations shows negligible variability of the results, with the maximum range within 4.1% for pure uniaxial tests, so the material can be considered to be insensitive to the built specimen orientation in fatigue performance. Nevertheless, the trends presented in Figure 6.12 reveal that even with minor difference the vertical specimens mean curves are above horizontal in cases of torsion and multiaxial fatigue loading conditions. On the other hand, uniaxial test results show that the horizontal specimen mean curve is above the vertical within a range between 48,700 and 255,300 cycles, otherwise the vertical specimens exhibit higher fatigue life. It was reported in previous studies that in certain test scenarios (fracture toughness[26] and fatigue crack growth[27]) ER100S-1 WAAM built specimens are insensitive to the built orientation, but their performance is highly dependent on the extraction location instead (top or bottom of the WAAM wall). Thus, further study needs to be carried out in future work to investigate the sensitivity of the fatigue performance of ER100S-1 WAAM specimens to the specimen extraction location.

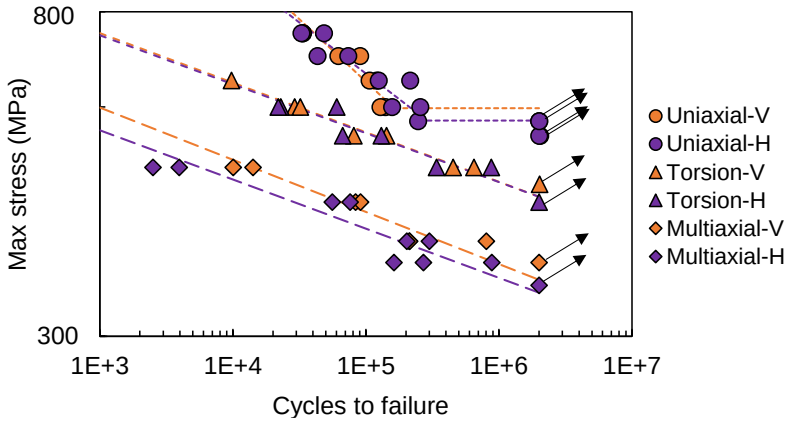

Figure 6.12: Comparison of all fatigue experimental data for ER100S-1 WAAM specimens

- **Comparison with the literature data on steel specimens and standard design curves**

The performance of the 50% uniaxial fatigue failure bands (i.e. mean curves) obtained from this study for WAAM ER100S-1 was further analysed for application in offshore structures, by comparing the data with the S-N fatigue C1 design curve, recommended by the DNV RP-C203 standard[28] for structures with the continuous welds and ground flush surface finish. The results from this comparison have been presented in log-log axes in Figure 6.13. It is seen in this figure that both vertical and horizontal specimen orientation trends fall above the recommended DNV standard C1 design curve. Moreover, the tested material is exhibiting the fatigue endurance limit at much higher stress range values and lower number of cycles than suggested in the standard. The slopes of the experimental curves are lower compared with the DNV C1 curve. To conclude, the stress-life plot proposed by the standard provides a conservative estimation of the ER100S-1 WAAM specimens tested under pure uniaxial loading conditions, hence this material and manufacturing technique can be considered for offshore structures production and repair.

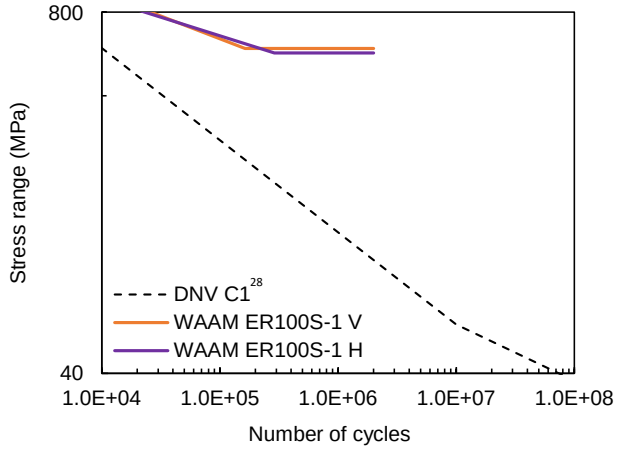

Figure 6.13: Comparison of uniaxial fatigue data for WAAM ER100S-1 specimens with DNV C1 recommended design curve

Extensive comparison with the data on uniaxial, torsion and multiaxial fatigue performance of other structural steels available in the literature was also conducted. Knowing that the fatigue behaviour of the material strongly depends on the testing parameters, such as load ratio *R*, and specimens design[29,30], all the collected data with various load ratios were normalised into a single fatigue plot using the effective stress σ_{eff} model, defined in Equation 6.3. This concept was invented for the direct comparison of fatigue data from different studies[31]; however, it does not consider the effects of different loading frequencies. Therefore, some limited effects from different fatigue frequencies and specimen designs are expected in the following comparison.

$$\sigma_{eff} = \sigma_{\max}\left(\frac{1-R}{2}\right)^{0.28} \qquad \text{Equation 6.3}$$

The mean uniaxial fatigue plots for ER100S-1 WAAM specimens were compared with the limited data sets on S355 wrought steel specimens available in the literature. S355 is a structural steel which is typically used in fabrication of offshore structures in renewable energy sector[32,33], hence such comparison will provide a better understanding of suitability of WAAM built components for marine renewable energy applications. The uniaxial fatigue data which were used for comparison include: the data obtained from large dog bone S355 specimens tested at *R*=0.1 tested by Anandavijayan et al.[34], the data from smaller dog bone S355 specimens examined at *R*=-1 by Corigliano et al.[35], the data from round bar S355 specimens assessed at *R*=0.01 by Dantas et al.[36] and at *R*=-1 by Aeran et al.[37], and finally the data from fillet welded cruciform S355 specimens tested at *R*=0 by Berto et al.[38] The S-N curve, generated for wrought cylindrical C40 carbon steel specimens at *R*=-1 by Atzori et al.[39] was also included into the comparison with the literature data. Along with limited results from studies on WAAM built specimens the ER70S-6 flat dog bone specimens tested at *R*=0.1 by Dirisu er al.[20] and G3Si1 as built (with rough surface) flat dog bone specimens with two different specimens designs examined at *R*=0.1 by Bartsch et al.[13] were also included in the comparison with the literature data. The above data sets were normalised to effective stress (see Equation 6.3) and presented in log-log axes in Figure 6.14 (a). it can be seen in this figure that the fatigue results obtained from ER100S-1 WAAM specimens fall above the collected data from the literature on wrought S355, C40 and WAAM ER70S-6 and G3Si1 steels. The slopes of the curves for ER100S-1 uniaxial fatigue are similar to some stress-life plots for S355 and WAAM G3Si1 specimens. Moreover, due to the fatigue endurance limit of ER100S-1 specimens, both data sets for vertical and horizontal orientations are not crossing the rest of the S-N curves even at higher number of cycles. However, it must be noted here that yield and ultimate tensile strengths of ER100S-1 material are relatively higher than any of the presented materials, thus it is expected that uniaxial fatigue performance is also found to be superior.

Only a few data sets on torsion and multiaxial fatigue were collected and presented in this comparative study due to limited availability of such data on structural steels in the literature. The comparison of the effective stress versus number of cycles to failure in log-log axes for the results obtained from this study with the literature data is presented in Figure 6.14 (b) and Figure 6.14 (c) for torsion and multiaxial fatigue loading conditions, respectively. A previous study reported that the performance of round bar C40 carbon steel specimens tested with loading ratio of *R*=-1 under torsion and with *R*=0 under multiaxial loading conditions by Atzori et al.[39]. Another study provided some data on round bar 39NiCrMo3 steel specimens assessed

at R=-1 by Berto et al.[40] . Additionally, a curve for multiaxial fatigue on round bar wrought S355 specimens examined at R=0.01 by Dantas et al.[36] was added for comparison. The biaxiality ratio for all presented multiaxial fatigue data in this analysis was $\lambda = 1$, with in phase loading angle of $\Phi = 0^0$. It can be seen in Figure 6.14 (b) and Figure 6.14 (c) that similar to the case of uniaxial fatigue, the results for torsion and multiaxial life assessment fall above the data from the literature. The trends for C40 and 39NiCrMo3 steels are below and parallel to the trends obtained from this study for ER100S-1 WAAM specimens under torsion fatigue condition. Moreover, the multiaxial behaviour of ER100S-1 has been found similar to the data on S355 wrought steel.

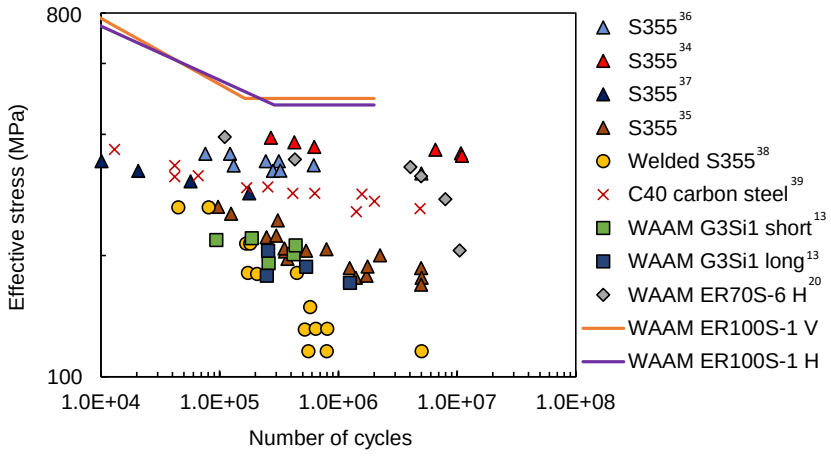

(a)

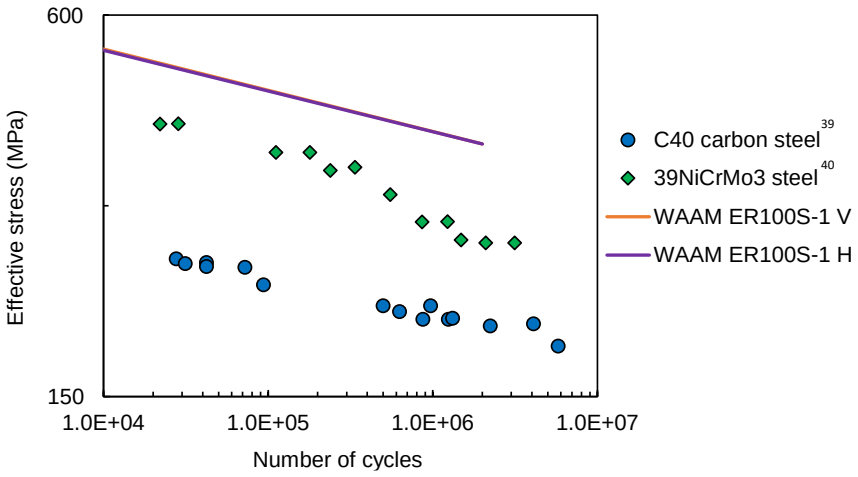

(b)

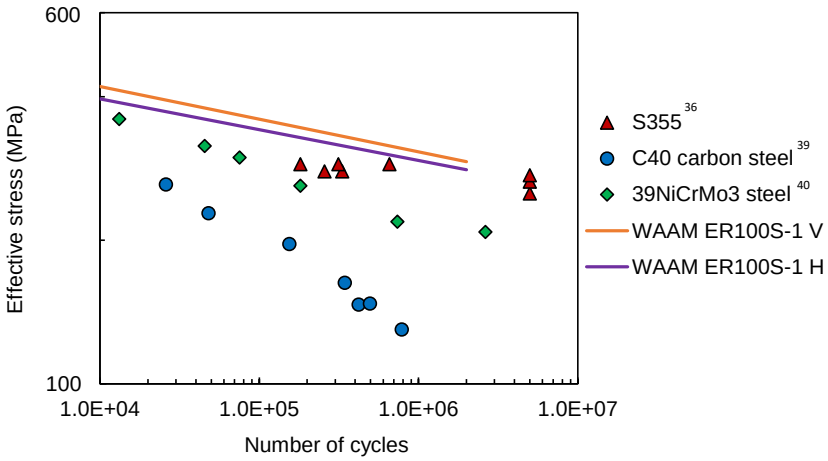

(c)

Figure 6.14: Comparison of fatigue data for WAAM ER100S-1 with data in the literature for (a) uniaxial, (b) torsion, and (c) multiaxial fatigue tests on steel

6.2.5. Fractography Analysis

The microstructural analysis of the tested specimens conducted using SEM revealed almost defect-free surfaces of WAAM built ER100S-1 specimens, with rare minor defects under 20 μm. The fractography assessment of the tested specimens was conducted in order to examine the fracture surfaces and establish any differences in failure mechanisms for specimens with different orientations tested under different fatigue loading conditions (i.e., uniaxial, torsion, and multiaxial). Figure 6.15 displays two fracture surfaces of (a) vertical and (b) horizontal specimens tested under pure uniaxial fatigue with maximum stress of 650 MPa. Four clear crack growth stages can be observed on both fracture surfaces: 1 – crack nucleation point, 2 – crack propagation, 3 – ductile failure due to unstable fatigue crack growth, and 4 – ductile failure caused by fast fracture. Moreover, the fracture surface of the vertical specimen in Figure 6.15 (a) exhibited two nucleation points, in which two cracks initiated simultaneously on parallel planes and then consequently converged into one crack in propagation region depicted as 2. White arrows in the figures indicate the direction of the crack growth in both specimens. The crack initiation in both cases started from the surface irregularities. The fatigue life of horizontal specimen was twice longer than for vertical, which can be caused by the two initial cracks nucleated in the vertical specimen contributing to the early final failure of the specimen. Examination of the crack growth regions at higher magnification shows that the transition from one grain to other leads to the change of the fracture plane caused by different orientation of individual grains. Moreover, the fatigue striations can be seen in crack initiation and propagation regions for both specimens (shown with yellow arrows), which are parallel to the crack propagation direction. Furthermore, in crack growth propagation region 2 in both specimens, elongated fracture features can be observed (highlighted with dashed yellow lines), which indicate the crack propagation direction. The fracture surfaces in regions 1 for both vertical and horizontal specimens present shallower ductile features, while in regions 2 the

dimples become bigger and deeper, and secondary cracks are visible. To conclude, no major difference in failure mechanisms was observed for specimens with different extraction orientations. Moreover, similar fracture features revealed during the analysis, which are in good agreement with similar uniaxial fatigue and mechanical performance of the vertical and horizontal ER100S-1 WAAM specimens.

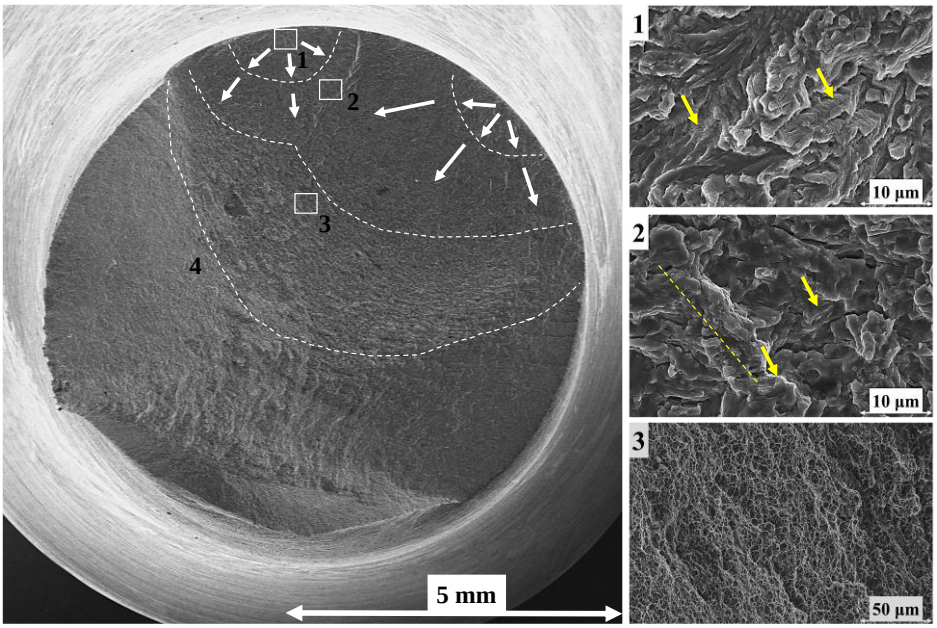

(a)

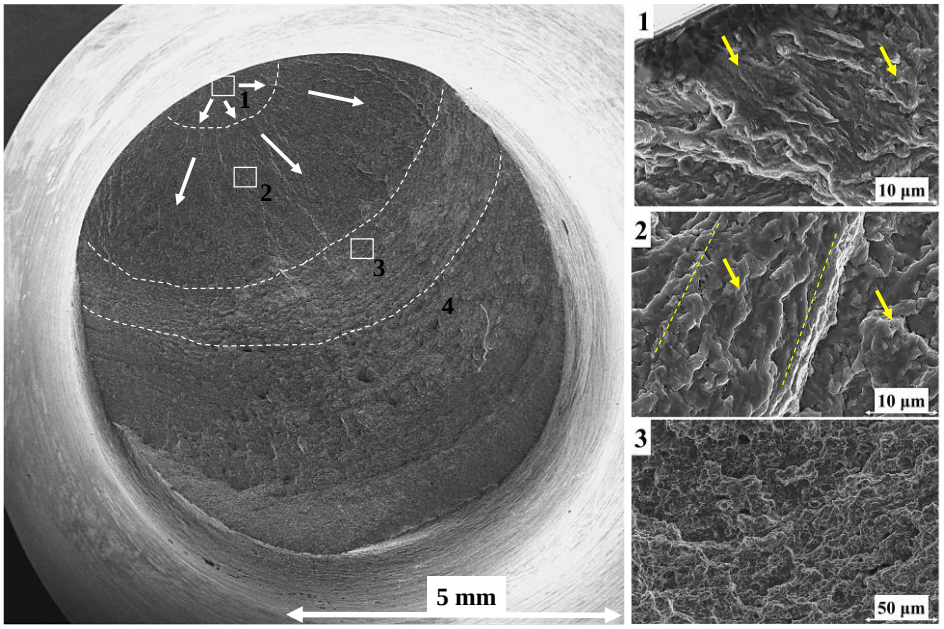

(b)

Figure 6.15: Fracture surfaces of ER100S-1 WAAM (a) vertical and (b) horizontal specimens tested under uniaxial fatigue loading condition

Two fracture surfaces for vertical and horizontal ER100S-1 WAAM specimens examined under pure torsion fatigue with maximum stress of 550 MPa are presented in Figure 6.16 (a) and (b) respectively. It is seen from the figures that in both cases the outer diameter of the

fracture surface is not entirely flat, consisting of the series of inclined surfaces, so called 'factory roof' morphology[40,41], initiated due to presence of torsion fatigue (out-of-plane shear in mode III) and transforming to pronounced inclined features under mode I. Larger area of fracture surface of the vertical specimen shows presence of abrasion, caused by mode III loading condition, demolishing the fracture features by rubbing two fracture surfaces against each other. For horizontal specimen the damaged area is much smaller (approximately half of the full fracture surface) and located in the centre of the fracture surface. This was also indicated in number of cycles to failure, which was 1.2 times lower for the horizontal specimen than for vertical. The area with remaining fatigue fracture features is a result of the final failure of the specimen under mode I loading condition, forming a cascade of fatigue fracture planes, also shown in the regions 1 in Figure 6.16. Closer examination of the area reveals the ductile fatigue facets (yellow arrows in region 1), that appear as river patterns under lower magnification (white arrows in region 1). Another interesting fatigue feature was observed near the edge of the fracture surface in both specimens – colonies of flat 'fish-bone' features, representing smaller and less ductile facets formed due to initial short crack growth, perpendicular to the fracture edge of the specimens (yellow arrows in region 2).

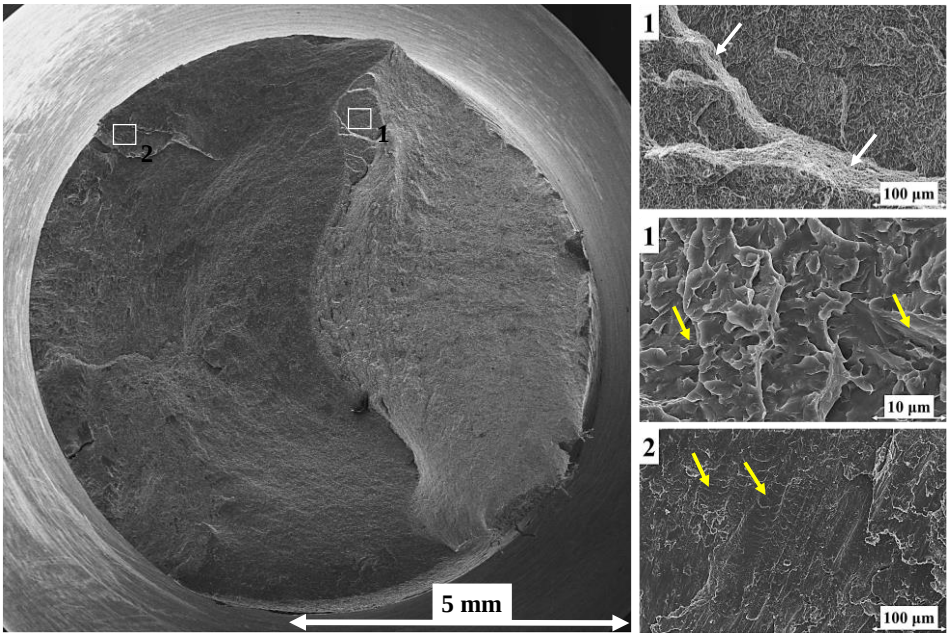

(a)

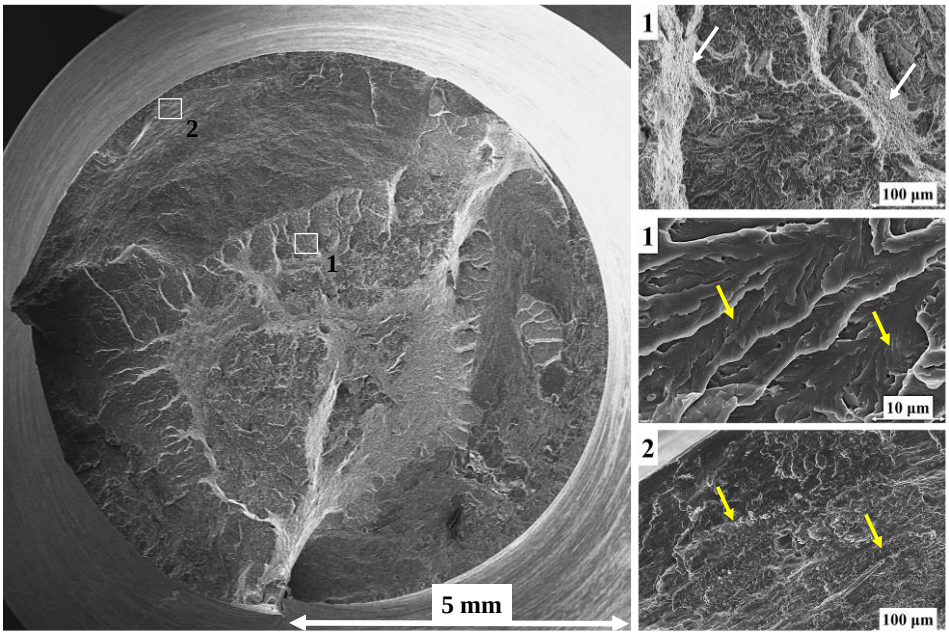

(b)

Figure 6.16: Fracture surfaces of ER100S-1 WAAM (a) vertical and (b) horizontal specimens tested under torsion fatigue loading condition

Lastly, two fracture surfaces of the specimens previously subjected to multiaxial fatigue loading conditions under maximum stress of 450 MPa were examined and shown in Figure 6.17 (a) for vertical and (b) for horizontal broken specimens. Similar to the specimens tested under torsion, the edges of the fracture surfaces in Figure 6.17 are not flat and present some 'factory roof' morphology with inclined surfaces formed in combination of applied mode I and III fracture loading conditions. Approximately 60% of the fracture surfaces (region A) indicate evidence of abrasion and wear, occurred under mode III out-of-plane shear mechanisms. Two main fatigue features were found in this region and are highlighted with yellow arrows: 1 - fatigue striations, and 2 – 'fish-bone' colonies, representing large striations near the fracture edges of the specimens. The latter feature appears in specimens tested under pure tension and multiaxial fatigue, hence is the evidence of the torsion fracture mechanisms resulted under mode III. The remaining fracture surface area depicted as B is due to the final specimen failure in fast fracture with corresponding cup and cone shape.

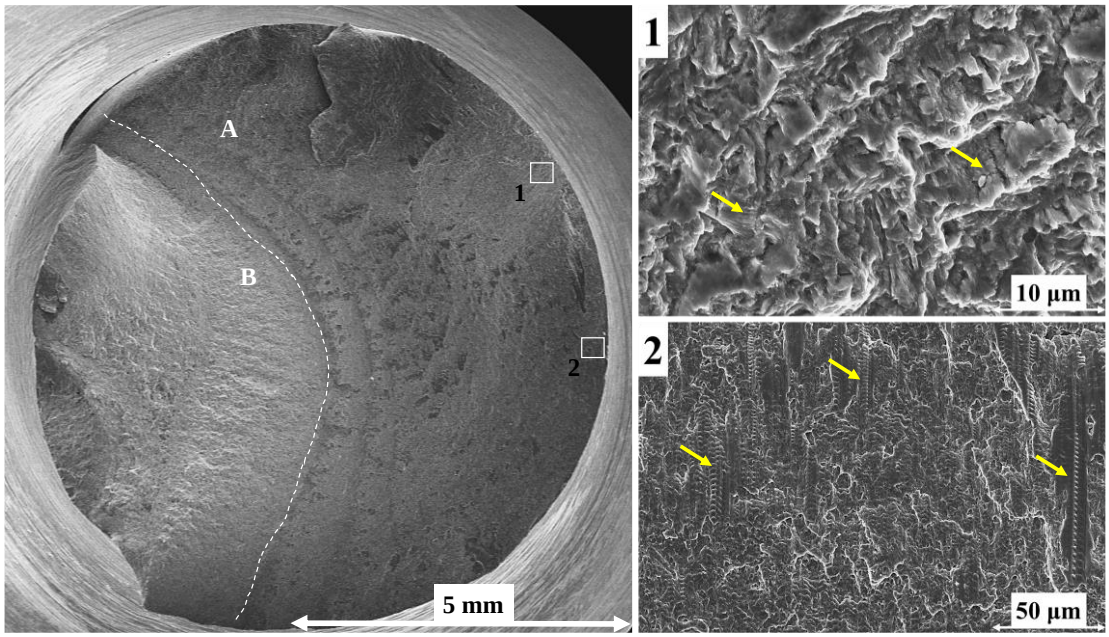

(a)

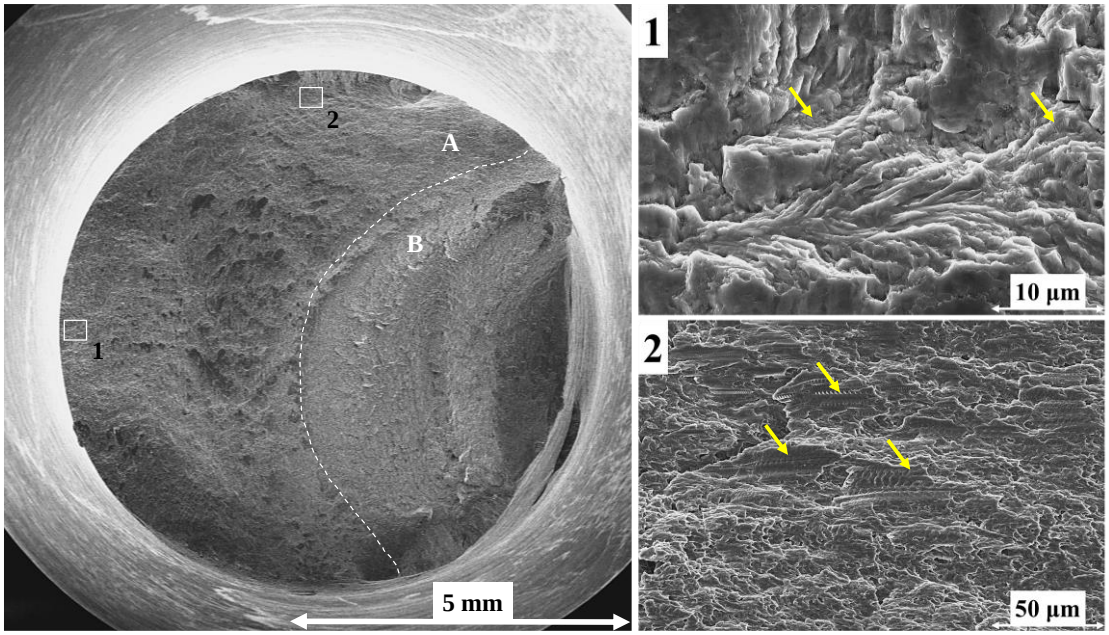

(b)

Figure 6.17: Fracture surfaces of ER100S-1 WAAM (a) vertical and (b) horizontal specimens tested under multiaxial fatigue loading condition

6.2.6. Conclusions

A series of fatigue tests were performed on WAAM built ER100S-1 specimens that were extracted along two different orientations: vertical and horizontal. Uniaxial, torsion, and multiaxial fatigue behaviour of the specimens was examined by developing the stress-life plots. The following observations and conclusions were made from this study:

- Uniaxial, torsion and multiaxial fatigue properties of WAAM ER100S-1 specimens are not dependant on the specimen orientation.
- The fatigue strength of the material obtained from torsion tests drops by 22.2% compared with uniaxial test results; and further by 23.6% under multiaxial fatigue loading.
- Trends for uniaxial, torsion and multiaxial fatigue show advantageous performance of WAAM ER100S-1 specimens compared with other structural steels, including S355 steel that is commonly used in offshore structures.
- The S-N fatigue behaviour of ER100S-1 WAAM built material can be conservatively predicted by DNV C1 standard design curve for structures with continues welds and ground flush surface finish.
- The study of fracture surfaces of six specimens revealed common fatigue features for each of the fatigue load types, with no significant variations between vertical and horizontal specimens.
- The examined WAAM built specimens were found to be almost defect-free, with minor defects of smaller than 20 μm.

6.2.7. Acknowledgements

This work was supported by grant EP/L016303/1 for Cranfield, Oxford and Strathclyde Universities' Centre for Doctoral Training in Renewable Energy Marine Structures – REMS CDT (http://www.remscdt.ac.uk/) from the UK Engineering and Physical Sciences Research Council (EPSRC).

References for paper XI

1. ISO/ASTM International. ISO/ASTM 52900: Additive manufacturing - General principles and Terminology. *Int. Stand.* **5**, 1–26 (2015).
2. Gibson, I., Rosen, D., Stucker, B. & Khorasani, M. *Additive Manufacturing Technologies. Yosetsu Gakkai Shi/Journal of the Japan Welding Society* **89**, (Springer, 2020).
3. Wu, B., Pan, Z., Ding, D., Cuiuri, D., Li, H., Xu, J. & Norrish, J. A review of the wire arc additive manufacturing of metals: properties, defects and quality improvement. *Journal of Manufacturing Processes* **35**, 127–139 (2018).
4. Seow, C. E., Zhang, J., Coules, H. E., Wu, G., Jones, C., Ding, J. & Williams, S. Effect of crack-like defects on the fracture behaviour of Wire + Arc Additively Manufactured nickel-base Alloy 718. *Addit. Manuf.* **36**, 101578 (2020).
5. Rodrigues, T. A., Duarte, V., Miranda, R. M., Santos, T. G. & Oliveira, J. P. Current Status and Perspectives on Wire and Arc Additive Manufacturing (WAAM). *Mater. 2019, Vol. 12, Page 1121* **12**, 1121 (2019).
6. Fotovvati, B., Namdari, N. & Dehghanghadikolaei, A. Fatigue performance of selective

laser melted Ti6Al4V components: State of the art. *Mater. Res. Express* **6**, (2019).

7. Baufeld, B., Brandl, E. & Van Der Biest, O. Wire based additive layer manufacturing: Comparison of microstructure and mechanical properties of Ti–6Al–4V components fabricated by laser-beam deposition and shaped metal deposition. *J. Mater. Process. Technol.* **211**, 1146–1158 (2011).

8. Ding, J., Colegrove, P., Mehnen, J., Ganguly, S., Almeida, P. M. S., Wang, F. & Williams, S. Thermo-mechanical analysis of Wire and Arc Additive Layer Manufacturing process on large multi-layer parts. *Comput. Mater. Sci.* **50**, 3315–3322 (2011).

9. Domashenkov, A., Plotnikova, A., Movchan, I., Bertrand, P., Peillon, N., Desplanques, B., Saunier, S. & Desrayaud, C. Microstructure and physical properties of a Ni/Fe-based superalloy processed by Selective Laser Melting. *Addit. Manuf.* **15**, 66–77 (2017).

10. Todai, M., Nakano, T., Liu, T., Yasuda, H. Y., Hagihara, K., Cho, K., Ueda, M. & Takeyama, M. Effect of building direction on the microstructure and tensile properties of Ti-48Al-2Cr-2Nb alloy additively manufactured by electron beam melting. *Addit. Manuf.* **13**, 61–70 (2017).

11. ASM. ASM International Fatigue. *Elem. Metall. Eng. Alloy.* 243–265 (2008).

12. Suresh, S. Fatigue of Materials. *Fatigue Mater.* (1998). doi:10.1017/CBO9780511806575

13. Bartsch, H., Kühne, R., Citarelli, S., Schaffrath, S. & Feldmann, M. Fatigue analysis of wire arc additive manufactured (3D printed) components with unmilled surface. *Structures* **31**, 576–589 (2021).

14. Biswal, R., Zhang, X., Shamir, M., Al Mamun, A., Awd, M., Walther, F. & Khadar Syed, A. Interrupted fatigue testing with periodic tomography to monitor porosity defects in wire + arc additive manufactured Ti-6Al-4V. *Addit. Manuf.* **28**, 517–527 (2019).

15. Pegues, J., Roach, M., Scott Williamson, R. & Shamsaei, N. Surface roughness effects on the fatigue strength of additively manufactured Ti-6Al-4V. *Int. J. Fatigue* **116**, 543–552 (2018).

16. Syed, A. K., Zhang, X., Caballero, A., Shamir, M. & Williams, S. Influence of deposition strategies on tensile and fatigue properties in a wire + arc additive manufactured Ti-6Al-4V. *Int. J. Fatigue* **149**, 106268 (2021).

17. Shamir, M., Syed, A. K., Janik, V., Biswal, R. & Zhang, X. The role of microstructure and local crystallographic orientation near porosity defects on the high cycle fatigue life of an additive manufactured Ti-6Al-4V. *Mater. Charact.* **169**, 110576 (2020).

18. Zulić, S., Rostohar, D., Kaufman, J., Pathak, S., Kopeček, J., Böhm, M., Brajer, J. & Mocek, T. Fatigue life enhancement of additive manufactured 316l stainless steel by LSP using a DPSS laser system. *https://doi.org/10.1080/02670844.2022.2060463* (2022). doi:10.1080/02670844.2022.2060463

19. Shrestha, R., Simsiriwong, J. & Shamsaei, N. Fatigue behavior of additive manufactured 316L stainless steel under axial versus rotating-bending loading: Synergistic effects of stress gradient, surface roughness, and volumetric defects. *Int. J. Fatigue* **144**, 106063 (2021).

20. Dirisu, P., Supriyo, G., Martina, F., Xu, X. & Williams, S. Wire plus arc additive manufactured functional steel surfaces enhanced by rolling. *Int. J. Fatigue* **130**, 105237 (2020).

21. *ER100S-G Data Sheet - Bohler Welding*. (2014).

22. Ermakova, A., Mehmanparast, A. & Ganguly, S. A review of present status and challenges of using additive manufacturing technology for offshore wind applications. *Procedia Struct. Integr.* **17**, 29–36 (2019).

23. Standard Practice for Conducting Force Controlled Constant Amplitude Axial Fatigue Tests of Metallic Materials. Available at: https://www.astm.org/e0466-21.html. (Accessed: 5th July 2022)

24. Testing, F. Standard Practice for Statistical Analysis of Linear or Linearized Stress-Life (. *Stat. Anal. Fatigue Data* **91**, 129-129–9 (2009).

25. BS ISO 12107-2003--[2022-07-06--10-12-27 AM].pdf.

26. Ermakova, A., Mehmanparast, A., Ganguly, S., Razavi, J. & Berto, F. Investigation of mechanical and fracture properties of wire and arc additively manufactured low carbon steel components. *Theor. Appl. Fract. Mech.* **109**, 102685 (2020).

27. Ermakova, A., Ganguly, S., Razavi, J., Berto, F. & Mehmanparast, A. Experimental investigation of the fatigue crack growth behavior in wire arc additively manufactured ER100S-1 steel specimens. *Fatigue Fract. Eng. Mater. Struct.* (2021). doi:10.1111/FFE.13598

28. (DNV) Det Norske Veritas. Fatigue Design of Offshore Steel Structures. *Recomm. Pract. DNV-RPC203* 126 (2005).

29. Berto, F., Campagnolo, A. & Lazzarin, P. Fatigue strength of severely notched specimens made of Ti-6Al-4V under multiaxial loading. *Fatigue Fract. Eng. Mater. Struct.* **38**, 503–517 (2015).

30. Razavi, S. M. J., Van Hooreweder, B. & Berto, F. Effect of build thickness and geometry on quasi-static and fatigue behavior of Ti-6Al-4V produced by Electron Beam Melting. *Addit. Manuf.* **36**, 101426 (2020).

31. Li, P., Warner, D. H., Fatemi, A. & Phan, N. Critical assessment of the fatigue performance of additively manufactured Ti-6Al-4V and perspective for future research. *Int. J. Fatigue* **85**, 130–143 (2016).

32. Mehmanparast, A., Taylor, J., Brennan, F. & Tavares, I. Experimental investigation of mechanical and fracture properties of offshore wind monopile weldments: SLIC interlaboratory test results. *Fatigue Fract. Eng. Mater. Struct.* **41**, 2485–2501 (2018).

33. Mehmanparast, A., Brennan, F. & Tavares, I. Fatigue crack growth rates for offshore wind monopile weldments in air and seawater: SLIC inter-laboratory test results. *Mater. Des.* **114**, 494–504 (2017).

34. Anandavijayan, S., Mehmanparast, A., Braithwaite, J., Brennan, F. & Chahardehi, A. Material pre-straining effects on fatigue behaviour of S355 structural steel. *J. Constr. Steel Res.* **183**, 106707 (2021).

35. Corigliano, P., Cucinotta, F., Guglielmino, E., Risitano, G. & Santonocito, D. Fatigue

assessment of a marine structural steel and comparison with Thermographic Method and Static Thermographic Method. *Fatigue Fract. Eng. Mater. Struct.* **43**, 734–743 (2020).

36. Dantas, R., Correia, J., Lesiuk, G., Rozumek, D., Zhu, S. P., de Jesus, A., Susmel, L. & Berto, F. Evaluation of multiaxial high-cycle fatigue criteria under proportional loading for S355 steel. *Eng. Fail. Anal.* **120**, 105037 (2021).

37. Aeran, A., Acosta, R., Siriwardane, S. C., Starke, P., Mikkelsen, O., Langen, I. & Walther, F. A nonlinear fatigue damage model: Comparison with experimental damage evolution of S355 (SAE 1020) structural steel and application to offshore jacket structures. *Int. J. Fatigue* **135**, 105568 (2020).

38. Berto, F., Mutignani, F. & Pittarello, L. Effect of hot-dip galvanization on the fatigue behaviour of welded structural steel. *Procedia Struct. Integr.* **2**, 1813–1820 (2016).

39. Atzori, B., Berto, F., Lazzarin, P. & Quaresimin, M. Multi-axial fatigue behaviour of a severely notched carbon steel. *Int. J. Fatigue* **28**, 485–493 (2006).

40. Berto, F., Lazzarin, P. & Yates, J. R. Multiaxial fatigue of V-notched steel specimens: A non-conventional application of the local energy method. *Fatigue Fract. Eng. Mater. Struct.* **34**, 921–943 (2011).

41. Berto, F., Lazzarin, P. & Marangon, C. Fatigue strength of notched specimens made of 40CrMoV13.9 under multiaxial loading. *Mater. Des.* **54**, 57–66 (2014).

6.3. Conclusion

The fatigue tests conducted on ER70S-6 and ER100S-1 WAAM built specimens provided valuable insights into their uniaxial, torsion, and multiaxial fatigue properties. For ER70S-6 specimens, sensitivity to specimen orientation was observed, with higher fatigue strength found in vertical specimens under uniaxial load and in horizontal specimens under torsion and multiaxial load. However, the difference between fatigue strength for different orientations reduced as the load type changed. The obtained S-N fatigue data for ER70S-6 specimens overlapped with the upper bound of fatigue results for wrought S355 steel, showing potential for offshore structure fabrication. Fracture analysis indicated an almost defect-free material.

On the other hand, for ER100S-1 specimens, the fatigue properties were independent of specimen orientation. The fatigue strength dropped as the load type changed from uniaxial to torsion and multiaxial. WAAM ER100S-1 specimens demonstrated advantageous performance compared to other structural steels, including commonly used S355 steel in offshore structures. Fracture analysis showed no significant variations between vertical and horizontal specimens, and the material was found to be almost defect-free.

The results of these fatigue tests provide essential data for the application of WAAM built components in various loading scenarios and highlight the potential for their utilisation in offshore structures. Furthermore, the conformity with standard design curves indicates their suitability for specific structural applications. The low presence of defects enhances confidence in their structural integrity. Overall, these findings advance the understanding of fatigue behaviour in WAAM materials, supporting their viability for offshore industry applications.

Chapter 7 : Life Enhancement Possibilities for Wire Arc Additively Manufactured Steel Components and Residual Stresses Examination

In this chapter, two surface treatment techniques were proposed for life enhancement of ER70S-6 and ER100S-1 WAAM specimens. The efficiency of the techniques was assessed by performing FCG and CFCG tests and analysing residual stress distribution in the specimens after the treatment. The chapter consists of the following papers:

Paper X: The influence of wire arc additive manufacturing deposition process on residual stress distribution and fatigue life in the presence and absence of surface treatment

Paper XI: The influence of laser shock peening on corrosion-fatigue behaviour of wire arc additively manufactured components parts

7.1. Paper X: The effect of surface treatment and orientation on fatigue crack growth rate and residual stress distribution of wire arc additively manufactured low carbon steel components

Anna Ermakova[a], Javad Razavi[b], Sandra Cabeza[c], Elzbieta Gadalinska[d], Mark Reid[e]

Anna Paradowska[e,f], Supriyo Ganguly[g], Filippo Berto[b], Ali Mehmanparast[a*]

[a] Department of Naval Architecture, Ocean and Marine Engineering, University of Strathclyde, Glasgow G1 1XQ, United Kingdom

[b] Norwegian University of Science and Technology (NTNU), Trondheim, Norway

[c] Institut Laue-Langevin (ILL), Grenoble, France

[d] Lukasiewicz Research Network – Institute of Aviation, Warsaw, Poland

[e] Australian Centre for Neutron Scattering, Sydney, Australia

[f] School of Civil Engineering, The University of Sydney, Sydney, Australia

[g] Welding Engineering and Laser Processing Centre, Cranfield University, Cranfield, MK43 0AL, United Kingdom

Abstract[10]

The directed energy deposition (DED) processes, such as laser metal deposition or Wire Arc Additive Manufacturing (WAAM), are gradually becoming the preferred method for fabrication of large-scale components using metal additive manufacturing (AM) technology. In this work, the possibility of fatigue life enhancement in WAAM built low carbon steel components, by means of rolling and laser shock peening surface treatment techniques, was investigated. A series of fatigue crack propagation tests were performed on surface treated ER70S-6 and ER100S-1 WAAM built specimens, and the results were analysed and compared with the untreated materials tested under the same loading conditions. The obtained results were interpreted in terms of the sensitivity of the cracking behaviour to the specimen orientation and extraction location. Furthermore, the residual stress profiles were measured, before and after applying the surface treatment techniques, and the effects of locked-in residual stresses on the fatigue performance of WAAM built components were discussed. Finally, a detailed texture analysis was performed on the surface treated and untreated regions of both WAAM built materials considered in this work. The obtained results from this study provide an insight into the advantages and disadvantages of various surface treatment techniques for fatigue life enhancement of WAAM built components with the view to extend the application of this advanced manufacturing technology to a wider range of industrial applications.

Keywords: Directed Energy Deposition; Wire Arc Additive Manufacturing; Fatigue; Surface Treatment; Residual Stress

---

[*] corresponding author

[10] Submitted manuscript in *Additive Manufacturing*. October 2022

7.1.1. Introduction

Fatigue is known as one of the main modes of failure in engineering structures, which are often subjected to cyclic loading conditions. Mechanical and fracture properties of alloys employed in engineering structures can be dramatically influenced by operation under severe environmental conditions such as harsh corrosive environments, leading to premature failure of structures and components during their service life[1]. Therefore, there is an essential need to improve the fatigue performance of engineering structures in order to achieve prolonged lifespans. Historically, a number of mechanical and surface treatment techniques have been developed and implemented for fatigue life enhancement purposes in industrial applications. An example of the mechanical technique, which is widely utilised to obtain extended fatigue lives in various industrial applications, is grinding. Using this technique, the stress concentration zones, particularly at the weld toes, are eliminated to reduce the local stress levels hence increasing the fatigue life[2]. In addition to the mechanical techniques, various surface treatment methods are available to use in isolation or in conjunction with mechanical design modifications. The most well-known surface treatment techniques which are implemented in a wide range of industrial applications are shot peening[3–7], laser shock peening[8–10], deep cold rolling[11–15], and vibro peening[16]. The general idea behind the surface treatment approach is to introduce a protective layer of compressive residual stresses that will decelerate crack initiation and propagation at the outer surface of the engineering components or structures. However, the extent of complexity, cost, required penetration depth and efficiency of different surface treatment techniques heavily depend on the material properties and operational loading conditions. Moreover, the formation of strain hardening and residual stresses during the surface treatment processes will alter the metallurgical features, hence the effects of microstructural changes on subsequent fatigue behaviour need to be fully investigated and understood for a given material and loading condition[1].

An efficient directed energy deposition (DED) process for metal additive manufacturing (AM) which has been found suitable for fabrication of large-scale components and structures is the wire arc additive manufacturing (WAAM) technology. This DED manufacturing technique, which can also be implemented for re-manufacturing and repair purposes, produces near shape components without the need for complex tooling or moulds. WAAM offers an immense potential for significant savings in cost, lead time and material waste as well as increased material efficiency and improved component performance[17,18]. However, the welding-based manufacturing process introduces residual stresses and distortions that would impact the fatigue life and may facilitate the crack initiation and propagation process in the WAAM built parts[19–21]. Also, another disadvantage of the WAAM process is the pronounced surface waviness that may introduce higher stress concentration sites between additively welded layers, which would undermine the fatigue performance[22]. For successful implementation of the WAAM method, the material properties should ideally meet or exceed those for the wrought counterparts. This can be difficult to achieve due to a considerably different manufacturing process that WAAM parts undergo, which involves a series of thermal cycles and continuous re-heating and cooling which will greatly affect the microstructure of the WAAM part[23]. In order to address the challenges that the WAAM technology brings, the surface treatment techniques were implemented in several studies with a view to improve the structural response and material characteristics of the additively manufactured parts.

The most common surface treatment method for life enhancement of WAAM parts that has been investigated in previous studies is inter-pass rolling that is normally applied on top of each deposited layer while building the WAAM parts. Colegrove et al.[24] concluded that inter-pass rolling of the deposited layers improved the mechanical properties of Ti-6Al-4V WAAM parts through microstructural refinement, increasing both the yield and tensile strength by up to 25%. Also, this method improved the fatigue properties due to high proof strength. The reported improvement may be also due to the reduced amount of induced porosity, which is known to degrade the fatigue performance. A different study[25] concluded that the effect of inter-pass rolling is reduced if rolling is applied on every fourth deposited layer, instead of each individual layer. In the research by Hönnige et al.[26], the rolling process was implemented on aluminium WAAM walls, and the results confirmed the efficiency of the treatment method to harden the material and improve the yield and tensile strength. Significant reduction of the peak residual stresses in longitudinal direction (i.e. WAAM building direction) was observed in several research studies by using inter-pass rolling on thin stainless steel and titanium WAAM walls[27,28]. The results have shown that the locked-in tensile residual stresses changed to compressive stresses after the surface treatment was applied. Similar effect of surface rolling on residual stress state was reported on wrought steel parts[29]. Moreover, it was concluded that the induced residual stress value using the rolling technique can be controlled by the magnitude of the applied pressure during rolling process.

Laser shock peening, which is often referred to as laser peening (LP), generally improves the resistance of metals and alloys to fatigue failure, by introducing strain hardening and compressive residual stresses into the part's surface using high energy pulsed laser source. The compressive residual stresses introduced by laser peening penetrate deeper below the surface than those from rolling or shot peening, usually resulting in higher fatigue life enhancement[3,8]. Thus, laser peening is commonly used for the mechanical components that have notches, holes or corners prone to fatigue failure, and potentially can help to overcome the limitations of the WAAM technology[30]. In the study by Sun et al.[31], application of LP post-processing method on aluminium WAAM specimens exhibited a significant refinement of the microstructure, improvements of micro-hardness, transition of damaging tensile residual stresses to beneficial compressive stresses, and an increase in yield strength by 72%. Comparable results were reported by Chi[32] and Luo[33], on tested titanium WAAM specimens, confirming the effectiveness of the surface treatment method for enhancement of mechanical characteristics of the material. Significant grain refinement was observed in microstructure of WAAM specimens treated with LP[34]. While various researchers conducted a limited number of aerospace application related studies to investigate the role of LP effects on the mechanical response of the aluminium and titanium WAAM parts, currently there is no published data available in the open literature on LP surface treatment effects on fatigue performance of WAAM steel parts.

The main focus of the present study is to thoroughly investigate the influence of two surface treatment techniques, rolling and laser shock peening, on fatigue crack propagation behaviour of WAAM built specimens made with two different grades of steel ER70S-6 and ER100S-1. The fatigue performance of surface treated specimens is assessed and discussed by considering the specimen extraction orientation and location with respect to the WAAM built geometry. Moreover, the residual stress state is measured and compared before and after applying the surface treatment to evaluate the efficiency of the treatment methods on the fatigue

performance of the WAAM parts. Last but not least, the material microstructure and texture were carefully examined and presented in this work. The strategic target of this study is to unlock the great potential of the WAAM technique for manufacturing, re-manufacturing and repair of offshore renewable energy structures. This would offer significant cost savings, particularly during the operation and maintenance phase of the asset life management and unveils the outstanding advantages of the WAAM technology to produce and maintain smart steel structures.

7.1.2. Materials and Fabrication Method

In the current study two types of steel welding wires were selected and employed, which are ER70S-6[35] and ER100S-1[36]. The chemical composition of these two steel wires is summarised in Table 7.1. Using each of these steel wires, a single WAAM wall was manufactured by the cold metal transfer (CMT) process, with the parameters shown in Table 7.2. Therefore, two thick WAAM walls were fabricated in total, with thickness of approximately 24 mm. The manufacturing set up, which is shown in Figure 7.1, consisted of a CMT power source and a programmed robotic arm with a CMT torch, which supplied both the welding wire and shielding gas during the fabrication process. Using an oscillation method[37], which is suitable for building thick WAAM walls, each wall was deposited on a base plate which was made of EN10025 rolled structural steel. As seen in Figure 7.1, the base plate was attached onto the working table with eight clamps, to minimise bending and distortion of the plate due to high manufacturing temperatures. The clamps were removed upon completion of the deposition process, after the WAAM walls were cooled down to ambient temperature.

Table 7.1: Chemical composition of the WAAM wires (wt.-%)[35,36]

	C	*Mn*	*Cr*	*Si*	*Ni*	*Mo*	*S*	*P*	*Cu*	*V*
ER70S-6	0.09	<1.60	0.05	0.09	0.05	0.05	0.007	0.007	0.20	0.05
ER100S-1	0.08	1.70	0.20	0.60	1.50	0.50	-	-	-	-

Table 7.2: CMT-WAAM fabrication parameters

Shielding gas	Ar+20% CO_2
Gas flow rate	15 L/min
Robot travelling speed	7.33 mm/sec
Wire diameter	1.2 mm
Wire feed speed	7.5 m/min
Dwell time	120 sec

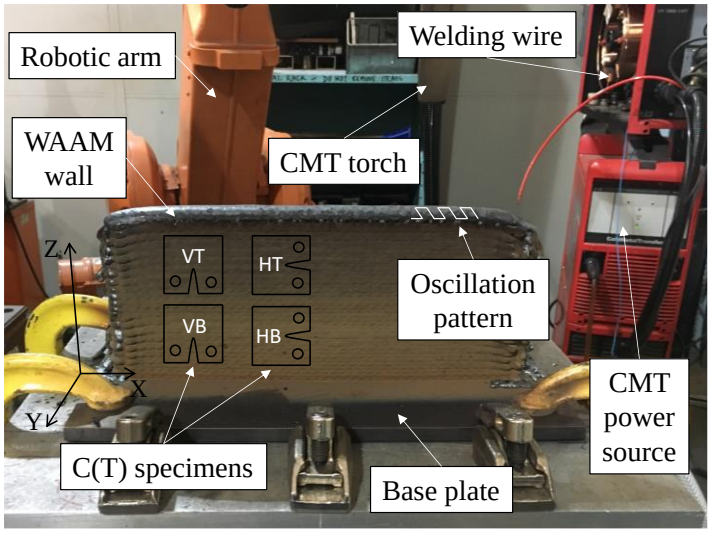

Figure 7.1: WAAM-CMT system set up with schematic specimen extraction map

Four notched compact-tension, C(T), specimens were then extracted from each of the WAAM walls using the Electrical Discharge Machining (EDM) method. Out of four C(T) specimens extracted from each material, two were machined from the top (T) of the wall while the other two were from the bottom (B). Also, for each of the extraction locations, the samples were extracted in two different orientations: vertical (V) – with the crack growth direction through AM layers, and horizontal (H) – with the crack path along AM layers. The combination of different specimen locations and orientations is schematically presented in Figure 7.1. The C(T) specimens were designed according to the ASTM E647 standard[38] with the width of W = 50 mm, height of H = 60 mm, total thickness of B = 16 mm and the initial crack length a_0 = 17 mm (before pre-fatigue cracking). Knife edges were machined at the crack mouth of the specimens following the instructions in the ASTM 1820 standard[39], to accommodate a clip gauge for crack growth monitoring using the compliance measurement technique during the fatigue crack growth tests.

7.1.3. Application of surface treatment on WAAM built specimens

Upon extraction of eight C(T) specimens from the WAAM walls, four made of ER70S-6 and four made of ER100S-1, surface treatment techniques were applied onto the test specimens. For each of the two materials considered in this study, half of the specimens were treated with the rolling technique and another half with laser shock peening method, to assess the fatigue life enhancement performance of these two surface treatment techniques compared to untreated material state.

- **Surface rolling**

Two C(T) specimens extracted from the top of the ER70S-6 WAAM wall, denoted 70-VT and 70-HT, and two specimens cut from the ER100S-1 WAAM wall, denoted 100-HT and 100-HB (see Figure 7.1), were selected for surface rolling (R) treatment. The rolling parameters were adopted from the finite element analysis (FEA) study of Pi et al.[40], where it was suggested to use a 20 mm wide roller with a diameter of 50 mm made of a high-strength steel and apply rolling starting from the crack tip of the C(T) specimens with 80 kN load, moving along the

crack path with a radial speed of 100 mm/s. The results from this FEA study[40] also showed that the optimum residual stress distribution was achieved by rolling the specimen for only 8 mm from the crack tip. Hence, the proposed parameters were implemented for the high pressure rolling on the C(T) specimens in the current study. The surface rolling treatment set up is shown in Figure 7.2 (a). As seen in this figure, the rolling process consisted of a moving frame with a roller, laser tag for specimen alignment and three clamps to prevent the C(T) specimens from any movements. Each specimen was rolled on both sides (i.e., free surfaces). This was done by performing the surface rolling on the first side and then the specimen was flipped around to repeat the surface rolling treatment on the opposite side. A rectangular rolled surface area with the dimensions of 20 × 8 mm was introduced ahead of the crack tip in C(T) specimens, which is visible in Figure 7.2 (b).

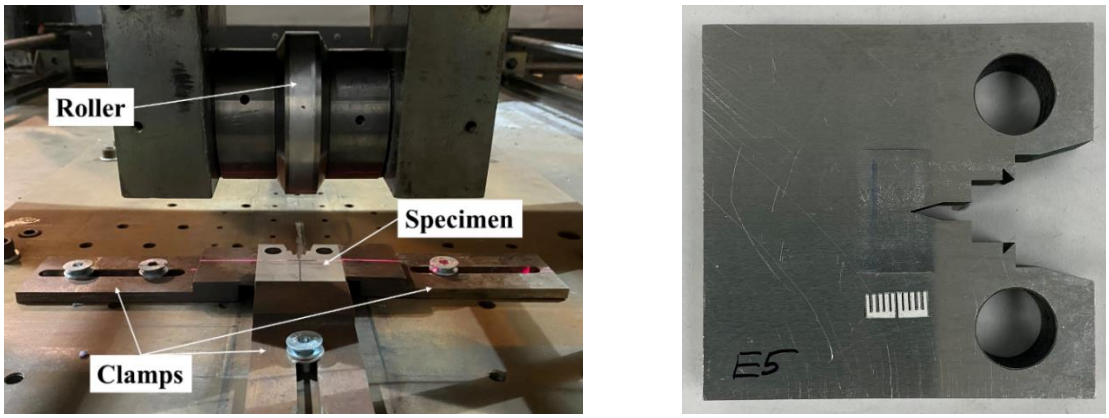

(a) (b)

Figure 7.2: Surface rolling process: (a) treatment set up, and (b) an example of a rolled surface on a C(T) specimen

- **Laser shock peening**

The remaining four C(T) specimens, two extracted from the ER70S-6 WAAM wall denoted 70-VB and 70-HB, and two cut from the ER100S-1 WAAM wall denoted 100-VT and 100-VB, were used to apply laser shock peening surface treatment technique. The treated area was identical to the rolled area (see Figure 7.2 (b)) for direct comparison between the two surface treatment techniques. Similar to the surface rolling treatment, the LP treatment was applied on both sides of the C(T) specimens with a 20 × 8 mm^2 rectangular treated area ahead of the notch tip. The laser shock peening treatment was applied onto the C(T) specimens using the spot size of 3 mm^2, energy level of 8.1 with the power density of J = 5 GW/cm^2, pulse duration of 18 ns, with three layers providing 300% coverage. An example of the specimen during the laser shock peening process with a patch attached onto the specimen is displayed in Figure 7.3 (a). An example of a specimen after LP treatment is shown in Figure 7.3 (b), where the treated area is visible on the specimen surface.

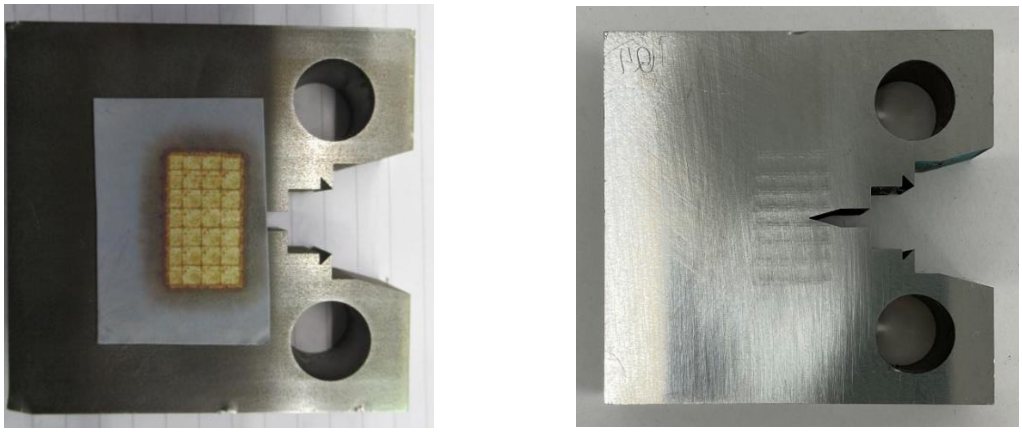

(a) (b)

Figure 7.3: An example of the laser shock peening specimen (a) during the surface treatment process, and (b) after the treatment process

7.1.4. Residual stress measurements on WAAM built specimens

Two non-destructive residual stress measurement techniques were used to characterise the residual stress distribution profiles in the C(T) specimens extracted from the WAAM walls: neutron diffraction and X-ray methods. The neutron diffraction (ND) technique was used to measure the change in residual stresses in WAAM built specimens before and after the surface treatment application. This method offers a much deeper penetration depth for residual stress measurements compared to other non-destructive methods, allowing the characterisation of the three components of stress, hence was found suitable for residual stress characterisation in 16 mm thick C(T) specimens examined in this study. Subsequently, the X-ray (XR) method was used to measure the residual stresses after the introduction of the surface treatment. This method offers high resolution and accuracy over a thin layer on the outer surface of metallic components, hence was found suitable to measure near surface residual stresses which were introduced into the WAAM built C(T) specimens by applying the surface treatment techniques. The details of the neutron diffraction and X-ray residual stress measurement techniques are described below. Two representative specimens extracted from the ER100S-1 WAAM wall were measured in this study to investigate the impact of surface treatment on residual stress distribution in WAAM built components at the neutron diffraction facilities.

- **Neutron diffraction technique**

In the current study, the initial residual stresses in four untreated ER100S-1 WAAM specimens were measured by a monochromatic strain diffractometer SALSA at the Institut Laue-Langevin (ILL)-France[41]. Upon completion of the surface treatment on these four specimens, the changes in the residual stress state were examined using the KOWARI strain scanner at the Australia's Nuclear Science and Technology Organisation (ANSTO). The measurement set up at SALSA is displayed in Figure 7.4 (a), which consists of a hexapod stage on which specimens are placed and aligned, a double bent Si monochromator and 2D-PSD He detector. The set up at KOWARI is presented in Figure 7.4 (c). In both cases the neutron wavelength was fixed (1.64 Å at SALSA and 1.67 Å at KOWARI) to measure the Fe α {211} family of crystallographic planes. This resulted in a diffraction angle near 90° and hence a near cuboid gauge volume. An incoming

beam of 2×2 mm^2 was defined by 2 mm radial collimators on the primary side together with a third radial collimator on the secondary or diffraction side (gauge volume of 2×2×2 mm^3) for these measurements on SALSA; and slits system, on both primary and secondary beam, was utilised on KOWARI. Strain mapping in neutron diffraction measurements was performed along the crack propagation line, to capture the residual stress profile ahead of the crack tip along the loading direction of C(T) specimens (i.e., perpendicular to the crack plane). In order to measure the through-thickness residual stress profile in untreated specimens at SALSA, the neutron diffraction measurements were conducted along three different lines with the first set of measurements carried out at the mid-thickness (which is shown with line L0 in Figure 7.4 (b)) and the other two with 3 mm (L3) and 5 mm (L5) distance from the mid-thickness of the specimen (see Figure 7.4 (b)). The mid-thickness measurement L0 was repeated on treated specimens at KOWARI. Additionally, using the gauge volume of 0.5×0.5×0.5 mm^3, the through-thickness lines were measured in the specimens: T1, T2, T3 and T4 with 1.5, 5, 10, and 16.5 mm away from the crack tip respectively (Figure 7.4 (d)), to examine the symmetry of the residual stresses in treated specimens. The component of stress normal to the crack path, representing the direction of the applied load on C(T) specimens (shown with black arrow in Figure 7.4 (b) and (d)), was used in further crack propagation analysis.

In order to assess the stress-free reference value of *d* spacing, d_0, a series of cubes with the dimensions of 5×5×5 mm^3 were extracted along the crack path from nominally identical specimens without any surface treatment[42]. Different sets of d_0 cubes, corresponding to different specimen locations and orientations extracted from the WAAM wall, were prepared, and measured to minimise the error in neutron diffraction results obtained from each specimen. All d_0 cubes were extracted using the EDM technique to avoid the machining effects on the obtained stress-free values. An example of the cubes extracted for d_0 measurements in two C(T) specimens is illustrated in Figure 7.4 (c). The extraction and measurement of d_0 cubes from WAAM build specimens enabled the material and microstructural variations along the crack path to be captured in residual stress measurements[42]. Therefore, the presented residual stress results in this study have higher accuracy with regards to additive manufactured specimens and their potential microstructural gradients compared to alternative d_0 measurement techniques, such as the stress equilibrium or measurement at the corner of the specimen, which are conventionally used for d_0 measurements in relatively homogenous materials.

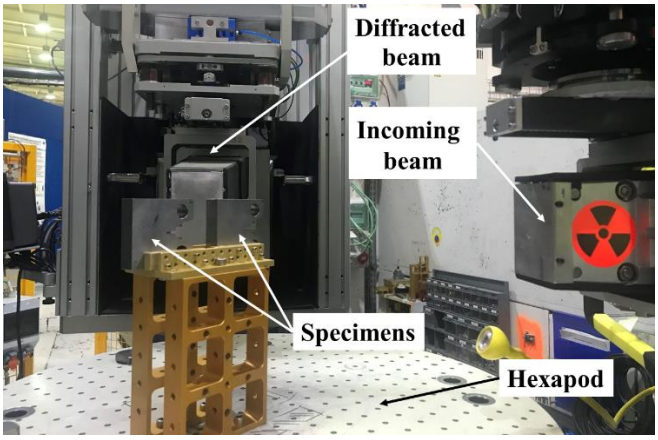

(a)

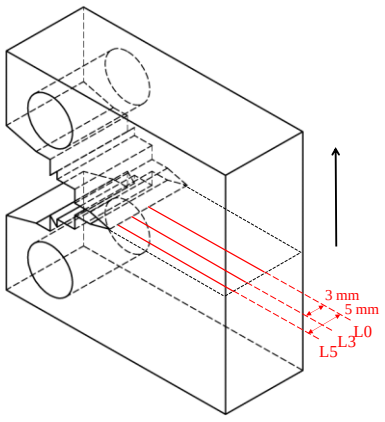

(b)

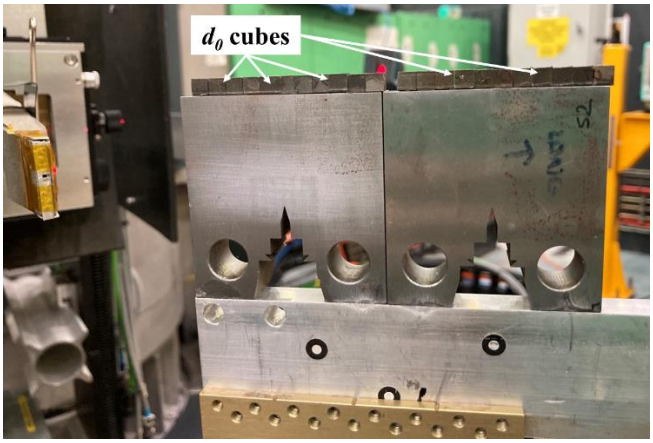

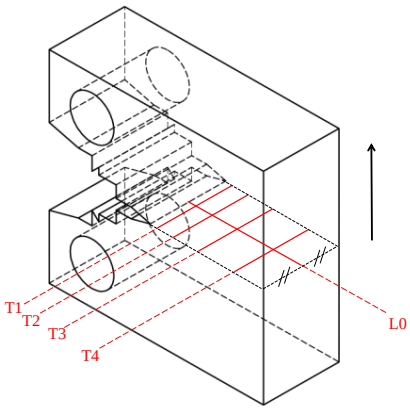

(c) (d)

Figure 7.4: Neutron diffraction (a) test set up at SALSA for untreated specimens, and (b) measurement lines with respect to the specimen thickness; (c) KOWARI set up for treated specimens with d_0 cubes measurements and (d) corresponding measurement lines (black arrows indicates the residual stress component of interest)

During the neutron strain diffraction measurements, the neutron wavelength was kept constant, and the diffraction angle was measured. Subsequently, the lattice parameter d was measured using Bragg's law[43]:

$$n\lambda_n = 2d_{hkl}sin\theta_{hkl} \quad \text{Equation 7.1}$$

where n is a constant, λ_n is the neutron wavelength, d is the lattice spacing or the distance between sets of parallel crystallographic planes characterised by Miller indices hkl, and θ is the scattering angle.

Effectively, the accurate measurements of the distance between similarly oriented planes of atoms can be used as a tool to measure elastic strain. Every change in the lattice spacing (Δd) represents a residual strain, which can be calculated using the following equation:

$$\varepsilon_{hkl} = \frac{\Delta d_{hkl}}{d_{0,hkl}} = \frac{d_{hkl} - d_{0,hkl}}{d_{0,hkl}} \quad \text{Equation 7.2}$$

where d_0 is the corresponding stress-free value of lattice spacing, obtained from the extracted cubes, at the point of measurement.

The residual stress in each direction can be calculated from the residual strains using Hooke's law, which can be described as:

$$\sigma_i = \frac{E}{(1+\nu)(1-2\nu)}\left[(1-\nu)\varepsilon_i + \nu(\varepsilon_j + \varepsilon_k)\right] \quad \text{Equation 7.3}$$

where E is the elastic Young's modulus and ν is Poisson's ratio. The crystallographic values of the elastic modulus and Poisson's ratio used in this study for Fe α {211} family of crystallographic planes were E=210 GPa and ν =0.25[44].

- **X-ray diffraction method**

Upon application of the surface treatment techniques onto the four ER100S-1 specimens, the near surface residual stress measurements were performed, to identify the residual stress profiles at the outer surface of C(T) specimens as a result of the treatment process. For this

purpose, diffraction measurements were conducted using laboratory X-ray diffractometers. Phase analysis was carried out using a Malvern Panalytical EMPYREAN diffractometer, enabling the location of diffraction reflections based on which the residual stresses were determined with high precision[45,46]. A copper X-ray tube generating the K_{α_1} radiation of the wavelength equal to $\lambda = 1.54$ Å was used in order to employ the planned phase composition analysis. Detection of the diffracted beam intensity was implemented by the PIXcel1D semiconductor detector with Soller slits 0.04° placed in the path of the diffracted beam. The spot size was 1 × 1 mm^2 and the phase composition was measured in 2θ angular range from 20° to 152.31° in classical Bragg-Brentano geometry. The step of 2θ angle was 0.0525° and the measurement time at each step was 3600s.

Similar to the neutron diffraction measurements, surface X-ray diffraction measurements were conducted along the crack path of the specimens starting from the crack tip. The stress component perpendicular to the crack path, which provides the crack driving force, was recorded during the X-ray measurements. An interval of 1 mm distance between the consecutive measurement points was selected for X-ray residual stress experiments. The maximum X-ray penetration depth for the experiments described above was 37.5 μm.

7.1.5. Fatigue crack growth testing and analysis

Fatigue crack growth (FCG) tests were conducted on all surface treated C(T) specimens using a 100 kN servo-hydraulic Instron machine under Mode I fracture mechanics loading conditions, in accordance with the ASTM E647 standard[38]. All tests were performed at the room temperature with the load ratio (i.e., P_{min}/P_{max}) of R = 0.1, where the maximum applied load was P_{max} = 10 kN. The FCG tests were performed using a constant amplitude sinusoidal cyclic waveform with 5 Hz frequency. Prior to FCG testing, all specimens were pre-cracked, under cyclic loading condition, from the initial machined notch of a_0 = 17 mm to approximately 20 mm ($a_{i,p}/W$ = 0.4) using the load decreasing approach, introducing infinitely sharp crack tip ahead of the machined notch. During the pre-cracking process, it was ensured that the value of maximum stress intensity factor K_{max} corresponding to P_{max} did not exceed the initial K_{max} in the actual FCG test, so that the FCG results were not influenced by any significant pre-existing plasticity ahead of the initial crack tip.

In order to estimate the instantaneous crack length a_i, during both pre-cracking and FCG tests, the unloading compliance method was implemented by calibrating and attaching a clip gauge onto the knife edges of the specimen (as shown in Figure 7.5). Furthermore, two high resolution cameras were placed on each side of the C(T) specimen to ensure that the crack growth occurred evenly on both sides of the specimen and cross check the estimated values of the crack length obtained from the compliance method. All C(T) specimens were tested until the estimated value of crack length reached 35 mm ($a_{f,c}/W$ = 0.7) at the end of the experiment. The FCG test set up is presented in Figure 7.5.

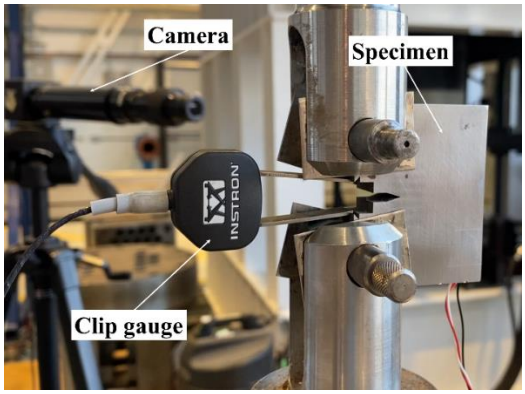

Figure 7.5: Fatigue crack growth test set up

During the FCG tests the number of cycles and instantaneous crack lengths, estimated using the compliance technique, were continuously recorded. Subsequently, the FCG rates, *da/dN*, were calculated employing a combination of the secant method (for the first and the last three data points), and seven-point incremental polynomial method (for the rest of the data points). The stress intensity factor (SIF) range, ΔK, was then computed following the shape function equation presented in Equation 7.4 that was developed by Mehmanparast et al.[47] and provides more accurate solutions for the shape function in a C(T) specimen for a wider range of crack lengths, $0.2 \leq a/W \leq 0.7$, compared to that recommended in the ASTM E647 standard. In Equation 7.4, α is the normalised crack length, a/W, and ΔP is the load range, which is defined as the difference between P_{max} and P_{min}.

$$\Delta K = \frac{\Delta P}{BW} \cdot \sqrt{a} \cdot (-372.12\alpha^6 + 1628.60\alpha^5 - 2107.46\alpha^4 + 1304.65\alpha^3 - 391.20\alpha^2 + 54.81\alpha + 7.57) \quad \text{Equation 7.4}$$

7.1.6. Experimental results and discussions

- **FCG test results**

Two sets of analyses were conducted on the FCG test data to examine the surface treatment effects on the fatigue performance of WAAM built specimens: based on their orientation and extraction location. The recorded raw data during the FCG tests, which included the crack length, *a*, and the number of cycles, *N*, were plotted against each other as shown in Figure 7.6. Also included in Figure 7.6, are the average FCG trends (AV) from nominally identical untreated specimens extracted from ER70S-6 WAAM wall[48] with vertical (70-V-AV) and horizontal (70-H-AV) orientations in Figure 7.6 (a), and from top (70-T-AV) and bottom (70-B-AV) of the walls in Figure 7.6 (b). Similarly, results obtained from treated samples were compared with the average trends from untreated specimens made with ER100S-1 steel[49] for different orientations in Figure 7.6 (c) and locations in Figure 7.6 (d).

The comparison of the crack growth trends in Figure 7.6 (a) demonstrates that both surface treatment techniques, LP and R, are effective for life enhancement of ER70S-6 vertical specimens, with surface rolling increasing the test duration by 2.1 times and laser shock peening by 2.5 times compared to the average trend from untreated specimens. On the other hand, for ER70S-6 horizontal specimens the surface treatment techniques were not found

beneficial, and both techniques have reduced the test duration on average by around 15% compared to untreated specimens. It is worth noting here, that both rolled specimens, despite of their orientation, showed similar performance. Laser shock peening of ER70S-6 vertical specimen has presented the longest test duration; however, in laser peened horizontal specimen the crack has propagated 1.5 times quicker than in untreated horizontal specimens. Evaluation of the FCG results based on the specimen location in ER70S-6 WAAM wall (Figure 7.6 (b)) shows that two rolled specimens extracted from the top of the wall have slightly improved test duration. Laser shock peening has demonstrated an increase in the test duration for one bottom specimen by 24%, and reduction by 18% for the second bottom specimen. It can be concluded that regardless of the comparison method (by orientation or location), the best performance for ER70S-6 wall was shown by laser peened specimen 70-VB-LP, though using the same surface treatment technique on 70-HB-LP specimen only worsens the fatigue life.

Analysing the FCG data for ER100S-1 specimens with different orientations (Figure 7.6 (c)), it can be seen that laser peening surface treatment increased the fatigue life in vertical specimens on average by 27%. The fatigue life enhancement was also observed in one rolled horizontal specimen, improving the test duration by 1.6 times. However, for the second horizontal specimen, 100-HB-R, surface treatment application was not beneficial, and the results are found to be very similar to the average results for untreated specimens. Further comparison of the FCG results for different extraction locations of ER100S-1 specimens (Figure 7.6 (d)) demonstrates that laser peening was a more effective surface treatment technique for both top and bottom specimens, increasing the number of cycles by 1.1 and 2.4 times, respectively. However, rolling not only did not improve the test duration but worsened the results for both extraction locations. It should be noted here, that for both examined materials, the worst results were presented by horizontal specimens extracted from the bottom of WAAM walls, regardless of the applied surface treatment method. Thus, the best life enhancement was achieved by laser peening technique applied on vertical bottom specimen 70-VB-LP for ER70S-6 steel and on vertical top specimen 100-VT-LP for ER100S-1.

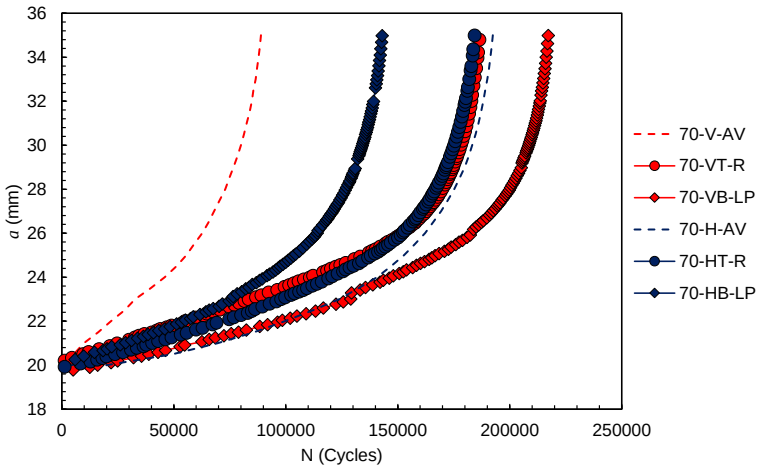

(a)

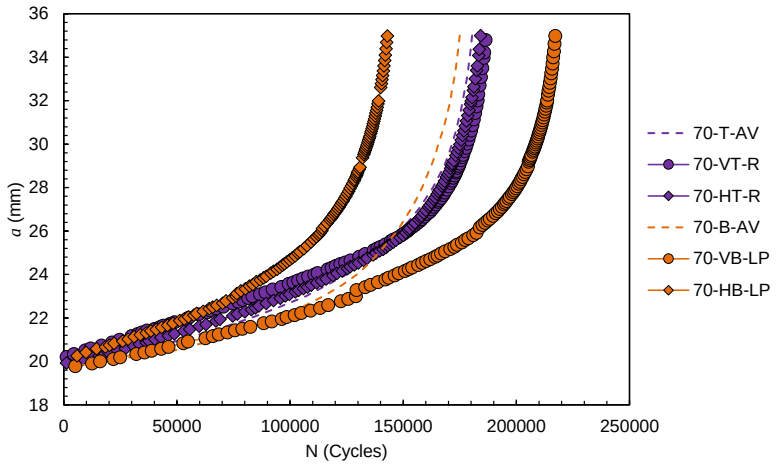

(b)

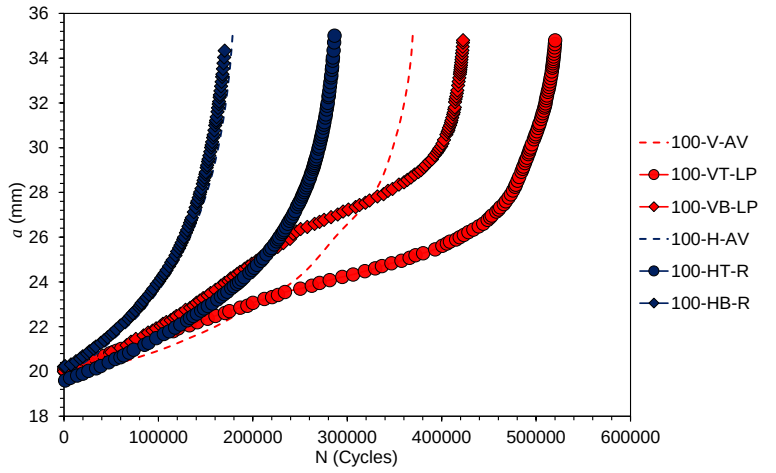

(c)

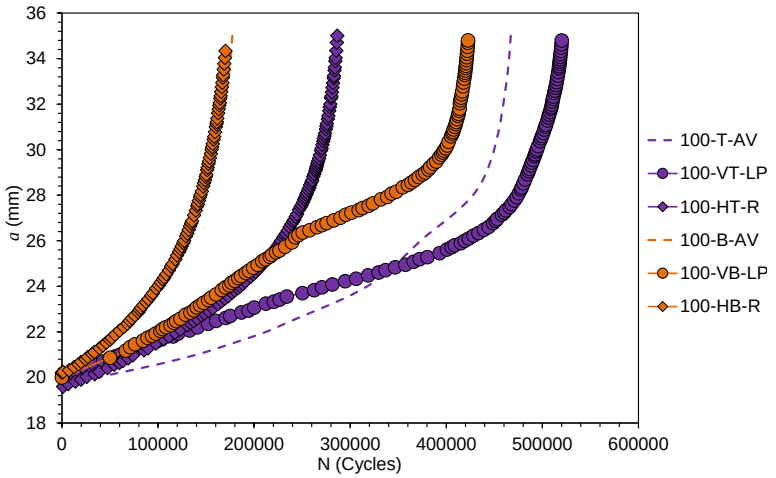

(d)

Figure 7.6: Comparison of FCG trends for surface treated WAAM specimens with average FCG trends from untreated specimens for (a-b) ER70S-6, and (c-d) ER100S-1 specimens

The FCG rates were obtained from the tests by calculating *da/dN* and then correlated with the SIF range, ΔK, the results are shown in Figure 7.7. Two sets of analyses were also carried out on the FCG rates data to investigate the sensitivity of the specimen orientation and location to the surface treatment. In Figure 7.7, the results obtained from this study on surface treated specimens are compared with the FCG data on nominally identical untreated specimens[48,49], for which the mean line (MN) was plotted along with mean ±2 standard deviation (SD) trends.

In Figure 7.7 (a) it can be seen that the FCG rates for surface treated ER70S-6 vertical specimens are up to 2 times lower than the mean–2SD line from untreated specimens for the SIF range of up to $\Delta K \approx 30.5$ MPa√m, which corresponds to the crack extension of approximately $\Delta a = 8$ mm – the length of the surface treated region. At higher ΔK values, the FCG rates for vertical specimens fluctuate about the mean line, but do not exceed the mean+2SD line for untreated specimens. The vertical surface treated specimens present the lowest trends. The FCG trend for rolled horizontal specimen is found similar to the vertical specimens; however, it is crossing the mean-2SD line for horizontal untreated specimens at $\Delta K \approx 25.4$ MPa√m, which corresponds to the crack extension of approximately $\Delta a = 6$ mm, then it falls upon the mean line until the end of the test. As for the laser peened specimen, which showed the shortest test duration among the treated specimens, 70-HB-LP, the FCG rates fluctuate between the mean±2SD lines throughout the test, without showing any deterioration in the rates.

Comparison of the results based on their extraction locations for ER70S-6 specimens in Figure 7.7 (b) shows FCG rate enhancement (below mean–2SD line) for rolled top specimens at a range of ΔK values up to approximately 25.5 MPa√m (corresponding to $\Delta a = 5.8$ mm). The laser peened vertical bottom specimen, 70-VB-LP, represents the lowest FCG rates at the beginning of the test (at low ΔK values), showing considerable improvement in the crack growth rates, with the lower FCG trend at a wide range of SIF of up to $\Delta K = 31$ MPa√m, corresponding to crack extension of $\Delta a = 8.7$ mm. Then it crosses the lower bound for untreated specimens and fluctuates along the mean line until the end of the test. On the other hand, another laser peened specimen from the bottom of the wall, 70-HB-LP, is showing the highest FCG trends at lower values of SIF and crossing the mean-2SD line at $\Delta K = 25.5$ MPa√m (corresponding to $\Delta a = 5.8$ mm). All four test results converge midway through the test. It can be concluded here that both surface treatment techniques are effective on ER70S-6 specimens, decreasing the FCG rates in the beginning of the test (while the crack grows through the treated area) and converging to the mean FCG trend from untreated specimens by the end of the test.

Evaluation of the FCG rates for ER100S-1 specimens with different orientations from Figure 7.7 (c) shows that the effect of surface treatment on this material is less pronounced compared with ER70S-6, as the trends for the treated specimens do not go beyond the mean±2SD lines, regardless of their orientation and selected surface treatment technique. However, an important point that can be noted here is that the results for vertical specimens are mostly located in the lower half between the mean and mean-2SD lines, indicating positive effect of laser peening treatment. Similar behaviour is observed for rolled horizontal specimen 100-HT-R, which starts at the mean-2SD line of horizontal untreated specimens and progresses towards the mean line by the end of the test. However, 100-HB-R specimen which had the shortest test duration among all experiments conducted in this research, presents the highest FCG rates compared to other specimens and its trend is mostly located between the mean and mean+2SD lines, confirming that no improvement was achieved by rolling this specimen.

From Figure 7.7 (d), which demonstrates a comparison of FCG rates for ER100S-1 specimens based on their extraction location, it can be seen that the FCG trend for laser peened 100-VB-LP specimen extracted from the bottom of WAAM wall is lower than mean-2SD line for the bottom untreated specimens throughout the test and presents the lowest FCG rates among all four tested specimens. This trend is the only example of sufficient FCG rate improvement achieved by surface treatment on ER100S-1 specimens as its trend starts and stays below the mean-2SD line for untreated specimens throughout the test. The trend with the highest FCG rates belongs to rolled specimen from the bottom of the wall 100-HB-R, though it fluctuates between the mean±2SD lines during the test. No life enhancement effect is seen for the top laser peened specimen 100-VT-LP, the results for which fluctuates about the mean line. The worst FCG performance compared to the mean line from untreated specimens is seen for top rolled specimen 100-HT-R, the trend for which is located in the upper half between the mean and upper bounds for untreated specimens. Thus, it can be concluded here that surface rolling is a less effective surface treatment technique compared to laser shock peening for ER100S-1 under the examined rolling parameters and testing conditions. Moreover, it should be noted here that regardless of the material and applied surface treatment technique, horizontal specimen extracted from the bottom of WAAM wall is showing the highest FCG rates and shortest test duration.

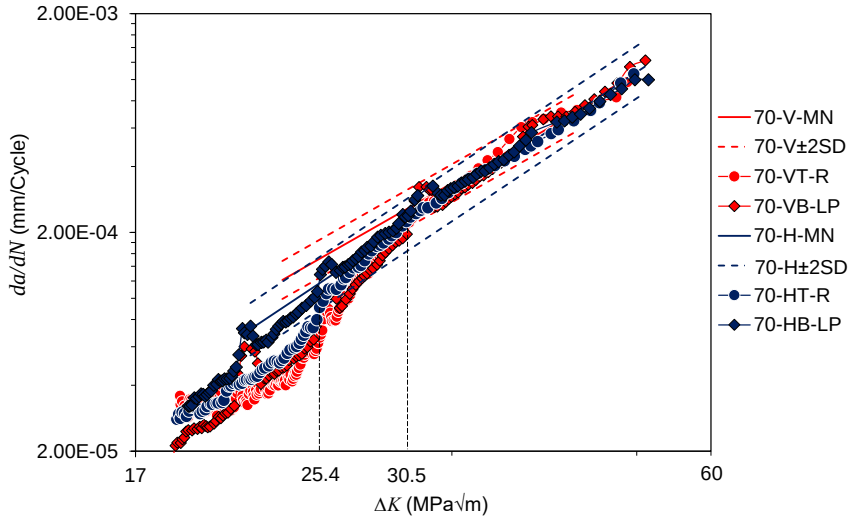

(a)

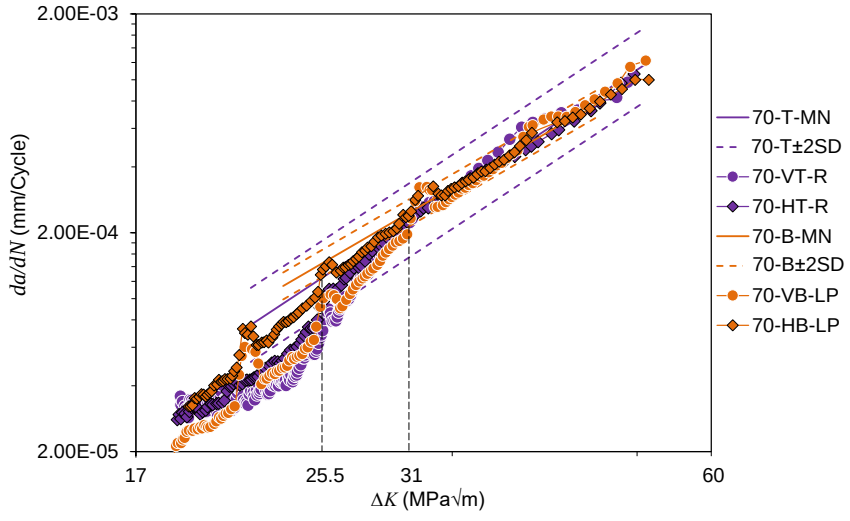

(b)

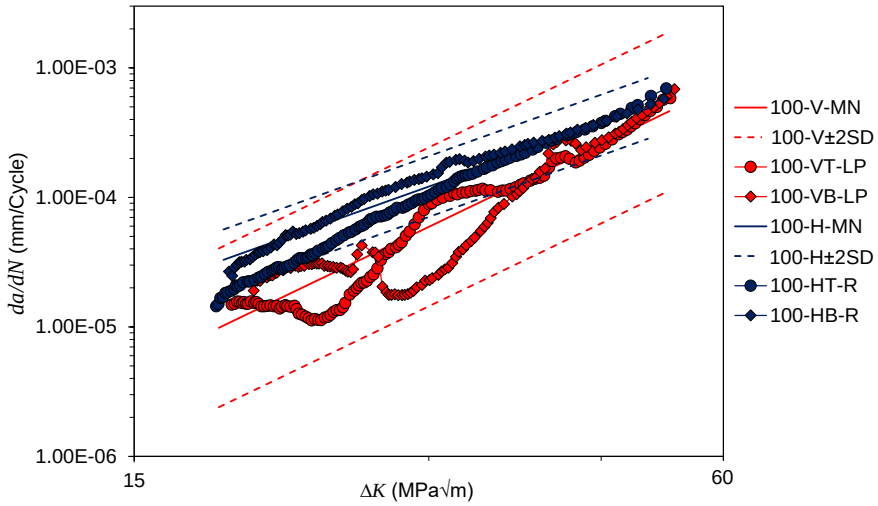

(c)

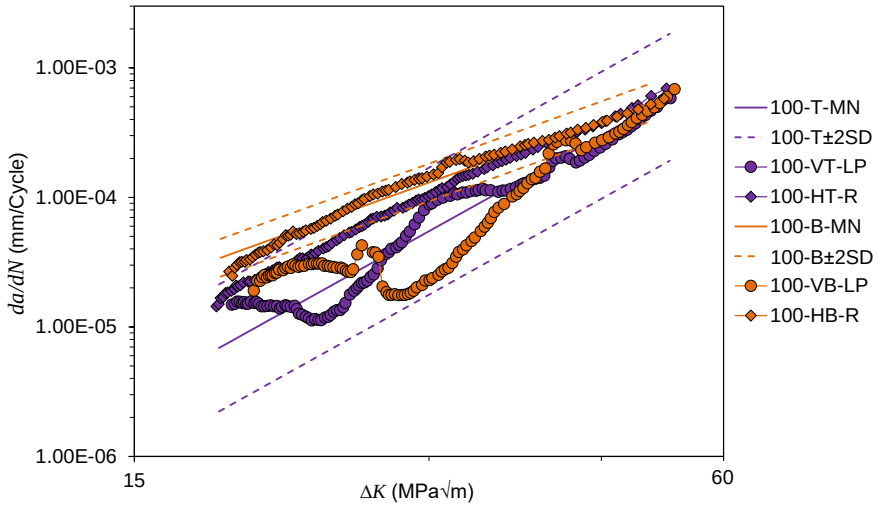

(d)

Figure 7.7: Comparison of the FCG test results for surface treated specimens with average FCG trends from untreated specimens for (a-b) ER70S-6, and (c-d) ER100S-1 specimens

- **Residual stress measurement results**

The residual stress measurements, before and after surface treatment, for ER100S-1 specimens with the longest (100-VT-LP) and shortest test durations (100-HB-R) are presented in Figure 7.8, showing the component of stress normal to the crack path (Figure 7.4 (c) and (d)). As mentioned in Section 7.1.4, neutron diffraction measurements were performed on untreated and treated specimens, with additional X-ray measurements in the near surface region of treated specimens. The error bars have shown minor variation within 10-20 MPa and were not included in the residual stress trends. It can be observed in Figure 7.8 (a) that 100-VT specimen had a pronounced state of tensile residual stresses ahead of the crack tip before any surface treatment, with a peak value of around 400 MPa within the bulk. As seen in Figure 7.8 (a), through thickness characterisation revealed generally similar residual stress profiles for L0, L3 and L5

at the distance between 0 to approximately 15 mm from the crack tip while a slightly higher residual stress value was identified for lower penetration depths from the specimen surface. However, as seen from the near surface X-ray results, laser shock peening introduced a significant compressive residual stress of around -260 MPa at the crack tip and further compressive stresses in the region between 1.5 to 9.5 mm from the crack tip, which corresponds to the region where the laser peening treatment was applied (see Section 7.1.3), shifting the peak of the tensile residual stresses further away from the crack tip. The mid-thickness ND measurement L0 in treated VT-LP specimen shows that application of LP at the surface of the specimen subsequently reduces the tensile residual stresses in the middle of the specimen, which becomes almost constant along the crack path, with average value of 70 MPa. The residual stress results are in excellent agreement with the FCG behaviour of 100-VT specimen observed in Figure 7.6 (c-d). Where an increased fatigue life was observed in the surface treated specimen with slowed down crack propagation rate in the peened region, caused by beneficial compressive residual stresses, followed by accelerated cracking behaviour beyond the peened area, caused by detrimental tensile residual stresses. Figure 7.8 (b) shows an opposite residual stress transition trend in 100-HB specimen before and after surface treatment. This specimen initially had a compressive residual stress field along the crack path within the bulk, reaching up to -100 MPa with no significant gradients across thickness at L0, L3 and L5. However, as shown by X-ray results, the surface rolling treatment introduced damaging tensile residual stresses on the surface with amplitude of between 100 and 400 MPa on the full length of the crack path. The ND measurements in mid-thickness of the treated specimen HB-R also detect the introduced tensile stresses along the crack path, with minor fluctuations and the average value of 105 MPa. This led to the shortest fatigue life discovered among all specimens in Figure 7.6 (c-d) and the highest FCG rates in Figure 7.7 (c-d). It is worth noting here, that minor fluctuations in the peak residual stresses measured before surface treatment application at L0, L3 and L5 are seen for both specimens, indicating generally lower peak stress values at the mid-thickness, which gradually grow towards the surface of the specimen. The observed through-thickness residual stress distribution field is in good agreement with previous studies[50,51].

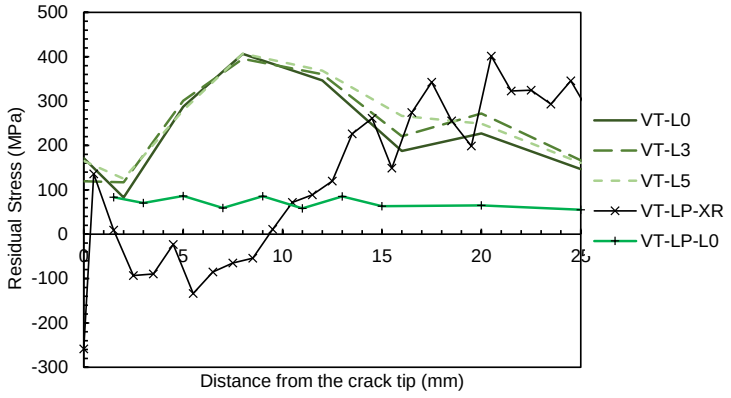

(a)

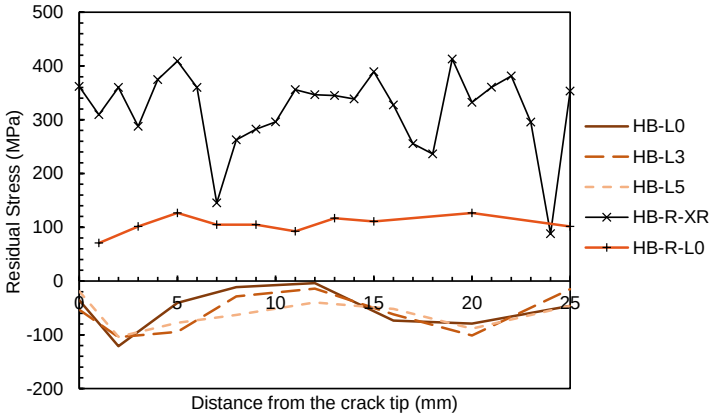

(b)

Figure 7.8: Residual stress distribution in ER100S-1 specimens before and after surface treatment (a) 100-VT specimen before and after laser shock peening, (b) 100-HB specimen before and after surface rolling

Comparison of Figure 7.8 (a) and (b) demonstrates that the residual stress before application of any surface treatment is lower in specimens extracted from the bottom of the WAAM wall. This can be associated with a higher number of thermal cycles applied on the layers deposited at the bottom of the WAAM wall which would relax the residual stresses in this region, compared to the top layers which are subjected to a lower number of thermal cycles. Moreover, the residual stress measurement results on ER100S-1 specimens show that laser shock peening is an effective surface treatment technique to remove the detrimental tensile residual stresses at the top region of the WAAM wall, hence increasing the fatigue life and decelerating the FCG rates, while the bottom region of the WAAM wall exhibits a better state of residual stress, owing to an enhanced fatigue performance, without applying any surface rolling treatment.

It should be noted that according to the study by Gornyakov et al.[52] during the surface rolling process on WAAM built components, a relatively high tensile residual stress zone can be developed behind the roller, in the treated region and near the outer surface of the component, which is due to the non-uniform distribution of plastic deformation. Also, it is known that laser shock peening is capable of introducing significant levels of compressive residual stresses due to relatively uniform surface hardening effects[53,54]. This shows that the conclusions from similar studies on the WAAM built components in the literature are consistent with the observations from this study.

The through-thickness residual stress distribution of treated vertical ER100S-1 specimens is presented in Figure 7.9 (a) for laser peened specimen and (b) for rolled specimen, showing the component of stress normal to the crack path (Figure 7.4 (c) and (d)). From these figures it can be seen that the residual stress trends are asymmetrical with respect to the mid-thickness plane of the specimens regardless of the surface treatment technique. The difference between stress values on the opposite sides of the specimen, 0.95 mm away from the surface, is up to 8 times for the laser peened specimen, whereas for the rolled specimen is up to 2.7 times. Moreover, it can be seen from the trends that application of LP surface treatment induces higher compressive stresses near specimen surface region, which gradually reduce within first 1.5-2 mm from the surface, and then balance with increasing tensile stresses towards the middle of the specimen. The trend for rolled specimen is not as clear and shows fluctuations in stress throughout the specimen thickness, with low tensile stress between 0-13 MPa in the middle of the specimen.

It is also seen that T1 measurement line (1.5 mm away from the crack tip) in rolled specimen shows absence of compressive residual stresses throughout the thickness of the specimen. The maximum compressive stress near the surface for LP specimen is 3.4 times higher than for rolled specimen, confirming higher efficiency of laser peening surface treatment technique on ER100S-1 WAAM built specimens. Further seen in the results is that the maximum tensile stress value in the middle of the specimen is 7.7 times higher in LP specimen than in rolled one. Asymmetrical residual stress distribution in treated specimens can be due to the selected procedure for the surface treatment application, which was not conducted simultaneously on both specimen sides, but instead was done on one side at a time.

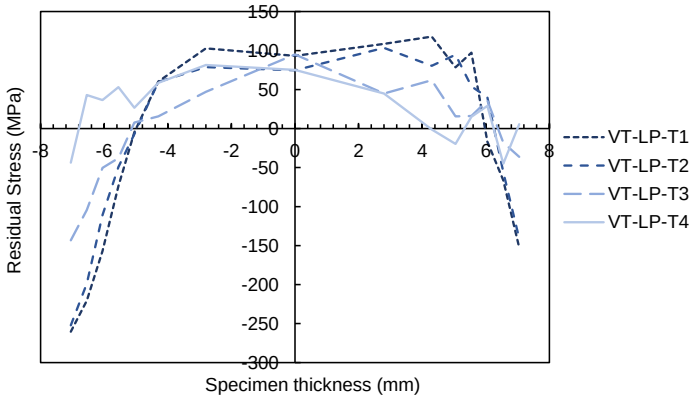

(a)

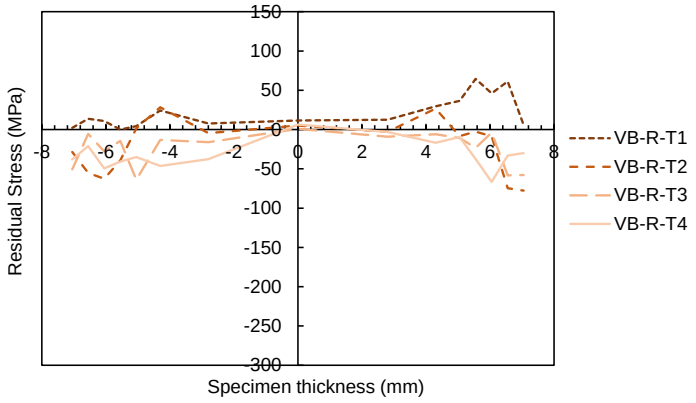

(b)

Figure 7.9: Through-thickness residual stress distribution in treated areas of ER100S-1 vertical specimens (a) laser peened and (b) rolled. (Specimen thickness is 16 mm).

- **Microstructural analysis**

Upon completion of the FCG tests, all eight specimens were broken-open into halves by initially soaking them in liquid nitrogen for a few minutes, to minimise the plastic deformation during fracture, and then pulling them apart using the servo-hydraulic machine. A 10×5×5 mm^3 coupon was extracted from each C(T) specimen using the EDM technique in such a way that along the 10 mm length, 5 mm was taken from the treated region and 5 mm from the untreated surface (see Figure 7.10). The coupons were mounted in a conductive resin, ground and polished to 1 µm surface finish, with final polishing conducted using colloidal silica suspension. Electron Backscatter Diffraction (EBSD) measurements were performed on the coupons using an Oxford Instruments Symmetry with accelerating voltage of 20 keV, beam

current of 5 nA, field of view of 300 um and step size of 0.7 um. The pole figures obtained from the untreated and treated regions of the specimens are presented in Figure 7.11. Furthermore, the texture indices were measured at the untreated and treated regions in each coupon and compared with each other in Table 7.3 and Figure 7.12.

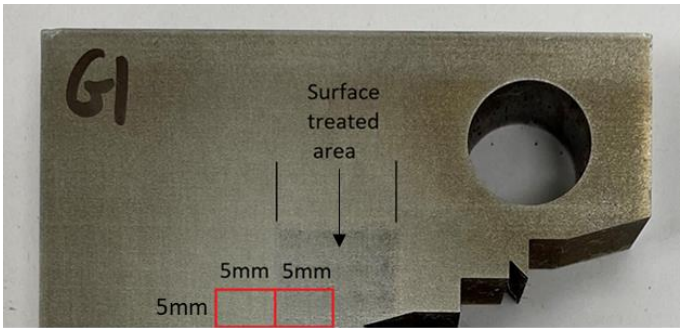

Figure 7.10: An example of the coupon extraction region on a surface treated sample

Analysis of the pole figures in Figure 7.11 shows that the surface treated regions have a higher texture compared to the untreated regions. Moreover, as seen in Figure 7.11 the maximum values of the Multiple of Uniform Density (MUD) are higher in the regions with the surface treatment. Comparison of the pole figures between the two materials shows that the untreated ER100S-1 has considerably higher texture compared to the untreated ER70S-6 material. A quantitative comparison of the texture indices in Table 7.3 also verifies that both surface treatment techniques (i.e. surface rolling and laser shock peening) introduced a higher texture into the WAAM built specimens; however, applying the laser shock peening has increased the texture index on average by 22.5%, whereas for rolling it is 8.3%. Another observation that can be made from Figure 7.12 is that the initial texture index for untreated specimens is higher in vertical specimens made of ER70S-6, compared to the horizontal samples, and for top specimens made of ER100S-1 material, compared to the bottom samples. This agrees with the general observation from the FCG analysis that ER70S-6 WAAM specimens were more sensitive to the extraction orientation[48], while ER100S-1 specimens showed more sensitivity to the extraction location[49]. Finally seen in Table 7.3 and Figure 7.12 is that for both materials examined in this study the jumps in the texture indices from the untreated region to the treated region were found to be generally higher by applying the laser shock peening treatment compared to the surface rolling treatment. It can be seen that the texture index is on average 2.7 times higher in the laser shock peened regions than the rolled specimens.

Specimen ID	Untreated area	Treated area
70-VT-R	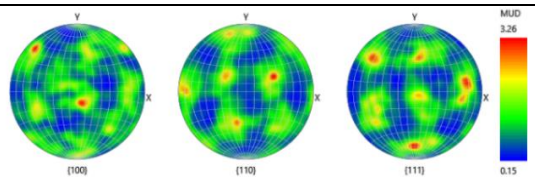	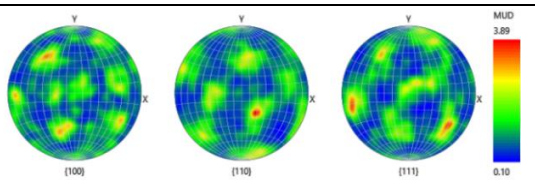
70-HT-R	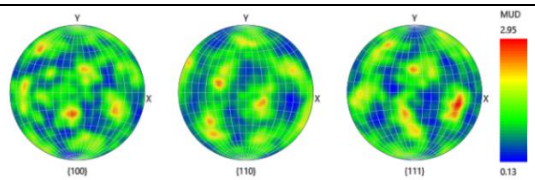	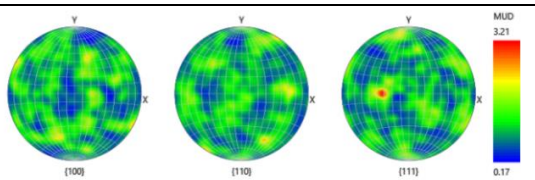

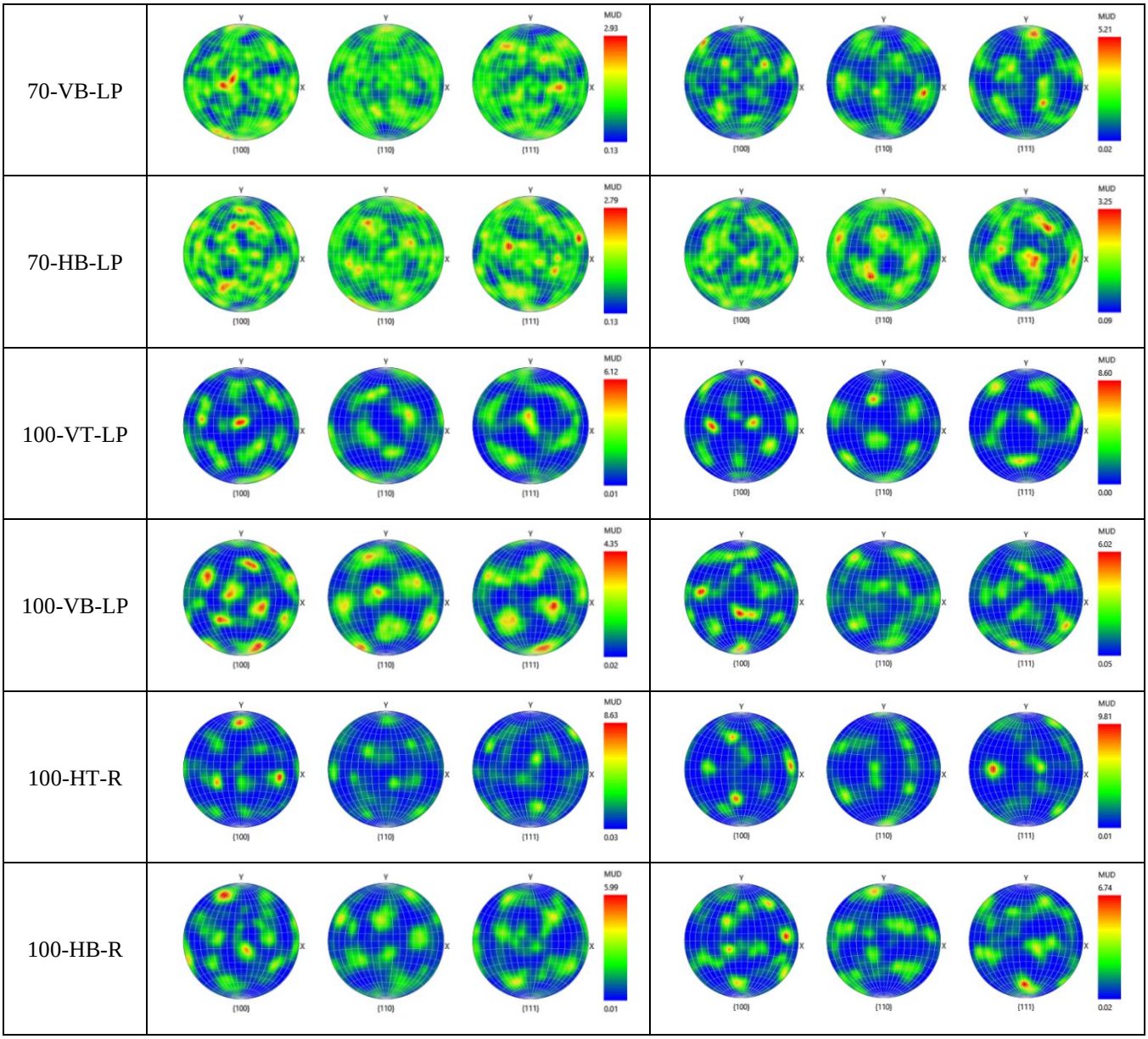

Figure 7.11: Comparison of the pole figures in untreated and treated regions in WAAM built specimens made of ER70S-6 and ER100S-1

Table 7.3: Comparison of the texture indices in untreated and treated regions

Specimen ID	Texture Index		
	Untreated	Treated	Difference
70-VT-R	1.29	1.43	11%
70-HT-R	1.02	1.05	3%
70-VB-LP	1.35	1.82	35%
70-HB-LP	1.04	1.10	6%
100-VT-LP	2.30	2.88	25%
100-VB-LP	1.76	2.19	24%
100-HT-R	2.60	2.89	11%
100-HB-R	2.17	2.34	8%

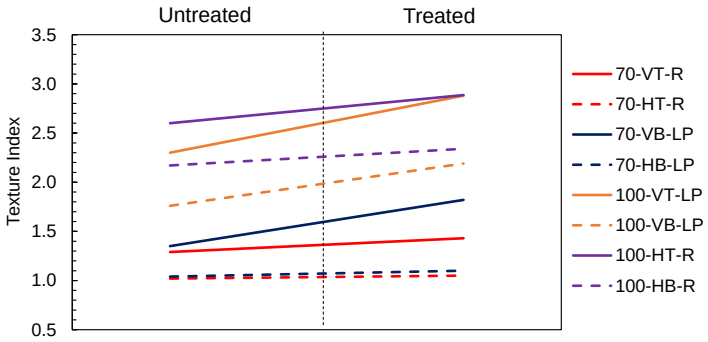

Figure 7.12: Visual representation of the change in the texture indexes from the untreated region (on the left-hand side) to the treated region (on the right-hand side)

The inverse pole figures in Z direction (IPF-Z) were captured for both untreated and treated specimen areas and are shown in Figure 7.13. As seen in this figure, larger grains are observed in ER70S-6 specimens compared to ER100S-1 specimens, which implies higher ductility and toughness parameters and lower strength for ER70S-6 WAAM built components[55]. There is no major grain refinement visible for both materials after applying the surface treatments using the considered treatment parameters. The grain size distribution analysis demonstrated that the total number of grains for ER70S-6 has increased on average by 10% for rolled and 25% for laser shock peened specimens, reducing the mean area of grains by 3% and 13%, respectively. For ER100S-1, the total number of grains raised only by 4% for rolled and 16% for laser shock peened specimens, refining the mean grain area by 15% and 7%, respectively. Finally seen in Figure 7.13 is that the cracking mode in FCG tests performed the WAAM built specimens made of both materials was transgranular.

Specimen ID	Untreated	Treated
70-VT-R	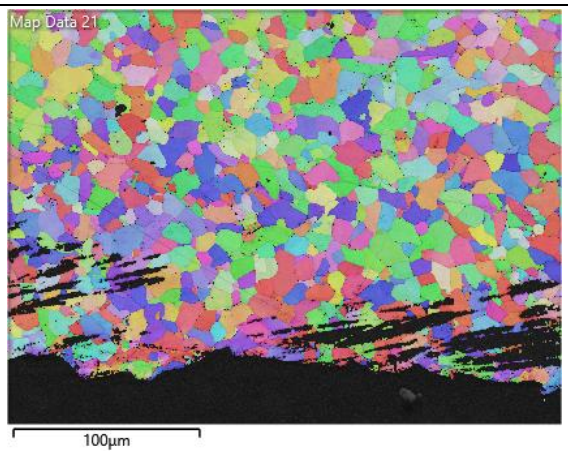	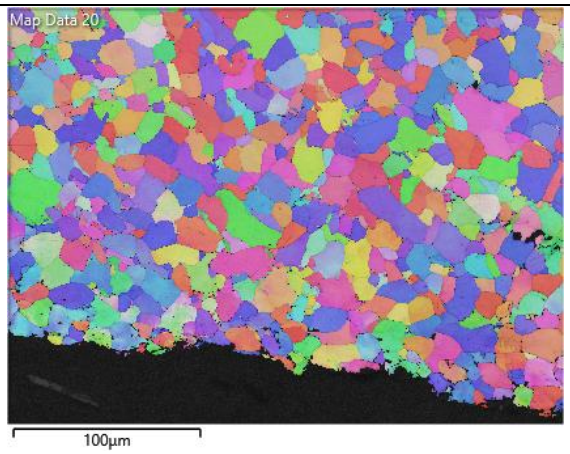

70-HT-R	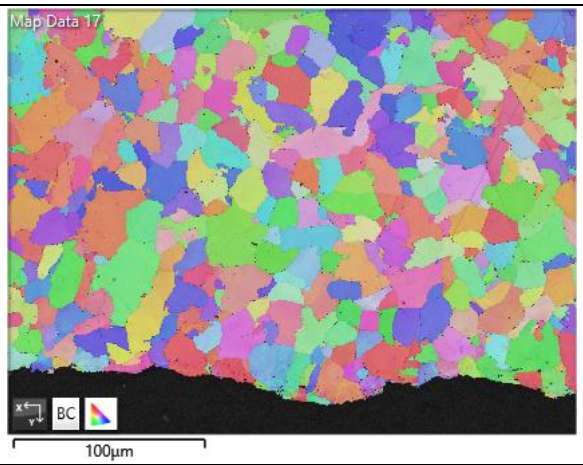	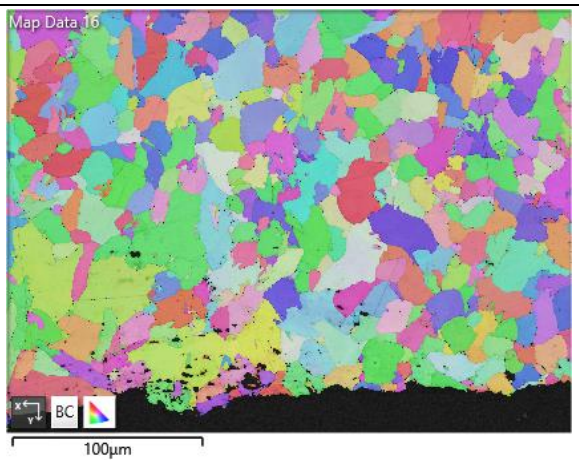
70-VB-LP	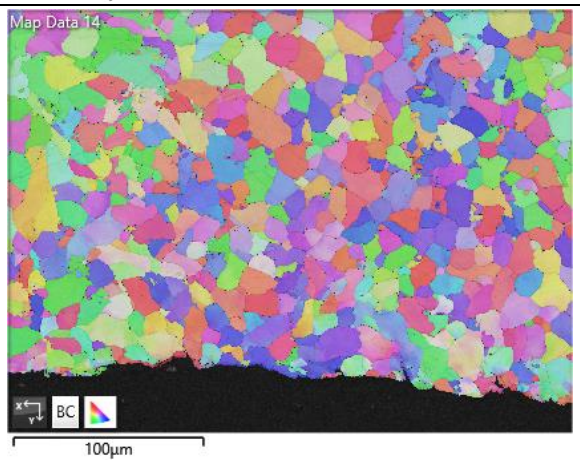	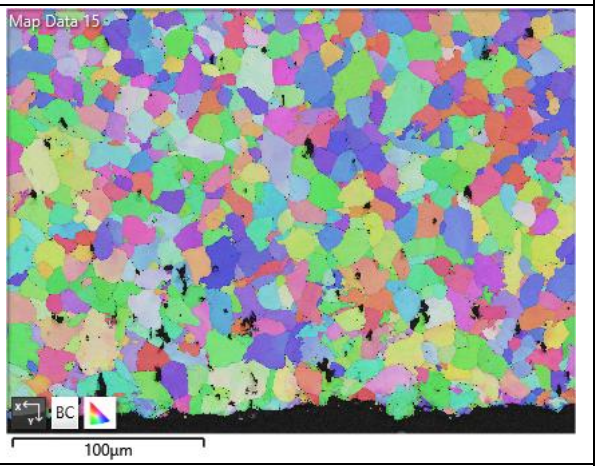
70-HB-LP	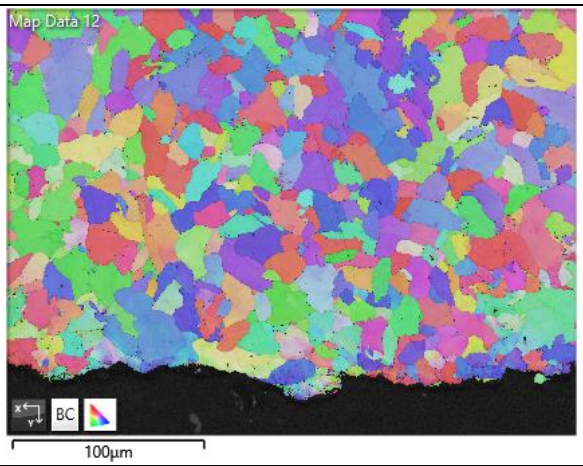	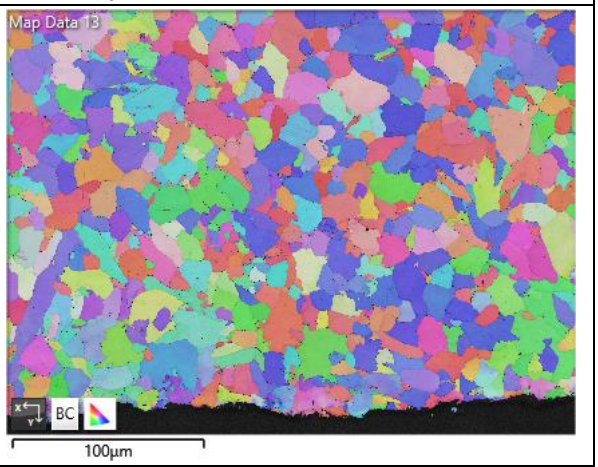
100-VT-LP	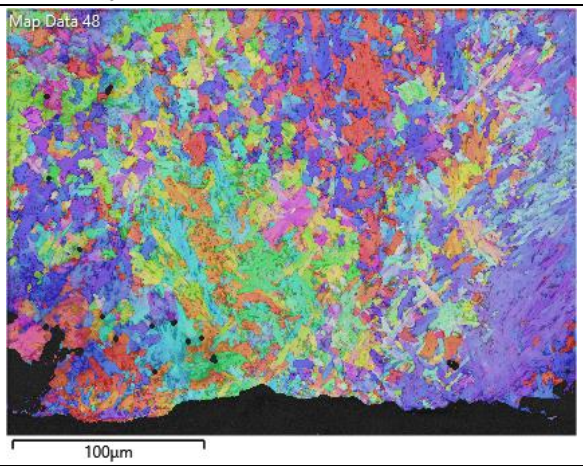	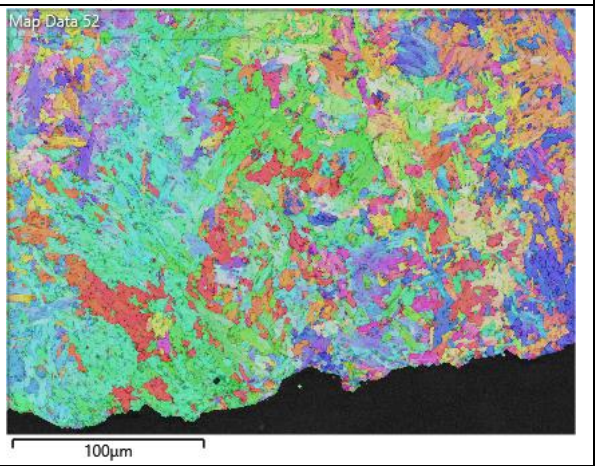

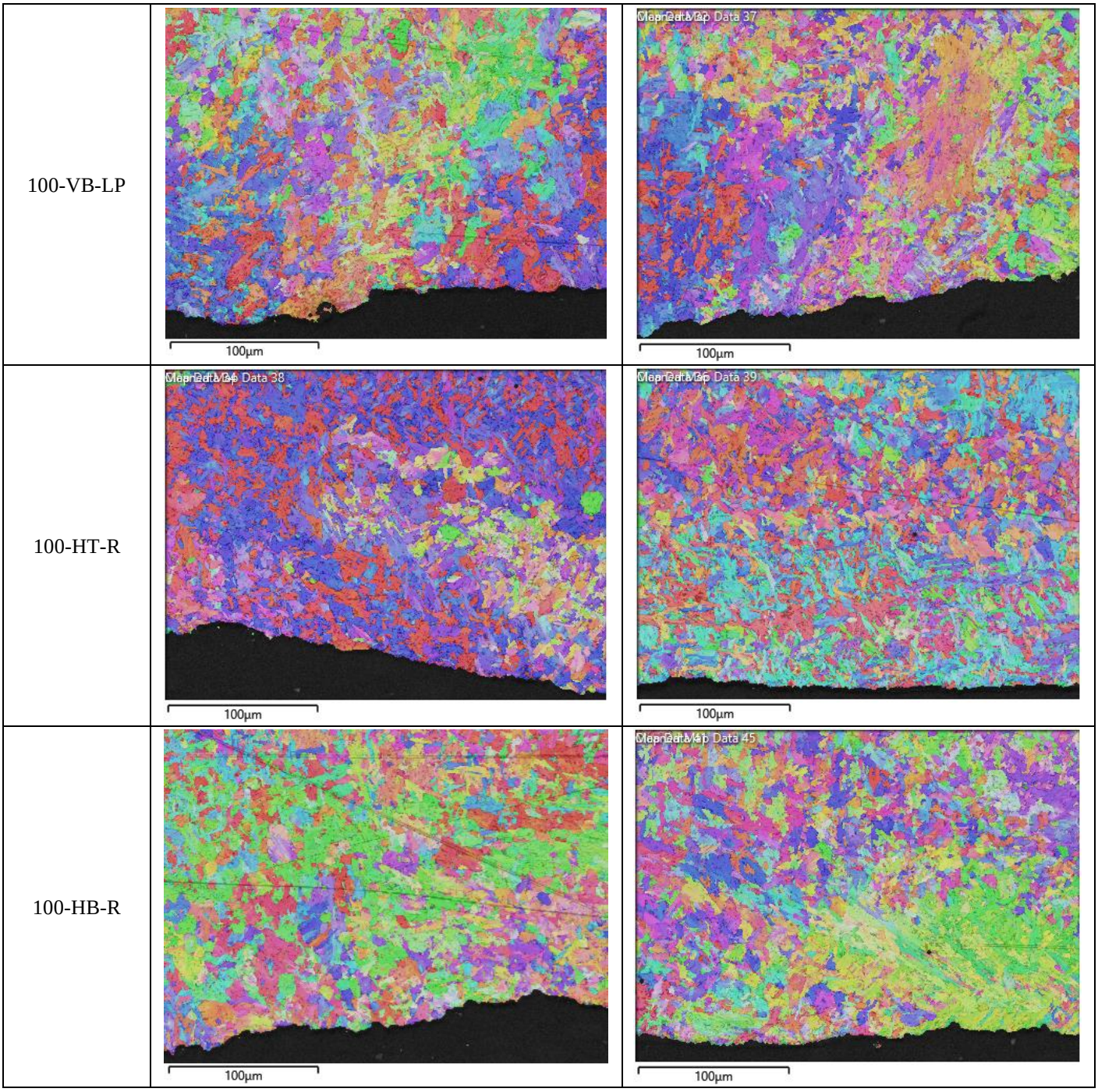

Figure 7.13: Inverse pole figures captured from the untreated and treated regions of WAAM built specimens

Finally, further microstructural analysis was conducted to evaluate the deformation mechanism through residual strain distribution and the results in form of the kernel average misorientation (KAM) maps are shown in Figure 7.14. In this analysis the same step size and settings were used to capture the residual strain distribution maps, therefore the obtained results are directly comparable with each other[56]. It can be seen in Figure 7.14 that the largest deformation, hence a higher level of residual strain, was found along the crack path in ER70S-6 specimens. For ER100S-1 specimens it can be clearly observed in Figure 7.14 that most of deformation in this material is located at the surface of the examined coupon, which is visible by the dominantly

green colour throughout the examined area. Very little difference in residual strains was found between the untreated and treated regions in each specimen.

Specimen ID	Untreated	Treated
70-VB-LP	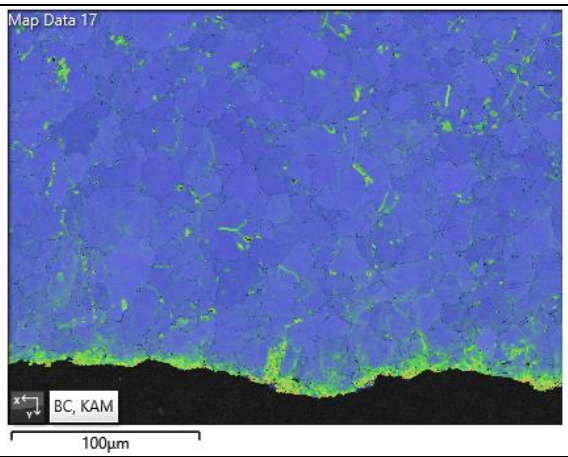	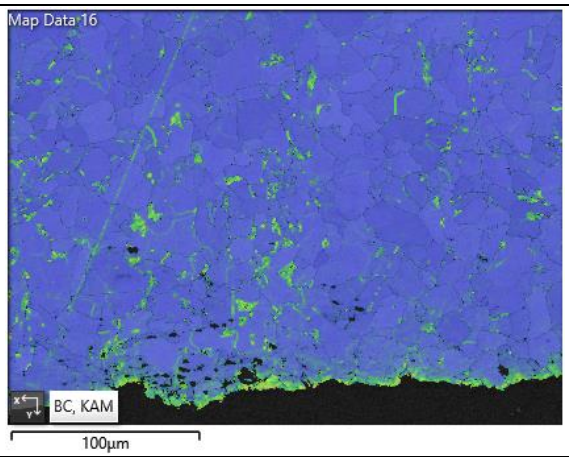
100-VB-LP	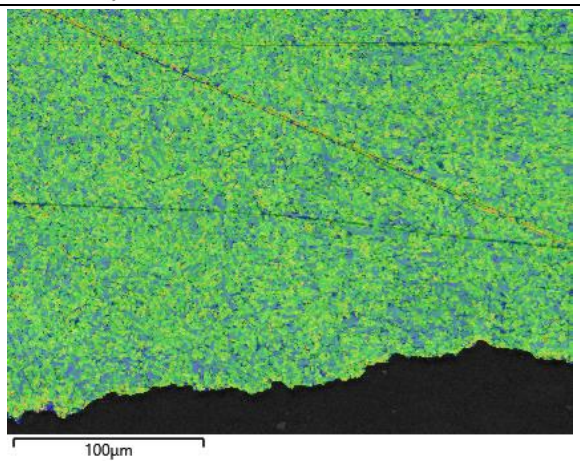	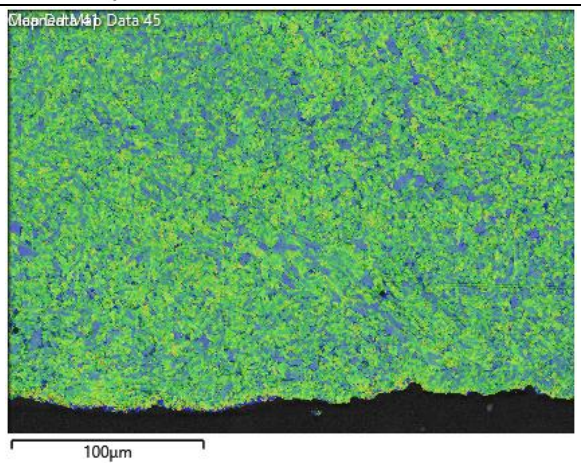

Figure 7.14: Residual strain analysis for WAAM built specimens made of ER70S-6 and ER100S-1

7.1.7. Conclusions

In this study the effects of laser shock peening and surface rolling treatments on the FCG behaviour were comprehensively examined, along with the residual stress distribution and material texture of WAAM built low carbon steel components. The following conclusions can be drawn based on the obtained results from this work:

- For ER70S-6 WAAM built components, both surface treatment techniques have been found to enhance the fatigue performance by reducing the FCG rates in the surface treated area compared to the untreated material.
- For both materials, the laser shock peening technique resulted in the longest fatigue lives compared to the untreated samples. The longest test durations in laser peened specimens were observed in the vertical specimens extracted from the bottom of ER70S-6 and the top of ER100S-1 WAAM walls.
- Application of rolling surface treatment, using the same parameters on both materials, was found to be inefficient for ER100S-1 specimens and resulting in a shorter fatigue life and higher FCG rates compared to the untreated material.

- The surface rolling treatment introduces high residual stresses in the near surface region of ER100S-1 specimens, which resulted in deterioration of FCG performance, whereas laser shock peening induced significant level of compressive residual stresses which were beneficial for fatigue performance and results in lower FCG rates.
- The residual stress measurements through-thickness of treated specimens showed asymmetrical stress distribution with respect to the mid-thickness plane, which can be due to non-symmetrical application of surface treatment techniques.
- The texture was found to increase by applying both surface treatment techniques; however, for laser shock peened specimens the texture index was found on average 2.7 times higher than the rolled specimens. Moreover, untreated specimens made of ER100S-1 material exhibited a higher texture compared to untreated ER70S-6 specimens.
- ER100S-1 has finer grains compared to ER70S-6 specimens while the cracking mode in both materials was found to be transgranular under fatigue loading conditions.
- A larger amount of residual strain was observed throughout ER100S-1 WAAM specimens, whereas in ER70S-6 specimens the highest residual strains were concentrated along the crack path.

7.1.8. Acknowledgements

This work was supported by grant EP/L016303/1 for Cranfield, Oxford, and Strathclyde Universities Centre for Doctoral Training in Renewable Energy Marine Structures – REMS CDT (http://www.rems-cdt.ac.uk/) from the UK Engineering and Physical Sciences Research Council (EPSRC). The authors would like to thank ILL-France for provision of the neutron beamtime for residual stress measurements under https://doi.ill.fr/10.5291/ILL-DATA.1-02-292 and ANSTO (Proposal 13422).

7.1.9. References for paper X

1. Kumar, D., Idapalapati, S., Wang, W. & Narasimalu, S. Effect of Surface Mechanical Treatments on the Microstructure-Property-Performance of Engineering Alloys. *Materials (Basel).* 429–436 (2019).

2. Ersdal, G., Sharp, J. V. & Stacey, A. Ageing and Life Extension of Offshore Structures: The Challenge of Managing Structural Integrity. Available at: https://books.google.no/books?id=tzB6DwAAQBAJ&pg=PA162&lpg=PA162&dq=grinding+life+extension+steels&source=bl&ots=mi7WNDonqm&sig=ACfU3U0IKLdC3UtdrW3JZXUPNkCiFC2eLQ&hl=en&sa=X&ved=2ahUKEwi4mpzh6sf3AhWuS_EDHTA-BQ4Q6AF6BAgPEAM#v=onepage&q=grinding life extens. (Accessed: 5th May 2022)

3. Luong, H. & Hill, M. R. The effects of laser peening and shot peening on high cycle fatigue in 7050-T7451 aluminum alloy. *Mater. Sci. Eng. A* **527**, 699–707 (2010).

4. Gujba, A. K. & Medraj, M. Laser Peening Process and Its Impact on Materials Properties

in Comparison with Shot Peening and Ultrasonic Impact Peening. *Mater. 2014, Vol. 7, Pages 7925-7974* **7**, 7925–7974 (2014).

5. Gao, Y. K. & Wu, X. R. Experimental investigation and fatigue life prediction for 7475-T7351 aluminum alloy with and without shot peening-induced residual stresses. *Acta Mater.* **59**, 3737–3747 (2011).

6. Wang, Z., Jiang, C., Gan, X., Chen, Y. & Ji, V. Influence of shot peening on the fatigue life of laser hardened 17-4PH steel. *Int. J. Fatigue* **33**, 549–556 (2011).

7. Zhang, P. & Lindemann, J. Influence of shot peening on high cycle fatigue properties of the high-strength wrought magnesium alloy AZ80. *Scr. Mater.* **52**, 485–490 (2005).

8. Hatamleh, O., Lyons, J. & Forman, R. Laser and shot peening effects on fatigue crack growth in friction stir welded 7075-T7351 aluminum alloy joints. *Int. J. Fatigue* **29**, 421–434 (2007).

9. Hatamleh, O. A comprehensive investigation on the effects of laser and shot peening on fatigue crack growth in friction stir welded AA 2195 joints. *Int. J. Fatigue* **31**, 974–988 (2009).

10. Ganesh, P., Sundar, R., Kumar, H., Kaul, R., Ranganathan, K., Hedaoo, P., Tiwari, P., Kukreja, L. M., Oak, S. M., Dasari, S. & Raghavendra, G. Studies on laser peening of spring steel for automotive applications. *Opt. Lasers Eng.* **50**, 678–686 (2012).

11. Kloos, K. H., Fuchsbauer, B. & Adelmann, J. Fatigue properties of specimens similar to components deep rolled under optimized conditions. *Int. J. Fatigue* **9**, 35–42 (1987).

12. Altenberger, I., Nalla, R. K., Sano, Y., Wagner, L. & Ritchie, R. O. On the effect of deep-rolling and laser-peening on the stress-controlled low- and high-cycle fatigue behavior of Ti–6Al–4V at elevated temperatures up to 550 °C. *Int. J. Fatigue* **44**, 292–302 (2012).

13. Wong, C. C., Hartawan, A. & Teo, W. K. Deep Cold Rolling of Features on Aero-Engine Components. *Procedia CIRP* **13**, 350–354 (2014).

14. Nalla, R. K., Altenberger, I., Noster, U., Liu, G. Y., Scholtes, B. & Ritchie, R. O. On the influence of mechanical surface treatments—deep rolling and laser shock peening—on the fatigue behavior of Ti–6Al–4V at ambient and elevated temperatures. *Mater. Sci. Eng. A* **355**, 216–230 (2003).

15. Tsuji, N., Tanaka, S. & Takasugi, T. Effect of combined plasma-carburizing and deep-rolling on notch fatigue property of Ti-6Al-4V alloy. *Mater. Sci. Eng. A* **499**, 482–488 (2009).

16. Feldmann, G., Wong, C. C., Wei, W. & Haubold, T. Application of Vibropeening on Aero – Engine Component. *Procedia CIRP* **13**, 423–428 (2014).

17. Rodrigues, T. A., Duarte, V., Miranda, R. M., Santos, T. G. & Oliveira, J. P. Current Status and Perspectives on Wire and Arc Additive Manufacturing (WAAM). *Mater. 2019, Vol. 12, Page 1121* **12**, 1121 (2019).

18. Cunningham, C. R., Flynn, J. M., Shokrani, A., Dhokia, V. & Newman, S. T. Invited review article: Strategies and processes for high quality wire arc additive manufacturing. *Addit. Manuf.* **22**, 672–686 (2018).

19. Dong, P. Residual stresses and distortions in welded structures: a perspective for engineering applications. *https://doi.org/10.1179/174329305X29465* **10**, 389–398 (2013).

20. Dong, P. & Brust, F. W. Welding Residual Stresses and Effects on Fracture in Pressure Vessel and Piping Components: A Millennium Review and Beyond. *J. Press. Vessel Technol.* **122**, 329–338 (2000).

21. Webster, G. A. & Ezeilo, A. N. Residual stress distributions and their influence on fatigue lifetimes. *Int. J. Fatigue* **23**, 375–383 (2001).

22. Rauch, M. & Hascoet, J. Improving additive manufactured surfaces properties with post processing techniques. (2021).

23. McAndrew, A. R., Alvarez Rosales, M., Colegrove, P. A., Hönnige, J. R., Ho, A., Fayolle, R., Eyitayo, K., Stan, I., Sukrongpang, P., Crochemore, A. & Pinter, Z. Interpass rolling of Ti-6Al-4V wire + arc additively manufactured features for microstructural refinement. *Addit. Manuf.* **21**, 340–349 (2018).

24. Colegrove, P. A., Donoghue, J., Martina, F., Gu, J., Prangnell, P. & Hönnige, J. Application of bulk deformation methods for microstructural and material property improvement and residual stress and distortion control in additively manufactured components. *Scr. Mater.* **135**, 111–118 (2017).

25. Colegrove, P. A., Coules, H. E., Fairman, J., Martina, F., Kashoob, T., Mamash, H. & Cozzolino, L. D. Microstructure and residual stress improvement in wire and arc additively manufactured parts through high-pressure rolling. *J. Mater. Process. Technol.* **213**, 1782–1791 (2013).

26. Hönnige, J. R., Colegrove, P. A., Ganguly, S., Eimer, E., Kabra, S. & Williams, S. Control of residual stress and distortion in aluminium wire + arc additive manufacture with rolling. *Addit. Manuf.* **22**, 775–783 (2018).

27. Saboori, A., Piscopo, G., Lai, M., Salmi, A. & Biamino, S. An investigation on the effect of deposition pattern on the microstructure, mechanical properties and residual stress of 316L produced by Directed Energy Deposition. *Mater. Sci. Eng. A* **780**, (2020).

28. Martina, F., Roy, M. J., Szost, B. A., Terzi, S., Colegrove, P. A., Williams, S. W., Withers, P. J., Meyer, J. & Hofmann, M. Residual stress of as-deposited and rolled wire+arc additive manufacturing Ti–6Al–4V components. *Mater. Sci. Technol. (United Kingdom)* **32**, 1439–1448 (2016).

29. Abrão, A. M., Denkena, B., Breidenstein, B. & Mörke, T. Surface and subsurface alterations induced by deep rolling of hardened AISI 1060 steel. *Prod. Eng.* **8**, 551–558 (2014).

30. Munther, M., Martin, T., Tajyar, A., Hackel, L., Beheshti, A. & Davami, K. Laser shock peening and its effects on microstructure and properties of additively manufactured metal alloys: A review. *Eng. Res. Express* **2**, (2020).

31. Sun, R., Li, L., Zhu, Y., Guo, W., Peng, P., Cong, B., Sun, J., Che, Z., Li, B., Guo, C. & Liu, L. Microstructure, residual stress and tensile properties control of wire-arc additive manufactured 2319 aluminum alloy with laser shock peening. *J. Alloys Compd.* **747**, 255–265 (2018).

32. Chi, J., Cai, Z., Wan, Z., Zhang, H., Chen, Z., Li, L., Li, Y., Peng, P. & Guo, W. Effects

of heat treatment combined with laser shock peening on wire and arc additive manufactured Ti17 titanium alloy: Microstructures, residual stress and mechanical properties. *Surf. Coatings Technol.* **396**, 125908 (2020).

33. Luo, S., He, W., Chen, K., Nie, X., Zhou, L. & Li, Y. Regain the fatigue strength of laser additive manufactured Ti alloy via laser shock peening. *J. Alloys Compd.* **750**, 626–635 (2018).

34. Manikandan, M., Mani Prabu, S. S., Jayachandran, S., Akash, K., Palani, I. A. & Karunakaran, K. P. Influence of Laser Shock Peening on Wire Arc Additive Manufactured Low Carbon Steel. 509–516 (2019). doi:10.1007/978-981-32-9425-7_45

35. Lincoln Electric Company, T. *LINCOLN ® ER70S-6 WELDING POSITIONS TYPICAL APPLICATIONS*.

36. *ER100S-G Data Sheet - Bohler Welding*. (2014).

37. Ermakova, A., Mehmanparast, A. & Ganguly, S. A review of present status and challenges of using additive manufacturing technology for offshore wind applications. *Procedia Struct. Integr.* **17**, 29–36 (2019).

38. ASTM E647−13. Standard Test Method for Measurement of Fatigue Crack Growth Rates. *Am. Soc. Test. Mater.* 1–50 (2014). doi:10.1520/E0647-15E01.2

39. American Society for Testing and Materials. ASTME-1820-11: standard test method for measurement of fracture toughness. *Annu. B. ASTM Stand.* 1–55 (2011). doi:10.1520/E1820-18

40. Pi, D., Ermakova, A. & Mehmanparast, A. Numerical Analysis of Surface Rolling Effects on Fatigue Life Enhancement of Wire Arc Additively Manufactured Parts. *J. Multiscale Model.* **2146001**, 1–16 (2022).

41. Pirling, T., Bruno, G. & Withers, P. J. SALSA—A new instrument for strain imaging in engineering materials and components. *Mater. Sci. Eng. A* **437**, 139–144 (2006).

42. Jacob, A., Oliveira, J., Mehmanparast, A., Hosseinzadeh, F., Kelleher, J. & Berto, F. Residual stress measurements in offshore wind monopile weldments using neutron diffraction technique and contour method. *Theor. Appl. Fract. Mech.* **96**, 418–427 (2018).

43. Pynn, R. & Liang, L. Neutron Scattering—A Non-destructive Microscope for Seeing Inside Matter. 15–36 (2009). doi:10.1007/978-0-387-09416-8_2

44. Hutchings, M. T., Withers, P. J., Holden, T. M. & Lorentzen, T. Introduction to the Characterization of Residual Stress by Neutron Diffraction. *Introd. to Charact. Residual Stress by Neutron Diffr.* (2005). doi:10.1201/9780203402818

45. Residual Stress Measurement by X-Ray Diffraction, 2003 Edition. Available at: https://www.sae.org/publications/books/content/hs-784/2003/. (Accessed: 8th April 2022)

46. BS EN 15305:2008 Non-destructive testing. Test method for residual stress analysis by X-ray diffraction - European Standards. Available at: https://www.en-standard.eu/bs-en-15305-2008-non-destructive-testing-test-method-for-residual-stress-analysis-by-x-ray-diffraction/. (Accessed: 8th April 2022)

47. Mehmanparast, A., Brennan, F. & Tavares, I. Fatigue crack growth rates for offshore wind monopile weldments in air and seawater: SLIC inter-laboratory test results. *Mater. Des.* **114**, 494–504 (2017).

48. Ermakova, A., Mehmanparast, A., Ganguly, S., Razavi, J. & Berto, F. Fatigue crack growth behaviour of wire and arc additively manufactured ER70S-6 low carbon steel components. *Int. J. Fract.* (2021). doi:10.1007/s10704-021-00545-8

49. Ermakova, A., Ganguly, S., Razavi, J., Berto, F. & Mehmanparast, A. Experimental investigation of the fatigue crack growth behavior in wire arc additively manufactured ER100S-1 steel specimens. *Fatigue Fract. Eng. Mater. Struct.* (2021). doi:10.1111/FFE.13598

50. Woo, W., Kim, D. K., Kingston, E. J., Luzin, V., Salvemini, F. & Hill, M. R. Effect of interlayers and scanning strategies on through-thickness residual stress distributions in additive manufactured ferritic-austenitic steel structure. *Mater. Sci. Eng. A* **744**, 618–629 (2019).

51. Woo, W., An, G. B., Em, V. T., De Wald, A. T. & Hill, M. R. Through-thickness distributions of residual stresses in an 80 mm thick weld using neutron diffraction and contour method. *J. Mater. Sci.* **50**, 784–793 (2014).

52. Gornyakov, V., Ding, J., Sun, Y. & Williams, S. Understanding and designing post-build rolling for mitigation of residual stress and distortion in wire arc additively manufactured components. *Mater. Des.* **213**, 110335 (2022).

53. Ganesh, P., Sundar, R., Kumar, H., Kaul, R., Ranganathan, K., Hedaoo, P., Raghavendra, G., Anand Kumar, S., Tiwari, P., Nagpure, D. C., Bindra, K. S., Kukreja, L. M. & Oak, S. M. Studies on fatigue life enhancement of pre-fatigued spring steel specimens using laser shock peening. *Mater. Des.* **54**, 734–741 (2014).

54. Lu, J. Z., Luo, K. Y., Zhang, Y. K., Sun, G. F., Gu, Y. Y., Zhou, J. Z., Ren, X. D., Zhang, X. C., Zhang, L. F., Chen, K. M., Cui, C. Y., Jiang, Y. F., Feng, A. X. & Zhang, L. Grain refinement mechanism of multiple laser shock processing impacts on ANSI 304 stainless steel. *Acta Mater.* **58**, 5354–5362 (2010).

55. Ermakova, A., Mehmanparast, A., Ganguly, S., Razavi, J. & Berto, F. Investigation of mechanical and fracture properties of wire and arc additively manufactured low carbon steel components. *Theor. Appl. Fract. Mech.* **109**, 102685 (2020).

56. Ryde, L. Application of EBSD to analysis of microstructures in commercial steels. *Mater. Sci. Technol.* **22**, 1297–1306 (2006).

7.2. Paper XI: The influence of laser shock peening on corrosion-fatigue behaviour of wire arc additively manufactured components

Anna Ermakova[a], Jarryd Braithwaite[b], Javad Razavi[c], Supriyo Ganguly[d], Filippo Berto[c], Ali Mehmanparast[a*]

[a] Department of Naval Architecture, Ocean and Marine Engineering, University of Strathclyde, Glasgow G1 1XQ, United Kingdom

[b] School of Aerospace, Transport and Manufacturing, Cranfield University, Cranfield, MK43 0AL, United Kingdom

[c] Norwegian University of Science and Technology (NTNU), Trondheim, Norway

[d] Welding Engineering and Laser Processing Centre, Cranfield University, Cranfield, MK43 0AL, United Kingdom

Abstract[11]

The need for increased manufacturing efficiency of large engineering structures has led to development of wire arc additive manufacturing (WAAM), which is also known as direct energy deposition (DED) method. One of the main barriers for rapid adoption of the WAAM technology in wider range of industrial applications is the lack of sufficient performance data on the WAAM components for various materials and operational conditions. The present study addresses this essential need by exploring the effects of laser shock peening surface treatment on corrosion-fatigue crack growth (CFCG) life enhancement of WAAM components made of ER70S-6 and ER100S-1 steel wires. The experimental results obtained from this study were compared with the CFCG trends from nominally identical specimens without surface treatment and prove the efficiency of the examined surface treatment method for corrosion-fatigue life enhancement and crack growth retardation of WAAM built steel components, regardless of the material type and specimen orientation. Furthermore, the residual stresses in the WAAM built specimens with and without surface treatment were measured to validate the influence of beneficial residual stresses, arising from surface treatment, on subsequent CFCG behaviour of the material. The residual stress profiles show the beneficial compressive stress fields in the surface treated areas which result in CFCG life enhancement. The results from this study make significant contribution to knowledge by evaluating the suitability of WAAM built steel components for application in offshore environments.

Keywords: Wire Arc Additive Manufacturing; Corrosion-Fatigue; Surface Treatment; Laser Shock Peening; Residual Stress

---

* corresponding author

[11] Submitted manuscript in *Surface & Coatings Technology*. October 2022.

7.2.1. Introduction

Nearly all engineering structures experience some form of cyclic loading condition during their lifetime, which results in fatigue damage. The fatigue performance of engineering structures can be significantly deteriorated in the presence of harsh environmental conditions. For example, the offshore structures in oil and gas, and renewable energy industries are subjected to cyclic loads caused by wind, waves, and current, while they operate in the highly corrosive marine environment[1]. A combination of these factors may lead to premature failure of the structures during their operation, making corrosion-fatigue the main mode of failure for offshore structures. Thus, it is essential to develop new high strength materials and manufacturing techniques to enhance the corrosion-fatigue resistance of offshore structures to extend their operational lifespan. A number of life enhancement techniques have been developed and implemented by various industries in the past, including mechanical and surface treatment methods, to improve the fatigue performance of engineering structures. Grinding is a widely used mechanical technique[2], designed particularly for the weld toes, to reduce high stress concentrations and subsequently increase the fatigue life of the welded component. Moreover, several surface treatment techniques can be used to induce compressive residual stress fields at the outer surface of the component and slow down the crack initiation and propagation processes. A number of surface treatment methods have already been actively implemented in a wide range of engineering applications such as surface rolling[3–7], shot peening[8–12], laser shock peening[13–15] and vibro peening[16]. They differ by the complexity of the treatment process, cost, penetration depth and hence the efficiency, which will also depend on the material properties and industrial application.

Wire arc additive manufacturing (WAAM), which is a type of direct energy deposition (DED) additive manufacturing (AM) technology, is a fabrication process to 3D print large scale metallic parts or repair the damaged components. Compared to conventional manufacturing methods for metals and other DED techniques, WAAM is an advantageous and cost-effective method for fabrication of large scale structures, which can improve the mechanical properties, and enable hybrid manufacturing by involving combination of materials[17,18]. However, on the other hand it presents some challenges, such as complex residual stress profiles and surface roughness, which directly affect the fatigue performance of the WAAM built parts[19–22]. The tensile residual stresses have damaging effect on structural integrity by accelerating the crack initiation and propagation. Therefore, material treatments are often required during deposition process or post- manufacturing to enhance the integrity of WAAM built components. The most common material treatment method that has been examined in the past for life enhancement of WAAM built parts is inter-pass rolling that is usually applied on top of each deposited AM layer, while building the part. Several research groups reported the effectiveness of this method, and its ability to lengthen the fatigue life of WAAM parts made of titanium[23,24], aluminium[25], steel[26] and stainless steel[27]. While inter-pass rolling has proved to enhance the fatigue behaviour of the WAAM built components, it considerably increases the manufacturing time, effort, and cost. Hence, there is need to examine alternative material treatment techniques, particularly post-manufacturing surface treatment processes, to enhance the fatigue response of WAAM built components in much shorter time scales.

Among all surface treatment techniques laser shock peening, which is also known as laser peening (LP), offers a greater penetration depth, hence higher values of induced compressive

residual stresses that subsequently result in higher fatigue resistance in the treated areas[8,13]. This is why LP is usually used for the critical mechanical components, which contain notches, holes, or sharp corners prone to fatigue failure. As reflected in the recent studies, this surface treatment method has great potential to address the main challenges involved in integrity management of WAAM components made of various metallic materials[28]. Laser peening, used as a post-processing method on WAAM built aluminium specimens by Sun et al.[29], showed microstructural refinement and increase in micro-hardness of the examined material, as well as transformation of tensile stresses into compressive stresses, resulting in 72% yield strength improvement. Comparable conclusions were drawn by Luo[30] and Chi[31], on tested WAAM specimens made of titanium, confirming the benefits of LP surface treatment technique[32]. Also, a study by Wang et al.[33] is available on LP treated wrought aluminium specimens, which presented promising results with an increase of corrosion-fatigue life by 29.3% using gradient laser pulse energies. The existing test data available in the literature are mainly focused on aerospace applications, hence why the past research attempts have been conducted on materials such as titanium and aluminium. However, no data is available on life enhancement options for WAAM built steels particularly for industrial applications where the structure is subjected to corrosion-fatigue loading conditions such as offshore structures. The above findings highlight the need for a systematic investigation of the effectiveness of the LP surface treatment technique for corrosion-fatigue life enhancement of WAAM built steel structures to expand the application of the WAAM technology to offshore environments.

In order to fill in the research gap, this study investigates the influence of LP surface treatment technique on corrosion-fatigue crack growth (CFCG) behaviour of WAAM built specimens made with different grades of steel, namely ER70S-6 and ER100S-1. The results obtained from this study are compared with the CFCG performance of nominally identical untreated WAAM specimens to quantify the extent of life enhancement in the presence of LP treatment. Furthermore, the results from CFCG tests were interpreted by measuring the residual stresses in untreated and treated specimens, revealing the cause of the beneficial impact of LP on CFCG behaviour of WAAM specimens.

7.2.2. Specimen fabrication and preparation

- **Manufacturing procedure**

For the current study, two WAAM walls were fabricated, one using the ER70S-6 and one using ER100S-1 steel wires. Four specimens were extracted in total; two from the WAAM wall fabricated using ER70S-6 mild steel[34], and two from WAAM wall made of ER100S-1 steel wire[35]. The chemical composition of both materials employed in this study is presented in Table 7.4. Both WAAM walls were manufactured by the Cold Metal Transfer (CMT) process, using parameters summarised in Table 7.5. The WAAM-CMT system set-up is shown in Figure 7.15, which typically consists of the CMT power source, that feeds the welding wire at a set speed. During this process, the wire is fed through a pre-programmed robotic arm, which also supplies shielding gas, and the electric arc melts the wire and deposits the material onto the base plate with the torch. The base plate was rigidly attached to the working table with clamps that prevented the plate and wall from distortion and bending due to extreme manufacturing temperatures. Once the deposited WAAM wall was cooled to ambient temperature, the clamps

were released. Due to the large thickness of the designed WAAM walls, the oscillation deposition strategy[36] was employed to achieve the thickness of 24 mm (Y-axis in Figure 7.15), with approximate length of 355 mm (X-axis), and height of 140 mm (Z-axis).

Table 7.4: Chemical composition of the steel wires (wt.-%)[34,35]

	C	*Mn*	*Cr*	*Si*	*Ni*	*Mo*	*S*	*P*	*Cu*	*V*
ER70S-6	0.09	<1.60	0.05	0.09	0.05	0.05	0.007	0.007	0.20	0.05
ER100S-1	0.08	1.70	0.20	0.60	1.50	0.50	-	-	-	-

Table 7.5: WAAM-CMT system fabrication parameters

Shielding gas	Ar+20% CO_2
Gas flow rate	15 L/min
Robot travelling speed	7.33 mm/sec
Wire diameter	1.2 mm
Wire feed speed	7.5 m/min
Dwell time	120 sec

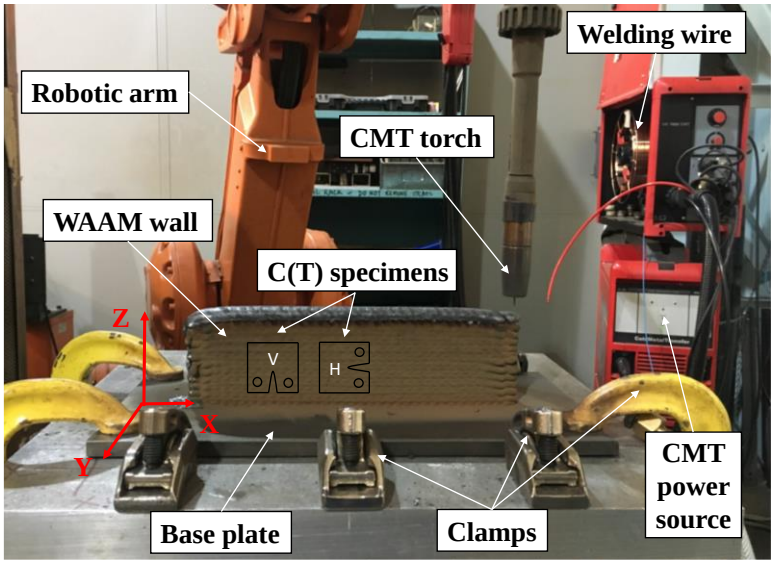

Figure 7.15: WAAM-CMT system set-up with schematic display of specimen orientations

Two compact tension, C(T), specimens were extracted from each WAAM wall using the Electrical Discharge Machining (EDM) method, in vertical (V) and horizontal (H) orientations. Specimens extracted from ER70S-6 wall were denoted as '70', and those from ER100S-1 wall denoted as '100'. As shown in Figure 7.15, in vertical specimen the crack plane is perpendicular to the deposited additive layers, whereas in horizonal specimen it is parallel to the deposited layers. The C(T) specimens were designed according to ASTM E647 standard[37], with the width

of W = 50 mm, height of H = 60 mm, thickness of B = 16 mm and the initial crack length before pre-cracking of a_0 = 17 mm. Also, according to the ASTM 1820 standard[38] knife edges were designed at the crack mouth of the specimens, in order to accommodate a Crack Opening Displacement (COD) gauge for crack growth monitoring during pre-cracking stage, which is required prior to CFCG tests.

- **Surface treatment on WAAM built specimens**

After extraction of the specimens from the WAAM walls, they were subjected to laser shock peening (LP) surface treatment. A small rectangular area with dimensions of 20 × 12 mm^2 was treated on both sides of C(T) specimens as shown in Figure 7.16 (a) and (b), where the area ahead of the notch tip was 20 × 8 mm^2, following the suggestion made in a study by Pi et al[39]. The following parameters were adopted during the treatment: spot size of 3 mm^2, pulse duration of 18 ns, energy level of 8.1 with the power density of J = 5 GW/cm^2, three layers of treatment, providing 300% coverage (presented in Figure 7.16 (a)). Following application of LP surface treatment on C(T) specimens, all four specimens were pre-cracked on Instron 100 kN servo hydraulic machine to approximately 20 mm (a/W=0.4) crack length using the load-decreasing approach, ensuring that the final value of maximum stress intensity factor K_{max} at the end of pre-cracking process is not exceeding the initial K_{max} at the beginning of CFCG tests. At the final stage of specimen preparation, strain gauges were attached at the back of the specimens (Figure 7.16 (c)) and then covered with protective polysulfide coating as shown in Figure 7.16 (d), to perform the crack growth measurements in seawater during CFCG tests, which is explained further in the following section.

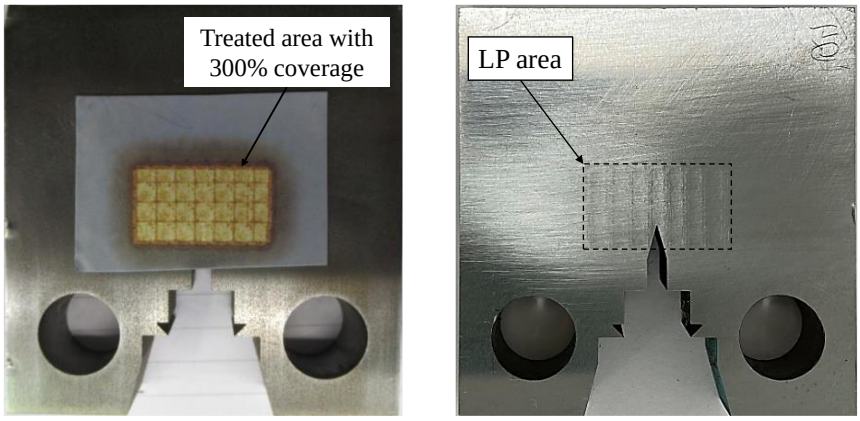

(a) (b)

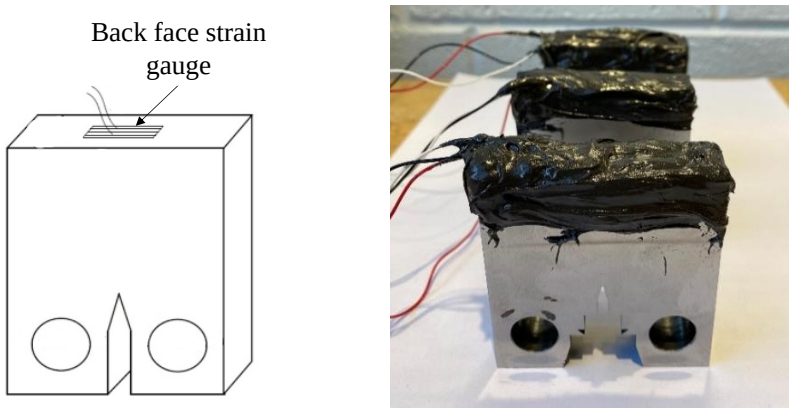

(c) (d)

Figure 7.16: C(T) specimen with (a) a patch after third layer of LP application (300% coverage), (b) after LP treatment process, (c) schematic illustration of BFS location, and (d) protective coating over the strain gauge attached to the back of the sample

7.2.3. Corrosion-fatigue crack growth testing and analysis procedure

- **Test set-up**

To replicate the free-corrosion environment for CFCG tests, the artificial seawater was prepared following the guidelines provided in ASTM D1141-98 standard[40] with deionised water and combination of chemicals, presented in Table 7.6. The pH level of the seawater was monitored to ensure it is maintained between 8.0 and 8.2, and once it dropped below 8.0 it was replaced with freshly prepared seawater. Prior to testing, specimens were soaked in the seawater for at least 24 hours, as advised in the standard. The CFCG test set-up is displayed in Figure 7.17, which consists of 100 kN servo hydraulic Instron machine, seawater tank that contained 60 L of seawater, water pumps that circulated seawater through the environmental chamber attached onto Instron machine at a constant rate of 4 L/min., The C(T) specimen was positioned in the chamber in such a way that the crack plane was constantly immersed in water throughout the test. A chiller maintained the temperature of the seawater between 8.0 and 10.0°C to replicate the conditions in the North Sea[1]. A camera was attached to the machine for constant observation and monitoring of the lengthy CFCG test. The CFCG tests were conducted under load-controlled mode, with the maximum load of P_{max} = 10 kN, load ratio of R = 0.1, and frequency of f = 0.3 Hz, which is typically used for corrosion-fatigue assessment of offshore wind turbine structures[41,42]. As shown in Figure 7.17, the C(T) specimen was marked prior to immersion in water to highlight the desired crack length of 35 mm ($a_{f,c}/W$ = 0.7), which indicated the end of test once the crack grew to length.

Table 7.6: The chemical used for preparation of artificial seawater[40]

	$NaCl$	$MgCl_2$	Na_2SO_4	$CaCl_2$	KCl	$NaHCO_3$	KBr	H_3BO_3	$SrCl_2$	NaF
Concentration (g/L)	24.53	5.20	4.09	1.16	0.695	0.201	1.101	0.027	0.025	0.003

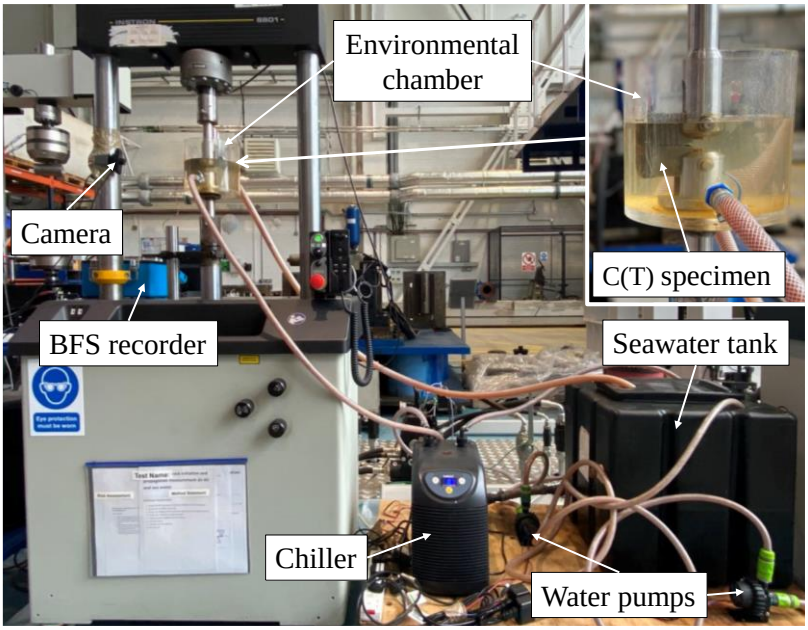

Figure 7.17: Corrosion-fatigue crack growth test set-up

- **Crack growth monitoring technique**

During the CFCG test, the specimen is located underwater limiting the access for visual or mechanical crack monitoring techniques. One of the few known methods for crack estimation applicable for environmental tests is the back face strain (BFS) technique[43,44]. The idea is to correlate the BFS data with the crack length of the specimen. For this purpose, strain gauges are attached to the back of the specimens at the mid-height and mid-thickness, which react to specimen deformation during the test (due to crack growth and hence specimen mouth opening and reduction in stiffness). The data is recorded by a strain gauge indicator recording device (BFS recorder) that monitors the variation in strain at the back of the specimen throughout the test (shown in Figure 7.17). In order to correlate the BFS data recorded during the CFCG test with the crack length, a calibration curve needs to be obtained from the FCG test in air on a nominally identical C(T) specimen. During the FCG calibration test, the BFS data from the strain gauge and the crack length obtained from the COD gauge using the unloading compliance method are recorded simultaneously to plot them against each other and develop empirical correlation for a particular C(T) specimen geometry with a given loading condition.

Therefore, prior to the main CFCG tests, four nominally identical C(T) specimens, with the same design, material, extraction orientations and LP surface treatment were tested in air. Knowing that the BFS calibration curve depends on the loading conditions, the FCG calibration tests were conducted under the exact same loading condition as the CFCG tests, which are summarised in Table 7.7. Four empirical correlations between BFS data and crack length were developed for WAAM ER70S-6 and ER100S-1, vertical and horizontal specimens.

Furthermore, to verify the accuracy of the crack length estimation obtained with the BFS technique, the beach marking (BM) method[45] was implemented during the tests in air and seawater. This method requires reduction of the maximum applied cyclic load and/or frequency for a short period of time during the test, which leaves a visible thin line on the fracture surface of the specimen, which is also known as beach mark. The duration of BM cycles has to be carefully selected to ensure that the crack does not considerably propagate during the process

and hence BFS value remains unchanged. When the BM method is employed, the corresponding value of BFS is recorded. Upon completion of the test, the crack length is measured on the fracture surface of the broken specimen and correlated with corresponding BFS value at particular beach marks. The BM method was first evaluated on the specimens tested for FCG in air. An example of the fracture surface of ER100S-1 specimen with beach marks is shown in Figure 7.18. Once the procedure and required outcome were verified, this method was implemented in the CFCG tests, repeating BM three times throughout each test to generate enough data points to cross-check the results from BFS method. Prior to the test, each C(T) specimen was marked on the outer surface to identify the approximate locations for the three pre-planned beach marks (Figure 7.17). The BM loading conditions for tests in air and seawater are shown in Table 7.7.

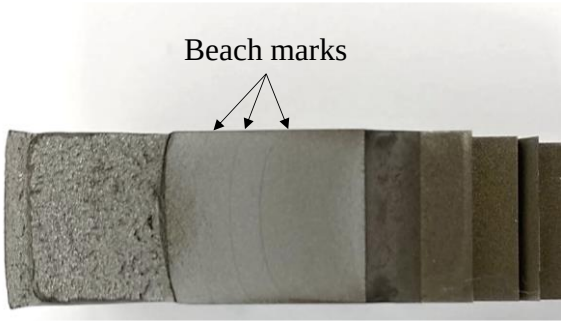

Figure 7.18: Visible beach marks on a broken ER100S-1 specimen FCG tested in air

Table 7.7: Test loading conditions for air and seawater environments

Test environment	The main test condition			Beach marking loading condition		
	P_{max} (kN)	R	f (Hz)	P_{max} (kN)	R	f (Hz)
Air	10	0.1	5	8	0.125	3
Seawater	10	0.1	0.3	8	0.125	0.1

Upon completion of the CFCG tests, all four C(T) specimens were broken open and their fracture surfaces were analysed, as displayed in Figure 7.19. It can be seen in this figure that all specimens were severely corroded during the tests, hence the BM lines were not as visible as the ones on the specimens tested in air (Figure 7.18). Thus, optical microscopy was used to identify the exact location of the marks in CFCG specimens. An example of the calibration curve obtained with the BFS method and additional BM data collected for 70-H-LP specimen are shown in Figure 7.20, which indicates good agreement and confirms the accuracy of crack estimation methods implemented in this study.

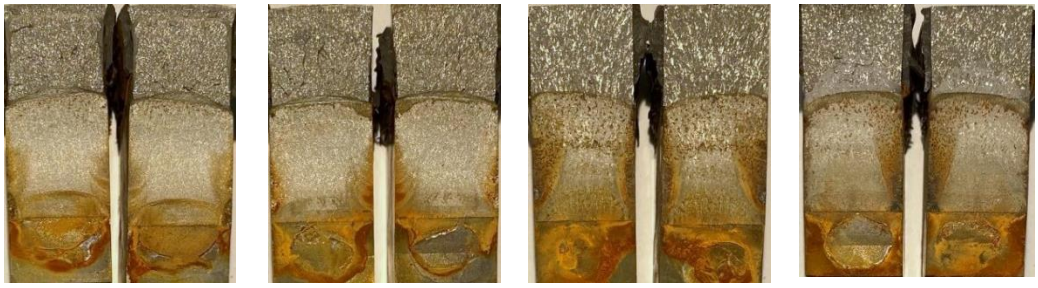

70-V-LP 70-H-LP 100-V-LP 100-H-LP

Figure 7.19: Fracture surfaces of the CFCG tested WAAM specimens

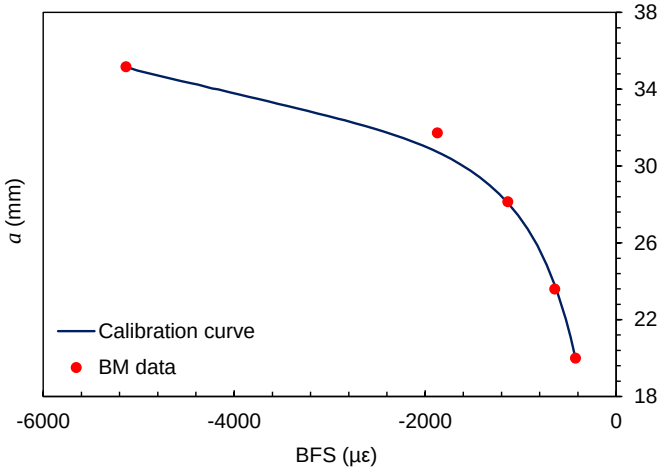

Figure 7.20: Comparison of the produced "crack length vs. BFS" calibration curve with the data collected through BM method for 70-H-LP specimen

- **Data analysis method**

Using the estimated crack lengths from the BFS method and the corresponding number of cycles, the CFCG rates, *da/dN* was computed by applying the secant method for the first three and last three data points, and seven-point incremental polynomial method for the rest of the data points. Subsequently, the stress intensity factor (SIF) was determined using the shape function equation proposed by Mehmanparast et al.[46] and shown in Equation 7.5, where $\alpha = a/W$ is the normalised crack length and ΔP is the difference between the maximum load P_{max} and the minimum load P_{min}.

$$\Delta K = \frac{\Delta P}{BW} \cdot \sqrt{a} \cdot (-372.12\alpha^6 + 1628.60\alpha^5 - 2107.46\alpha^4 + 1304.65\alpha^3 - 391.20\alpha^2 + 54.81\alpha + 7.57) \quad \text{Equation 7.5}$$

7.2.4. Results and discussions

The results obtained from this study on LP surface treated specimens were plotted and compared with the results of CFCG tests on nominally identical specimens without surface treatment from previous studies by Ermakova et al. on ER70S-6[47] and ER100S-1[48] C(T) specimens. The results were initially evaluated in terms of the test duration by plotting the crack length values, *a*, against number of cycles, *N*, as shown in Figure 7.21 (a) for ER70S-6

and Figure 7.21 (b) for ER100S-1 specimens. It can be seen from the figure, that for both materials and orientations the required number of cycles to propagate the crack to 35 mm has increased for LP specimens despite the material type and extraction orientation. Also, it can be noted here that the increase in number of cycles is comparatively smaller for horizontal specimens (2.4% for 70-H-LP and 19.3% for 100-H-LP), whereas for vertical specimens the shift is more pronounced (45.8% for 70-V-LP and 40.5% for 100-V-LP specimens). The obtained trends indicate that the duration of the test increased mostly while the crack was growing through the treated area of the specimens (treated area after pre-cracking is from 20 mm to approximately 25 mm of the crack length) and once the crack extends outside the surface treatment area the trends for treated and untreated specimens gradually become almost parallel. The dashed grey lines in Figure 7.21 (a) and (b) divide the crack growth into two regions: the first one affected by the surface treatment at the crack length of between 20 and approximately 28 mm, and the second area without surface treatment, which starts from a crack length of approximately 28 mm. It is expected that this effect is caused by induced compressive stresses from LP surface treatment technique and redistribution of the initial residual stresses in the specimens, which is discussed in Section 7.2.5.

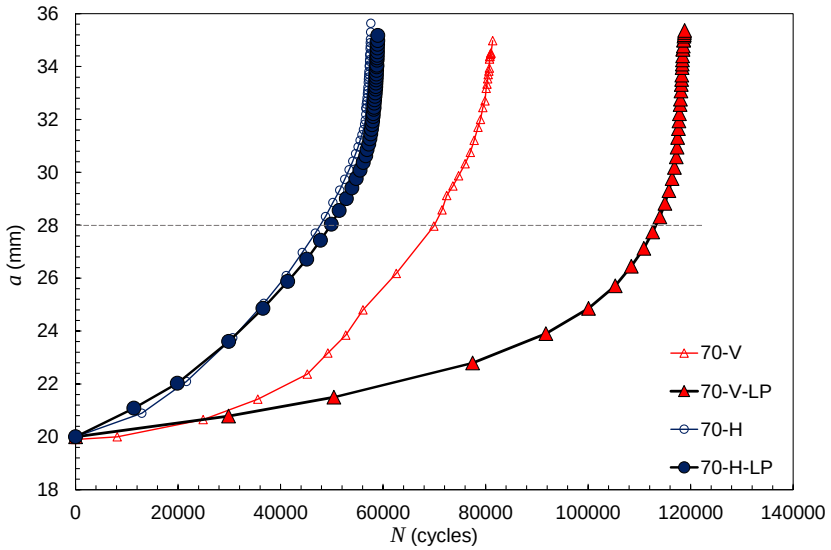

(a)

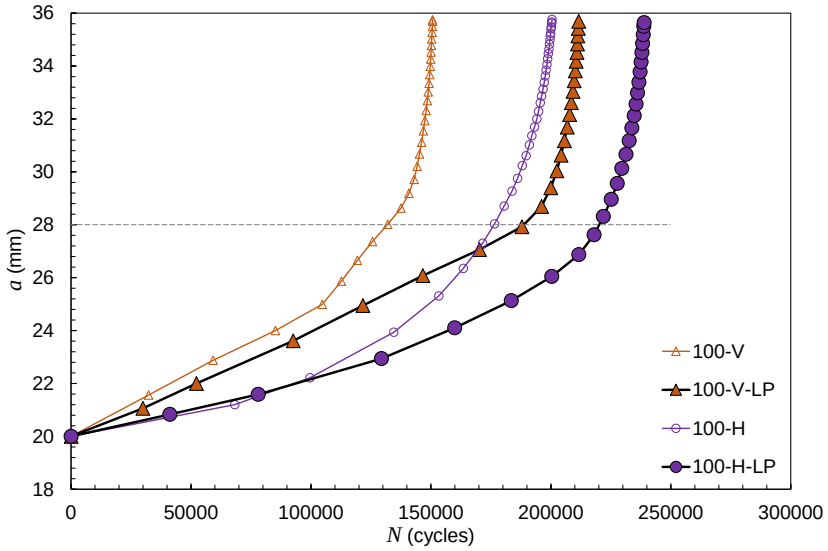

(b)

Figure 7.21: Comparison of the crack growth trends from WAAM specimens with and without LP surface treatment for (a) ER70S-6, and (b) ER100S-1 materials

The CFCG rates calculated for each LP specimen were plotted against the SIF, ΔK, and compared with the results from untreated specimens in Figure 7.22 for (a) ER70S-6 and (b) R100S-1 specimens. It can be observed from the figure that at lower values of ΔK, hence shorter crack lengths, and all four surface treated specimens show improved CFCG rates in comparison with the results for untreated specimens. The best result is presented by 100-V-LP specimen, in which the CFGC rate is lower than untreated specimen throughout the test. It can be seen in Figure 7.22 that the CFCG rate in 100-V-LP specimen was almost constant up to 26 mm (which corresponds to the end of the LP treated area ahead of the crack tip), beyond which the CFCG trend started to follow the trend of the untreated specimen, although with cracking rate of on average 30% lower. Very close trend pattern is also seen for 70-H-LP and its untreated counterpart, where the cracking rates show minor improvement up to 30 mm of crack growth. The trend for 70-V-LP specimen is very steep compared with untreated specimen results, indicating the enhanced crack growth rates for the period of test (up to 26.5 mm) when the crack was growing through the treated area; however, with the increase in the crack length and ΔK values, the corrosion-fatigue resistance was reduced dramatically compared with the corresponding untreated specimen. Similarly, 100-H-LP specimen demonstrated improved CFCG behaviour at the lower values of ΔK (up to 27.6 mm), which is then undertaken by untreated specimen. The above observations lead to a conclusion that despite the material and specimen extraction orientation, corrosion-fatigue life enhancement is achievable by LP surface treatment technique for WAAM fabricated mild steel specimens within the treated area. Furthermore, the effect of LP strongly depends on the size of the treated area, as shown by test duration (Figure 7.21) and CFCG rate (Figure 7.22) results.

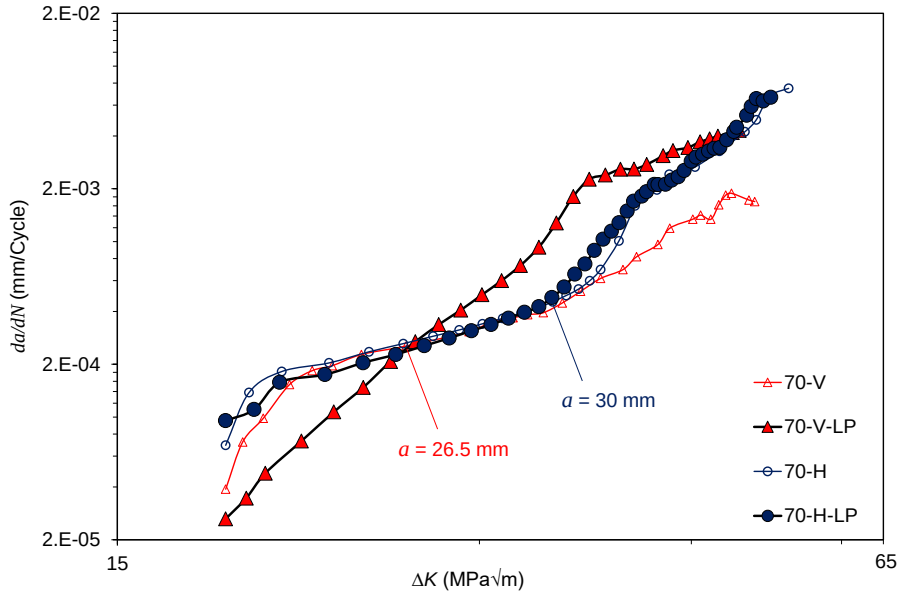

(a)

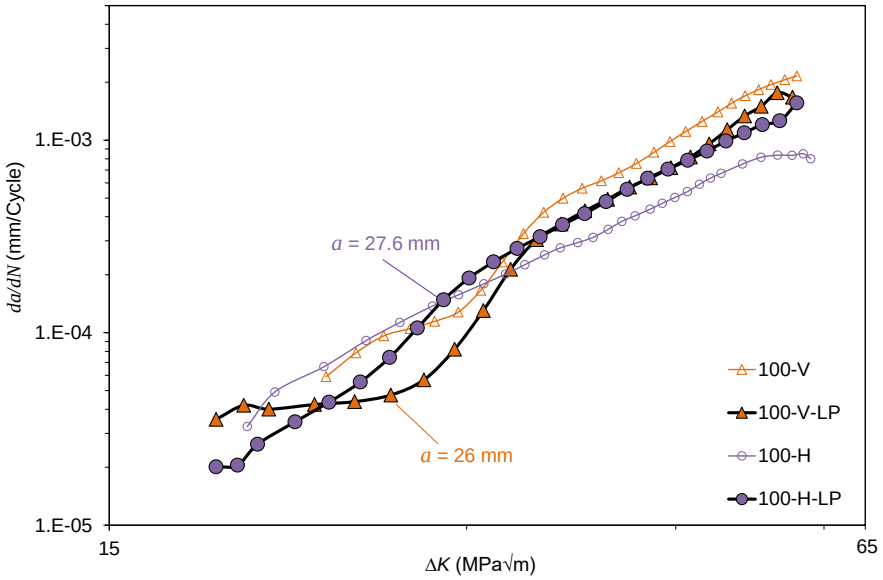

(b)

Figure 7.22: Comparison of CFCG rates from WAAM specimens with and without LP surface treatment for (a) ER70S-6, and (b) ER100S-1 materials

7.2.5. Residual stress assessments

In order to have an accurate interpretation of the CFCG results from the surface treated specimens presented in the previous section, the residual stress distribution profiles in ER100-1 vertical specimens (100-V) were examined before and after LP application. Two non-destructive techniques were used in this study: neutron diffraction and X-ray. The neutron diffraction method offers a deeper penetration depth compared with X-ray, which only captures the stresses in the near surface region. Thus, the changes in residual stress state in the middle

of the specimen caused by LP treatment were measured using the neutron diffraction method while the X-ray technique was used to depict the residual stresses at the outer surface of the treated specimen.

- **Neutron diffraction measurements**

The initial residual stresses in the 100-V untreated specimen were measured by SALSA strain diffractometer at the Institut Laue-Langevin (ILL)-France[49]. After applying the LP surface treatment, the specimen's residual stress profile was measured again using KOWARI strain scanner at the Australia's Nuclear Science and Technology Organisation (ANSTO). A similar set-up was employed in both institutes (see Figure 7.23 (a)), where the neutron wavelength was fixed, and the diffraction angle was measured. Subsequently, the lattice spacing parameter *d* was calculated using Bragg's law[50]:

$$n\lambda_n = 2d_{hkl}sin\theta_{hkl} \qquad \text{Equation 7.6}$$

where *n* is a constant, λ_n is the neutron wavelength, *d* is the lattice spacing or the distance between sets of parallel crystallographic planes characterised by the Miller indices *hkl*, and θ is the scattering angle. In the next step, the elastic strain was computed by employing the changes in the lattice spacing (Δd) using the following equation:

$$\varepsilon_{hkl} = \frac{\Delta d_{hkl}}{d_{0,hkl}} = \frac{d_{hkl} - d_{0,hkl}}{d_{0,hkl}} \qquad \text{Equation 7.7}$$

where d_0 is stress-free value of lattice spacing, measured in the cubes with the dimensions of 5×5×5 mm^3, extracted along the crack path from nominally identical specimens without any surface treatment. The selected approach for d_0 on multiple cube samples, minimises the error in neutron diffraction results by considering the variations in heterogeneous properties of AM specimens.

The residual stress in each direction was then calculated from the residual strains using Hooke's law, which can be described as:

$$\sigma_i = \frac{E}{(1+\nu)(1-2\nu)}\left[(1-\nu)\varepsilon_i + \nu(\varepsilon_j + \varepsilon_k)\right] \qquad \text{Equation 7.8}$$

where *E* is the elastic Young's modulus and ν is Poisson's ratio. The crystallographic values of the elastic modulus and Poisson's ratio used in this study were *E*=210 GPa and ν =0.25[51]. Gauge volume was set to 2×2×2 mm^3 for the experiments, conducting the measurements in the middle of the specimen along the crack propagation line, depicted as L0 in Figure 7.23 (b). In this figure, the stress component of interest is shown with black arrow, which is normal to the crack plane.

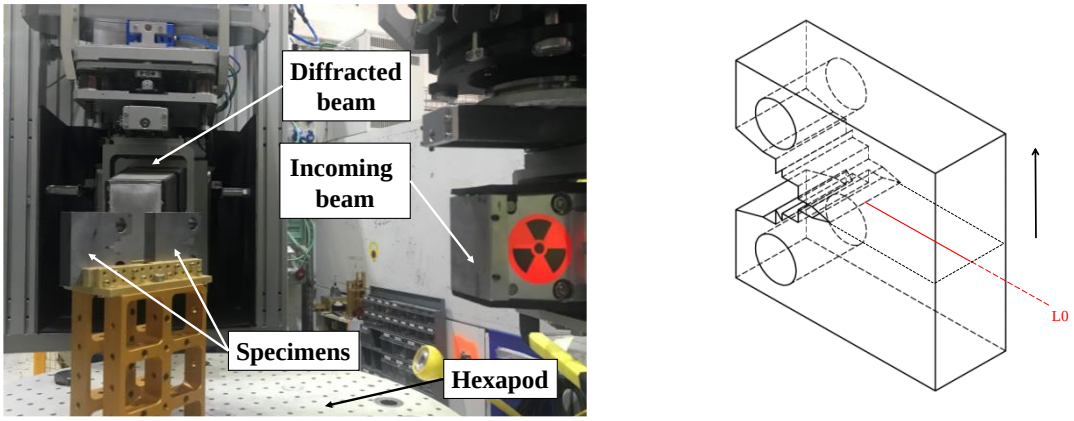

(a) (b)

Figure 7.23: Neutron diffraction (a) measurement set-up, and (b) measurement line with respect to the specimen thickness (the arrow indicates the residual stress component of interest)

- **X-ray diffraction method**

During application of the LP surface technique onto 100-V specimen (100-V-LP), the residual stresses at the outer surface of the specimen were measured using a Malvern Panalytical EMPYREAN diffractometer. The maximum penetration depth of the measurement was 37.5 μm from the outer surface. Similar to the neutron diffraction measurements, surface X-ray (XR) examination was conducted along the crack path, ahead of the crack tip of the specimen, with intervals of 1 mm. The component of stress perpendicular to the crack plane was recorded, which represents the direction of the applied load during the CFCG tests.

- **Residual stress distribution trends**

The residual stress measurement results obtained on ER100S-1 vertical specimen before and after LP treatment are presented in Figure 7.24. It can be seen in this figure that the initial residual stress state at the mid thickness of the specimen (100-V-L0) consists of the tensile stresses up to 407 MPa. However, once the LP was applied (100-V-LP-L0) the residual stresses in the middle of the specimen were reduced dramatically to values between 25 – 86 MPa of tensile stress. As for the residual stresses at the specimen surface measured with X-ray technique (100-V-LP-XR), a clear trend of compressive stresses introduced in the treated area of the specimen can be observed. The maximum amplitude of compressive stress is -134 MPa, and the compressive stress region is up to the crack length of 27 mm, even though the edge of the LP treated zone is at approximately 25 mm. From 27 mm onwards the overall residual stress distribution in the sample is balanced by the tensile stress profile, with the maximum amplitude of 401 MPa, in the region beyond the surface treated area. The observed behaviour of the residual stresses in the specimen caused by the LP application can explain the improved CFCG performance in the LP surface treated region at low values of ΔK, as described in Section 7.2.4. It can be concluded that the enhancement of the CFCG behaviour, which was observed for at least the first 8 mm of the crack propagation region (up to 28 mm crack length) in Figure 7.21 (b) and in almost constant CFCG rates for up to 26 mm of the crack length in Figure 7.22 (b), is corresponding to the compressive stress region highlighted by the X-ray residual stress measurements in the same region up to 27 mm. Subsequently, the CFCG rates deterioration at larger crack length (Figure 7.22 (b)) is corresponding to the tensile stress profile region shown by the X-ray measurements (beyond 27 mm crack length). The influence of residual stresses

on the CFCG rates can be explained through the effective stress intensity factor, presented in Equation 7.9, where K_{ap} is the applied SIF during CFCG tests, and K_{RS} is the residual stress SIF[52].

$$K_{eff} = K_{ap} + K_{RS} \qquad \text{Equation 7.9}$$

It is evident from this equation that the compressive residual stresses, located near the crack tip region, reduce the value of the effective SIF, which simultaneously leads to an exponential reduction in the CFCG rates, as seen in Equation 7.10, where *C* and *m* are material constants. Conversely, the tensile residual stresses could increase the CFCG rates as a result of increase in the effective SIF value.

$$da/dN = C\Delta K^m \qquad \text{Equation 7.10}$$

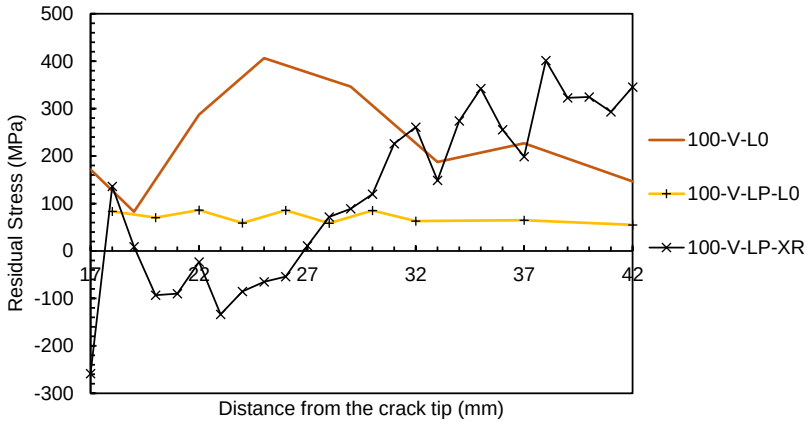

Figure 7.24: Residual stress distribution in 100-V specimen before and after surface treatment

7.2.6. Conclusions

In the current study the effectiveness of surface treatment techniques on CFCG life enhancement of ER70S-6 and ER100S-1 WAAM built C(T) specimens were examined by applying laser shock peening at the area near the crack tip. The CFCG tests were performed on specimens with laser shock peening treatment and the results were compared with those without any surface treatment. The following results and observations could be made from this study:

- Laser shock peening was found to be an efficient method for deceleration of CFCG rates and improvement of lifespan in WAAM built specimens made of two different steel wires examined in this study.
- The laser shock peening surface treatment improved the CFCG performance despite the specimen orientation with respect to WAAM deposition direction.
- The best CFCG life enhancement in both materials was observed in vertical specimens, increasing the lifespan of ER70S-6 specimen by 45.8% and ER100S-1 by 40.5%.

- The effect of laser shock peening is pronounced while the crack is propagating through the treated area and can result in a deteriorating trend within the untreated region of the sample.
- Neutron and X-ray diffraction measurements revealed that LP introduces compressive residual stresses at the outer surface of the specimen within the treated area, which subsequently slows down the CFCG rates and prolongs the lifespan of the surface treated specimens.

7.2.7. Acknowledgements

This work was supported by grant EP/L016303/1 for Cranfield, Oxford, and Strathclyde Universities Centre for Doctoral Training in Renewable Energy Marine Structures – REMS CDT (http://www.rems-cdt.ac.uk/) from the UK Engineering and Physical Sciences Research Council (EPSRC). The authors would like to thank ILL-France for provision of the neutron beamtime for residual stress measurements under https://doi.ill.fr/10.5291/ILL-DATA.1-02-292 and ANSTO (Proposal 13422).

7.2.8. References for paper XI

1. Adedipe, O., Brennan, F. & Kolios, A. Review of corrosion fatigue in offshore structures: Present status and challenges in the offshore wind sector. *Renew. Sustain. Energy Rev.* **61**, 141–154 (2016).

2. Ersdal, G., Sharp, J. V. & Stacey, A. Ageing and Life Extension of Offshore Structures: The Challenge of Managing Structural Integrity. Available at: https://books.google.no/books?id=tzB6DwAAQBAJ&pg=PA162&lpg=PA162&dq=grinding+life+extension+steels&source=bl&ots=mi7WNDonqm&sig=ACfU3U0IKLdC3UtdrW3JZXUPNkCiFC2eLQ&hl=en&sa=X&ved=2ahUKEwi4mpzh6sf3AhWuS_EDHTA-BQ4Q6AF6BAgPEAM#v=onepage&q=grinding life extens. (Accessed: 5th May 2022)

3. Kloos, K. H., Fuchsbauer, B. & Adelmann, J. Fatigue properties of specimens similar to components deep rolled under optimized conditions. *Int. J. Fatigue* **9**, 35–42 (1987).

4. Altenberger, I., Nalla, R. K., Sano, Y., Wagner, L. & Ritchie, R. O. On the effect of deep-rolling and laser-peening on the stress-controlled low- and high-cycle fatigue behavior of Ti–6Al–4V at elevated temperatures up to 550 °C. *Int. J. Fatigue* **44**, 292–302 (2012).

5. Wong, C. C., Hartawan, A. & Teo, W. K. Deep Cold Rolling of Features on Aero-Engine Components. *Procedia CIRP* **13**, 350–354 (2014).

6. Nalla, R. K., Altenberger, I., Noster, U., Liu, G. Y., Scholtes, B. & Ritchie, R. O. On the influence of mechanical surface treatments—deep rolling and laser shock peening—on the fatigue behavior of Ti–6Al–4V at ambient and elevated temperatures. *Mater. Sci. Eng. A* **355**, 216–230 (2003).

7. Tsuji, N., Tanaka, S. & Takasugi, T. Effect of combined plasma-carburizing and deep-rolling on notch fatigue property of Ti-6Al-4V alloy. *Mater. Sci. Eng. A* **499**, 482–488 (2009).

8. Luong, H. & Hill, M. R. The effects of laser peening and shot peening on high cycle fatigue in 7050-T7451 aluminum alloy. *Mater. Sci. Eng. A* **527**, 699–707 (2010).

9. Gujba, A. K. & Medraj, M. Laser Peening Process and Its Impact on Materials Properties in Comparison with Shot Peening and Ultrasonic Impact Peening. *Mater. 2014, Vol. 7, Pages 7925-7974* **7**, 7925–7974 (2014).

10. Gao, Y. K. & Wu, X. R. Experimental investigation and fatigue life prediction for 7475-T7351 aluminum alloy with and without shot peening-induced residual stresses. *Acta Mater.* **59**, 3737–3747 (2011).

11. Zhang, P. & Lindemann, J. Influence of shot peening on high cycle fatigue properties of the high-strength wrought magnesium alloy AZ80. *Scr. Mater.* **52**, 485–490 (2005).

12. Wang, Z., Jiang, C., Gan, X., Chen, Y. & Ji, V. Influence of shot peening on the fatigue life of laser hardened 17-4PH steel. *Int. J. Fatigue* **33**, 549–556 (2011).

13. Hatamleh, O., Lyons, J. & Forman, R. Laser and shot peening effects on fatigue crack growth in friction stir welded 7075-T7351 aluminum alloy joints. *Int. J. Fatigue* **29**, 421–434 (2007).

14. Hatamleh, O. A comprehensive investigation on the effects of laser and shot peening on fatigue crack growth in friction stir welded AA 2195 joints. *Int. J. Fatigue* **31**, 974–988 (2009).

15. Ganesh, P., Sundar, R., Kumar, H., Kaul, R., Ranganathan, K., Hedaoo, P., Tiwari, P., Kukreja, L. M., Oak, S. M., Dasari, S. & Raghavendra, G. Studies on laser peening of spring steel for automotive applications. *Opt. Lasers Eng.* **50**, 678–686 (2012).

16. Feldmann, G., Wong, C. C., Wei, W. & Haubold, T. Application of Vibropeening on Aero – Engine Component. *Procedia CIRP* **13**, 423–428 (2014).

17. Rodrigues, T. A., Duarte, V., Miranda, R. M., Santos, T. G. & Oliveira, J. P. Current Status and Perspectives on Wire and Arc Additive Manufacturing (WAAM). *Mater. 2019, Vol. 12, Page 1121* **12**, 1121 (2019).

18. Cunningham, C. R., Flynn, J. M., Shokrani, A., Dhokia, V. & Newman, S. T. Invited review article: Strategies and processes for high quality wire arc additive manufacturing. *Addit. Manuf.* **22**, 672–686 (2018).

19. Dong, P. Residual stresses and distortions in welded structures: a perspective for engineering applications. *https://doi.org/10.1179/174329305X29465* **10**, 389–398 (2013).

20. Dong, P. & Brust, F. W. Welding Residual Stresses and Effects on Fracture in Pressure Vessel and Piping Components: A Millennium Review and Beyond. *J. Press. Vessel Technol.* **122**, 329–338 (2000).

21. Webster, G. A. & Ezeilo, A. N. Residual stress distributions and their influence on fatigue lifetimes. *Int. J. Fatigue* **23**, 375–383 (2001).

22. Rauch, M. & Hascoet, J. Improving additive manufactured surfaces properties with post

processing techniques. (2021).

23. Colegrove, P. A., Donoghue, J., Martina, F., Gu, J., Prangnell, P. & Hönnige, J. Application of bulk deformation methods for microstructural and material property improvement and residual stress and distortion control in additively manufactured components. *Scr. Mater.* **135**, 111–118 (2017).

24. Martina, F., Roy, M. J., Szost, B. A., Terzi, S., Colegrove, P. A., Williams, S. W., Withers, P. J., Meyer, J. & Hofmann, M. Residual stress of as-deposited and rolled wire+arc additive manufacturing Ti–6Al–4V components. *http://dx.doi.org/10.1080/02670836.2016.1142704* **32**, 1439–1448 (2016).

25. Hönnige, J. R., Colegrove, P. A., Ganguly, S., Eimer, E., Kabra, S. & Williams, S. Control of residual stress and distortion in aluminium wire + arc additive manufacture with rolling. *Addit. Manuf.* **22**, 775–783 (2018).

26. Colegrove, P. A., Coules, H. E., Fairman, J., Martina, F., Kashoob, T., Mamash, H. & Cozzolino, L. D. Microstructure and residual stress improvement in wire and arc additively manufactured parts through high-pressure rolling. *J. Mater. Process. Technol.* **213**, 1782–1791 (2013).

27. Saboori, A., Piscopo, G., Lai, M., Salmi, A. & Biamino, S. An investigation on the effect of deposition pattern on the microstructure, mechanical properties and residual stress of 316L produced by Directed Energy Deposition. *Mater. Sci. Eng. A* **780**, (2020).

28. Munther, M., Martin, T., Tajyar, A., Hackel, L., Beheshti, A. & Davami, K. Laser shock peening and its effects on microstructure and properties of additively manufactured metal alloys: A review. *Eng. Res. Express* **2**, (2020).

29. Sun, R., Li, L., Zhu, Y., Guo, W., Peng, P., Cong, B., Sun, J., Che, Z., Li, B., Guo, C. & Liu, L. Microstructure, residual stress and tensile properties control of wire-arc additive manufactured 2319 aluminum alloy with laser shock peening. *J. Alloys Compd.* **747**, 255–265 (2018).

30. Luo, S., He, W., Chen, K., Nie, X., Zhou, L. & Li, Y. Regain the fatigue strength of laser additive manufactured Ti alloy via laser shock peening. *J. Alloys Compd.* **750**, 626–635 (2018).

31. Chi, J., Cai, Z., Wan, Z., Zhang, H., Chen, Z., Li, L., Li, Y., Peng, P. & Guo, W. Effects of heat treatment combined with laser shock peening on wire and arc additive manufactured Ti17 titanium alloy: Microstructures, residual stress and mechanical properties. *Surf. Coatings Technol.* **396**, 125908 (2020).

32. Manikandan, M., Mani Prabu, S. S., Jayachandran, S., Akash, K., Palani, I. A. & Karunakaran, K. P. Influence of Laser Shock Peening on Wire Arc Additive Manufactured Low Carbon Steel. 509–516 (2019). doi:10.1007/978-981-32-9425-7_45

33. Wang, C., Luo, K., Bu, X., Su, Y., Cai, J., Zhang, Q. & Lu, J. Laser shock peening-induced surface gradient stress distribution and extension mechanism in corrosion fatigue life of AISI 420 stainless steel. *Corros. Sci.* **177**, 109027 (2020).

34. Lincoln Electric Company, T. *LINCOLN ® ER70S-6 WELDING POSITIONS TYPICAL APPLICATIONS*.

35. *ER100S-G Data Sheet - Bohler Welding*. (2014).

36. Ermakova, A., Mehmanparast, A. & Ganguly, S. A review of present status and challenges of using additive manufacturing technology for offshore wind applications. *Procedia Struct. Integr.* **17**, 29–36 (2019).

37. ASTM E647−13. Standard Test Method for Measurement of Fatigue Crack Growth Rates. *Am. Soc. Test. Mater.* 1–50 (2014). doi:10.1520/E0647-15E01.2

38. American Society for Testing and Materials. ASTME-1820-11: standard test method for measurement of fracture toughness. *Annu. B. ASTM Stand.* 1–55 (2011). doi:10.1520/E1820-18

39. Pi, D., Ermakova, A. & Mehmanparast, A. Numerical Analysis of Surface Rolling Effects on Fatigue Life Enhancement of Wire Arc Additively Manufactured Parts. *J. Multiscale Model.* **2146001**, 1–16 (2022).

40. International, A. D1141-98 Standard Practice for the Preparation of Substitute Ocean Water. *ASTM Int.* **98**, 1–3 (2013).

41. Henderson, A. Hydrodynamic Loading of Offshore Wind Turbines. (2003).

42. Jacob, A., Mehmanparast, A., D'Urzo, R. & Kelleher, J. Experimental and numerical investigation of residual stress effects on fatigue crack growth behaviour of S355 steel weldments. *Int. J. Fatigue* **128**, 105196 (2019).

43. Adedipe, O., Brennan, F. & Kolios, A. Corrosion fatigue load frequency sensitivity analysis. *Mar. Struct.* **42**, 115–136 (2015).

44. Newman, J. C., Yamada, Y. & James, M. A. Back-face strain compliance relation for compact specimens for wide range in crack lengths. *Eng. Fract. Mech.* **78**, 2707–2711 (2011).

45. Hou, C. Y. Fatigue analysis of welded joints with the aid of real three-dimensional weld toe geometry. *Int. J. Fatigue* **29**, 772–785 (2007).

46. Mehmanparast, A., Brennan, F. & Tavares, I. Fatigue crack growth rates for offshore wind monopile weldments in air and seawater: SLIC inter-laboratory test results. *Mater. Des.* **114**, 494–504 (2017).

47. Ermakova, A., Ganguly, S., Razavi, J., Berto, F. & Mehmanparast, A. Corrosion-fatigue crack growth behaviour of wire arc additively manufactured ER70S-6 steel parts in marine environments. *Eur. J. Mech. A/Solids* **96**, 104739 (2022).

48. Ermakova, A., Ganguly, S., Razavi, J., Berto, F. & Mehmanparast, A. Corrosion-fatigue crack growth behaviour of wire arc additively manufactured ER100S-1 steel specimens. *Eng. Fail. Anal.* **138**, 106362 (2022).

49. Pirling, T., Bruno, G. & Withers, P. J. SALSA—A new instrument for strain imaging in engineering materials and components. *Mater. Sci. Eng. A* **437**, 139–144 (2006).

50. Pynn, R. & Liang, L. Neutron Scattering—A Non-destructive Microscope for Seeing Inside Matter. 15–36 (2009). doi:10.1007/978-0-387-09416-8_2

51. Hutchings, M. T., Withers, P. J., Holden, T. M. & Lorentzen, T. Introduction to the Characterization of Residual Stress by Neutron Diffraction. *Introd. to Charact. Residual Stress by Neutron Diffr.* (2005). doi:10.1201/9780203402818

52. Barsoum, Z. & Barsoum, I. Residual stress effects on fatigue life of welded structures

using LEFM. *Eng. Fail. Anal.* **16**, 449–467 (2009).

7.3. Conclusion

This chapter was dedicated to investigation of the effects of laser shock peening and surface rolling treatments on the fatigue crack growth, and residual stress distribution of WAAM built low carbon steel components.

The study concluded that both surface treatment techniques enhanced fatigue performance in ER70S-6 WAAM built components by reducing FCG rates in the treated area compared to untreated material. Laser shock peening yielded the longest fatigue lives, particularly in vertical specimens extracted from the bottom of ER70S-6 and the top of ER100S-1 WAAM walls. However, the rolling surface treatment proved inefficient for ER100S-1 specimens, leading to shorter fatigue life and higher FCG rates.

The surface rolling treatment introduced high residual stresses in the near-surface region of ER100S-1 specimens, causing a deterioration of FCG performance, while laser shock peening induced significant compressive residual stresses, beneficial for fatigue performance, and resulted in lower FCG rates.

The research also revealed that both surface treatment techniques increased material texture, with laser shock peened specimens exhibiting a texture index 2.7 times higher than rolled specimens. Moreover, untreated ER100S-1 specimens had a higher texture compared to untreated ER70S-6 specimens.

In terms of corrosion-fatigue crack growth, laser shock peening proved effective for decelerating CFCG rates and improving the lifespan of WAAM built specimens made of ER70S-6 and ER100S-1 materials. The treatment significantly enhanced CFCG performance regardless of the specimen orientation with respect to WAAM deposition direction. The best CFCG life enhancement was observed in vertical specimens, increasing the lifespan of ER70S-6 by 45.8% and ER100S-1 by 40.5%.

Neutron and X-ray diffraction measurements confirmed that laser shock peening introduced compressive residual stresses at the outer surface of the treated specimens, effectively slowing down the CFCG rates and prolonging the lifespan of the surface treated specimens within the surface treated area.

Overall, this study provides valuable insights into the benefits of laser shock peening and surface rolling treatments in improving the fatigue and corrosion-fatigue performance of WAAM built components, supporting their potential application in various industries, particularly in offshore structures.

Chapter 8 : Conclusions and Future Work

8.1. Conclusions

The structural integrity assessment of WAAM built steel specimens made with ER70S-6 and ER100S-1 steel wires has been conducted in this work. In order to fully characterise the performance of WAAM components made of two materials, the following tests have been conducted: hardness, tensile, fracture toughness, fatigue crack growth, corrosion-fatigue crack growth, uniaxial, torsion and multiaxial fatigue. The sensitivity of the results to specimen extraction location and orientation has been analysed and discussed. The possibility of life enhancement of WAAM built steel specimens have been examined by applying two distinct surface treatment techniques, namely surface rolling and laser shock peening, onto the specimens surface. The fatigue life of the surface treated specimens was analysed and compared with the behaviour of untreated specimens. Moreover, the residual stress trends were determined for specimens before and after the surface treatment application to explore its impact on the fatigue life enhancement. The main conclusions, outcomes, and observations of the research are presented below.

Tensile properties

- ER70S-6 WAAM built specimens presented a lower yield strength of 377.5 MPa and higher tensile strain at failure of 0.74 mm/mm compared to ER100S-1 with 537 MPa and 0.64 mm/mm, respectively.
- The UTS value for ER100S-1 on average is 816.5 MPa, which is 56% higher than for ER70S-6 specimens.
- The stress-strain curves are slightly higher (by 6.8%) for specimens with horizontal orientation than for vertical regardless of the tested materials. Hence, tensile properties of the tested WAAM steel specimens are sensitive to the extracted orientation of the specimen.
- Specimens extracted from ER100S-1 walls exhibit slightly higher yield and UTS than S355 wrought steel specimens, whereas ER70S-6 shows similar performance as S355.
- The corrosive environment leads to reduction of yield strength of the material for both examined WAAM materials.

Hardness properties

- The hardness value varies for each deposited WAAM layer.
- ER100S-1 steel has higher hardenability than ER70S-6.
- Hardness value for ER100S-1 on average is 251 HV, which is about 61% higher than for ER70S-6 (155 HV).
- The hardness trend along the WAAM wall height is almost constant for ER100S-1 material and shows slight hardening at the top and bottom of WAAM wall for ER70S-6 steel.

- The repeated thermal cycles associated with WAAM manufacturing process presented more pronounced effect in material with lower yield stress (ER70S-6), hence hardness variability.
- Hardness of wrought S355 steel, reported in the literature, is equal to the average between ER70S-6 and ER100S-1 hardness values.

Fracture toughness properties

- Specimens extracted from ER70S-6 WAAM walls exhibit much higher *R*-curve trends than ER100S-1, hence more energy is required to propagate the crack in ER70S-6 specimens.
- The average fracture toughness values for ER70S-6 and ER100S-1 are 420 kJ/m^2 and 49 kJ/m^2, respectively.
- The comparison of fracture toughness *R*-curves shows that behaviour of both materials does not depend on extracted orientation of the specimens.
- Moreover, the performance of ER70S-6 WAAM specimens is not sensitive to the specimen's extraction location.
- Specimens extracted from the bottom of ER100S-1 WAAM walls present 48% lower values of fracture toughness than specimens extracted from the top, thus fracture toughness of ER100S-1 specimens is sensitive to the location on the WAAM built wall.
- Fracture toughness of ER70S-6 specimens is twice lower than wrought S355 steels.
- The corrosive environment increases the fracture toughness *R*-curve trends for both tested materials.
- The fracture toughness value for ER100S-1 corroded specimens is 61% higher than for specimen without environmental exposure.

Fatigue crack growth characteristics

- FCG behaviour of the tested ER70S-6 specimens was not sensitive to the extraction location from the WAAM wall, however, depends on the specimen orientation.
- The observation for tested ER100S-1 specimens is the opposite, as FCG performance highly depends on extraction location of the specimens, instead of orientation. Though, the orientation of the specimen affects the shape of the FCG trend and level of scatter. Irregular wavy FCG pattern was observed in ER100S-1 vertical specimens, which is caused by crack propagation through boundaries between adjacent WAAM layers.
- Different load levels for FCG tests introduce variations in ER70S-6 WAAM built specimens response. Horizontal specimens exhibit twice longer fatigue life under applied load of 10 kN, whereas when the load is increased to 11 kN, the vertical specimens withstand fatigue life of 1.3 times longer instead.
- The collected FCG data for both materials in present research fall below the recommended BS7910 trends.
- Further comparison of FCG trends for WAAM specimens with performance of wrought S355 shows that FCG curves for ER70S-6 vertical specimens fall slightly higher than the average results for wrought S355. Results for horizontal ER70S-6 and bottom

ER100S-1fall close with the upper bound of S355 steel data. Top ER100S-1 specimens present the best FCG rates, which are equal or below the bottom bound for S355 steels.

Corrosion-fatigue crack growth characteristics

- CFCG rates for ER70S-6 specimens are sensitive to specimen location, whereas for ER100S-1 there is sensitivity to specimen orientation. This behaviour is opposite to observations in results from FCG tests in air.
- The obtained CFCG trends for both examined materials in this research fall below BS7910 recommended crack growth lines.
- Similarly, to FCG results in air, the CFCG rates for ER70S-6 fall slightly above (bottom specimens) or on top (top specimens) of existing test data on CFCG performance of S355 wrought and HAZ steels. The trends for ER100S-1 specimens overlap with the cloud of S355 data.
- The corrosion-fatigue life of ER70S-6 WAAM built specimens is three times longer than S355 HAZ steel, and 9.7 times longer for ER100S-1 specimens.

Uniaxial, torsion and multiaxial fatigue properties

- Uniaxial, torsion and multiaxial fatigue response of ER100S-1 WAAM specimens is not dependant on specimen orientation. Fatigue results for ER70S-6 specimens demonstrated variability based on orientation of the extracted specimens, and better fatigue strength was presented by vertical specimens under uniaxial loading conditions, however, horizontal specimens were more fatigue resistant under torsion and multiaxial load.
- As expected, the uniaxial fatigue strength for both materials was higher than torsion fatigue strength, with the lowest strength under multiaxial load.
- Uniaxial, torsion and multiaxial fatigue strength of ER100S-1 WAAM built specimens on average is 1.4, 1.3 and 1.5 times higher than for ER70S-6, respectively.
- The S-N curves for both tested materials are conservatively predicted by DNV C1 design curve for structures with continuous welds.
- Comparison of fatigue performance of ER70S-6 WAAM steel is similar with existing data on S355 and other carbon steels, whereas ER100S-1 specimens show beneficial behaviour when compared with fatigue data on wrought steels.

Life enhancement

- Laser shock peening surface treatment technique have been found effective for fatigue life enhancement of both WAAM steels, decelerating FCG and CFCG rates and improving the lifespan of the specimens by up to 45.8%.
- The profound effect of LP is observed while the crack is propagating through the treated area of the specimen, which declines once the crack enters the untreated area.
- Rolling surface treatment technique was reported as less efficient for improving the FCG performance of ER70S-6 WAAM specimens than LP. Application of rolling

technique was inefficient on ER100S-1 specimens, leading to higher FCG rates and shorter lifespan.

- The residual stress measurements revealed that rolling technique introduces high torsion stresses near the surface of the specimen that cause deterioration of FCG life. While LP forms compressive stresses in the treated area that beneficially affect the FCG performance.
- Through-thickness residual stress measurements demonstrate small asymmetry in stress distribution in surface treated areas of the specimens. This can be related to non-symmetrical application of the surface treatment techniques or material inhomogeneity.
- Application of rolling and laser peening surface techniques increases the texture. LP improves the texture index 2.7 times higher than rolling.

Microstructure analysis

- ER100S-1 WAAM built specimens demonstrate finer grains compared with ER70S-6.
- Both materials showed transgranular cracking mode under fatigue loading conditions.
- In FCG tests, ER70S-6 specimens presented high residual strain concentrated along the crack propagation path. However, in ER100S-1 specimens, residual strain was observed throughout the specimen thickness.
- The microstructural deformation mechanisms in FCG and CFCG tests strongly depend on specimen orientation. Vertical specimens are more heterogenous, as the crack travels through different WAAM layers.
- Fracture surfaces after uniaxial, torsion, multiaxial fatigue tests did not reveal any significant variations between vertical and horizontal specimens for both materials, presenting common fatigue features observed in wrought materials.
- Tested specimens were examined throughout the research and found to be almost defect-free. Some minor defects were observed with diameter smaller than 30 μm.

General conclusions

- Throughout the research it has been observed that the performance of WAAM built components highly depends on extraction location and orientation, which in turn depends on the performed test, load level and environment. This confirms the importance of creating a new data base for all new AM techniques and materials, without generalisation based on similar materials and manufacturing methods.
- The WAAM technique examined in this research has shown a great potential for applications in offshore structures, in particular for manufacturing and repair of offshore wind turbines. Furthermore, the inspected types of steel ER70S-6 and ER100S-1 have presented the comparable or beneficial mechanical and fatigue properties compared with the performance of currently used S355 wrought steels, thus can be considered as substitution for production of critical components or components with complex geometry and hence expensive manufacturing cost, such as flanged connections.

8.2. Future work

A comprehensive test programme was conducted in the current research to characterise the behaviour of WAAM built ER70S-6 and ER100S-1 specimens. Nevertheless, some additional work needs to be done for better overall understanding on performance of WAAM steel specimens. A few suggestions arising from the current study are listed below.

Based on the allocated timeframe to complete the research, the number of specimens produced and tested were limited. Therefore, it is suggested to conduct repeat tests (minimum three) to confirm the preliminary trends presented in this thesis, verify level of scatter, and expand the available testing database for the new WAAM technique and materials. Particularly focusing on orientation/location sensitivity analysis for each tested property. Moreover, different load levels can be investigated to learn the material response.

Location dependence analysis was not performed in tensile and uniaxial, torsion and multiaxial fatigue tests, which is recommended to be completed in future work, to fully understand the behaviour of steel components extracted from different parts of WAAM walls.

Tensile properties of corroded WAAM steel specimens need to be examined, in order to accurately design the specimen for fracture toughness tests and validate the blunting and exclusion lines for fracture toughness values determination. Furthermore, other mechanical and fatigue properties of WAAM steel specimens previously exposed to corrosive environment can be determined, for further considerations of such materials and manufacturing method in marine applications.

Examination of residual stresses in more specimens with various location/orientation combinations before and after surface treatment application will help to predict and control FCG and CFCG response and enable life enhancement possibilities of WAAM built steel specimens. Hence, additional ND through-thickness and X-ray near surface measurements are suggested in future work.

A comprehensive economic study must be undertaken to assess the feasibility of adopting WAAM technique and materials for offshore structures, comparing them with the current costs incurred through conventional manufacturing methods. Furthermore, this study can identify the potential parts of interest with reduced levelised cost to initiate the adoption of WAAM process within the offshore industry.

Appendix: Other co-authored papers

Appendix consists of the following papers:

Paper XII: A review of life extension strategies for offshore wind farms using technoeconomic assessments

Paper XIII: Numerical analysis of surface rolling effects on fatigue life enhancement of wire arc additively manufactured parts

Paper XII: A review of life extension strategies for offshore wind farms using technoeconomic assessments

Benjamin Pakenham[a], Anna Ermakova[a] and Ali Mehmanparast[a]*

[a] Offshore Renewable Energy Engineering Centre, Cranfield University, Cranfield MK43 0AL, UK

Abstract[12]

The aim of this study is to look into the current information surrounding decommissioning and life extension strategies in the offshore wind sector and critically assess them to make informed decisions upon completion of the initial design life in offshore wind farms. This was done through a two-pronged approach by looking into the technical aspects through comprehensive discussions with industrial specialists in the field and also looking into similar but more mature industries such as the Offshore Oil and Gas sector. For the financial side of the assessment, a financial model was constructed to help portray a possible outcome to extend the life for a current offshore wind farm, using the existing data. By employing a techno-economic approach for critical assessment of life extension strategies, this study demonstrates the advantages and disadvantages of each strategy and looks to inform the offshore wind industry the best course of action for current wind farms, depending on their size and age.

Keywords: Decommissioning; Life extension; Repowering; Offshore structures; Wind power

* corresponding author

[12] *Energies*. 2021, 14(7), 1936. (DOI: 10.3390/en14071936)

Paper XIII: Numerical analysis of surface rolling effects on fatigue life enhancement of wire arc additively manufactured parts

Dingkun Pi[a], Anna Ermakova[a,b*], Ali Mehmanparast[a,b]

[a] Offshore Renewable Energy Engineering Centre, Cranfield University, Cranfield, MK43 0AL, UK

[b] Department of Naval Architecture, Ocean and Marine Engineering, University of Strathclyde, Glasgow G1 1XQ, United Kingdom

Abstract[13]

With the advancements in the additive manufacturing (AM) technologies, it is expected that fast and efficient production using the AM techniques will gradually replace the traditional manufacturing processes. An important consideration in the design and life assessment of AM built parts is the asset integrity management and in particular fatigue life enhancement of such components. Surface rolling treatment is known to be an efficient way to introduce deep compressive residual stresses into engineering components, and therefore it has been considered as a practical and effective life enhancement technology. In this study, the surface rolling effects on the fatigue life enhancement of wire arc additively manufactured (WAAM) parts has been investigated. For this purpose, a compact tension specimen geometry was modelled in ABAQUS and the rolling process was simulated by means of finite element simulations to predict the extent of compressive residual stresses induced into a WAAM built part. The simulation results have been discussed in terms of the beneficial effects of surface rolling on fatigue life enhancement of WAAM built parts.

Keywords: WAAM, Rolling effects, FEA.

* corresponding author

[13] *Journal of Multiscale Modelling*. 2022. (DOI: 10.1142/S175697372146001X)